
Numerical Investigation of Rotors in Floating Ring Bearings using Co-Simulation

Numerische Untersuchung von Rotoren in Schwimmbuchsenlagern mittels Co-Simulation

Gerrit Edgar Nowald

Darmstadt, November 2018



TECHNISCHE
UNIVERSITÄT
DARMSTADT



Numerical Investigation of Rotors in Floating Ring Bearings using Co-Simulation

Vom Fachbereich Maschinenbau
an der Technischen Universität Darmstadt
zur Erlangung des Grades
eines Doktor-Ingenieurs (Dr.-Ing.)
genehmigte

Dissertation

von
Gerrit Edgar Nowald, M.Sc.
aus Darmstadt

Berichterstatter: Prof. Dr.-Ing. Bernhard Schweizer

Mitberichterstatter: Prof. Dr. rer. nat. Michael Schäfer

Tag der Einreichung: 12.06.2018

Tag der mündlichen Prüfung: 10.10.2018

Darmstadt, 2018

D17

Nowald, Gerrit Edgar:

Numerical Investigation of Rotors in Floating Ring Bearings using Co-Simulation

Darmstadt, Technische Universität Darmstadt

Tag der mündlichen Prüfung: 10.10.2018

Jahr der Veröffentlichung auf TUprints: 2018

URN: urn:nbn:de:tuda-tuprints-81865



Veröffentlicht unter CC BY-NC-ND 4.0 International

<https://creativecommons.org/licenses/by-nc-nd/4.0/>

Vorwort

Diese Arbeit entstand während meiner Zeit als wissenschaftlicher Mitarbeiter am *Institut für Angewandte Dynamik* von Prof. Schweizer. Die erfolgreiche Durchführung einer Promotion erfordert die Unterstützung vieler Personen, denen ich an dieser Stelle herzlich danken möchte.

Meinem Doktorvater Prof. Schweizer danke ich für das Angebot des spannenden Forschungsthemas, für die intensive fachliche Betreuung bei gleichzeitig eingeräumter Freiheit sowie das entgegengesetzte Vertrauen in der Lehre und bei Industrieprojekten. Prof. Markert danke ich dafür, dass er mein Interesse an der Dynamik, der Strukturdynamik und insbesondere der Rotordynamik geweckt hat und mich langfristig an das Institut gebunden hat. Prof. Schäfer danke ich für die bereitwillige Übernahme des Koreferats, das vermittelte Wissen über Numerik und den angenehmen Kontakt.

Dr. Robert Schmoll danke ich für zahlreiche Telefonate zu den Themen dynamisch-statische Solverkopplung und Co-Simulation sowie die produktive Zusammenarbeit. Dr. Aydin Boyaci danke ich für die intensive fachliche Betreuung zu Beginn meiner Arbeit. Dr. Daixing Lu danke ich für seine grenzenlose Geduld und seine schnelle Hilfe bei vielen administrativen und technischen Problemen. Für das Korrekturlesen danke ich Dr. Bastian Pfau, Marcel Bauer, Dr. Robert Schmoll und ganz besonders Victoria. Meinen Kollegen Dr. Dirk Simon und Dr. Jan Kratochvil danke ich für viele tiefgreifende fachliche Diskussionen. Dr. Jens Bauer danke ich für das entgegengebrachte Vertrauen und den gewährten Freiraum für die Vorbereitung zur Disputation. Timm Schröder und Gregor Knust danke ich für das gemeinsame Laufen, das in den letzten Jahren ein großer Ausgleich zur Arbeit war. Für fachlichen Austausch und Zerstreung danke ich meinen ehemaligen Kollegen Marcel Bauer, Huaxin Dong, Dr. Wolfgang Köhl, Jan Kraft, Dr. Andreas Lehn, Marcel Mahner, Tobias Meyer, Dr. Bastian Pfau, Dr. Benjamin Siegl und Pascal Zeise.

In den letzten Jahren habe ich studentische Arbeiten von Patrick Stolzenburg, Abdulmecit Küçükdümlü, Jens Jungblut, Oliver Jorg, Michael Zeitler, Marcel Bauer, Huaxin Dong und Florian Narrog betreut oder mitbetreut, was mir immer viel Freude bereitet und neue Perspektiven eröffnet hat. Auch dafür Danke.

Ein Großer Dank gebührt Maria Rauck und Helga Lorenz im Sekretariat, deren Tür immer offen stand und die mir bei jedem administrativem Problem zur Seite standen.

Meinen Freunden, Eltern und Verwandten danke ich für Ihre Unterstützung wenn ich Sie am meisten gebraucht habe.

Victoria danke ich dafür dass sie immer an mich geglaubt und mir unermüdlich Rückhalt gegeben hat.

Darmstadt, im November 2018

Gerrit Nowald

Abstract

In this work, the nonlinear oscillation behavior of rotors in floating ring bearings is investigated numerically by means of transient run-up simulations. Non plain bearing designs are considered, which are commonly used in turbocharger applications. Furthermore, a mass-conserving cavitation model based on two-phase theory is employed, which is well suited for transient journal motions due to subsynchronous oscillations. Special axial boundary conditions are introduced, which better reflect open-ended bearings. In contrast to classical cavitation approaches, which assume degassing of dissolved air as the main mechanism, this boundary condition leads to sucking-in of air from the surroundings during squeeze motion of the journal. The numerical model is separated into a rotor and a bearing model, which are implemented in commercial software tools. Both subsystems are joined by means of one of two coupling methods, which enables the creation of detailed, easily interchangeable and updateable subsystems. Dynamic-static solver coupling is used for rotors in single film bearings with non mass-conserving cavitation models. An explicit co-simulation approach is employed for rotors in floating ring bearings or bearings with a mass-conserving cavitation model. In the first case, only the rotor subsystem is time-dependent. In the latter case, both subsystems are time-dependent and are solved with their respective solvers. All time-dependent subsystems use stable, implicit BDF solvers. The rotor is modeled using multibody dynamics software. The partial differential equation of the bearing subsystem is discretized with the Finite Element method, which yields high flexibility concerning the gap geometry.

The influences of the bearing geometry and different parameters are investigated using a symmetric JEFFCOTT rotor. Also, an asymmetric, heavy turbocharger is considered. A non mass-conserving penalty cavitation approach yields a smooth pressure profile. The run-up behavior and the stability threshold are almost identical to the often-used half-SOMMERFELD (GÜMBEL) condition. The hydrodynamic pressure in pockets or grooves is negligible due to their large gap size. However, the hydrostatic pressure has to be considered, which can stabilize or destabilize the system, depending on the lubricant supply geometry. The differences between non mass-conserving and the mass-conserving cavitation model are small for purely synchronous oscillations due to small unbalance. The two-phase model yields a lower stability threshold rotor speed, which is further decreased for open-ended bearings. Non mass-conserving models implicitly assume that the bearing gap is completely filled with lubricant at all times. During squeeze motion, the pressure build-up upon load-reversal is instantaneous. The pressure build-up is delayed for the mass-conserving cavitation model, which yields reduced radial damping. Furthermore, the circumferential extend of the pressure profile during whirl motion is smaller due to cavitation for mass-conserving models. The load carrying capacity is decreased, which may often yield higher eccentricities during subsynchronous oscillations. A two-phase model can also entail a different bifurcation behavior, especially for insufficient lubricant supply.

Contents

Vorwort	iii
Abstract	iv
List of Figures	ix
List of Tables	x
Symbol Directory	xi
1. Introduction	1
1.1. Literature Review	4
1.2. Problem Formulation	10
1.3. Outline	11
2. Rotor Models	12
2.1. Physical Description	12
2.1.1. Symmetric Rigid Rotor	12
2.1.2. Symmetric JEFFCOTT Rotor	13
2.1.3. Turbocharger Rotor	14
2.2. Numerical Modeling	15
2.2.1. Multibody Dynamics	15
2.2.2. Numerical Time Integration	16
3. Hydrodynamic Lubrication Theory	18
3.1. Derivation of the REYNOLDS Differential Equation	18
3.2. Radial Journal Bearings	20
3.2.1. Boundary Conditions	21
3.2.2. Temperature-dependent Viscosity	22
3.2.3. Hydrodynamic Forces	23
3.2.4. Bearing Torque	23
3.2.5. Dimensionless REYNOLDS Equation	25
3.3. Cavitation	27
3.3.1. Cavitation Mechanisms	28
3.3.2. Non Mass-Conserving Cavitation Models	29
3.3.3. Mass-Conserving Cavitation Models	31
3.3.3.1. Complimentary ELROD Algorithm	32
3.3.3.2. Two-Phase PEEKEN Model	34
3.3.3.3. Mixture Viscosity	35

3.4. Solution of the REYNOLDS Equation	35
3.4.1. Discretization Methods	36
3.4.2. Mesh	37
4. Journal Bearing Model	39
4.1. Bearing Geometry	39
4.1.1. Cylindrical Bearings	39
4.1.2. Circumferential Grooves	40
4.1.3. Axial Grooves	41
4.1.4. Lubricant Supply	42
4.1.5. Floating Ring Bearings	43
4.1.5.1. Input Variables for the Inner and Outer Fluid Film	44
4.1.5.2. Equations of Motion for the Floating Ring	46
4.1.5.3. Rotating Bearing Geometry	47
4.1.5.4. Change of Bearing Gaps During Operation	48
4.1.5.5. Connecting Channels	51
4.2. Mass-Conserving Cavitation Model for Rotordynamic Simulations	53
4.2.1. General Two-Phase REYNOLDS Equation	53
4.2.1.1. Relation between Pressure and Lubricant Fraction	54
4.2.1.2. Axial Boundary Conditions and Lubricant Supply	57
4.2.1.3. Artificial Diffusion	57
4.2.1.4. Influence on the Bearing Torque	60
4.2.2. Comparison with Non Mass-Conserving Cavitation Approaches	60
4.2.2.1. Pure Rotation	61
4.2.2.2. Squeeze Motion	63
4.2.2.3. Whirl Motion	64
5. Solver Coupling	67
5.1. Dynamic-Static Solver-Coupling	67
5.2. Dynamic Co-Simulation	68
5.2.1. Sequential Gauß-Seidel Scheme	69
6. Jeffcott Rotor in Single Film Bearings	71
6.1. System Parameters	71
6.2. Solver Parameters	72
6.3. Comparison of Half-SOMMERFELD and Penalty Cavitation Approaches	73
6.4. Mass-Conserving Cavitation	74
6.4.1. Mesh Resolution and Steepness of the Ansatz Function	75
6.4.2. Rotordynamic Stability	78
6.4.3. Ambient Boundary Conditions	79
6.4.4. Lubricant Supply	81
6.4.4.1. Axial Feeding Groove	82
6.4.4.2. Circumferential Feeding Groove	84
6.4.5. Rotor Shaft Stiffness	86

6.4.6. Rotor Unbalance	87
7. Rotors in Floating Ring Bearings	88
7.1. Floating Ring Geometry	88
7.2. Jeffcott Rotor	89
7.2.1. Cavitation Approach	90
7.2.2. Run-down	95
7.2.3. Outer Bearing Gap Size	96
7.2.4. Supply pressure	96
7.2.5. Bearing Torque	99
7.2.6. Connecting Channels	100
7.3. Exhaust Turbocharger	101
7.3.1. Supply pressure 2 bar	102
7.3.2. Supply pressure 1.2 bar	105
8. Conclusion	108
8.1. Summary	108
8.2. Outlook	112
A. Tables	113
B. Extended Short Bearing Theory	115
Bibliography	117

List of Figures

1.1. Cross-section of a cylindrical journal bearing with lubricant supply at the top	1
1.2. Cross-section of an automotive exhaust turbocharger with full-floating ring bearings	2
2.1. Kinematics and kinetics of a symmetric rigid rotor	13
2.2. Kinematics and kinetics of a symmetric JEFFCOTT Rotor	13
2.3. Schematic representation of a turbocharger rotor with floating rings	15
3.1. General hydrodynamic gap with gap size h and surface velocities in Cartesian coordinates	19
3.2. Geometry and kinematics of a cylindrical radial bearing	20
3.3. Developed gap geometry of a plain cylindrical bearing	22
3.4. Onset of cavitation in form of streamers	28
3.5. Relation between pressure p and lubricant fraction ϑ for the ELROD model	33
3.6. Relation between pressure p and lubricant fraction ϑ for the PEEKEN model	35
4.1. Developed gap geometry with a central circumferential groove	41
4.2. Developed gap geometry with three evenly spaced axial grooves	42
4.3. Calculation of the hydrostatic lubricant supply force inside the inlet	42
4.4. Full-floating rings with plain surfaces (left) and with a circumferential groove in the outer surface (right)	44
4.5. Kinematics of a floating ring bearing	45
4.6. Free-body diagram of a floating ring bearing	46
4.7. Coordinates for rotating bearing geometry	47
4.8. Radial temperature field in a floating ring for two different turbocharger applications	50
4.9. Centrifugal pressure in connecting channels of full-floating ring bearings	52
4.10. Step-like ansatz function for the lubricant fraction ϑ as a function of the pressure p	55
4.11. Comparison of the ansatz function $\vartheta(p)$ with ELROD, PEEKEN and PRIEST cavitation models	56
4.12. Visualization of necessary condition for $Pe < 1$ with Consistent Artificial Diffusion	59
4.13. Pressure profile p and lubricant fraction ϑ during pure rotation for different cavitation models with circumferential groove	61
4.14. Pressure profile p and lubricant fraction ϑ during pure rotation for different cavitation models with axial groove	62
4.15. Vertical bearing force during three periods of vertical, harmonic squeeze motion	63
4.16. Hydrodynamic pressure at the bottom of the bearing during three periods of circular whirl motion	65
5.1. Explicit co-simulation approach: sequential GAUSS-SEIDEL Master-Slave scheme	70
6.1. Comparison of Half-SOMMERFELD and penalty cavitation approach	74
6.2. Rectangular mesh of one axial half of the bearing with 10×20 elements	75
6.3. Convergence study for the mass-conserving cavitation model	76

6.4. Pressure profile p and lubricant fraction ϑ for different steepness parameters x_1 in one subdomain of a cylindrical bearing with a circumferential feeding groove	77
6.5. Stability analysis of a rigid rotor without unbalance	78
6.6. Comparison of axial boundary conditions	80
6.7. Pressure profile p and lubricant fraction ϑ for oil bath and free-to-air axial boundary conditions in one subdomain of a cylindrical bearing with a circumferential feeding groove	81
6.8. Developed gap geometry and boundary conditions of the cylindrical bearing with one axial lubricant feeding groove	82
6.9. Comparison of penalty approach and two-phase cavitation model for different groove pressures p_{SUP} in cylindrical bearings with one axial feeding groove at the top	83
6.10. Half pressure profiles p for different groove pressures p_{SUP} of a cylindrical bearing with one axial feeding groove at the top of the bearing	84
6.11. Comparison of penalty approach and two-phase cavitation model for different groove pressures p_{SUP} in cylindrical bearings with a circumferential feeding groove	85
6.12. Pressure profiles p for different groove pressures p_{SUP} in one subdomain of a cylindrical bearing with a circumferential feeding groove	86
6.13. Comparison of penalty approach and two-phase cavitation model for different shaft stiffnesses c of the JEFFCOTT rotor in cylindrical bearings with one axial feeding groove at the top	86
6.14. Comparison of penalty approach and two-phase cavitation model for different unbalances U of the JEFFCOTT rotor in cylindrical bearings with one axial feeding groove at the top	87
7.1. Schematic cross-section of a floating ring with circumferential groove and connecting channels	88
7.2. Rectangular mesh of one axial half of the bearing with bores, discretized with 10×24 elements	89
7.3. Comparison of half-SOMMERFELD, penalty and mass-conserving cavitation models	91
7.4. Hysteresis effect of run-up and run-down simulation	95
7.5. Influence of outer gap size C_o for penalty and two-phase cavitation models	97
7.6. Influence of lubricant supply pressure p_{SUP} for penalty and two-phase cavitation models	98
7.7. Influence of contributing terms in the friction torque on the oscillation behavior	99
7.8. Influence of the geometry of the inner lubricant film using the penalty approach	100
7.9. Influence of the pressure difference Δp due to centrifugal acceleration using the penalty approach	101
7.10. Comparison of penalty and mass-conserving cavitation model for an exhaust turbocharger with $p_{\text{SUP}} = 2$ bar	103
7.11. Comparison of penalty and mass-conserving cavitation model for an exhaust turbocharger with $p_{\text{SUP}} = 2$ bar (continued)	104
7.12. Comparison of penalty and mass-conserving cavitation model for an exhaust turbocharger with $p_{\text{SUP}} = 1.2$ bar	106
7.13. Comparison of penalty and mass-conserving cavitation model for an exhaust turbocharger with $p_{\text{SUP}} = 1.2$ bar (continued)	107

List of Tables

4.1. Bearing parameters	60
6.1. Reference parameters of the JEFFCOTT rotor	71
6.2. Time-dependent solver parameters	72
6.3. Settings for NEWTON's method in <i>Comsol Multiphysics</i>	73
7.1. Reference parameters of the JEFFCOTT rotor in floating ring bearings	90
7.2. Efficiency of different cavitation models and simulation methods	94
A.1. Reynolds number Re for critical turbocharger parameters, calculated with (3.3)	113
A.2. Deformations of rotor shaft, floating ring and housing assuming a two-dimensional stress state	114

Symbol Directory

Latin Symbols

Symbol	Meaning	Unit
a	Angular Acceleration Penalty Prefactor	rad/s ² Pa s/m ²
b	Penalty Exponent-Factor Subdomain Width	1 m
A	Area	m ²
A_{oil}	Viscosity Parameter	K
\mathbf{A}	System Matrix	
B	Width	m
c	Shaft Stiffness Diffusion Coefficient	N/m s/m ²
C	Radial Gap Size	m
C_{oil}	Viscosity Parameter	1
d	Damping Coefficient Force Coefficient	Ns/m N
d_x, d_y	Dimensionless Displacements	1
D_x, D_y	Displacements	m
e	Eccentricity	m
\mathbf{e}	Unit Vector	1
E	YOUNG'S Modulus	Pa
f	Dimensionless Force Frequency Scale-Function	1 Hz 1
\mathbf{f}	Nonlinear Function Vector	
F	Force	N
g	Gravity Switch Function Penalty Function	m/s ² 1 1/s
\mathbf{g}	Vector of Algebraic Constraint Equations	
\mathbf{G}	JACOBIAN	
h	Gap Thickness Solver Step Size Micro-Step Size Mesh Size	m s s 1
H	Dimensionless Gap Function Macro-Step Size	1 s
m	Mass	kg
m_ϑ	Scaled Slope	1
M	Torque	Nm
M_R	Friction Torque	Nm
\mathbf{M}	Mass Matrix	kg
N_c	Number of Coupling Variables	1
N_f	Number of Lubricant Films	1
l	Length	m
p	Pressure	Pa
p_0	Atmospheric/Ambient Pressure	Pa
p_{cav}	Cavitation Pressure	Pa

\tilde{p}	Scaled Pressure Function	1
P	Penalty Term	Pa s/m ²
Pe	PECLET Number	1
\mathbf{q}	Vector of Generalized Coordinates System State Vector	
r	Bubble Fraction	1
r, R	Radius	m
So	SOMMERFELD Number	1
t	Time	s
t_1	Time Constant	s
T	Temperature Output Step Size	K s
u	Input	
U	Unbalance	kg m
u, v, w	Flow Velocities	m/s
U, V, W	Surface Velocities	m/s
V	Volume	m ³
\dot{V}	Volume Flow	m ³ /s
$V_{g,s}$	Dissolved Gas Volume	m ³
\mathbf{v}	Velocity Vector	m/s
w_0	Mass-Fraction	1
x, y, z	Displacements Cartesian Coordinates	m
$\tilde{x}, \tilde{y}, \tilde{z}$	Gap Coordinates	m
\bar{x}, \bar{z}	Dimensionless Gap Coordinates	1
x_0, x_1	Steepness Parameter	1
y	Output	

Greek Symbols

Symbol	Meaning	Unit
α	Rotor/Ring Orientation Velocity Vector Orientation	rad
α_B	BUNSEN Coefficient	1
α_T	Thermal Expansion Coefficient	1/K
β	Bulk Modulus Convection Coefficient	Pa s/m
γ	Diffusion Parameter	1
δ	Angular Displacement	rad
Δ	Difference	
ϵ	Strain	1
ε	Relative Eccentricity	1
η	Dynamic Viscosity	Pa s
ϑ	Lubricant Fraction	1
Θ	Relative Angular Coordinate	rad
Θ_g	Groove Opening Angle	rad
λ	Vector of LAGRANGE Multipliers	
ν	POISSON'S Ratio	1

Π	Dimensionless Pressure	1
ρ	Mixture Density	kg/m ³
σ	Stress	Pa
τ	Dimensionless Time	1
τ_{xy}	Shear stress	Pa
ϕ	Absolute Angular Coordinate	rad
ψ	Nominal Gap Size	1
ω	Angular Velocity	rad/s
ω_0	Reference Angular Velocity	rad/s
Ω_0	Dimensionless Angular Velocity Ratio	1

Indices

Index	Meaning
0	Ambient Initial
δ ϕ	Circumferential
ad	Artificial Diffusion
cc	Connecting Channel
cf	Centrifugal
CM	Center of Mass
D	Disk
F	Floating Ring
g	Gas
H	Housing
i	Inner Internal Subsystem
J	Journal
l	Liquid
M	Master
n	Current Solver Step
o	Outer
r	Radial
rhs	Right-Hand Side
R	Rotor
sup	Supply
S	Shell Slave



1 Introduction

The demand for more efficient machinery with higher power density leads to an increase of the rotation speed of rotor systems. Combined with lightweight design, this yields a rise of unwanted oscillations, which reduce the efficiency, the comfort and the operational lifetime of the machinery or may even lead to its destruction.

Rotors with high rotation speeds are often supported in hydrodynamic fluid film bearings due to their high damping compared to rolling element bearings. The cross-section of a journal bearing is exemplary shown in figure 1.1. The rotor journal has an eccentric position with respect to the bearing shell. The liquid lubricant is dragged into the converging gap through the rotation of the journal. This generates a hydrodynamic pressure in the lubricant film, which lifts the rotor journal and completely separates rotor and stator. The lubricant is usually supplied through openings in the bearing shell and leaves the bearing in axial direction (not shown).

Rotors supported in hydrodynamic journal bearings are subject to nonlinear effects due to the fluid-structure interaction. At a certain rotor-speed, self-excited oscillations with a frequency below the rotor-speed emerge, the so-called oil whirl. This frequency can lock into a natural frequency of the rotor-bearing system, which leads to the so-called oil whip, see e.g. [KB08; Sze11; Cra90]. The amplitudes of these sub-synchronous oscillations often exceed those of the synchronous unbalance oscillation and

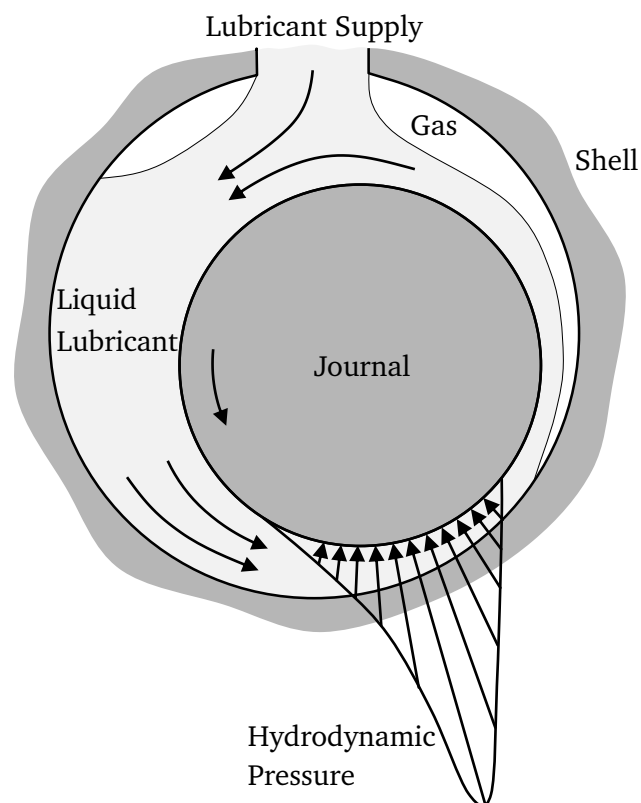


Figure 1.1.: Cross-section of a cylindrical journal bearing with lubricant supply at the top

prevent the safe operation of the rotor-bearing system above a threshold rotor-speed. Sub-synchronous oscillations are also the main cause for undesired acoustics in automotive turbochargers, see e.g. [NS15; Sch10]. Additionally, combination frequencies and jump phenomena occur. This behavior strongly depends on the nonlinear fluid-dynamics of the lubricant films and the geometry of the bearings. Journal bearings are subject to cavitation, which occurs due to the limited ability of fluid lubricants to support tensile stresses, see e.g. [BH10; DT79]. The oil in the lubrication cycle usually contains some dissolved air, which has no time to excrete in the oil reservoir, see [PB85; Nik99]. When the local pressure decreases, dissolved air is released. Additionally, air enters the bearing gap through the axial ends of the bearing and the lubricant evaporates at very low pressures. The lubricant film ruptures, resulting in cavities filled with gas and/or vapor, which is also schematically shown in figure 1.1. These cavities have very little density and viscosity compared to the liquid lubricant film and thus the load carrying capacity and damping is reduced drastically, see e.g. [Boe10; ZV88; Phe61]. Lightweight rotors – such as turbocharger rotors – are characterized by non-static operational behavior and large journal movements, see e.g. [Sch10], and are thus likely to be influenced by cavitation. Often, simple approaches are used to model cavitation, such as the well-known half-SOMMERFELD (GÜMBEL) or REYNOLDS boundary conditions, see e.g. [KB08; Sze11]. These approaches yield satisfactory results under stationary conditions and high bearing loads, see e.g. [DT79], yet they do not take into account the conservation of mass.

Turbochargers are rotor systems with high and transient rotor-speed, low weight and low static load. Figure 1.2 shows a CAD representation of an automotive turbocharger. The hot exhaust gas from an internal combustion engine drives a turbine wheel, which is connected over a shaft to a compressor wheel. The remaining energy in the exhaust gas is used to compress the intake air, which increases the power and overall efficiency of the combustion engine. Today, turbochargers are used to downsize the cylinders of engines while keeping their power constant, in order to reduce fuel consumption. Often, floating ring bearings are used for light rotors with high rotation speeds. This creates a series

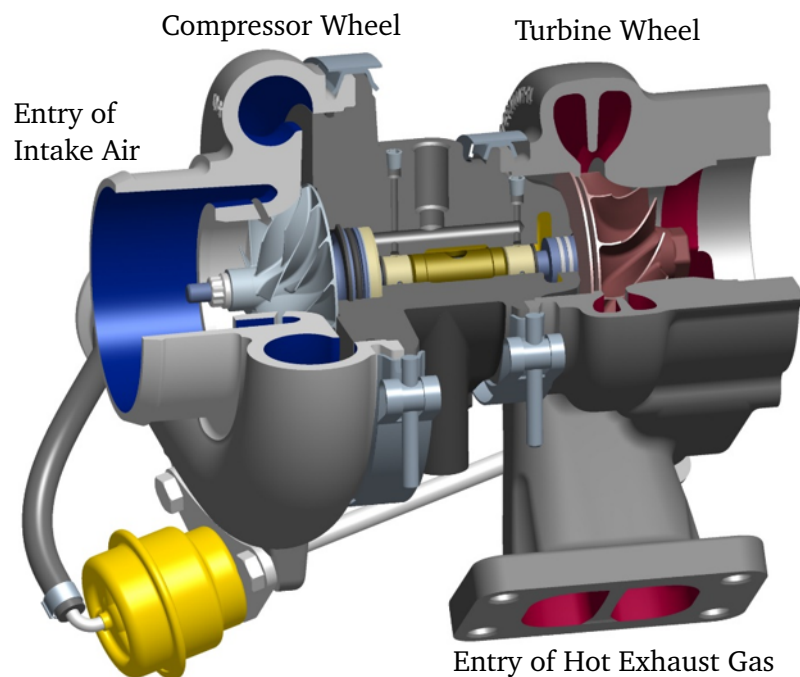


Figure 1.2.: Cross-section of an automotive exhaust turbocharger with full-floating ring bearings

connection of two lubricant films in each bearing. The oil whirls/whips occurring in one lubricant film are mutually damped by the other lubricant film, which enables operation speeds above the threshold rotor-speed of single-film bearings. The manufacturing costs are lower compared to more sophisticated journal bearing designs such as tilting-pad bearings, which are used in heavy turbomachinery to increase the threshold speed. If the floating rings are allowed to rotate freely – a so-called *full-floating* configuration – a synchronization of the oil whirl/whip of the inner and the outer oil film can occur, the so-called *total instability*, which entails very high amplitudes and may result in the destruction of the turbocharger, see [Sch09b]. In the so-called *semi-floating* configuration, the rotation of the floating ring is prevented and the outer lubricant film acts as a squeeze-film damper. This setup is favorable concerning sub-synchronous oscillations, yet it entails higher friction losses, see e.g. [BS15].

Today, numerical models are widely used to efficiently and economically analyze the behavior, to improve the performance and to insure the safe operation of complex technical systems. Validated models can reduce the amount of costly experiments. Nonlinear rotor systems – such as turbochargers in floating ring bearings – are sensitive to parameter changes and are thus often investigated through transient run-up simulations. The hydrodynamics of the lubricant films are often simplified to reduce the calculation time. Analytic solutions such as the short bearing theory are very fast, yet are limited to plain bearing designs and non mass-conserving cavitation approaches. More accurate is the calculation of the hydrodynamics using numerical discretization methods. The results can be calculated a-priori and saved in look-up tables, which reduces the calculation time. Yet the amount of data increases exponentially with the number of dependent variables, which reduces the efficiency for more complex bearing designs and more accurate physical modeling. Due to advances in computer hardware, the solution of the discretized equations in every time-step of the simulation becomes increasingly common.

The equations of motion of the rotor system and the partial differential equations governing the hydrodynamics of the lubricant films can be solved in a single, so-called *monolithic* model. Yet this yields a large equation system and a trade-off for the numerical solver, which cannot be optimized for one type of equations. Furthermore, not many existing software tools are multi-purpose – e.g. multibody dynamics and finite elements – and thus the equation system has to be implemented manually in low-level programming tools, e.g. *FORTRAN*, *C* or *MATLAB*. This may yield fast software tools, yet requires high effort, deep knowledge of several fields and is inflexible concerning changes of the model.

Many existing commercial software tools are tailored to a specific task, e.g. rotor dynamics, multibody dynamics or fluid dynamics. These tools facilitate the modeling of subsystems by specialized engineers, which allows a higher level of detail. For example, rotor shafts with complex geometry can be discretized with finite elements. Bearing models can consider complex geometries and accurate physics descriptions such as mass-conserving cavitation models. The subsystems can be coupled to form an overall system by means of a co-simulation approach, see e.g. [Bus12; Sch15; VAS09]. All subsystems use specialized solvers with their respective time-step sizes, usually implicit solvers with error-dependent time-step control. The coupling variables are exchanged at to-be-defined time points and approximated in between. Co-simulation also enables the straightforward update and exchange of the subsystems. In some cases, it can also be advantageous with respect to the simulation time, e.g. for mechanical systems with many bodies. These systems can be separated into many weakly coupled subsystems, which are then solved in parallel, see e.g. [KS17].

1.1 Literature Review

In the last decades, sophisticated bearing models have been developed which include many different effects such as mass-conserving cavitation, influence of lubricant supply, thermal models and complex bearing geometries, e.g. [Mit90; Fuc02; Mer08; Bob08; Hag12]. These tools are well suited to perform detailed analyses for different steady-state operating conditions, yet they are usually not directly coupled with rotor models due to their high calculation times. Look-up tables are derived for transient run-up simulations, see e.g. [NS13].

The influence of the bearing geometry on the stability of rotor systems in single lubricant film bearings has been comprehensively discussed in literature, see e.g. [AME80; AF81; BAG77; LFL82; LCA80]. Cylindrical bearings often include grooves to improve the lubricant supply. The influence of axial grooves has been investigated e.g. in [FL82; FKB02] and the influence of circumferential grooves e.g. in [Dow+85; NCL10; Cho+11]. Bearings with preloaded geometry, so-called *multilobe bearings*, rise the onset frequency of the instability of rotor systems, see e.g. [FL82; LF82]. Tilting-pad bearings have a very good stability behavior, yet are expensive to manufacture, see e.g. [NFG17; SAKH17].

Most of these studies consider linear stability-analyses for rigid rotors in single film journal bearings under stationary operating conditions, which give no insight into the transient behavior and on sub-synchronous oscillations. Thus, the results can not be directly adapted to more complex rotor systems under transient operation. Furthermore, bearings with non rotating shells are usually considered. Floating ring bearings consist of a series connection of an inner and an outer fluid film, which are mutually influenced. Additional research is required to study the influence of the bearing geometry on transient rotor systems in floating ring bearings.

Cavitation effects in journal bearings have received a lot of attention in the last sixty years. A recent literature review is given in [BH10].

The early investigations of cavitation in journal bearings have been restricted to steady-state operation, i.e. a purely rotating journal, where the shape and location of the cavity are similar to figure 1.1 and remain stationary. In order to model cavitation, the fluid film was divided into a fully-developed fluid film area, which contains only liquid lubricant, and a cavitated area, which contains lubricant and gas. The mass-conserving description of the boundaries between these areas led to the JFO-theory, see [JF57; Ols65]. This procedure is based on experimental observations, yet the phenomena leading to cavitation are not physically described. Furthermore, only the pressure in the fully-developed fluid film is calculated, while it is set to a constant value – usually ambient pressure – in the cavitated area.

The most prominent application of the JFO-theory is the algorithm developed by ELROD, see [Elr81]. It is explained in section 3.3.3.1. Variations have been published in [VK89; KB91a; SP02; AOE15]. These algorithms are complimentary, since different equations and different unknowns are used in the fully-developed fluid film area than in the cavitated area. Usually, the whole bearing gap is discretized, which might lead to problems if grid points alternately belong to either the fully-developed fluid film or the cavitated area. This requires a fine mesh and numerous iterations, which makes this approach unfeasible for run-up simulations. Possible solutions are the smoothing of the boundary, see [Nit+16], or a transformation of the solution domain into the fully-developed fluid film area using ALE-techniques, see e.g. [Sch09a].

Numerical results agree well with experiments for moderate to heavy loads. In this case, the difference

in the hydrodynamic pressure predicted by non mass-conserving and mass-conserving cavitation models is often negligible, see [KB91b; Goo+07]. A reduction of the load-carrying capacity for mass-conserving cavitation models has been observed for low eccentricities, which are related to high rotation speeds, see [PB85]. Additionally, mass-conserving models yield more accurate predictions of thermal properties and friction losses, see [BH10].

In dynamically loaded bearings, the cavitated area changes drastically during operation. However, the effect leading to cavitation remains the same, namely a local expanding bearing gap, see [GPP06]. Only scarce literature exists on cavitation in dynamically loaded journal bearings.

Cavitation has a large influence on the performance of squeeze-film dampers, which has been thoroughly investigated in literature. In these bearings, the journal does not rotate and usually performs a whirling motion. Whirling motions with high amplitudes are also encountered in journal bearings during sub-synchronous oscillations. ZEIDAN and VANCE investigated gaseous and vaporous cavitation regimes in squeeze-film dampers with high-speed pictures and measurements of the rotating pressure profile, see [ZV88]. No cavitation takes place for very low whirl speeds or high supply pressure. A large cavity forms for slightly higher whirl speeds, which follows the movement of the journal without affecting the positive pressure, resembling the cavitation in a journal bearing with constant rotor-speed. This cavity breaks up into small bubbles for increasing whirl speed. The bubbles do not collapse in the high pressure region, which results in a reduced area of the fully developed lubricant film and thus a lower load carrying capacity. More and smaller gas bubbles appear with higher whirl speed. The build-up of pressure is delayed, which reduces the effective damping of the bearing.

Further experiments on the same test rig have been reported in [DSA98]. It was found that for higher air entrainment, the fluid viscosity and damping capability decrease. Furthermore, an increasing area in the fluid film was observed, where no pressure is generated due to gaseous cavitation. The authors further noticed that for high amounts of air entrainment, the cavitation regime is unstable and leads to unreproducible pressures for consecutive cycles of the journal motion. Thus, worse correlation between experiments and numerical models is usually achieved for squeeze-film dampers and dynamically loaded bearings than for stationary loaded bearings.

BOEDO numerically investigated the influence of mass-conserving cavitation models by considering a bearing under sinusoidal loads, see [Boe10]. The complimentary, finite element cavitation algorithm presented in [KB91a] was used. It was found that at the load reversal, a cavity has formed in the expanded part of the bearing gap, which has to be filled again with lubricant in order to support the load. This behavior can only be captured with mass-conserving models, which consider the spatial and temporal time history of the fluid density. Non mass-conserving models on the other hand assume a completely filled lubricant gap at all times, which wrongly yields that the complete load carrying capacity of the film is available upon load reversal. However, comparison to experimental results given in [Phe61] revealed that good agreement is only achieved for small bearing gaps used in engine bearings and when vaporous cavitation is assumed. Open-ended bearings with greater gaps such as turbochargers or squeeze-film dampers favor gaseous cavitation, see [ZV88].

Complimentary cavitation models do not consider the cavitated area and assume a constant pressure, usually ambient pressure. It has been observed experimentally that the pressure in the cavitated area can become smaller than ambient pressure due the surface tension of gas bubbles, see [DT79; BH84]. The tensions remain moderate due to the release of gas. Two-phase models consider the physical processes of bubble generation and collapse. A homogeneous mixture fluid is assumed, whose density and viscosity

locally depend on the amount of free gas. The fully-developed fluid film and the cavitated area are not clearly separated. The pressure in the cavitated area is also calculated and can become lower than ambient pressure. Gaseous cavitation is considered as the main mechanism.

Mixtures of NEWTONIAN liquid and ideal gas exhibit non NEWTONIAN behavior, see [Cha+93]. Analytical relations between the mixture pressure and its density and viscosity have been derived e.g. in [PB85; FH86; Nik99; GPP06; Goo+07]. Empirical ansatz-functions for the solubility of air in the lubricant have been used in [ES10; ES11; Li+12]. The mixture density decreases with higher amounts of released gas, see e.g. [Nik99]. The derivation is straightforward and is almost equal for isothermal and adiabatic conditions, see [FH86]. The mixture viscosity is more complicated to obtain, since it depends on the size of the air bubbles and the shear rate, see [PB85]. Several existing viscosity models are reviewed in [FH86]. Small bubbles require more time to excrete the mixture, see [Nik99]. However, small bubbles coalesce over time to larger bubbles, see [Goo+07]. Bubbles in dynamically loaded journal bearings and squeeze-film dampers can become as large as the local gap size, see [DSA01a].

Two-phase models have been derived and applied to journal bearings by several authors. CHAMNIPRASART et al. derived a binary mixture model derived from the continuum theory of mixtures consisting of two coupled nonlinear differential equations describing the component densities, see [Cha+93]. The fluid is assumed homogeneous and isotropic, which implies a small bubble size. Calculation of a bearing submerged in an oil bath under steady-state operation yielded qualitative agreement with experimental results conducted in [BH84]. However, the model is sophisticated and requires several parameters, which are difficult to obtain. Furthermore, the change of the mixture viscosity has not been considered. A model for squeeze-film dampers was presented in [DSA01a]. Relations for the mixture density and viscosity derived in [Dia99] were plugged into the compressible REYNOLDS equation. Good agreement with experimental results was found for the damping force.

A similar model has been derived by PEEKEN and BRENNER in [PB85], which was used by several authors, see [Fuc02; Mer08; NS13]. This model is explained in section 3.3.3.2.

Most studies neglect sucking-in of air from the surroundings, since bearings are assumed with tight axial seals or which are submerged in an oil bath. This is a rare case in practice. Journal bearings and squeeze-film dampers are often axially open to the surroundings. Air is sucked into the bearing gap due to translational motion of the journal. This effect increases with higher frequencies and amplitudes, see [ZV88; Raj+93; Wan+17].

Another important aspect is the mass-transfer between liquid and air. Usually, an equilibrium between the gas and the liquid phase is assumed, i.e. the collapse and reformation of the fully-developed fluid film occur instantaneously according to the change of the bearing gap. This assumption is in good agreement with the non mass-conserving REYNOLDS boundary condition under steady-state operation, see [GPP06; Li+12]. However, this assumption may become inaccurate at high frequencies and journal amplitudes, since air bubbles persist in the high-pressure zone of the lubricant film, see [ZV88]. Degassing and reabsorption of gas in liquid are slow processes compared to typical revolution times in journal bearings, see [SB92]. The case that the bubbles are not reabsorbed has been considered in [FH86; GPP06]. This yields significantly different pressure profiles and journal equilibrium positions and entails transient behavior even for steady-state operation. However, the increased compressibility of the mixture allows better adaption to geometry changes, see [GPP06]. The rate of air absorption is difficult to obtain. The actual behavior probably is in between the two extreme cases of instant and no reabsorption.

Two-phase models may be not applicable for heavily loaded journal bearings with constant speed, since

they underestimate the load-carrying capacity, see [Raj+93]. The physical modeling of the liquid/air interaction makes them feasible for bearings under transient loads such as squeeze-film dampers or journal bearings for light rotors such as turbochargers.

Additionally, a pressure build-up in the cavitated area has been observed experimentally in submerged bearings. GROPER and ETSION theoretically related this effect to transient flow reversal at the end of the cavitated area, see [GE02]. The influences of shear of the cavity or mass-transfer between liquid and gas phase on the pressure build-up in the cavitated area was found to be negligible, see [GE01].

Cavitation influences the dynamic behavior of rotors in journal bearings. Reduced damping due to dissolved air in the lubricant has been observed for squeeze-film dampers in [ZV88; DSA98; Wan+17] and also for tilting-pad bearings in [NFG17; SAKH17]. Cavitation also influences the rotordynamic stability and whirl amplitudes, see [Bre86]. KÖHL experimentally observed bubbly flow in the bearing of a turbocharger during sub-synchronous oscillations using a transparent bearing housing, see [KKF14; Köh15]. This is also apparent in the outflow of the bearing and has been noticed by other researchers, see e.g. [ZV88; DSA98]. Increased sub-synchronous amplitudes due to cavitation have been experimentally observed for a rotor supported in tilting-pad bearings in [NFG17]. This effect increases for insufficient oil supply and increasing rotor-speed and decreases for higher bearing loads. NITZSCHKE et al. investigated the influence of mass-conserving cavitation for an elastic rotor in multilobe bearings using a multibody model and the ELROD cavitation algorithm. The oil whip occurred at a lower rotation speed than for the non mass-conserving half-SOMMERFELD model, see [Nit+13].

Insufficient oil supply might lead to flow starvation, which has been numerically investigated for a rotor in tilting-pad bearings in [SAKH17]. It has been found that cavitation firstly occurs in the unloaded sections of the bearing. The amount of oil in the bearing gaps decreases with higher shaft speeds, therefore the systems natural frequencies are reduced due to the increased compressibility of the lubricant film.

The drag torque of the lubricant film determines the speed of the floating rings in turbochargers, which has a large influence on the occurrence of sub-synchronous oscillations. A reduced drag torque due to cavitation has been observed in [SAKH17]. WANG et al. performed a CFD analysis of a floating ring with a two-phase model, see [WR17]. They found that the ring-speed decreases with higher amounts of air in the lubricant films. This effect had a stronger influence than the heating of the lubricant due to friction.

Turbocharger systems have been thoroughly investigated in the last decade, both experimentally and numerically. Numerical run-up simulations provide a fast and cost-effective way to analyze the effects of different parameters on the oscillation behavior during the design process. SCHWEIZER has made a detailed analysis of the nonlinear bifurcation behavior during run-ups of turbocharger rotors in full-floating ring bearings with plain geometry using a flexible multibody model in [Sch10]. The influences of different parameters have been investigated and the results have been compared to experiments. DANIEL et al. performed a sensitivity analysis of different bearing parameters with design methods, see [Dan+13]. The geometry of the bearings and the shaft have also been tuned systematically using a sensitivity analysis and neural networks in [Kou+15]. An important parameter for the dynamical bifurcation behavior of turbocharger rotors are the rotation speeds of the floating rings. KÖHL replaced the cast iron bearing housing with a transparent acrylic glass housing and optically measured the ring speed, see [KKF14]. The above mentioned studies treat turbochargers in full-floating ring bearings. Semi-floating ring bearings have been investigated e.g. in [SAV10; BS15].

Additionally to the rotor itself, various authors have investigated the influence of the housing, which is mounted to the internal combustion engine. BOYACI examined the transmission behavior of the turbocharger housing using a multibody software and the short bearing theory for the bearings, see [BS17]. A resonance of the housing is excited and effectively transmits the second sub-synchronous oscillation into the driver cabin. The transmitting behavior can be improved by detuning the eigenfrequencies of the housing. However, a careful design of the bearings is still inevitable in order to prevent damage to the system. It has also been found that the feedback from the housing oscillations to the bearing gap sizes is negligible and the housing can be considered rigid for the calculation of the bearings.

Engine induced oscillations have been investigated in [SA+10; TWP11]. Super-synchronous frequencies which are multiples of the combustion engine speed are common according to the number of cylinders. Yet these frequencies are low-frequency sub-synchronous oscillations concerning the turbocharger rotor due to its high rotor-speed.

For run-up simulations used in industry during the design process, bearing forces are often calculated with analytical approximations such as the short bearing theory, see e.g. [Kou+15; BS17], or using look-up tables, see e.g. [NS13]. The influences of complex, non plain bearing geometries, non constant lubricant temperatures and mass-conserving cavitation are often neglected. On the contrary, detailed CFD analyses of floating ring bearings are performed, which take several hours for one operating point, see e.g. [EOR15b; Por+14; Wan+17; WR17]. Recent publications aim to close the gap between these different approaches using nonlinear rotor-bearing models for run-up simulations. An overview is given in the following.

The influence of axial thrust bearings on the lateral rotor oscillations has been investigated in [Cha+16]. Axial thrust provides additional damping to the system and may shift the sub-synchronous oscillations to higher rotor-speeds. The inclusion of a thermal model is important for the accurate prediction of the behavior at high rotor-speeds. A decoupled thermo-hydrodynamic model is sufficient for transient run-up simulations.

The design of floating ring bearings of turbochargers usually includes grooves to optimize the oil supply for the inner oil film. The grooves also affect the sub-synchronous oscillations. Compared to floating ring bearings with plain surfaces, a circumferential groove in the outer gap entails a reduced frequency range of the second sub-synchronous oscillation. On the contrary, the load carrying capacity of the outer lubricant film is reduced, which yields larger outer eccentricities and a decreased onset frequency of the third sub-synchronous oscillation, see [Now+15b]. The same tendency has been observed in [Wos+15]. A reduced frequency range of the second sub-synchronous oscillation can also be achieved using floating rings with axial grooves in their inner surfaces, see [Now+15a]. Experiments with a large number of different full-floating ring geometries performed in [Kir14] also show that axial grooves can lower the amplitude of sub-synchronous oscillations.

The influence of preloaded bearing geometry in floating ring bearings has been investigated in [EOR15a; Ber+17]. It has been found that this geometry reduces sub-synchronous oscillations compared to plain bearing designs with the cost of increased friction losses.

NITZSCHKE et al. have investigated the influence of misalignment and the connecting channels in floating ring bearings, see [Nit+11]. The pressure in the inner and outer lubricant films has been coupled using a penalty formulation. The influence of misalignment and the connecting channels on the sub-synchronous oscillations is rather small except for the onset of the total instability, see [Sch09b]. Differences between

numerical and experimental results have been attributed to the lack of a thermal model and the flexibility of the rotor shaft, which was not considered.

Additionally to non plain bearing designs, recent publications aim to improve the modeling of cavitation effects. NGUYEN-SCHÄFER has carried out run-up simulations of a turbocharger with a two-phase model from [PB85] using look-up tables, see [NS13].

In [Eli+16], Eling et al. investigated the influence of the model depth using three bearing models with increasing complexity. The rotor-bearing system was implemented as a monolithic model in *Comsol Multiphysics*. The bearing models differ in their lubricant supply geometry, the consideration of tilting, their thermal model and their cavitation model. For mass-conserving cavitation, a modified ELROD algorithm introduced in [AOE15] has been used. The authors concluded that the fast short bearing approach already gives a good indication of the system behavior. A distributed thermal model has only little effect compared to a lumped thermal model. The influence of mass-conserving cavitation was found to be small, yet only single-film bearings were considered. On the other hand, the lubricant supply showed a significant influence due to the hydrostatic load on the journal.

Recently, NITZSCHKE investigated the effect of mass-conserving cavitation on the oscillation behavior of automotive turbochargers in floating ring bearings, see [Nit17]. In contrast to this work, a monolithic model has been implemented as compiled code. This yields a fast model, yet the adaption of the model or exchange of components requires a sufficient knowledge of the overall system. The lubricant gap has been discretized with finite volumes, which are flow-conservative by design, yet less flexible concerning the geometry than finite elements. Mass-conserving cavitation has been considered by means of a regularized ELROD algorithm, see [Nit+16]. The time-dependency of the modified REYNOLDS equation due to the compressibility of the lubricant/gas mixture is considered with backward differences using stored values of the lubricant fraction. The bearing model is a sub-function of the rotor model and thus uses the same time-step size. The bearing model includes a lumped thermal model, which gives constant temperatures during one time-step and neglects the coupling between the REYNOLDS and the energy equation, see [SAK04; SA+12]. The model has been compared to less sophisticated bearing models concerning their prediction of the sub-synchronous oscillations for different bearing gaps and rotor unbalances. It has been observed that the ELROD and half-SOMMERFELD models behave analogous to parameter changes except for the unbalance. Furthermore, results obtained with the short bearing solution are closer to more sophisticated models than a look-up table solution. The minimal bearing gap during operation is smaller when mass-conserving cavitation is considered. The regularized ELROD algorithm has also been applied to an elasto-hydrodynamic (EHD) problem, namely the piston rod bearing on a crankshaft of an internal combustion engine, see [NWD17].

The level of detail of numerical turbocharger models used for run-up simulations has significantly improved in the last decade. Yet most authors use their own in-house bearing models, which are programmed in low-level programming languages and are integrated into the rotor model as sophisticated sub-functions.

Coupling of different software tools facilitates the development of subsystems with easy-to-use, specialized software tools developed by specialized engineers. This can help to further improve the model depth of the investigated systems, since the engineers working on the individual subsystems only require a basic knowledge of the other components to define the coupling variables.

BUSCH developed a dynamic-static interface for the coupling of commercial multibody and commercial finite-element software and performed run-up simulations of an automotive turbocharger, see [BS12].

Yet for bearing models with classical non mass-conserving cavitation modeling, this coupling approach requires a large amount of parallel processes.

SCHMOLL developed a dynamic-dynamic coupling interface for commercial software tools, which was applied to hydraulic, electrodynamic and flexible mechanical systems, see [Sch15]. This approach requires far less parallel processes and is also applicable to rotor-bearing systems, when mass-conserving cavitation is considered.

1.2 Problem Formulation

This work aims to further improve the numerical modeling of light rotors in floating ring bearings such as turbochargers. Highly accurate rotor-bearing models can be used to predict the influences of design parameters and reduce the amount of expensive experiments. The numerical model is used to perform transient run-up simulations to study the influences of modeling assumptions on the nonlinear oscillation behavior.

The rotor is represented by a multibody system. The equations of motion consist of a set of nonlinear differential-algebraic equations. The commercial multibody system software *MSC Adams* is used for the modeling and the numerical integration of the system. A JEFFCOTT rotor is used for preliminary studies. Flexible shafts are often modeled using TIMOSHENKO beam elements, see e.g. [Eli+16; Nit17]. Here, a modally reduced finite element representation is used to model the shaft of a turbocharger.

In contrast to approximate solutions such as the short-bearing solution, the discretization of the REYNOLDS equation with finite-elements facilitates the implementation of non plain bearing geometries and additional effects, with the cost of longer computation times. The commercial software *COMSOL Multiphysics* is used.

Mass-conserving cavitation has a large impact on the load carrying and damping capacity provided by the lubricant films. This is especially relevant in floating ring bearings due to the series connection of the inner and outer lubricant films. The literature review shows that complimentary cavitation models such as the ELROD algorithm might not be suited for transient journal movements with high amplitudes. In this work, the REYNOLDS equation is expanded with a two-phase flow cavitation approach, which yields a single differential equation for the whole lubricant gap. A complementary problem and the use of a switch function are avoided by introducing pressure-dependent mixture density and viscosity. A simple ansatz function is used for the relation between pressure and the local lubricant fraction, which can be easily adopted to different physical cavitation models. In this work it is tuned to reflect the ELROD algorithm for better comparison with classical non mass-conserving cavitation models. An artificial diffusion approach is used to numerically stabilize the solution. Many existing studies consider axially sealed bearings and do not consider sucking-in of air from the surroundings. A special axial boundary condition is introduced, which describes open-ended bearings more accurately.

In order to close the gap between academic research and application in industry, commercial software tools are used to implement the rotor and the bearing models. These tools use implicit solvers with variable time-step size. User-created sub-functions are used in both tools to exchange input and output values. For non mass-conserving cavitation models, a semi-implicit dynamic-static coupling approach is used, see [BS12]. Mass-conserving cavitation models on the other hand entail a time-dependent

REYNOLDS equation, which is difficult to implement in commercial software when the bearing model is realized as a sub-function of the rotor model, see [Nit+13]. Instead, an explicit co-simulation technique is used, see [Sch15].

The coupled rotor-bearing model is used for transient run-up simulations. A JEFFCOTT rotor in single film bearings and floating ring bearings and a turbocharger in floating ring bearings are considered. Different bearing geometries and parameter variations emphasize the differences between non mass-conserving and mass-conserving cavitation models.

1.3 Outline

The physical properties of the rotor models used in this work are explained in chapter 2. Furthermore, the solver is briefly explained.

The hydrodynamic lubrication theory is laid out in chapter 3. The bearing forces acting on the rotor and the floating rings are calculated with the REYNOLDS equation. A review of cavitation mechanisms and well-known mass-conserving cavitation modeling approaches is given in section 3.3.

The bearing model is explained in chapter 4. Firstly, different bearing designs used in turbochargers and the influence of lubricant supply are discussed. Floating ring bearings are explained in detail. The mass-conserving cavitation model used in this work is introduced in section 4.2. It is compared to other cavitation models by means of pre-defined motions of the journal.

The solver coupling methods used in this work are explained in chapter 5.

Transient run-up simulations are performed with the coupled rotor-bearing model. Firstly, the two-phase cavitation approach is compared to classical cavitation models using a JEFFCOTT rotor in single oil films in chapter 6. The influences of the axial boundary conditions, lubricant supply with different geometries, shaft stiffness and unbalance on the stability threshold and the sub-synchronous oscillations are investigated.

Then, a JEFFCOTT rotor and a turbocharger in floating ring bearings are considered in chapter 7. Especially the nominal gap sizes and the lubricant supply pressure strongly influence the oscillation behavior. Finally, the work is summarized and an outlook is given in chapter 8.

2 Rotor Models

The physical properties of the different rotor models used in this work are discussed in the next section. The rotors are modeled using the commercial multibody software *MSC Adams*, which yields a nonlinear differential-algebraic equation system. An implicit *Backward Differential Formula* (BDF) method is used for the time integration, which is briefly explained in section 2.2.2. Ordinary differential equations of simple rotor models are given for clarity. Usually, the floating rings are also part of the multibody system. They are treated in section 4.1.5. The numerical model and the time integration are explained in section 2.2.

2.1 Physical Description

The interaction between the nonlinear stiffness and damping properties of the bearings with the rotor yields sub-synchronous oscillations. In order to understand the influence of the bearing model described in chapter 4, the complexity of the rotor is gradually increased. The simplest rotor in journal bearings is a rigid journal, which is described in the next section. However, no oil whip occurs due to the infinitely high critical bending speed. A *JEFFCOTT* rotor is the simplest flexible rotor, which is explained in section 2.1.2. Finally, a turbocharger model is discussed in section 2.1.3.

2.1.1 Symmetric Rigid Rotor

A symmetric rigid rotor without tilting can be treated as a point mass at the position of its center of mass. The rotor has the mass m and the (predefined) rotation speed $\dot{\alpha}_R$. The unbalance is $U = me_{CM}$, where e_{CM} is the eccentricity of the center of mass CM with respect to the geometrical center J of the journal, see figure 2.1. The relations between these two points are

$$\begin{aligned}x_{CM} &= x_J - e_{CM} \sin \alpha_R, \\y_{CM} &= y_J + e_{CM} \cos \alpha_R.\end{aligned}\tag{2.1}$$

Without loss of generality, the phase angle of the unbalance is set to zero. This can be changed by adding an offset angle to α_R .

The bearing forces F_x and F_y act in point J and depend nonlinearly on the displacement and velocity of the journal. The rotor is subject to gravity g . *NEWTON's* law applied to the rotor yields

$$\begin{aligned}m\ddot{x}_{CM} &= 2F_x(x_J, \dot{x}_J, y_J, \dot{y}_J, \alpha_R, \dot{\alpha}_R), \\m\ddot{y}_{CM} &= 2F_y(x_J, \dot{x}_J, y_J, \dot{y}_J, \alpha_R, \dot{\alpha}_R) - mg.\end{aligned}\tag{2.2}$$

By inserting equation (2.1), the equations of motion for the geometrical center of the rotor J are derived,

$$\begin{aligned} m\ddot{x}_J &= 2F_x(x_J, \dot{x}_J, y_J, \dot{y}_J, \alpha_R, \dot{\alpha}_R) + U [\ddot{\alpha}_R \cos \alpha_R - \dot{\alpha}_R^2 \sin \alpha_R] , \\ m\ddot{y}_J &= 2F_y(x_J, \dot{x}_J, y_J, \dot{y}_J, \alpha_R, \dot{\alpha}_R) + U [\ddot{\alpha}_R \sin \alpha_R + \dot{\alpha}_R^2 \cos \alpha_R] - mg . \end{aligned} \quad (2.3)$$

The two equations are coupled through the anisotropic bearing forces F_x and F_y .

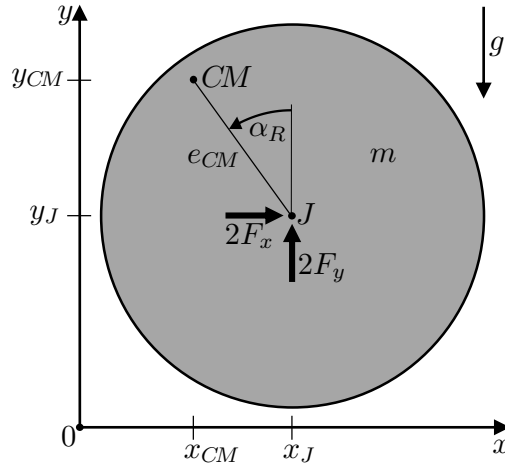


Figure 2.1.: Kinematics and kinetics of a symmetric rigid rotor

2.1.2 Symmetric JEFFCOTT Rotor

The JEFFCOTT rotor is a simple, yet powerful model to study the behavior of flexible rotors. Also, some effects of turbochargers can be shown with this simple rotor model. Since the rotor only has one natural mode, fewer sub-synchronous oscillations are present than in a turbocharger, see chapter 7.

The rotor consists of a rigid disk with mass m_D and a massless flexible shaft with stiffness c , see figure 2.2. Additionally, stiffness-proportional shaft damping d_i and external damping d_o acting on the disk are considered. The rotor-speed $\omega_R(t) = \dot{\alpha}_R$ is predefined. A symmetric rotor is considered, thus both

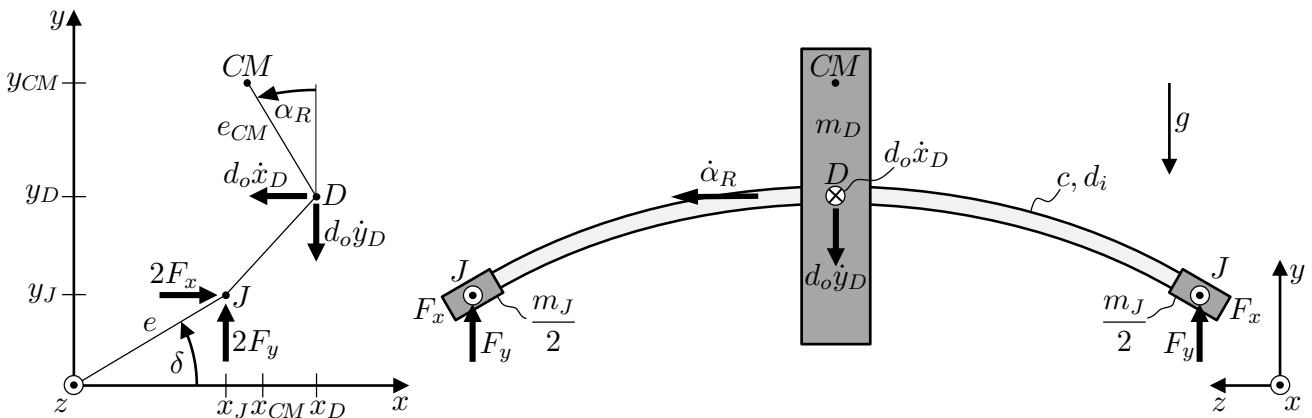


Figure 2.2.: Kinematics and kinetics of a symmetric JEFFCOTT Rotor

journals perform the same motion and can be treated as a single body. A small mass m_J is considered to entail an invertible mass matrix. The center of mass CM of the disk is eccentric with the distance e_{CM} from the geometrical center D of the disk, where the flexible shaft is connected. The nonlinear bearing forces F_x and F_y act on the journals at the point J .

NEWTON's law is applied to the disk and the journals. By inserting equation (2.1), the equations of motion for the journals J and the geometrical center of the disk D are derived, see e.g. [GNP02],

$$\begin{aligned}
 & \begin{bmatrix} m_J & & & \\ & m_D & & \\ & & m_J & \\ & & & m_D \end{bmatrix} \begin{bmatrix} \ddot{x}_J \\ \ddot{x}_D \\ \ddot{y}_J \\ \ddot{y}_D \end{bmatrix} + \begin{bmatrix} d_i & -d_i & & \\ -d_i & d_i+d_o & & \\ & & d_i & -d_i \\ & & -d_i & d_i+d_o \end{bmatrix} \begin{bmatrix} \dot{x}_J \\ \dot{x}_D \\ \dot{y}_J \\ \dot{y}_D \end{bmatrix} + \\
 & + \begin{bmatrix} c & -c & & \\ -c & c & & \\ & & c & -c \\ & & -c & c \end{bmatrix} \begin{bmatrix} x_J \\ x_D \\ y_J \\ y_D \end{bmatrix} = \begin{bmatrix} 2 F_x(x_J, \dot{x}_J, y_J, \dot{y}_J, \dot{\alpha}_R) \\ U(\ddot{\alpha}_R \cos \alpha_R - \dot{\alpha}_R^2 \sin \alpha_R) \\ 2 F_y(x_J, \dot{x}_J, y_J, \dot{y}_J, \dot{\alpha}_R) - m_J g \\ U(\ddot{\alpha}_R \sin \alpha_R + \dot{\alpha}_R^2 \cos \alpha_R) - m_D g \end{bmatrix}. \tag{2.4}
 \end{aligned}$$

The motion of the disk and the journals is coupled by means of the shaft stiffness c and damping d_i . The horizontal and the vertical direction are only coupled by means of the anisotropic journal bearing forces F_x and F_y . The right-hand side corresponds to that of the rigid rotor (2.3), yet the unbalance and bearing forces act on different bodies.

2.1.3 Turbocharger Rotor

Figure 2.3 schematically shows a turbocharger rotor with floating rings. The compressor wheel on the left and the turbine wheel on the right are assumed to be rigid bodies. They are connected with a flexible shaft, which is represented by a modally reduced finite-element model. The compressor wheel is plugged on the shaft and fixed with a nut. The turbine wheel is joined to the shaft through friction welding and is heavier than the compressor wheel. Unbalance masses are considered at the compressor and at the turbine wheel. The shaft is assumed to be dynamically balanced due to its small radius. The rotational speed of the turbine is given via a kinematic constraint and is linearly increased during a run-up simulation. The maximum rotor-speed can be as high as 5000 Hz for light turbochargers.

The two floating ring bearings are located in between the compressor and the turbine wheel. The axial bearing is not considered in this work. The floating rings are modeled as rigid bodies. Since tilting is not considered, they are restricted to planar motion through constraints. The bearing forces and torques are calculated in the bearing model and are externally applied on the shaft and the floating rings, corresponding to each oil film.

The motion of the rotor is dominated by rigid body modes, which are superimposed by slight bending of the shaft. In the so-called *conical mode*, the rotor moves in an hourglass shape, while the center of the rotor stays approximately still. In the so-called *cylindrical mode*, all points of the rotor perform a circular whirl motion with the same phase, see also [Sch10]. Due to the overhanging masses of the compressor

wheel and the turbine wheel, gyroscopic torques act on the rotor, which split the natural frequencies into forward and backward modes, yet only the forward modes are excited by the unbalance and the journals. In practice, measurements of the shaft oscillation and rotation are conducted at the nut of the compressor wheel, due to its accessibility and large oscillation amplitudes. Thus, the waterfall diagrams showed in this work are also calculated from the oscillations at this point.

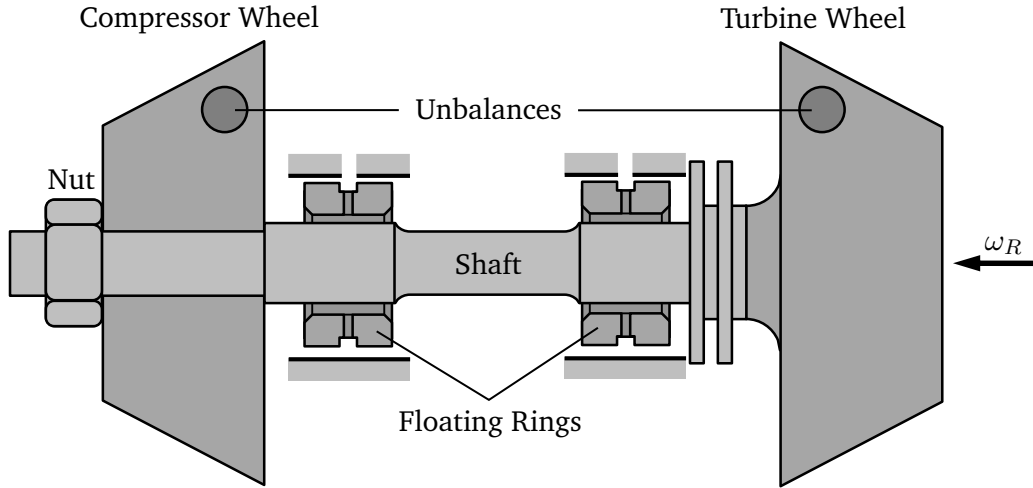


Figure 2.3.: Schematic representation of a turbocharger rotor with floating rings

2.2 Numerical Modeling

In this section, firstly the general equations of motion of a multibody system are given. Then, the time-dependent solver is explained.

2.2.1 Multibody Dynamics

Ordinary differential equations for every degree of freedom of each rigid body with respect to its center of mass are formulated. Additionally, equations of motion of the flexible bodies are considered. The degrees of freedom are restricted by nonlinear algebraic constraint equations $\mathbf{g}(\mathbf{q}, t)$, which formulate e.g. a fixed connection, an alignment condition or a joint. This yields a system of nonlinear differential algebraic equations, see [Sha13],

$$\begin{aligned} \mathbf{M}(\mathbf{q})\ddot{\mathbf{q}} &= \mathbf{F}(\mathbf{q}, \dot{\mathbf{q}}, t, \mathbf{u}) - \mathbf{G}^T(\mathbf{q}, t)\boldsymbol{\lambda} \quad \text{with} \quad \mathbf{q}(t=t_0) = \mathbf{q}_0 \quad \text{and} \quad \dot{\mathbf{q}}(t=t_0) = \dot{\mathbf{q}}_0, \\ \mathbf{0} &= \mathbf{g}(\mathbf{q}, t), \quad \mathbf{y} = \mathbf{y}(\mathbf{q}, \dot{\mathbf{q}}). \end{aligned} \quad (2.5)$$

The symmetric mass matrix is denoted by $\mathbf{M}(\mathbf{q})$. The vectors of generalized coordinates and velocities are \mathbf{q} and $\dot{\mathbf{q}}$, respectively. The initial displacements and velocities at the time t_0 are denoted with \mathbf{q}_0 and $\dot{\mathbf{q}}_0$. The vector \mathbf{F} contains the applied, gyroscopic and elastic forces. The forces/torques generated by the lubricant films are collected in the input vector \mathbf{u} , which is provided by the bearing model. The

vector \mathbf{g} contains the algebraic constraint equations. The resulting constraint forces are $-\mathbf{G}^T(\mathbf{q}, t)\boldsymbol{\lambda}$ with the JACOBIAN $\mathbf{G}^T(\mathbf{q}, t) = \partial\mathbf{g}/\partial\mathbf{q}$ and the vector of LAGRANGE multipliers $\boldsymbol{\lambda}$. The term $\mathbf{y}(\mathbf{q}, \dot{\mathbf{q}})$ indicates the output vector of the multibody system, containing the relevant kinematic quantities needed for the calculation of the lubricant films, which are transferred to the bearing model.

Constraint equations can be formulated regarding displacements, velocities and accelerations. In this work, constraints on the velocity level are also used, the so-called *Index 2* formulation. The equation system is stabilized by including auxiliary LAGRANGE multipliers, which force the system to fulfill the constraints also on the position level, see [Sha13].

2.2.2 Numerical Time Integration

The solution of time-dependent differential equations requires initial conditions, which leads to an *Initial Value Problem*

$$\dot{\mathbf{q}} = \mathbf{f}(\mathbf{q}(t), t), \quad \mathbf{q}(t_0) = \mathbf{q}_0. \quad (2.6)$$

The vector \mathbf{q} contains the states of the system with the initial conditions \mathbf{q}_0 at time t_0 . The vector \mathbf{f} usually contains nonlinear functions of \mathbf{q} and t . For linear systems with time-independent coefficients, $\mathbf{f} = \mathbf{A}\mathbf{q}$, where \mathbf{A} is a matrix with constant coefficients. Usually no analytic solution exists for nonlinear systems and an approximate numerical solution has to be calculated. Differential equations with higher order derivatives can be reduced to first order systems through transformation into state space. Partial differential equations are reduced to ordinary differential equation systems by spatial discretization, which is described in section 3.4.1.

Equation (2.6) is solved approximately and step-wise with the usually variable step-size h . Many different methods exist, which have different properties concerning numerical stability, error, numerical damping and efficiency. They can be divided into two categories:

- For *explicit methods*, the state at the next time-step t_{n+1} only depends on states of the past, e.g. $\mathbf{q}(t_{n+1}) = \mathbf{q}(t_n) + h\mathbf{f}(\mathbf{q}(t_n), t_n)$. The state at the next step is directly calculated, thus no nonlinear equation system has to be solved. For partial differential equations, the size of the time-steps is limited through the spatial mesh size, since the spatial propagation of information is limited, see [Sch99].
- For *implicit methods*, the state at the next time-step also depends on states which are not yet calculated, e.g. $\mathbf{q}(t_{n+1}) = \mathbf{q}(t_n) + h\mathbf{f}(\mathbf{q}(t_{n+1}), t_{n+1})$. Thus, a usually nonlinear equation system has to be solved. This is mostly done approximately using NEWTON's method. Implicit methods are stable for larger time-steps than explicit methods, especially for stiff systems. Yet a large numerical effort is required to compute the JACOBIAN. For partial differential equations, changes in the solution at one node affect all nodes in the next time-step. This removes the stringent limit on the time-step size of explicit methods.

In this work, *Backward Differential Formula* (BDF) methods are used, which are implicit multi-step methods suited for stiff problems. The time-derivative $\dot{\mathbf{q}}(t_{n+1})$ at the next time-step is approximated with polynomials with variable order using past time-steps. BDF methods are often implemented as predictor-

corrector schemes. In the predictor-step, an initial guess for the next state is calculated using an explicit extrapolation with a polynomial using past time-steps. Then, an implicit iteration at the current time-step is performed using NEWTON's method, the so-called corrector-steps. The iteration is aborted, when a specified error is reached. Usually, the JACOBIAN does not change significantly during the corrector-steps. Thus, many solvers give the possibility to reduce the number of these time-consuming calculations.

The time-steps t_n which the method takes are usually free and depend on the error and the specified tolerance. The results are saved at pre-defined, equidistant output-steps, which are either directly calculated or interpolated from the free time-steps. The output step-size ΔT_{out} has to be chosen small enough that the highest frequency f_{max} is resolved. This can be checked using the NYQUIST-SHANNON sampling theorem: The sampling frequency f_{out} should be larger than twice the maximum frequency f_{max} . This yields

$$\Delta T_{\text{out}} < \frac{1}{2 f_{\text{max}}} . \quad (2.7)$$

In this work, the output step-size $\Delta T_{\text{out}} = 5 \cdot 10^{-5}$ s is used, which fulfills the NYQUIST-SHANNON theorem for frequencies up to 10.000 Hz. The rotor-journal-bearing systems investigated in this work mostly experience synchronous and sub-synchronous oscillations. Thus, the maximum occurring frequency f_{max} equals the maximum rotor-speed $\omega_{R,\text{max}}$.

3 Hydrodynamic Lubrication Theory

The basic hydrodynamic lubrication theory is recapitulated in this chapter. Many books exist on this subject, e.g. [Bar10; KB08; LS78; PS61; Hor06; Sze11]. The REYNOLDS equation is used for the calculation of the pressure in thin fluid films, which are characteristic for journal bearings. Its derivation from the NAVIER-STOKES equation and the continuity equation is briefly reviewed in the next section. Then, the geometry and kinematics of radial journal bearings are explained. General equations for the bearing forces and the bearing torque are given. A dimensionless form of the REYNOLDS equation presented in section 3.2.5 reduces the number of coupling variables in a coupled simulation. In order to achieve realistic results, cavitation has to be considered. A physical explanation of cavitation effects and an overview of existing modeling approaches is given in section 3.3. The numerical solution using finite elements are explained in section 3.4.

3.1 Derivation of the REYNOLDS Differential Equation

In order to calculate the current state of a fluid, conservation laws for mass, momentum and energy are formulated. The solution of these differential equations using appropriate boundary conditions and material laws yields the current density, velocity, pressure, inner energy and temperature of the fluid. The conservation of mass for a compressible fluid is defined by the continuity equation

$$\frac{\partial \rho}{\partial t} + \nabla \cdot (\rho \mathbf{v}) = 0 \quad (3.1)$$

with the local fluid density ρ and the current velocity vector \mathbf{v} , which reads $\mathbf{v} = [u, v, w]^T$ in Cartesian coordinates.

The conservation of momentum of a fluid with friction is described by the NAVIER-STOKES equation. For a compressible NEWTONIAN fluid – which is a good approximation for oil – it reads

$$\rho \frac{D\mathbf{v}}{Dt} = -\nabla p + \eta \left[\nabla^2 \mathbf{v} + \frac{1}{3} \nabla (\nabla \cdot \mathbf{v}) \right] + \mathbf{F}, \quad (3.2)$$

see e.g. [Bar10; Sze11]. D/Dt is the material derivative. The pressure is denoted with p , η is the dynamic viscosity of the fluid. The vector \mathbf{F} contains volume forces such as gravitation. Equations (3.1) and (3.2) are sufficient for the calculation of isothermal flow. If non isothermal flow is considered, additionally the conservation of energy has to be taken into account, see e.g. [Bar10; Pin90; Hor06; Sze11].

For laminar flow, the inertia forces on the left side and the volume forces \mathbf{F} in (3.2) are negligible compared to the forces generated by pressure and viscosity. The REYNOLDS number Re is the ratio be-

tween inertia forces and viscous forces in a fluid and is used to determine, whether a flow is laminar or turbulent. Adjusted to radial bearings the condition for laminar flow reads

$$Re = \frac{\rho v l}{\eta} = \frac{\rho \omega R C}{\eta} < 2300, \quad (3.3)$$

see [Mit90]. The velocity v is derived from the radius R and the angular velocity ω of the fluid film. In floating ring bearings, ω depends on the ring speed and the rotor-speed and is larger in the inner fluid film. The problem-specific characteristic length l is chosen as the nominal gap size C (see figure 3.2), which is usually larger for the outer fluid film. Due to the larger velocities, the lubricant temperature is higher in the inner fluid film, resulting in a lower dynamic viscosity η . Table A.1 on page 113 lists values of Re for two turbocharger applications using extremal values. For all bearings investigated in this work, condition (3.3) is fulfilled even at maximum rotation speed. Thus, no turbulent flow has to be considered. However, turbulent flow may be relevant for squeeze film dampers with large gap sizes or bearings with steps, which have been studied in [Fuc02].

Figure 3.1 shows a bearing gap with the velocities of the two rigid surfaces in Cartesian coordinates. In hydrodynamic bearings, the thickness $h(\tilde{x})$ of the fluid film is 2 to 3 orders of magnitude smaller than the other dimensions of the gap. Thus, the change of the fluid velocity w and the pressure p in z -direction are negligible. Furthermore, the gradients in \tilde{z} -direction dominate compared to gradients in other directions, $\partial/\partial\tilde{x}, \partial/\partial\tilde{y} \ll \partial/\partial\tilde{z}$. Taking all of the above into account, the NAVIER-STOKES equation (3.2) simplifies to

$$\frac{\partial p}{\partial \tilde{x}} = \eta \frac{\partial^2 u}{\partial \tilde{z}^2}, \quad \frac{\partial p}{\partial \tilde{y}} = \eta \frac{\partial^2 v}{\partial \tilde{z}^2} \quad \text{and} \quad \frac{\partial p}{\partial \tilde{z}} = 0. \quad (3.4)$$

Integration of equations (3.4) yields the fluid velocities u and v in \tilde{x} - and \tilde{y} -direction. The integration constants are eliminated using the assumption that the fluid sticks to the surfaces, i.e. $u(\tilde{z}=0)=U_1$ and $u(\tilde{z}=h)=U_2$. If the relative movement of journal and bearing shell in axial direction is neglected, $V_1=V_2=0$ and the resulting flow velocities are

$$u = \frac{1}{2\eta} \frac{\partial p}{\partial \tilde{x}} (\tilde{z} - h)\tilde{z} + U_1 \left(1 - \frac{\tilde{z}}{h}\right) + U_2 \frac{\tilde{z}}{h} \quad \text{and} \quad v = \frac{1}{2\eta} \frac{\partial p}{\partial \tilde{y}} (\tilde{z} - h)\tilde{z}. \quad (3.5)$$

The flow velocity u consists of two parts, namely the pressure-driven HAGEN-POISEUILLE flow and the shear-driven TAYLOR-COUPETTE flow. By inserting (3.5) into the continuity equation (3.1) and integrating

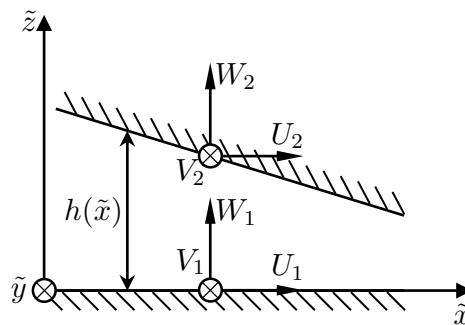


Figure 3.1.: General hydrodynamic gap with gap size h and surface velocities in Cartesian coordinates

over the height h of the bearing gap, the REYNOLDS differential equation is derived. For compressible fluids it reads

$$\frac{\partial}{\partial \tilde{x}} \left[\frac{\rho h^3}{\eta} \frac{\partial p}{\partial \tilde{x}} \right] + \frac{\partial}{\partial \tilde{y}} \left[\frac{\rho h^3}{\eta} \frac{\partial p}{\partial \tilde{y}} \right] = \frac{1}{2}(U_1 + U_2) \frac{\partial(h\rho)}{\partial \tilde{x}} + \frac{\partial(h\rho)}{\partial t}, \quad (3.6)$$

see e.g. [Bar10; LS78; KB08; Sze11]. Note that $\partial h / \partial t = W_2 - W_1$. In (3.6), $p(\tilde{x}, \tilde{y})$ denotes the unknown pressure distribution, η the dynamic fluid viscosity, ρ the fluid density and U_1, U_2 the surface velocities in \tilde{x} -direction. The gap function $h(\tilde{x}, \tilde{y}, t)$ describes the height of the fluid film. For constant parameters η and ρ , the pressure field $p(\tilde{x}, \tilde{y})$ does not explicitly depend on time, since $h(\tilde{x}, \tilde{y}, t)$ is a known function of the surface displacements and velocities.

3.2 Radial Journal Bearings

The general REYNOLDS equation (3.6) can be applied to many hydrodynamic lubrication problems with thin fluid films. The most common applications in rotordynamics are radial and axial hydrodynamic bearings. In this section, equations and assumptions for radial journal bearings are given. The special case of a cylindrical bearing is discussed, which is the foundation for more complex bearing geometries explained in section 4.1.

The geometry of a radial, cylindrical journal bearing is shown in figure 3.2. The kinematics applies to non cylindrical bearings as well. The bearing shell and the journal are assumed parallel, since misalignment is not considered in this work. The origin of the absolute xyz -coordinate system is the center of the shell. The radii of the shell and the journal are R and r , respectively. The diameter of the shell is $D = 2R$. The axial width of the bearing in z -direction is B . The nominal gap size is denoted with $C = R - r$. The displacement of the journal relative to the shell is described with the Cartesian displacements D_x and

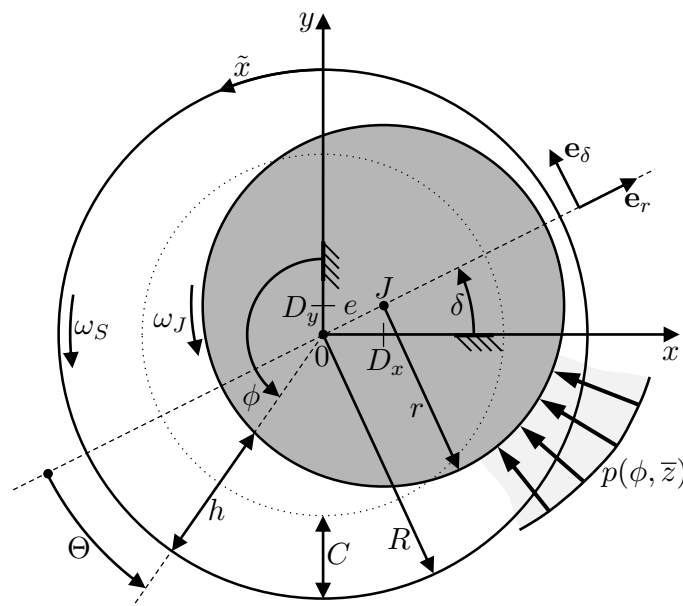


Figure 3.2.: Geometry and kinematics of a cylindrical radial bearing (dotted line: central position of the journal)

D_y or with the radial displacement e and the angle δ with respect to the x -axis. Often, the dimensionless eccentricity

$$\varepsilon = e/C = \frac{1}{C} \sqrt{D_x^2 + D_y^2} \quad (3.7)$$

is used to describe the radial displacement. The angular speed of the shell and the journal are ω_S and ω_J , respectively. The local gap size $h(\tilde{x})$ depends on the position of the journal relative to the shell and the bearing geometry.

The absolute angle $\phi = \tilde{x}/R$ and the dimensionless axial coordinate $\bar{z} = \tilde{y}/B$ are introduced. The \tilde{y} -axis and the z -axis are identical. Since $h \ll R$, a relation between the surface velocities U_1 , U_2 and the angular speeds ω_S , ω_J can be formulated:

$$U_1 + U_2 \approx R(\omega_J + \omega_S) = R\omega. \quad (3.8)$$

With the dimensionless gap function $H = h/C$ and the relative nominal gap size $\psi = C/R$, equation (3.6) can be written as

$$\frac{\partial}{\partial \phi} \left[\frac{\psi^2 \rho}{12 \eta} H^3 \frac{\partial p}{\partial \phi} \right] + \left(\frac{R}{B} \right)^2 \frac{\partial}{\partial \bar{z}} \left[\frac{\psi^2 \rho}{12 \eta} H^3 \frac{\partial p}{\partial \bar{z}} \right] = \frac{\omega}{2} \frac{\partial(H\rho)}{\partial \phi} + \frac{\partial(H\rho)}{\partial t}. \quad (3.9)$$

The terms on the left side of (3.9) are the diffusion in circumferential and axial direction, respectively. They result from the pressure-driven HAGEN-POISEUILLE flow in equation (3.5) and compensate discontinuities in the pressure profile over time.

The terms on the right side induce the pressure in the bearing gap due to the motions of journal and shell. The first term results from the shear-driven TAYLOR-COUPETTE flow in equation (3.5) and describes the pressure build-up due to rotation of the journal and the shell. The derivative of the gap function H with respect to the circumferential coordinate ϕ describes the spatial change of the gap. Hydrodynamic pressure is generated as the lubricant is pulled into a converging gap by the moving surfaces. In literature this is often referred to as the *physical wedge* and is the main effect in hydrodynamic journal bearings for separating the journal and the shell during operation. No pressure is generated by this term in cylindrical bearings if $\varepsilon = 0$, since then $H = \text{const.}$

The second term describes the pressure build-up due to a temporal change of the bearing gap at a fixed location and is neglected in stationary studies. The pressure is generated by a radial motion of the journal, which is called the *squeeze film damper* effect in literature. Furthermore, also the circular whirl motion of the journal with respect to the shell is included in this term, which diminishes the physical wedge.

3.2.1 Boundary Conditions

For the solution of equation (3.9), boundary conditions for the pressure p have to be formulated. The curvature of the surfaces in a thin fluid film is negligible. Thus, the gap geometry is developed into a 2-dimensional surface, see figure 3.3. Additionally to the dimensionless axial coordinate \bar{z} , the dimensionless circumferential coordinate $\bar{x} = \phi/(2\pi)$ is used in the implementation. For the sake of brevity, the

angle ϕ is used here.

The edges $\phi=0$ and $\phi=2\pi$ are identical. This is enforced in the solution by applying the periodic boundary condition

$$p(\phi=0, \bar{z}) = p(\phi=2\pi, \bar{z}) \quad \text{and} \quad \left[\frac{\partial p}{\partial \phi} \right]_{\phi=0, \bar{z}} = \left[\frac{\partial p}{\partial \phi} \right]_{\phi=2\pi, \bar{z}} . \quad (3.10)$$

In most bearing applications, the fluid film is open to the surroundings at the axial boundaries. Thus, the pressure on the boundaries $\bar{z}=0$ and $\bar{z}=1$ equals the atmospheric pressure p_0 . This is imposed by the DIRICHLET boundary conditions

$$p(\phi, \bar{z}=0) = p(\phi, \bar{z}=1) = p_0 . \quad (3.11)$$

So far, only plain bearings were considered. More complex geometries such as grooves or bore holes enforce additional boundary conditions or partially replace those mentioned above, see section 4.1.

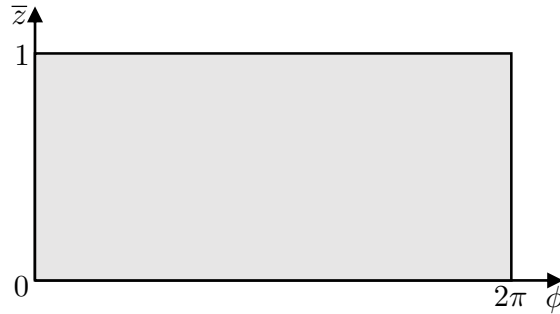


Figure 3.3.: Developed gap geometry of a plain cylindrical bearing

3.2.2 Temperature-dependent Viscosity

The dynamic viscosity η of oil strongly depends on the temperature T , see e.g. [Pin90]. This relation can be approximated with an exponential function for usual oil types,

$$\eta(T) = \eta_0 e^{\frac{A_{\text{oil}}}{\Delta T} + C_{\text{oil}}} . \quad (3.12)$$

The constant parameters A_{oil} and C_{oil} are determined by a curve fitting method using measured viscosities for different temperatures. In this work, an isothermal model is used. Thus, the lubricant viscosity η is calculated a-priori assuming a constant temperature T during run-up.

3.2.3 Hydrodynamic Forces

For rotordynamic simulations, the hydrodynamic bearing forces are required to calculate the current state of the rotor. The resulting pressure profile $p(\phi, \bar{z})$ is decomposed into the components $p_x(\phi, \bar{z})$ and $p_y(\phi, \bar{z})$ in x - and y -direction, respectively. The resulting forces F_x and F_y acting on the journal in x - and y -direction are calculated by integration of the pressure components p_x and p_y over the surface area A of the developed gap geometry,

$$F_x = \iint_A p_x dA = A \int_0^{2\pi} \int_0^1 p(\phi, \bar{z}) \sin\phi d\bar{z} d\phi, \quad (3.13)$$
$$F_y = \iint_A p_y dA = - A \int_0^{2\pi} \int_0^1 p(\phi, \bar{z}) \cos\phi d\bar{z} d\phi.$$

Using the resulting hydrodynamic bearing force $F = \sqrt{F_x^2 + F_y^2}$, the SOMMERFELD-number So can be calculated,

$$So = \frac{\psi^2}{DB\eta\omega} F, \quad (3.14)$$

see e.g. [GNP02; LS78]. It can be interpreted as a dimensionless bearing force. If the location of the journal is stationary, i.e. $\dot{D}_x = \dot{D}_y = 0$ and $\omega = \text{const.}$, the SOMMERFELD-number So is a measurement for the load carrying capacity of the bearing. The force F then equals the external load on the journal, e.g. a part of the weight of the rotor. An equilibrium position of the shaft in the bearing sets in, which is a function of the SOMMERFELD-number So . This enables a classification of rotor systems supported in journal bearings:

- A large So represents a *heavy* rotor (or a rotor subjected to high load) with a small rotation speed whose equilibrium position has a relatively high eccentricity ε . Typical applications are immobile turbines for electrical power generation.
- A small So denotes a *light* rotor with a high rotation speed whose equilibrium position is close to the center of the bearing shell. Turbochargers and vertical rotors belong to this group, see e.g. [GNP02].

3.2.4 Bearing Torque

A torque develops due to the shear of the fluid film, which acts on the journal and the shell and is the main reason for power losses in rotor systems supported in journal bearings. For floating ring bearings, the angular speed of the floating ring is determined by the torques in the inner and outer fluid films and heavily affects the occurrence of subsynchronous oscillations. The accurate calculation of the bearing torque is thus important for the design of rotors supported by journal bearings.

The shear stress τ_{xy} of a NEWTONIAN fluid in laminar flow is proportional to the velocity gradient. The shear stress at the surface of the journal is

$$\tau_{xy} = -\eta \left. \frac{\partial u}{\partial \tilde{z}} \right|_{\tilde{z}=h} \quad (3.15)$$

with the velocity u in \tilde{x} -direction, see figure 3.1. The bearing torque acting on the journal is calculated by integration of the shear stress τ_{xy} over the surface A of the journal,

$$M_R = R \iint_A \tau_{xy} dA. \quad (3.16)$$

Using equation (3.5) with $h = CH$ and $U_2 - U_1 \approx R(\omega_J - \omega_S)$ yields

$$M_R = -\frac{R^2 \eta}{C} (\omega_J - \omega_S) \iint_A \frac{1}{H} dA - \frac{RC}{2} \iint_A \frac{\partial p}{\partial \tilde{x}} H dA. \quad (3.17)$$

The first term results from the shear-driven TAYLOR-COUPETTE flow and is proportional to the difference of the angular velocities ω_J and ω_S of journal and shell.

The second term resulting from the pressure-driven HAGEN-POISEUILLE flow is often neglected due to high shear. Yet only scarce literature exists on its influence. In [Köh15], KÖHL derived an analytical expression for the bearing torque resulting from the HAGEN-POISEUILLE flow based on the short bearing theory and compared it to the torque resulting from the TAYLOR-COUPETTE flow for typical turbocharger applications. In most cases, the influence of the HAGEN-POISEUILLE flow is negligible. Its importance increases for high journal eccentricities ε and a large ratio B/D . This tendency is stronger in the inner lubricant film. Furthermore, the influence of the HAGEN-POISEUILLE flow is less pronounced in a circular whirl motion (e.g. sub-synchronous oscillation) than in pure rotation (e.g. synchronous vibration with small unbalance). Since the REYNOLDS equation is solved in every time-step in this work, this term can be easily evaluated. Its influence is investigated in section 7.2.5.

The bearing torque acting on the shell is analogously calculated, yet the shear stress τ_{xy} has to be evaluated at the surface of the shell, i.e. $\tilde{z}=0$, see e.g. [Hor06]. This changes the sign of the second term in equation (3.17). The first term remains unchanged, since the velocity gradient due to the TAYLOR-COUPETTE flow is linear and is thus equal on both surfaces.

An advantage of neglecting the HAGEN-POISEUILLE flow is that the bearing torque does not depend on the pressure gradient. This enables its calculation on the rotor side of the coupled simulation, which reduces the number of coupling variables, see also section 3.2.5. In [Fel16], FELSCHER reformulated the bearing torque as a function of the bearing forces, which makes the integration of the pressure gradient in (3.17) unnecessary.

3.2.5 Dimensionless REYNOLDS Equation

In this work, bearing models which use non mass-conserving cavitation models are coupled to the rotor model using semi-implicit dynamic-static solver coupling, which is explained in section 5.1. For this method, the calculation of a partial derivative is required for each coupling variable in order to compute the JACOBIAN matrix for the BDF solver of the rotor model. Usually, finite differences are used to approximate the partial derivatives, which results in $N_f(N_c+1)$ parallel computations of the REYNOLDS equation for N_c coupling variables and N_f lubricant films. This is computationally expensive and might even make run-up simulations of turbochargers in floating ring bearings unfeasible on computers with a small number of cores. Thus, it is advantageous to reduce the number of input variables of the bearing model.

The number of input variables is determined by the evaluated right-hand side of the REYNOLDS equation. For a cylindrical bearing described with the absolute angular coordinate ϕ , the right-hand side given in equation (4.5) contains 5 input variables, namely the Cartesian displacements (d_x, d_y) and velocities (\dot{d}_x, \dot{d}_y) of the journal with respect to the shell in x - and y -direction as well as the sum ω of the angular velocities ω_J and ω_S of journal and shell, see section 4.1.1. The sum ω of the angular velocities can only be used as a coupling variable instead of the individual angular velocities ω_J and ω_S , if the HAGEN-POISEUILLE flow in the bearing torque (3.17) is neglected and the torque is evaluated in the rotor model. As long as tilting of the journal with respect to the shell is not considered, 5 input variables are sufficient to calculate the hydrodynamic bearing forces, also for more complex geometries such as bearings with bore holes, pockets, grooves and bearings with preloaded pads.

The number of input variables can be reduced by introducing a dimensionless time $\tau = \omega_0 t$ with the reference angular velocity ω_0 . Thus, the derivatives with respect to time are written as

$$(\dot{\dots}) = \frac{\partial}{\partial t}(\dots) = \omega_0 \frac{\partial}{\partial \tau}(\dots) = \omega_0(\dots)'. \quad (3.18)$$

For $\rho = \text{const.}$, a dimensionless REYNOLDS differential equation for cylindrical bearings is derived from equation (3.9), see [Vra01; Boy11],

$$\frac{\partial}{\partial \phi} \left(H^3 \frac{\partial \Pi}{\partial \phi} \right) + \left(\frac{R}{B} \right)^2 \frac{\partial}{\partial \bar{z}} \left(H^3 \frac{\partial \Pi}{\partial \bar{z}} \right) = \Omega_0 \frac{\partial H}{\partial \phi} + 2 \frac{\partial H}{\partial \tau} \quad (3.19)$$

with the dimensionless pressure

$$\Pi = \frac{\psi^2}{6\eta\omega_0} p \quad (3.20)$$

and the dimensionless angular velocity ratio $\Omega_0 = \omega/\omega_0$. Only the dimensionless parameter R/B remains. If the reference angular velocity ω_0 is defined equal to ω , $\Omega_0 = 1$ and ω is not needed as a coupling variable.

The dimensionless REYNOLDS equation (3.19) has a singularity at $\omega_0 = 0$, which makes the choice $\omega_0 = \omega$

not suitable for squeeze film dampers. Furthermore, since the dimensionless pressure Π depends on ω_0 , constant pressure boundary conditions change during run-up if ω_0 changes. This is circumvented by choosing a constant ω_0 , with the disadvantage that no reduction of coupling variables is achieved.

For a cylindrical bearing, $H = 1 + \varepsilon \cos \Theta$ (see e.g. [LS78]). Using the relation $\phi = \Theta + \delta + \pi/2$ (see figure 3.2), the right-hand side of (3.19) is evaluated as

$$\Omega_0 \frac{\partial H}{\partial \phi} + 2 \frac{dH}{d\tau} = \varepsilon(\Omega_0 - 2\delta') \cos(\phi - \delta) + 2\varepsilon' \sin(\phi - \delta) \quad (3.21)$$

with 4 dimensionless input variables, namely the eccentricity ε , see equation (3.7), the angle δ and the dimensionless velocities

$$\varepsilon' = \frac{\dot{\varepsilon}}{\omega_0} = \frac{\dot{e}}{C\omega_0} = \frac{D_x \dot{D}_x + D_y \dot{D}_y}{C^2 \omega_0 \varepsilon} \quad \text{and} \quad \delta' = \frac{\dot{\delta}}{\omega_0} = \frac{D_x \dot{D}_y - D_y \dot{D}_x}{C^2 \omega_0 \varepsilon^2}. \quad (3.22)$$

The term $(\Omega_0 - 2\delta')$ in (3.21) is the so-called effective hydrodynamic angular velocity of the fluid film, see [LS78]. By inserting (3.20) into (3.13), the dimensionless forces f_x and f_y are defined,

$$\begin{aligned} f_x &= 3 \int_0^{2\pi} \int_0^1 \Pi(\phi, \bar{z}) \sin \phi \, d\bar{z} \, d\phi, \\ f_y &= -3 \int_0^{2\pi} \int_0^1 \Pi(\phi, \bar{z}) \cos \phi \, d\bar{z} \, d\phi. \end{aligned} \quad (3.23)$$

The dimensioned forces are $F_x = d f_x$ and $F_y = d f_y$ with

$$d = \frac{DB\eta}{\psi^2} \omega_0. \quad (3.24)$$

The norm of the dimensionless force vector equals the SOMMERFELD-number So ,

$$So = \sqrt{f_x^2 + f_y^2}, \quad (3.25)$$

see equation (3.14).

When a plain cylindrical bearing is considered, the absolute angular position δ of the journal is not required to describe the pressure profile, but only the relative angular coordinate Θ starting at the widest gap, see figure 3.2. In this case, the partial derivatives with respect to ϕ in the REYNOLDS equation (3.19) are replaced with partial derivatives with respect to Θ . This yields

$$\Omega_0 \frac{\partial H}{\partial \Theta} + 2 \frac{dH}{d\tau} = \varepsilon(2\delta' - \Omega_0) \sin(\Theta) + 2\varepsilon' \cos(\Theta) \quad (3.26)$$

for the right-hand side of (3.19). The calculation of the pressure in a relative coordinate system does not yield additional terms in the REYNOLDS equation, since inertia forces are neglected, see section 3.1.

The whirl speed δ' has to be incorporated manually into equation (3.26), since the derivatives of H are evaluated in a relative coordinate system, see [LS78]. The resulting bearing forces are also evaluated in the relative coordinate system,

$$\begin{aligned} f_r &= 3 \int_0^{2\pi} \int_0^1 \Pi(\Theta, \bar{z}) \cos \Theta \, d\bar{z} \, d\Theta, \\ f_\delta &= 3 \int_0^{2\pi} \int_0^1 \Pi(\Theta, \bar{z}) \sin \Theta \, d\bar{z} \, d\Theta. \end{aligned} \quad (3.27)$$

Here, f_r is the dimensionless force in radial \mathbf{e}_r -direction and f_δ is the dimensionless force in tangential \mathbf{e}_δ -direction, see figure 3.2. They are transformed into the absolute xy -coordinate system by means of

$$\begin{bmatrix} f_x \\ f_y \end{bmatrix} = \begin{bmatrix} \cos \delta & -\sin \delta \\ \sin \delta & \cos \delta \end{bmatrix} \begin{bmatrix} f_r \\ f_\delta \end{bmatrix}. \quad (3.28)$$

The transformation is performed in the rotor side of the coupled simulation. Thus, this coordinate transformation reduces the coupling variables to ε , ε' and δ' . However, this is only possible for bearings which are plain in circumferential direction, which includes bearings with circumferential grooves, see section 4.1.2.

3.3 Cavitation

The REYNOLDS equation assumes that the bearing gap is completely filled with lubricant at all times. If a single-phase liquid lubricant is considered, the density ρ is assumed constant, since liquids are almost incompressible. During pure rotation of the journal, the continuity of mass causes the lubricant in the convergent part of the gap to flow out of the bearing in axial direction. The lubricant in the divergent part of the bearing gap would need to expand in order to fill the gap, which results in tensions in the fluid. The resulting theoretical pressure in the divergent gap is below ambient pressure p_0 . Other reasons for tensions in the fluid are squeezing or whirling motions of the journal, which lead to a local expansion of the gap. Liquids only support very small tensions in the same order of magnitude than the surface tension, see e.g. [BH10]. Thus, the lubricant film ruptures where $p < p_0$ is predicted. These regions are partially filled with gas or vapor and the pressure remains above a to-be-defined cavitation pressure $p_{\text{cav}} \leq p_0$. Gas and vapor have a much lower density and dynamic viscosity than the lubricant and are much more compressible. An overview of different cavitation mechanisms is given in the next section.

Many cavitation models exist which prevent unrealistic pressures below the ambient pressure. Usually, simple and efficient approaches are used for rotordynamic simulations, which do not take into account the conservation of mass. Such approaches are explained in section 3.3.2.

An efficient and physically accurate cavitation model is needed to correctly model the mass flow in the bearing, especially for further research on the influence of oil connecting channels and the development of a sophisticated thermal model. In order to be mass-conserving, the REYNOLDS equation has to be modified to account for a mixture consisting of liquid lubricant and gas or vapor. Mass-conserving

cavitation models are explained in section 3.3.3. The cavitation model used in this work is given in section 4.2.

3.3.1 Cavitation Mechanisms

Detailed overviews of cavitation phenomena and available model approaches are laid out in [BH10; DT79; BBK89]. Three main effects can be distinguished:

Gaseous cavitation

Motor oil usually contains dissolved air, which is released when the pressure falls below the saturation pressure, analogous to sparkling water or soda. The saturation pressure of air in oil is close beneath the ambient pressure p_0 , see [BH10].

Experiments in [PB85] show that dissolved gas does not affect the density and viscosity of the lubricant, but only the undissolved gas. When the pressure falls beneath the saturation pressure of the dissolved gas, bubbles start to grow either at the rough surfaces of journal and shell or at small particles dispensed in the lubricants. The probability of outgassing can be reduced by applying a high external pressure on the bearing, see [ZV88]. As the pressure increases in the converging part of the bearing gap, the gas bubbles are re-absorbed in the liquid lubricant. However, the absorption is a slower process than the release of gas, see [GPP06]. Thus at high rotation speeds, the air bubbles may persist in the high pressure region of the fluid film, see [ZV88]. They move with the same speed as the surrounding liquid, thus homogeneous flow can be assumed. Since the rate of absorption is difficult to obtain, the release and re-absorption of gas are usually assumed instantaneous in literature. The other extremal case, namely that no re-absorption takes place, is investigated in [FH86; GPP06].

The bubbles start to grow with decreasing pressure and form large gas cavities, which are stationary for pure rotation of the journal. The liquid is transported in between, above or below the cavity, see figure 3.4. The pressure in the cavities equals the cavitation pressure p_{cav} , if the surface tension is neglected, see [GPP06]. In this case, it can be assumed that no evaporated lubricant is present in the gas cavities due to the low vapor pressure of oil, see [BH84].

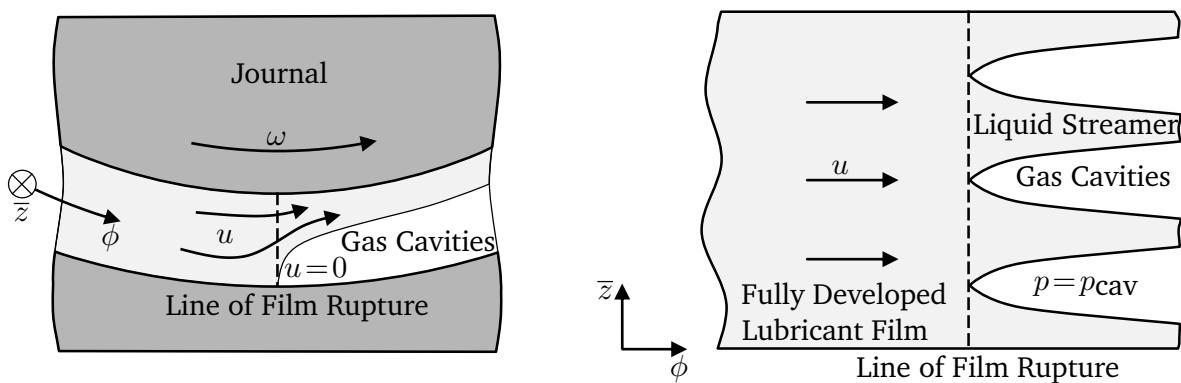


Figure 3.4.: Onset of cavitation in form of streamers (fingers); left: cross-section of the journal bearing; right: top view of the developed lubricant film; figures analogous to [BH10]

The amount of dissolved gas in the lubricant at atmospheric pressure p_0 is given by the BUNSEN-coefficient $\alpha_B = V_{g,s}/V$ with the total volume V of the fluid and the volume $V_{g,s}$ of the dissolved gas. For air in motor oil $\alpha_B \approx 8-12\%$, see [PS61]. The value of α_B does only weakly depend on the pressure and temperature, see [PB85]. Since the volume of the liberated gas is small, this effect is not dominant in open-ended bearings, see [SA10].

Sucked-in air

The lubricant film is open to the atmosphere in most journal bearing applications and thus air is sucked into the fluid film, if the pressure is below the ambient pressure p_0 . This is also called *Ventilation*. Most journal bearings are open-ended, i.e. axially open to the surroundings and sucking-in of air is more probable than the slow degassing of dissolved air. This is especially the case for bearings with transient journal movements such as in turbochargers and squeeze film dampers. Ventilation is amplified at high whirl-frequencies and large amplitudes, see [ZV88].

Vaporous cavitation

If the pressure falls below the evaporation pressure – which is usually far beneath the ambient pressure p_0 – the lubricant evaporates. Evaporation is a very fast process compared to gaseous cavitation, see [SB92]. Usually, very low pressures beneath the evaporation pressure of motor oil only occur in bearings, which are axially sealed or submerged in an oil bath. Furthermore, the lubricant has to be very pure, since small impurities facilitate gaseous cavitation, which suppresses vaporous cavitation, see [ZV88]. In [BH84], the chemical content of the cavitation area was investigated experimentally for a fully submerged bearing. It was found that the bubbles mostly contain air. Vapor bubbles do not persist in the positive pressure region and immediately collapse as soon as the pressure increases above the vapor pressure of the lubricant, thus not affecting the positive pressure, see [ZV88].

High flow velocities can decrease the pressure below the evaporation pressure almost instantaneously, e.g. in steam turbines or near ship propellers (BERNOULLI's principle). The vapor bubbles can implode rapidly, which can severely damage the surfaces. Such damages are seldom observed in usual journal bearing applications. This effect is the so-called *bubble cavitation*, which is often just called cavitation. In this work, cavitation refers to the general occurrence of cavities filled with gas or vapor.

3.3.2 Non Mass-Conserving Cavitation Models

Non mass-conserving models approximately account for cavitation effects. While they do not consider the detailed mechanisms leading to cavitation explained in the last section, they prevent unrealistic pressures below the ambient pressure and are usually easy to implement and efficient.

If the REYNOLDS equation (3.9) with constant lubricant density ρ is solved without additional measures, pressures below the ambient pressure p_0 are predicted. The neglect of cavitation effects is the so-called SOMMERFELD boundary condition. While it is non physical in most applications, it yields a smooth solution and is valid for bearings with high external pressure, see [Fuc02].

Widely used in literature is the half-SOMMERFELD or GÜMBEL model. Firstly, the pressure is calculated using the SOMMERFELD boundary condition. Then, the pressure is set equal to the cavitation pressure p_{cav} wherever $p < p_{\text{cav}}$. Usually, the cavitation pressure is set equal to the ambient pressure p_0 . Effective pressures are sufficient for the calculation of the hydrodynamic forces. If the ambient pressure is set to 0, a possible implementation is

$$p_{\text{hS}} = \frac{1}{2}(p + |p|) . \quad (3.29)$$

This condition is easily implemented and numerically efficient. The fact that it is enforced a-posteriori leads to problems if the pressure is coupled to other variables, since pressures below the cavitation pressure p_{cav} occur during the solution process. An example are the connecting channels in floating ring bearings, where the pressures in the inner and outer lubricant films are coupled, see section 4.1.5.5. Furthermore, the gradient of the pressure and thus the lubricant flow is discontinuous at the borders of the cavitation area. Generally this does not cause any problems in rotordynamic simulations, since only the integrated pressure is used as a coupling variable.

An unsteady gradient is prevented by applying the REYNOLDS or SWIFT-STIEBER cavitation boundary condition

$$p(\phi = \phi^*) = 0 \quad \text{and} \quad \left[\frac{\partial p}{\partial \phi} \right]_{\phi=\phi^*} = 0 \quad (3.30)$$

at the unknown coordinate ϕ^* . During the solution, ϕ^* has to be determined iteratively such that (3.30) is fulfilled. The REYNOLDS condition is mass-conserving for the full lubricant film, yet not for the cavitated region, see [Bar10]. The flow in the bearing gap is continuous except at the onset of the cavitation zone, see [BH10]. While generally preferable to the simple half-SOMMERFELD condition, the REYNOLDS condition is less numerically efficient.

Another possible solution to circumvent discontinuous flow and $p < p_{\text{cav}}$ during the solution process is a penalty approach, see e.g. [Wu86; SM09]. A pressure-dependent penalty term $P(p)$, which becomes very large for $p < p_{\text{cav}}$, is subtracted from the right-hand side of the REYNOLDS equation (3.9). This acts as an additional source term for the hydrodynamic pressure, which elevates p to p_{cav} in the cavitated area. The penalty term P should be almost zero for $p \geq p_{\text{cav}}$ in order to affect the pressure in the full lubricant film region as little as possible. The resulting pressure profile is similar to one obtained with the REYNOLDS boundary condition. The penalty approach is not mass-conserving, since lubricant is generated in the cavitated area. A suitable penalty function for $p_{\text{cav}} = p_0$ is

$$P = a e^{-b \frac{p-p_0}{p_0}} . \quad (3.31)$$

The parameters a and b have no physical meaning and have to be adjusted to the specific lubrication problem. The prefactor a should be small to ensure $P \approx 0$ for $p \geq p_{\text{cav}}$. The exponent-factor b should be large to ensure $p \approx p_{\text{cav}}$ in the cavitation area. There is no lower boundary for p and for some kinematic input values, p might drop well below p_{cav} , if b is not large enough.

The REYNOLDS equation (3.9) becomes nonlinear in p with the penalty approach. The solution may not converge for extremal values of a and b , especially for high eccentricities ε . In practice, it became apparent that a non-constant $b(\varepsilon)$ enables good convergence while still ensuring that $p \approx p_{cav}$ in the cavitation area. The relation

$$b = 10^{4-2\varepsilon} \tag{3.32}$$

is used in this work. The prefactor is chosen as $a = 0.01$.

3.3.3 Mass-Conserving Cavitation Models

The underlying phenomena of cavitation, namely the appearance, growth, interaction and collapse of bubbles filled with air or vapor, are microscopic and random. For this reason, usually a macroscopic approach is chosen to model cavitation in journal bearings. The two-phase mixture is approximated with a single-phase pseudo-fluid, see [Car92]. The appearance of gas is accounted for by a mixture density ρ and a mixture dynamic viscosity η , which are reduced locally in the area of cavitation.

The amount of liquid lubricant is described with the *lubricant fraction* $\vartheta = V_l/V$, where V is the total volume of the mixture and V_l the volume of the liquid lubricant. The complementary part $1 - \vartheta = V_g/V$ is called *void fraction* or *aeration ratio*, where V_g is the volume of the gas in the mixture. The density ratio ρ/ρ_l is also commonly used, with the density ρ_l of liquid lubricant at atmospheric pressure p_0 . A cavitation model has to ensure the conservation of liquid mass in the whole bearing gap in order to be mass-conserving. On the other hand, the mass of the gas is usually neglected. Then, a relation between the lubricant fraction ϑ and the mixture density ρ can be derived

$$\frac{\rho}{\rho_l} = \frac{m_l + m_g}{V\rho_l} \approx \frac{m_l}{V\rho_l} = \frac{V_l}{V} = \vartheta. \tag{3.33}$$

The total masses of liquid and gas in the mixture are m_l and m_g , respectively.

Existing mass-conserving cavitation models can be roughly divided into two categories, see [Bar10]:

- *Complimentary models* divide the fluid film domain into two subdomains, namely the fully developed lubricant film, which is completely filled with liquid, and the cavitated area, which contains a mixture of lubricant and gas. During the solution process, the areas of the subdomains have to be determined iteratively. The most prominent example is the well-known ELROD-algorithm, which is explained in the next section.
- *Two-phase models* express the mixture density ρ in the compressible REYNOLDS equation (3.6) as a function of the pressure p , which yields an equation valid for the whole fluid film. This method is explained in further detail in section 3.3.3.2. This is also the basis for the cavitation model used in this work, which is described in section 4.2.

3.3.3.1 Complimentary ELROD Algorithm

The cavitation boundary condition developed by JAKOBSSON and FLOBERG, see [JF57], as well as OLSSON, see [Ols65], is an enhancement of the REYNOLDS cavitation boundary condition, see section 3.3.2. This so-called *JFO*-condition enforces continuity additionally at the onset of the cavitation area and is mass-conserving for the whole bearing gap. The film thickness in the cavitated area is allowed to be smaller than the local gap size. The velocity u at the onset of the cavitation area is zero, see figure 3.4.

It is assumed that $p = p_{\text{cav}}$ in the cavitated area and usually $p_{\text{cav}} = p_0$ is chosen. Thus, the derivatives of p on the left-hand side of the REYNOLDS equation (3.9) vanish in the cavitated area and the liquid lubricant is only transported via TAYLOR-COUETTE flow in streamers. The fluid film is separated into two subdomains with different differential equations and usually different unknown variables:

- In the fully developed fluid film, $\vartheta = 1$ and the pressure p is unknown.
- In the cavitated area, $p = p_{\text{cav}}$ and the lubricant fraction ϑ is unknown.

The *JFO*-condition yields equations for the calculation of the cavitation boundaries. Bubble dynamics are not considered and thus the boundaries of the cavitation zone change instantly with changes of the bearing gap. Furthermore, no mass-transfer between the liquid lubricant and the gas phase is considered. The results agree well with experimental data for medium to high loads, see [BH10].

The well-known cavitation algorithm developed by ELROD, see [Elr81], with extensions from VIJAYARAGHAVAN and KEITH, see [VK89], fulfills the *JFO*-condition without solving it directly. The lubricant fraction ϑ and the pressure p are linked by assuming a compressible lubricant. The compressibility of a single phase fluid is described with the bulk modulus β ,

$$\beta = \rho \frac{\partial p}{\partial \rho}. \quad (3.34)$$

Equation (3.34) is integrated with the boundary condition $\rho = \rho_l$ for $p = p_{\text{cav}}$, which yields

$$p(\vartheta) = p_{\text{cav}} + g \beta \ln \vartheta \quad (3.35)$$

with $\vartheta = \rho / \rho_l$. In order to vary the pressure only in the fully developed fluid film, the switch function $g(\vartheta)$ is introduced,

$$\begin{aligned} g &= 0 & \text{for } \vartheta < 1 \\ g &= 1 & \text{for } \vartheta \geq 1 \end{aligned} \quad (3.36)$$

Inserting (3.35) into (3.9) yields

$$\frac{\partial}{\partial \phi} \left[\frac{\psi^2}{12\eta} H^3 g \beta \frac{\partial \vartheta}{\partial \phi} \right] + \left(\frac{R}{B} \right)^2 \frac{\partial}{\partial \bar{z}} \left[\frac{\psi^2}{12\eta} H^3 g \beta \frac{\partial \vartheta}{\partial \bar{z}} \right] = \frac{\omega}{2} \frac{\partial(H\vartheta)}{\partial \phi} + \frac{\partial(H\vartheta)}{\partial t}. \quad (3.37)$$

This differential equation is solved for ϑ . During the solution process, the switch function $g(\vartheta)$ is updated for each node separately. The left-hand side of (3.37) vanishes for $g=0$. If $\vartheta < 1$, ϑ is interpreted as the lubricant fraction and $p=p_{cav}$. If $\vartheta \geq 1$, ϑ is interpreted as the ratio of densities and the pressure p is calculated using (3.35). This relation is illustrated in figure 3.5. The logarithmic function (3.35) appears linear due to the large bulk modulus β . Since the area of the cavity is not known a-priori, several iterations have to be performed until an accurate solution is reached. The mesh has to be relatively fine in order to resolve the cavitated area. In reality, the bulk modulus β of oil is very high, $\beta \approx 10^9$ Pa. To achieve a numerically stable solution, β is usually chosen orders of magnitude smaller and loses its physical meaning. The bulk modulus β in figure 3.5 is chosen small in order to qualitatively demonstrate the compressibility of the lubricant.

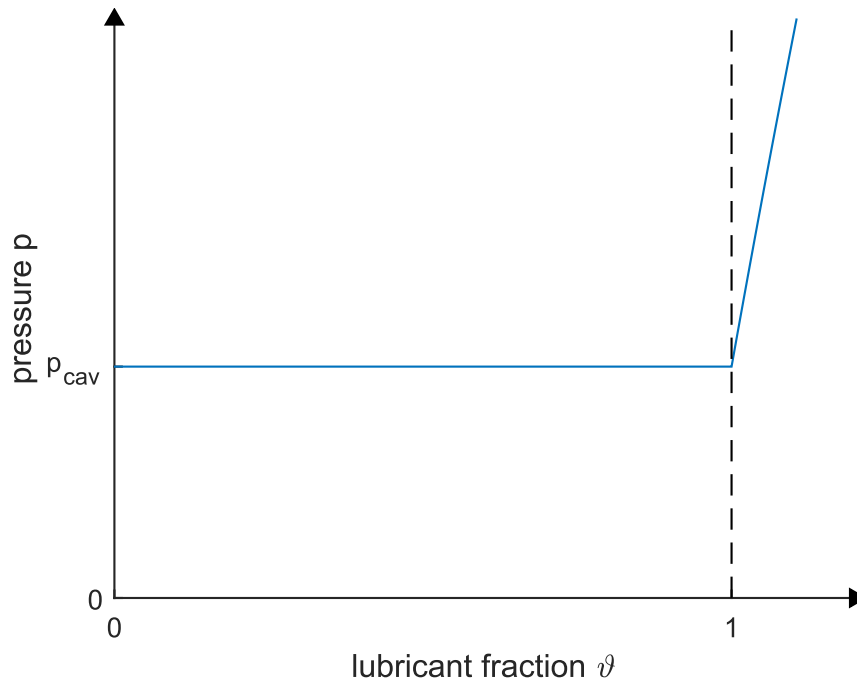


Figure 3.5.: Relation between pressure p and lubricant fraction ϑ for the ELROD model, $\beta = 2 \cdot 10^6$ Pa

Several modifications of the ELROD algorithm have been proposed. Numerical oscillations due to a high bulk modulus β can be reduced with artificial viscosity, see [Sze11]. The algorithm was adopted to Finite Elements in [KB91a] with the assumption of a non-compressible liquid. A single universal variable, which incorporates the pressure p and the lubricant fraction ϑ , was introduced in [SP02]. The switch function was replaced by Boolean expressions of this universal variable in [AOE15]. A smoothing of the switch function g proposed in [Nit+16] combines two independent differential equations for easier treatment and enables a coarser mesh solution. All complimentary approaches have in common that no change of the fluid properties in the cavitated region is considered. This is acknowledged with two-phase models.

3.3.3.2 Two-Phase PEEKEN Model

In the complimentary cavitation models discussed so far, it is assumed that $p = p_{\text{cav}} = p_0$ in the cavitated area. However, it has been shown experimentally that $p < p_0$ can occur, see [DT79; BH84]. Liquids can support tensions in the order of magnitude of the surface tension, see [FH86; Bar10]. Furthermore, the transport of mass between the liquid and gas phase has been neglected so far.

Two-phase models derive a relation for the lubricant fraction ϑ with the use of fundamental laws for bubble growth. Gaseous cavitation, namely the release of dissolved air in the lubricant, is usually considered as the main mechanism, see e.g. [Cha+93; GPP06; Li+12]. It is assumed that the liquid is not oversaturated with gas, i.e. at atmospheric pressure p_0 , the liquid contains the maximal amount of dissolved gas. Additionally, an equilibrium state for the diffusion between the liquid and the gas phase is implied, i.e. the release and re-absorption of gas at cavitation pressure is instantaneous. The total mass of the gas in the bearing is constant, thus no sucking-in from air is considered.

The bubble fraction $r = V_g/V_l$ is defined. Its relation to the lubricant fraction ϑ is

$$\vartheta = \frac{V_l}{V_l + V_g} = \frac{1}{1+r}. \quad (3.38)$$

The laws of HENRY-DALTON and BOYLE-MARIOTTE give a relation between the bubble fraction r , the pressure p and the temperature T , which yields the relation $\vartheta(p, T)$. In [PB85], PEEKEN determined the change of the gas volume V_g using the ideal gas law under the assumption of isothermal flow, since the mass of gas is negligible. Assuming that no bubbles are present at the cavitation pressure p_{cav} , i.e. $r(p = p_{\text{cav}}) = 0$, yields

$$r = -\alpha_B \frac{p - p_{\text{cav}}}{p}. \quad (3.39)$$

This relation is only applicable in the partially filled film. In the fully developed fluid film, $p > p_{\text{cav}}$ and $\vartheta = 1$ is enforced manually. The relation between the pressure p and the lubricant fraction ϑ is exemplary shown in figure 3.6. In contrast to complimentary cavitation models, the pressure in the cavitated area is variable.

It was discussed in section 3.3.1 that gaseous cavitation may not be the main effect in dynamically loaded bearings. In section 4.2, a cavitation model is introduced which uses an arbitrary relation $\vartheta(p)$. This enables the consideration of mass-conserving cavitation with a single differential equation. In this work, the function $\vartheta(p)$ is adopted to reflect the ELROD algorithm.

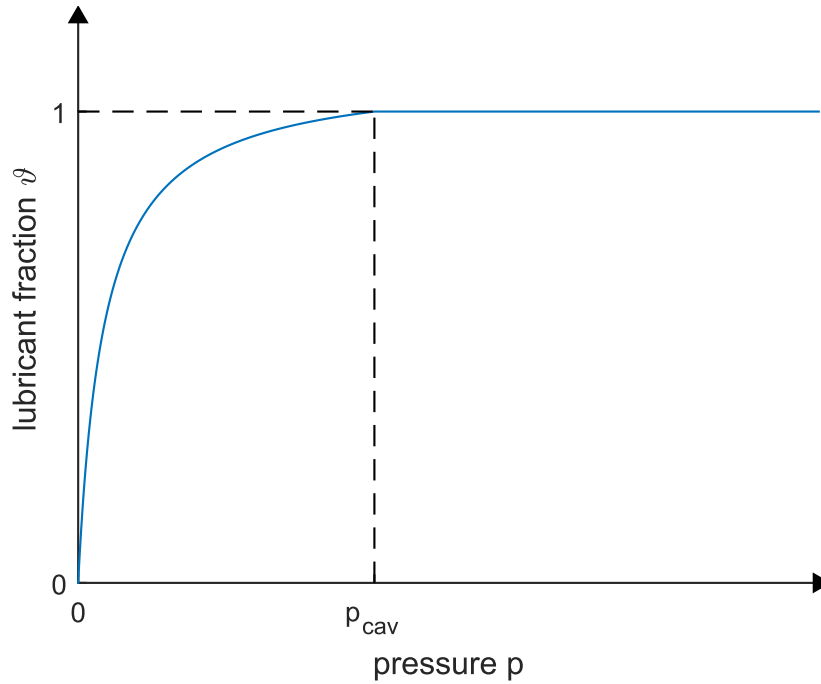


Figure 3.6.: Relation between pressure p and lubricant fraction ϑ for the PEEKEN model

3.3.3.3 Mixture Viscosity

The mixture viscosity η is influenced by two opposing effects and depends on the size of the air bubbles and the shear rate, see [PB85]. Small bubbles are dominated by surface tension and the viscosity increases with the bubble size, see [Ein05; Nik99; Goo+07]. Large bubbles are more deformable and are dominated by shear tension. The mixture viscosity decreases with increasing bubble radius, see [Nik99]. This is the usual case in journal bearings, see [PB85]. Since the viscosity of gas is negligible compared to that of liquid lubricant, an approach analogous to equation (3.33) can be made for the mixture viscosity, see [Car92]. The proportional relation

$$\frac{\rho}{\rho_l} = \frac{\eta}{\eta_l} \quad (3.40)$$

was proposed in [KB91a], where η_l is the lubricant viscosity. This approach is also used in this work, see section 4.2.

3.4 Solution of the REYNOLDS Equation

A classification of rotor systems supported by journal bearings based on the SOMMERFELD-number So is made in section 3.2.3. The rotor-speed ω of *heavy* rotors usually changes very slowly during operation or stays constant, e.g. for electrical power generation it is coupled to the power grid frequency. Then, the rotor shaft performs small whirl motions around the equilibrium position in the bearing, e.g. due to unbalance. This enables the linearization of the hydrodynamic forces with respect to the equilibrium position. This is done for several constant rotor-speeds ω , which results in stiffness and damping coef-

ficients. These rotor-speed-dependent coefficients are calculated a-priori and stored in look-up tables. The coefficients are interpolated during simulations.

For *light* rotors such as turbochargers, the rotation speed of the rotor changes rapidly. Furthermore, various sub-synchronous whirl motions above the linear stability threshold occur in the operating range and the oscillations due to unbalance are not small. Thus, linearizing the bearing forces with respect to stationary equilibria is not valid for such systems.

Since no closed-form solution of the REYNOLDS equation (3.6) exists, all solutions are approximate. Transient solutions can be separated into analytical solutions of a simplified REYNOLDS equation or numerical discretizations of the full REYNOLDS equation.

Possible simplifications of the REYNOLDS equation are the assumption of an infinitely short or an infinitely long bearing, see e.g. [LS78]. In both approaches, the diffusion in one film direction is neglected, enabling a closed-form solution of the bearing forces for plain cylindrical bearings. These approaches are very efficient and do not depend on a numerical mesh, yet they are only valid in a certain range of the ratio B/R and are restricted to simple cylindrical bearing designs. However, especially the short bearing theory yields acceptable results and is still widely used in analytical studies and in industry.

In order to calculate bearings with finite length and more complex gap geometries, numerical discretization methods are used. This also enables the consideration of additional effects, such as sophisticated cavitation or temperature models. The numerical solution is either calculated a-priori and stored in look-up tables, see e.g. [Bob08; Fuc02; Mer08; Mit90] or computed in every time-step, see e.g. [Boy11; Nit+13; Sch10]. The former method is fast and yields accurate results. Yet the amount of stored data increases exponentially with the number of input variables, which makes the method unfeasible for more sophisticated bearing models. The effort can be reduced by a separate solution and superposition of pure journal rotation and pure squeeze motion, yet this entails an error due to different cavitation regimes. Thus, no look-up table solutions are used in this work, but the REYNOLDS equation is solved in every time-step. An overview of commonly used discretization methods and considerations for the generation of the mesh are given in the next section.

3.4.1 Discretization Methods

Partial differential equations on complex geometries are solved approximately with the use of discretization methods. An a-priori defined mesh divides the geometry into a finite number of elements in which the partial differential equation is approximately solved. This results in linear or nonlinear equation systems. The unknowns are the state variables of the partial differential equation at discrete points in the geometry which are defined by the mesh.

The most important discretization methods are Finite Differences (FD), Finite Volumes (FV) and Finite Elements (FE). A comparison between these methods is made in [DR06], which is briefly recapitulated here:

- The main idea of the Finite Difference method is the approximation of the derivatives with difference quotients. This method is very accurate and easy to implement for simple geometries. However, high effort is required to adapt the method to more complex geometries.

-
- In the Finite Volume method, the partial differential equation is integrated over the volume elements. The volume integrals are converted into surface integrals using GAUSS's theorem. The fluxes of adjacent volume elements are set equal, which makes the discretized equations conservative. This makes the method popular in computational fluid dynamics. The solutions are usually computed in the center of the volumes. The method is easier to implement than the FE method, yet the realization of higher degree approximations is more difficult. The method is more flexible with regard to geometry than FD, but less than FE.
 - The Finite Element method is a special case of the GALERKIN method. A residual function is generated by inserting trial functions into the partial differential equation and integrating over the volume. The trial functions depend on the unknown solution. The residual function is then minimized, resulting in discrete equations for each element, which are composed in an equation system for the whole geometry. The use of the weak form of the partial differential equation reduces the requirements for the differentiability of the solution ansatz functions.

The Finite Element method is far developed in structural mechanics, where it derives from the principle of virtual work. In the last decades, its importance in fluid modeling increased, see [Rod91]. Its main advantages are its total flexibility with regard to geometry, see e.g. [ANG77], and the simple realization of higher degree approximations. On the other hand, its implementation is more complex than FD or FV. Since the discretized equations are not exactly conservative, numerical oscillations may occur in convection-dominated problems. In this case, artificial diffusion can be used for stabilization, see section 4.2.1.3.

In this work, the commercial finite-element software *COMSOL Multiphysics* is used for the calculation of the hydrodynamic forces and torques.

3.4.2 Mesh

Additionally to the choice of the discretization method, the structure of the numerical mesh has a high influence on the accuracy and efficiency of the calculation. The following considerations are partially taken from [Sch99].

Discretization meshes can be categorized into unstructured and structured meshes. Unstructured meshes are predominantly constructed using triangles in two-dimensional and tetrahedrons in three-dimensional space. This enables automatic mesh generation for arbitrary geometries, which makes them popular in structural mechanics. On the contrary, more elements are needed to fill up the geometry and less accuracy is achieved compared to structured meshes with equal element size.

Structured meshes usually are constructed using quadrangles in two-dimensional and hexahedrons in three-dimensional space. This requires a higher implementation effort, yet less storage usage. This also enables a simple identification of neighbor elements. Especially rectangular grids entail a minimal bandwidth of the system matrix and have a high accuracy, since errors from opposing edges partially cancel out. For these reasons, structured rectangular-like grids are widely used in computational fluid dynamics, where a low numerical error and high efficiency are more important than structural flexibility. In order to minimize the numerical error, the shape of the mesh elements has to fulfill some requirements:

-
- Sharp or reflex angles entail large gradients in the ansatz functions, which leads to higher numerical errors. This is avoided in automatic mesh generation e.g. by minimizing the smallest angle in each element. Especially rectangular meshes enable a simple calculation of the diffusion fluxes.
 - The edges of the elements should have similar lengths to improve convergence of the solution.
 - Adjacent elements should not strongly vary in size, especially in areas where large solution gradients are expected. Otherwise, the order of the discretization method is significantly reduced.

In contrast to the last statement, the efficiency of the calculation may be improved by using more and smaller elements in areas where large solution gradients are expected and less elements elsewhere. These areas are usually located at boundaries with sharp angles or large curvature, e.g. near the lubricant supply.

In this work, a Cartesian equidistant mesh is used for the discretization wherever possible and quadrangles elsewhere. Quadratic element ansatz functions are chosen for the approximation of the solution, which are a good compromise between accuracy and efficiency, see [Sch99].

4 Journal Bearing Model

After the general theory of hydrodynamic lubrication has been laid out, bearing geometry and mass-conserving cavitation modeling are treated in this chapter. Bearing designs which are commonly used in turbochargers are discussed in section 4.1. Particular attention is paid to floating ring bearings in section 4.1.5. The mass-conserving cavitation model used in this work is introduced in section 4.2.

4.1 Bearing Geometry

The geometry of the fluid film gap is described through the gap function $h(\phi, \bar{z})$, see figure 3.2 on page 20. Arbitrary bearing designs can be described with $h(\phi, \bar{z})$, as long as the fluid film is thin and its curvature is negligible compared to the other dimensions of the bearing. The bearings used in turbochargers usually are cylindrical. The governing equations are given in the next section.

In most applications of journal bearings, the shell, the journal or both do not have plain surfaces due to indentations such as grooves, bore holes or pockets. These features are used to supply lubricant to the gap or to alter the pressure profile, usually to improve the stability of the system. On the contrary, the load carrying capacity is reduced with respect to a plain bearing. Compared to the thin fluid film, these indentations are large chambers and the fluid inside does not generate significant hydrodynamic pressure. Since the REYNOLDS equation is only valid in thin fluid films, these areas are omitted in its solution and the resulting pressure profile p is only defined in the remaining area. There is no difference for the mathematical treatment whether the indentations are in the journal or the shell. The pressure inside the indentations is assumed constant and acts as a boundary condition for the thin fluid film. The pressure in the omitted areas applies a hydrostatic load on the shell and the journal, which has to be accounted for in the bearing forces. Furthermore, the shear stress in the indentations is not significant for the generation of the bearing torque, which results in a reduced surface area A in equation (3.17). The special cases of circumferential grooves and axial grooves are discussed in sections 4.1.2 and 4.1.3. The influences of lubricant supply are explained in section 4.1.4. Floating ring bearings are often used in turbocharger applications. Their properties are examined in detail in section 4.1.5.

4.1.1 Cylindrical Bearings

The gap function h of a cylindrical bearing shown in figure 3.2 is given by

$$h_{\text{cyl}} = C + e \cos(\Theta), \quad (4.1)$$

see e.g. [LS78]. The relation between the relative angle Θ and the absolute angle ϕ is

$$\phi = \Theta + \delta + \frac{\pi}{2}. \quad (4.2)$$

This yields

$$h_{\text{cyl}} = C + e \sin(\phi - \delta) = C + e (\cos \delta \sin \phi - \sin \delta \cos \phi) . \quad (4.3)$$

With the relations $D_x = e \cos \delta$ and $D_y = e \sin \delta$, the dimensionless gap function $H = h/C$ is written as

$$H_{\text{cyl}} = 1 + d_x \sin \phi - d_y \cos \phi \quad (4.4)$$

with the dimensionless Cartesian displacements $d_x = D_x/C$ and $d_y = D_y/C$. The use of Cartesian coordinates instead of ε - δ -coordinates facilitates the coupling with the rotor model, since no coordinate transformation has to be carried out.

If a non mass-conserving cavitation approach from section 3.3.2 is used, the fluid is assumed incompressible (i.e. $\rho = \text{const.}$) and ρ cancels out in the REYNOLDS equation (3.9). With the use of (4.4), the right-hand side of (3.9) is evaluated which yields

$$\frac{\omega}{2} \frac{\partial H_{\text{cyl}}}{\partial \phi} + \frac{\partial H_{\text{cyl}}}{\partial t} = \left(\frac{\omega}{2} d_x - \dot{d}_y \right) \cos \phi + \left(\frac{\omega}{2} d_y + \dot{d}_x \right) \sin \phi . \quad (4.5)$$

This further illustrates that the hydrodynamic pressure in the fluid film gap can be generated by two parts: the physical wedge is a combination of the relative displacements d_x , d_y and the angular velocity $\omega = \omega_J + \omega_S$ of the journal and the shell; the squeeze film damper effect is caused by the relative velocities \dot{d}_x , \dot{d}_y .

A simple formula for the bearing torque – which is widely used in literature – is derived for cylindrical bearings if the HAGEN-POISEUILLE flow in (3.17) is neglected:

$$M_{R,\text{cyl}} \approx -\frac{R^2 \eta}{C} (\omega_J - \omega_S) \frac{A}{\sqrt{1 - \varepsilon^2}} \quad (4.6)$$

with the hydrodynamic effective surface area A of the fluid film, which is $A = \pi DB$ for plain cylindrical bearings. The areas of grooves, pockets or bore holes have to be subtracted from A .

4.1.2 Circumferential Grooves

Circumferential grooves are usually used to improve the oil supply of the bearing gap by distributing the oil over the whole circumference. They can be located at one of the axial boundaries, e.g. in squeeze film dampers, or in one of the surfaces of the bearing gap, e.g. in the outer surface of a floating ring, see figure 4.4. The main difference to the ambient boundary condition is the higher pressure due to the oil supply. Bore holes which connect to the groove do not have to be modeled since the hydrodynamic pressure in the grooves is neglected and their area is omitted in the calculation of the REYNOLDS equation. The hydrostatic forces cancel out for a constant pressure in the groove. Furthermore, the rotation of the surfaces does not need to be considered in floating rings since the geometry is rotationally symmetric.

Thus, the dimensionless REYNOLDS equation with the minimal number of three input variables can be used, see section 3.2.5.

As an example, figure 4.1 shows the developed gap geometry of a bearing with a central circumferential groove. The groove separates the fluid film into two subdomains. Each subdomain is rectangular with the length $2\pi R$ and the width $b=B/2$. Since tilting of the journal is omitted, the resulting pressure profile and the shear stress distribution in both subdomains is symmetric. Thus, it is sufficient to solve the REYNOLDS equation only for one subdomain and double the resulting forces and torque. Furthermore, the axial extent of the groove does not influence the result. The boundary conditions are periodicity in circumferential direction, constant ambient pressure p_0 for the outer axial boundaries and constant groove pressure $p_{\text{sup}} \geq p_0$ for the inner axial boundaries.

The width b of each subdomain is small compared to the bearing radius R , which permits the use of the short bearing approximation. A modified short bearing solution with asymmetric axial boundary conditions is given in appendix B.

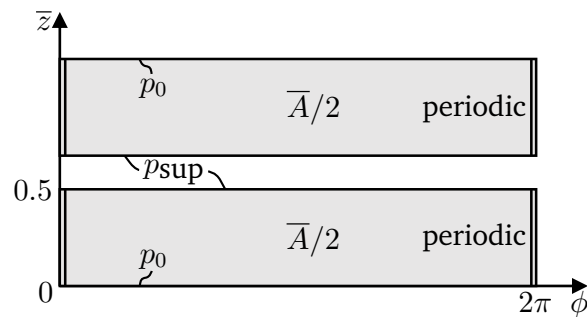


Figure 4.1.: Developed gap geometry with a central circumferential groove

4.1.3 Axial Grooves

Axial grooves extent over the whole width of a radial bearing and divide the surface into several bearing sections. They are usually used to improve the stability of a rotor system by influencing the pressure profile in the bearing gap. Axial grooves are by design present in bearings with preload such as lemon bore or multilobe bearings, but they are also used in cylindrical bearings. Figure 4.2 exemplarily shows the developed gap geometry of a bearing with three evenly spaced axial grooves, which was investigated in [Now+15a]. The pressure in the grooves equals the ambient pressure p_0 , if the grooves are open to the environment. The area A of the fluid film is reduced compared to a plain surface and the pressure profile is divided, which decreases the load carrying capacity. To compensate, the axial width B of the bearing can be increased. If the bearing has more than one groove and they are evenly spaced over the circumference, the hydrostatic force cancels out.

Axial grooves also influence the bearing torque, as the integrals in (3.17) have to be evaluated for each bearing section separately. The resulting torque is smaller compared to that of a plain cylindrical bearing. Equation (4.6) with the effective hydrodynamic fluid film area A is a good approximation for the bearing torque. For axial grooves in a floating ring, their rotation has to be considered during the solution of the REYNOLDS equation, see section 4.1.5.3.

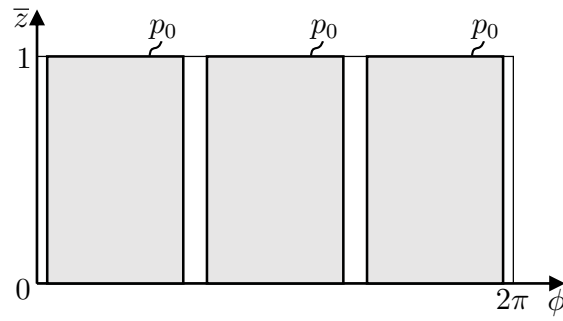


Figure 4.2.: Developed gap geometry with three evenly spaced axial grooves

4.1.4 Lubricant Supply

In radial journal bearings, the lubricant flows out of the bearing gap at the axial boundaries and thus has to be replaced continuously. The lubricant is usually supplied through an inlet in the shell of the bearing. The inlet often opens into a larger pocket or groove to distribute the lubricant over a wider area. Typically the lubricant supply pressure p_{sup} is higher than the ambient pressure p_0 in order to ensure that the bearing gap does not run dry.

It is assumed that the pressure inside the inlet equals the supply pressure p_{sup} , since the thin bearing gap acts as a throttle for the lubricant. The supply pressure p_{sup} is imposed as a boundary condition for the lubricant film. The influence of the boundary condition on the hydrodynamic pressure profile is determined by the magnitude of diffusion, which is proportional to H^3 , see equation (3.9). The lubricant supply affects the pressure only locally for a small gap size H , while it affects a larger area for a larger gap size.

For lightweight rotors, the hydrostatic pressure inside the inlet has a substantial effect on the stability of the system. The pressure acts normal to the journal surface, see figure 4.3. Without loss of generality, the y -axis is placed in the center of the inlet, which is assumed symmetric with respect to the y -axis. The angular extend of the inlet is Θ_g . To calculate the hydrostatic force F_{sup} acting on the journal, the vertical component of the effective radial pressure

$$p_{\text{stat}} = p_{\text{sup}} - p_0 \quad (4.7)$$

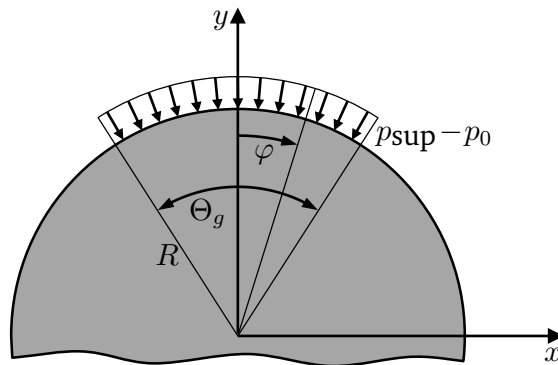


Figure 4.3.: Calculation of the hydrostatic lubricant supply force inside the inlet

has to be integrated over the curved inlet area A_{in} ,

$$F_{\text{sup}} = -p_{\text{stat}} \iint_{A_{in}} \cos \varphi dA_{in}. \quad (4.8)$$

There is no force in x -direction since the horizontal pressure components cancel out.

For a rectangular pocket or groove with axial width b this yields

$$F_{\text{sup, pocket}} = -p_{\text{stat}} \int_{-\Theta_g/2}^{\Theta_g/2} \int_0^b \cos \varphi R d\varphi dz = -p_{\text{stat}} bD \sin\left(\frac{\Theta_g}{2}\right). \quad (4.9)$$

The curvature of the inlet can usually be neglected for inlet geometries with small angular extend Θ_g such as bore holes without groove or pocket. This yields

$$F_{\text{sup, bore}} \approx -A_{\text{bore}} p_{\text{stat}}, \quad (4.10)$$

where A_{bore} is the surface area of the inlet. Even for small bearing diameters D – such as the inner fluid film in floating ring bearings from typical turbocharger applications – the error is negligible.

The deflection of the lubricant from the inlet into the gap generates another force component. However, it is negligible compared to the hydrostatic force (4.8) for typical journal bearing applications, see [Now10; Bau11].

The ambient pressure p_0 is specified as the initial condition for the pressure field in the numerical solution of the REYNOLDS equation. This leads to an inconsistency in the first time-step, if a supply pressure $p_{\text{sup}} > p_0$ is imposed at a boundary. This is circumvented by multiplying the pressure boundary condition at the inlet and the hydrostatic force (4.8) with the time-dependent scale function $f(t)$,

$$f = 1 - e^{-t/t_1}. \quad (4.11)$$

This function is 0 for $t=0$ and quickly tends to 1 as t increases, $f > 0.99$ for $t \geq 4.7 t_1$. The time constant t_1 is chosen as 10 ms in this work, which is small enough to not significantly influence the run-up behavior, yet large enough that the micro-step size of the solver does not decrease.

4.1.5 Floating Ring Bearings

A floating ring is a hollow cylinder, which embeds the rotor shaft and moves independently from the housing and the rotor. Figure 4.4 exemplarily shows two full floating rings with different surface geometries. The clearances between rotor, floating ring and housing are filled with lubricant, which results in two serially connected fluid films, see figure 4.5. Floating ring bearings enable operation speeds above the linear stability threshold of the rotor system, since the whirl or whip in one fluid film is mutually

damped by the other fluid film. Furthermore, manufacturing costs are low compared to more complex bearing geometries with improved stability behavior such as multilobe or tilting-pad bearings. For these reasons, floating ring bearings are usually used in turbocharger applications. If only one long floating ring is used and its rotation around the rotor axis is blocked, the configuration is termed *semi floating*, while two separate floating rings which rotate freely are called *full floating*.

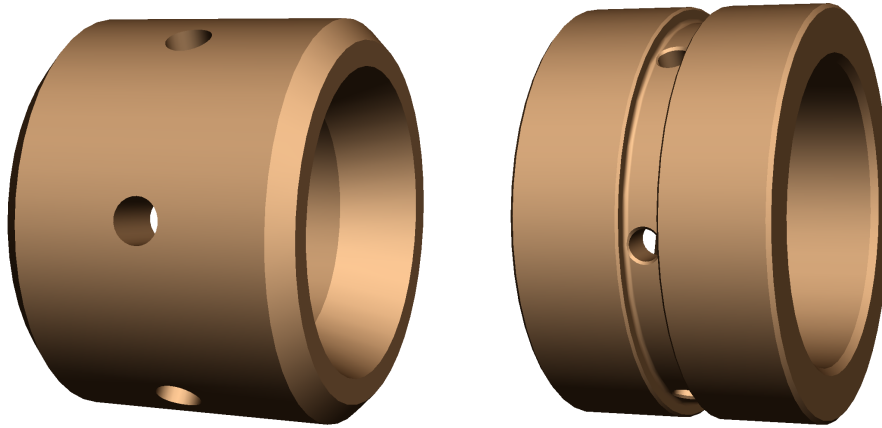


Figure 4.4.: Full-floating rings with plain surfaces (left) and with a circumferential groove in the outer surface (right)

Only the outer fluid film is supplied directly with lubricant through inlets in the housing. In order to supply lubricant to the inner fluid film, the fluid films are connected through channels in the floating ring. In many studies, these connecting channels holes are neglected, see e.g. [Boy11; Eli+16; Sch10; Wos+15]. Section 4.1.5.5 gives some insight on their influence.

If the coupling of the inner and outer fluid film is neglected, the bearing forces in each film are calculated analogous to a single fluid film. In the next section, the input variables for both fluid films – deriving from the motion of the rotor shaft and the floating ring – are explained. The equations of motion of a floating ring are given in section 4.1.5.2. If the surfaces of the floating ring are not rotationally symmetric, it is beneficial to solve the REYNOLDS equation in a coordinate system, which is fixed to the floating ring, see section 4.1.5.3. Lastly, the floating ring deforms due to temperature and rotation, which is discussed in section 4.1.5.4.

4.1.5.1 Input Variables for the Inner and Outer Fluid Film

In order to solve the REYNOLDS equation (3.9) for floating ring bearings, the following input variables are required for the inner and outer bearing gap:

- the relative displacements (D_x, D_y) of the journal with respect to the shell,
- the relative velocities (\dot{D}_x, \dot{D}_y) ,
- the angular velocities ω_J and ω_S of journal and shell, respectively.

Let (x_F, y_F) denote the absolute displacements of the floating ring with respect to the center of the bearing housing, see figure 4.5. The displacements in the outer fluid film are

$$D_{x,o} = x_F \quad \text{and} \quad D_{y,o} = y_F. \quad (4.12)$$

With the absolute displacements (x_J, y_J) of the rotor journal, the relative displacements in the inner fluid film are written as

$$D_{x,i} = x_J - x_F \quad \text{and} \quad D_{y,i} = y_J - y_F. \quad (4.13)$$

The relations for the relative velocities (\dot{D}_x, \dot{D}_y) are analogous to those of the relative displacements (D_x, D_y) . The absolute displacements (x_J, y_J) and the corresponding velocities (\dot{x}_J, \dot{y}_J) of the rotor journal at the location of the bearing are calculated in the rotor model, see section 2.1. Analogous to equation (3.7), the outer and inner eccentricities ε_o and ε_i can be defined,

$$\varepsilon_o = \frac{1}{C_o} \sqrt{D_{x,o}^2 + D_{y,o}^2} \quad \text{and} \quad \varepsilon_i = \frac{1}{C_i} \sqrt{D_{x,i}^2 + D_{y,i}^2}, \quad (4.14)$$

with the outer and inner nominal gap sizes C_o and C_i .

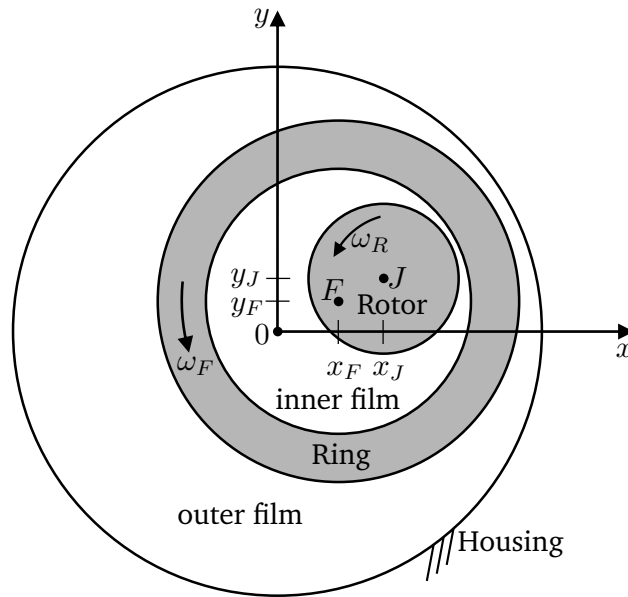


Figure 4.5.: Kinematics of a floating ring bearing

The angular velocities ω_J and ω_S of journal and shell for the outer fluid film are

$$\omega_{J,o} = \omega_F \quad \text{and} \quad \omega_{S,o} = 0 \quad (4.15)$$

and for the inner fluid film

$$\omega_{J,i} = \omega_R \quad \text{and} \quad \omega_{S,i} = \omega_F \quad (4.16)$$

with the angular velocities ω_R and ω_F of the rotor and the floating ring, see figure 4.5. This yields $\omega_o = \omega_F$ in the outer and $\omega_i = \omega_R + \omega_F$ in the inner fluid film for the sum of the angular velocities ω in the right-hand side of the REYNOLDS equation (3.9).

4.1.5.2 Equations of Motion for the Floating Ring

When the hydraulic coupling due to the connecting channels is neglected, the hydrodynamic forces (3.13) in the inner and outer fluid film are calculated separately and the kinetics of the floating ring are calculated inside the rotor model. If both the inner and the outer fluid film are solved simultaneously in one bearing model, the kinetics of the floating ring are incorporated into the bearing model.

The hydrodynamic forces in the outer fluid film are denoted with $F_{x,F}$ and $F_{y,F}$ and are applied in the center F of the floating ring, see figure 4.5. The forces in the inner fluid film are $F_{x,J}$ and $F_{y,J}$. They are applied in the center J of the rotor journal (actio) and negatively in F on the floating ring (reactio), see figure 4.6. The bearing torque (3.17) is denoted with M_F for the outer fluid film and acts on the floating ring. The torque M_J of the inner fluid film acts positively on the rotor shaft (actio) and negatively on the floating ring (reactio). Then, the equations of motion for the floating ring read

$$\begin{aligned} m_F \ddot{x}_F &= F_{x,F} - F_{x,J} \\ m_F \ddot{y}_F &= F_{y,F} - F_{y,J} - m_F g \\ \theta_F \dot{\omega}_F &= M_F - M_J \end{aligned} \tag{4.17}$$

with the mass m_F and the moment of inertia θ_F of the floating ring. The sign of the second term in the bearing torque (3.17) is changed for M_J acting on the floating ring, since in this case, the shear torque has to be evaluated at the surface of the shell.

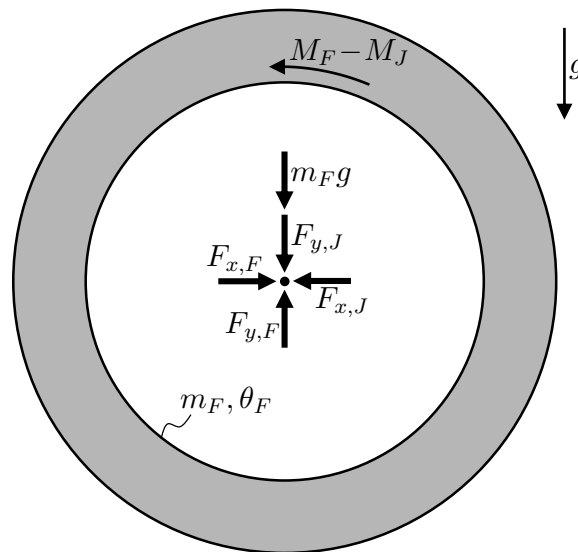


Figure 4.6.: Free-body diagram of a floating ring bearing

The bearing subsystem is not time-dependent when a non mass-conserving cavitation model is used. Thus, dynamic-static solver coupling is used for the calculation of the rotor-bearing system, see section 5.1. This method requires partial derivatives of the forces with respect to each coupling variable, which is computationally expensive, see section 3.2.5. The inclusion of the time-dependent differential equations (4.17) into the bearing model enables the use of co-simulation approaches, which do not require partial derivatives, see section 5.2. Then, both lubricant films have to be solved simultaneously in one bearing model, which increases the calculation time of one time-step. The resulting bearing model has more degrees of freedom, and the calculation of the inner and outer film cannot be fully parallelized. However, this approach is still more efficient for non mass-conserving models with floating ring bearings, since more parallel computations can be performed on one PC. This is not necessary when the mass-conserving two-phase model explained in section 4.2 is used, since the time-dependent REYNOLDS equation (4.31) directly enables the use of a co-simulation method.

4.1.5.3 Rotating Bearing Geometry

Floating rings feature connecting channels to supply lubricant to the inner fluid film. Additionally, other non plain geometries such as grooves or preloaded pads (e.g. [EOR15a]), can be present in the surfaces. The REYNOLDS equation (3.9) is formulated using the absolute angle ϕ , see figure 3.2. If the surfaces of the floating ring are not rotationally symmetric, it is beneficial to use a rotating coordinate system which is fixed to the floating ring. Otherwise, the position of connecting channels or grooves changes with time and thus the FE mesh has to be changed in every time-step.

Figure 4.7 shows the coordinates for the inner bearing gap. The relative position of the journal with respect to the shell is given through the Cartesian coordinates $(D_{x,i}, D_{y,i})$ or the cylindrical coordinates e and δ . The relative angle Θ is measured from the widest gap and is used for the description of the

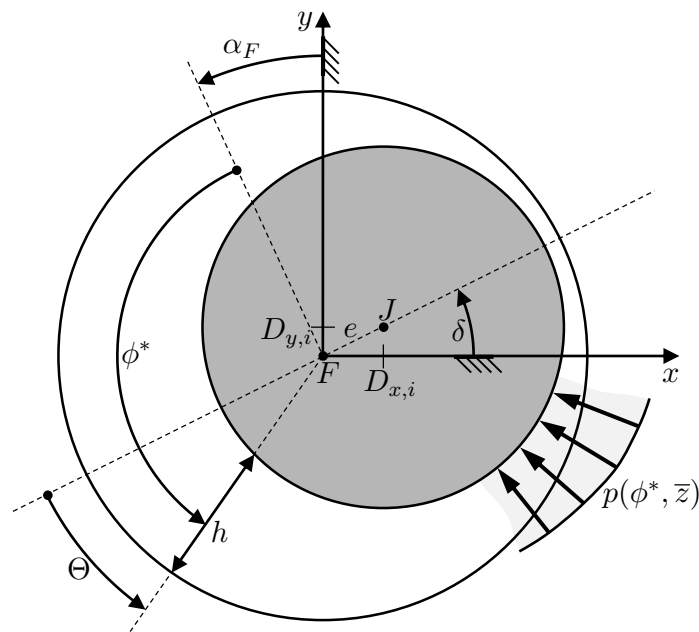


Figure 4.7.: Coordinates for rotating bearing geometry

gap function h . The angular displacement of the floating ring geometry is given through the absolute angle α_F with

$$\omega_F = \dot{\alpha}_F. \quad (4.18)$$

The angle ϕ^* is the relative circumferential coordinate with respect to the rotating shell. The relation between the coordinates is

$$\phi^* + \alpha_F = \Theta + \delta + \frac{\pi}{2}. \quad (4.19)$$

By comparing this expression to equation (4.2), it follows that

$$\phi = \phi^* + \alpha_F. \quad (4.20)$$

Thus, ϕ has to be substituted in the gap function (e.g. equation (4.4)), in the right-hand side of the REYNOLDS equation (e.g. equation (4.5)), and in the calculation of the bearing forces (3.13). Since the inertia forces of the fluid film are neglected, no additional terms occur due to the relative coordinate system. Note that $\partial\phi = \partial\phi^*$ and no additional term on the right-hand side due to $\partial H/\partial t$ occurs, since the angular velocity $\omega_S = \dot{\alpha}_F$ of the surface of the shell is already accounted for.

These relations can also be used for the outer bearing gap, e.g. if the outer surface of the floating ring is not rotationally symmetric.

4.1.5.4 Change of Bearing Gaps During Operation

The gap sizes of the inner and the outer fluid films change during operation due to deformations of the rotor shaft, the floating rings and the housing. This effect cannot be neglected, since the resulting bearing forces and torques strongly depend on the gap size, which enters the REYNOLDS equation through the relative gap size ψ , see e.g. equation (3.9). The resulting relative gap size of the inner or outer film is

$$\psi = \frac{C}{R} + \epsilon_{r,o} - \epsilon_{r,i} \quad (4.21)$$

where $\epsilon_{r,o}$ and $\epsilon_{r,i}$ are the radial strains of the outer and inner surface, respectively, which result from heating and centrifugal acceleration. The deformation of the solids due to the hydrodynamic or hydrostatic pressure is usually neglected for turbochargers. However, it is important in applications with very high load, e.g. crank shafts, [KSR15; NWD17], or with elastic housings, e.g. aero engines, [Wan+17].

The relation between strain and stress in a linear elastic solid is given by Hooke's law. For a 2-dimensional stress state in cylindrical coordinates it reads

$$\epsilon_r = \frac{1}{E}(\sigma_r - \nu \sigma_\phi) + \alpha_T \Delta T, \quad (4.22)$$

see [Mar11]. The material properties of the solid are YOUNG's modulus E , POISSON's ratio ν and the thermal expansion coefficient α_T . The radial and circumferential stresses σ_r and σ_ϕ are determined by the balance of momentum for an infinitesimal small element. This leads to differential equations for the stresses which are solved by formulating appropriate boundary conditions. Stresses are also caused by non constant temperature fields. In [Mar11], solutions for a 2-dimensional stress state and the resulting strains are given. The second term in (4.22) is the thermal expansion for a constant temperature difference ΔT with respect to ambient temperature.

Table A.2 on page 114 lists resulting strains of the rotor shaft, the floating ring and the housing due to rotation and thermal expansion for two different turbocharger applications. Worst case parameters are used which maximize the influences of rotation and non-constant temperature fields.

The temperature T_R in the rotor shaft is assumed constant due to the high thermal conductivity of steel and equal to the lubricant temperature T_i of the inner fluid film. Thus, the stresses σ_r and σ_ϕ only result from the rotation speed ω_R . The deformation due to rotation at maximum rotation speed is one order of magnitude smaller than the deformation due to constant temperature. This is reasonable due to the relatively small radius of the rotor shaft.

The temperature in the floating ring decreases in radial direction and is a function of the lubricant temperatures T_i and T_o in the inner and outer fluid film, which act as boundary conditions. The stationary thermal conduction equation for solids without heat sources and constant conductivity is $\nabla^2 T = 0$. In cylindrical coordinates it reads

$$\frac{\partial^2 T}{\partial r^2} + \frac{1}{r} \frac{\partial T}{\partial r} + \frac{1}{r^2} \frac{\partial^2 T}{\partial \phi^2} + \frac{\partial^2 T}{\partial z^2} = 0, \quad (4.23)$$

see e.g. [Spu13]. The temperatures in the fluid films are assumed homogeneous, thus the temperature gradient in circumferential ϕ -direction vanishes. Furthermore, also the temperature gradient in axial z -direction is neglected since the heat transfer from the solid to the liquid lubricant is much larger than the heat transfer in axial direction to the surrounding air. Figure 4.8 shows two numerical solutions of (4.23) using *Comsol Multiphysics* with the assumption of thermal radiation in axial direction. The resulting temperature profile is almost linear in radial direction.

For comparison, the thermal expansion is also calculated assuming a constant medium temperature $T_F = (T_i + T_o)/2$. The difference to the thermal expansions assuming a linear temperature distribution is small, see table A.2.

The rotation speed ω_F of the floating rings is a fraction of the rotor-speed ω_R , usually $\omega_F < 0.4 \omega_R$. The deformations due to rotation at maximum rotation speed are smaller than the thermal expansion, especially for the outer surface.

The temperature T_H of the housing is assumed constant and equal to the lubricant supply temperature T_{SUP} , which is usually smaller than the temperature T_o of the outer fluid film. The housing exhibits the smallest relative deformation due to the relatively low temperature.

Due to the strains of the surfaces, the inner bearing gap increases while the outer bearing gap decreases. The expansions of the rotor shaft and the floating ring due to rotation were approximated with a 2-dimensional stress state. In reality, the stress state is three-dimensional and it is assumed that the

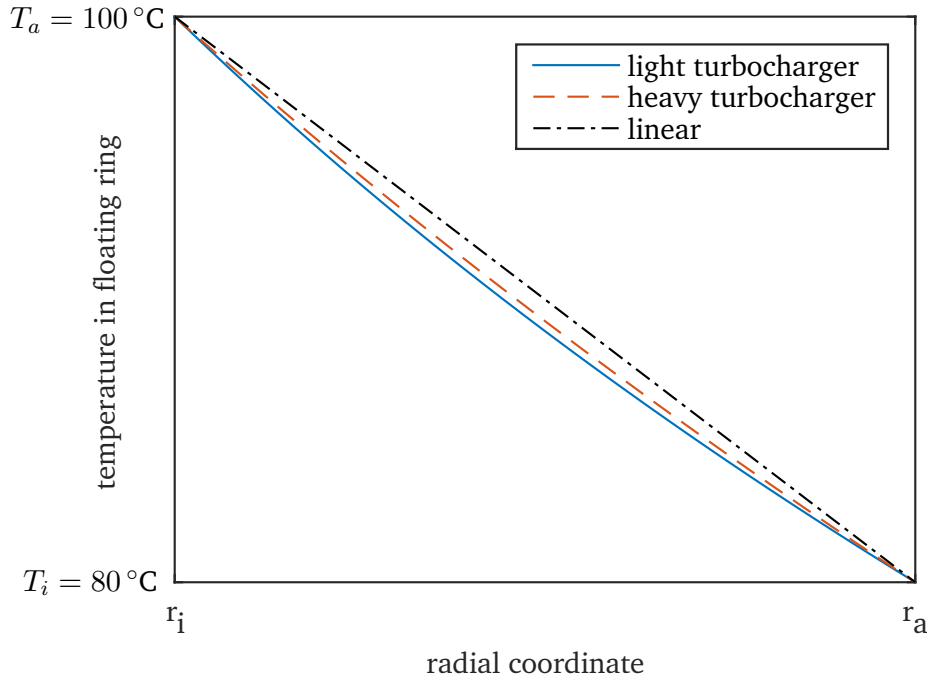


Figure 4.8.: Radial temperature field in a floating ring for two different turbocharger applications, see table A.2

deformations in radial direction are smaller due to the additional stress in axial direction. Furthermore, the deformations increase quadratically with the rotation speed. Even at maximum rotation speed, the thermal expansion remains the biggest influence on the bearing gaps. Additionally, the temperatures in the fluid films probably increase during run-up due to higher friction, which is not considered in the isothermal approach. Without a sophisticated thermal model and realistic boundary conditions, the temperatures of the solids have to be calculated using the lubricant temperatures, which are estimated from measured lubricant supply and outflow temperatures. Thus in future work, the inclusion of a thermal model should be prioritized over the consideration of centrifugal stresses in the floating rings. An approximate formula for the change of the relative bearing gaps is derived by assuming a constant temperature in the solids and neglecting the stresses due to rotation. Inserting (4.22) into (4.21) yields

$$\psi_o \approx \frac{C_o}{R_o} + \alpha_{T,H}\Delta T_H - \alpha_{T,F}\Delta T_F \quad \text{and} \quad (4.24)$$

$$\psi_i \approx \frac{C_i}{R_i} + \alpha_{T,F}\Delta T_F - \alpha_{T,J}\Delta T_R.$$

With this simple formula, the gap sizes are calculated a-priori without introducing additional state variables, while still accounting for the most important influence.

4.1.5.5 Connecting Channels

Similar to oil inlet geometries and grooves, the connecting channels in floating ring bearings are not thin fluid films and thus the REYNOLDS equation is not valid there. The channels are holes in the 2-dimensional fluid film geometry and the inner and outer fluid film have to be coupled using boundary conditions for these holes.

Only scarce literature on connecting channels and their influence exists. In [EOR15b], three-dimensional CFD simulations (full NAVIER-STOKES-equations) of a connecting channel have been performed. These calculations are computationally expensive, since a fine mesh is required to resolve the thin fluid films. It was found that the flow inside the channels is rather complicated and results in pressure spikes due to a throttle effect at the transition from the channel to the thin gap. Yet also a pressure balance between the inner and the outer fluid film takes place.

The actual flow cannot be captured accurately with the REYNOLDS equation. Thus, some simple approaches have been made, which consider the coupling by setting the pressure at the connecting channel boundaries in the inner and outer fluid film equal, see e.g. [Por+14; Wos+11]. Results show that the influence on the pressure distribution in the bearing gaps is only local, due to the small diffusion in thin films, see equation (3.9).

The coupling requires the simultaneous calculation of the pressure in both fluid films. This favors the calculation of the kinetics of the floating ring in the bearing model, see section 4.1.5.2. The flow through the connecting channels is only realistic, if mass-conserving cavitation models are used. This is especially important for the implementation of a realistic thermal model.

For the rotor systems with floating ring bearings investigated in chapter 7, the holes of the connecting channels in the outer bearing gap are contained within a circumferential groove, see figure 7.1. Since the pressure in the groove is assumed constant, the pressure in the connecting channels is also constant and no hydraulic coupling has to be considered. However, two other effects are considered in this work, which are explained in the following.

The mass of the fluid inside the connecting channels is not negligible and is accelerated in radial direction due to the rotation of the floating ring. This results in a pressure difference at the channel boundaries in the inner and outer fluid film.

Let A_{cc} denote the projected area of the connecting channels, see figure 4.9. The inner and outer radii of the floating ring are R_i and R_o . A cylindrical volume element of lubricant inside the connecting channel with the infinitesimal small radial extent dR located at radius R has the infinitesimal small mass dm . Then, the infinitesimal centrifugal force dF_{cf} acting on a fluid volume is

$$dF_{cf} = A_{cc} dp = R \omega_F^2 dm, \quad (4.25)$$

with the angular velocity ω_F of the floating ring. The mass dm can be expressed as $dm = \rho_l A_{cc} dR$ with the lubricant density ρ_l , which yields

$$dp = R \omega_F^2 \rho_l dR. \quad (4.26)$$

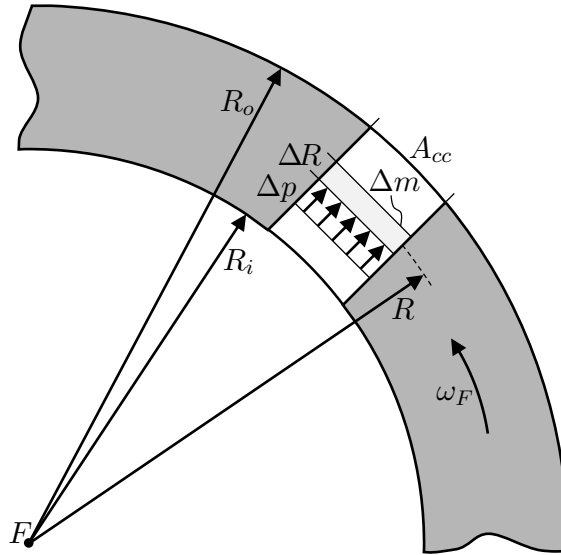


Figure 4.9.: Centrifugal pressure in connecting channels of full-floating ring bearings

Integration of the infinitesimal pressure dp over the radial extent of the connecting channels yields the pressure difference Δp between the inner and outer fluid film,

$$\Delta p = \int_{R_i}^{R_o} dp = \omega_F^2 \rho_l \int_{R_i}^{R_o} R dR = \omega_F^2 \frac{\rho_l}{2} (R_o^2 - R_i^2) , \quad (4.27)$$

see also [EOR15b]. The relation between the inner and outer pressure boundaries $p_{\text{channel},i}$ and $p_{\text{channel},o}$ is

$$p_{\text{channel},o} = p_{\text{channel},i} + \Delta p . \quad (4.28)$$

In chapter 7, the pressure in the connecting channels is given through the pressure p_{sup} in the circumferential groove in the outer fluid film. It is assumed that the pressure difference is divided equally between the inner and outer fluid film. Thus, the boundary condition for the connecting channels in the inner fluid film is

$$p_{\text{channel},i} = p_{\text{sup}} - \frac{\Delta p}{2} . \quad (4.29)$$

It is assumed that the pressure in the circumferential groove is not influenced significantly due to the connecting channels due to its large volume.

The hydrostatic pressure inside a connecting channel applies the radial force (4.10) on the rotor shaft and the housing. The forces acting on the floating ring cancel out. If the pressure in all connecting channels is equal, e.g. due to a circumferential groove, the sum of the forces cancels out. If both fluid films are fully coupled, the pressure in the connecting channels results from the hydrodynamic pressure profiles in both fluid films and is different for each channel. This results in a hydrostatic force with time-dependent magnitude and orientation on the shaft.

4.2 Mass-Conserving Cavitation Model for Rotordynamic Simulations

The cavitation model used in this work was introduced in [NSS16]. It uses a predefined function $\vartheta(p)$ for the lubricant fraction, which is inserted into the REYNOLDS equation (3.9). This yields a single equation in p , which is valid in the whole fluid film and is easily implemented in commercial software. The modified REYNOLDS equation is derived in the next section. The model can be adopted with different functions $\vartheta(p)$, to reflect a complimentary model (section 3.3.3.1) or a model with bubble dynamics (section 3.3.3.2). In this work, the function $\vartheta(p)$ is tuned to reflect the ELROD algorithm, see section 4.2.1.1. Special attention is paid to the axial boundary conditions in section 4.2.1.2, which cannot be adopted directly from classical approaches. Numerical oscillations can occur when using finite elements for convection-dominated problems, which have to be stabilized with artificial diffusion, see section 4.2.1.3. Furthermore, the assumption of a liquid/gas mixture influences the bearing torque, which is explained in section 4.2.1.4. The model is compared to non mass-conserving cavitation approaches in section 4.2.2.

4.2.1 General Two-Phase REYNOLDS Equation

The two-phase flow is approximated by a compressible single-phase fluid with mixture density ρ and mixture viscosity η . The lubricant content is described with the lubricant fraction ϑ . The relation between ρ and ϑ is given by equation (3.33). For the mixture viscosity η , the density-proportional relation proposed in [KB91a] is used. This yields

$$\vartheta = \frac{\rho}{\rho_l} = \frac{\eta}{\eta_l}. \quad (4.30)$$

Equation (4.30) is used to eliminate the mixture density ρ and the mixture viscosity η in the compressible REYNOLDS equation (3.9). Assuming that the lubricant fraction ϑ is pressure-dependent yields

$$-H \frac{\partial \vartheta}{\partial p} \frac{\partial p}{\partial t} + \frac{\partial}{\partial \phi} \left[\frac{\psi^2}{12\eta_l} H^3 \frac{\partial p}{\partial \phi} \right] + \left(\frac{R}{B} \right)^2 \frac{\partial}{\partial \bar{z}} \left[\frac{\psi^2}{12\eta_l} H^3 \frac{\partial p}{\partial \bar{z}} \right] - \frac{\omega}{2} H \frac{\partial \vartheta}{\partial p} \frac{\partial p}{\partial \phi} = \vartheta \left[\frac{\omega}{2} \frac{\partial H}{\partial \phi} + \frac{\partial H}{\partial t} \right]. \quad (4.31)$$

The liquid lubricant density ρ_l cancels out. Equation (4.31) explicitly depends on time t and is nonlinear in p . The derivative $\partial \vartheta(p)/\partial p$ can be calculated a-priori, since $\vartheta(p)$ is a known function. The bearing forces do not directly depend on the lubricant fraction ϑ and are calculated analogously to non mass-conserving models. In the fully developed lubricant film, $\vartheta = 1$ and (4.31) simplifies to a bearing with incompressible lubricant and the SOMMERFELD cavitation condition. The function $\vartheta(p)$ is defined in the next section.

A dimensionless form of (4.31) analogous to section 3.2.5 requires the introduction of a dimensionless time τ . Since the bearing model is coupled to rotor models and the time t is a coupling variable, the dimensioned form (4.31) is used.

Equation (4.31) is solved using the commercial finite element software *Comsol Multiphysics*. For the time

discretization, an implicit BDF method with variable time-step size and variable polynomial degree up to 5 is used, see also section 2.2.2.

4.2.1.1 Relation between Pressure and Lubricant Fraction

A pre-defined relation between the pressure p and the lubricant fraction ϑ is used, similar to the two-phase model explained in section 3.3.3.2. There, the relation $\vartheta(p)$ is derived from bubble dynamics assuming gaseous cavitation. It is argued in section 3.3.1 that this may not be the main cause in open-ended bearings, especially under high dynamic loads. The ELROD algorithm is a more general approach to model cavitation. As soon as the pressure drops to the cavitation pressure p_{cav} , a cavity forms, which can also be open to the surrounding atmosphere, thus reflecting the sucking-in of air. The disadvantages of the complimentary ELROD algorithm are

- the neglected changes of fluid properties in the cavity which yields $p = p_{cav}$,
- the discrete division of the bearing gap into the fully developed fluid film and the cavitated region, which requires a fine mesh.

In order to reflect the ELROD algorithm, $\vartheta(p)$ resembles the inverse function of figure 3.5 on page 33. A smoothed step function is used for $\vartheta(p)$ in order to reduce the stiffness of the numerical model. Cavitation occurs for $p < p_{cav}$. The film is completely filled with liquid lubricant for $p \geq p_{cav}$. The function has to be steep at $p \approx p_{cav}$ in order to achieve an approximate complimentary problem with a continuous function:

- For $p \geq p_{cav}$, the fluid film is assumed fully developed. The liquid lubricant is considered incompressible, thus $\vartheta \approx 1$. The pressure p changes to fulfill the REYNOLDS equation (4.31).
- For $p < p_{cav}$, the fluid film is assumed cavitated. Due to a steep gradient $\partial\vartheta/\partial p$ at $p \approx p_{cav}$, the pressure p only drops slightly below p_{cav} and the lubricant fraction ϑ varies in the cavitated area.

If the pressure drops further, ϑ tends to zero, thus the gap is completely filled with gas or vapor. Yet this can be prevented by ensuring sufficient lubricant supply and did not occur in any simulations performed in this work. The relation is shown in figure 4.10.

The gradient $\partial\vartheta/\partial p$ must not become zero, otherwise the first term in equation (4.31) vanishes, which causes an error in the time-dependent solver. This is circumvented by incorporating a very small gradient $\vartheta'_0 = 10^{-3}$, which is greatly exaggerated shown in figure 4.10. A third degree polynomial is chosen for the step and linear functions elsewhere:

$$\vartheta(p) = \begin{cases} \vartheta'_0 \frac{p}{p_{cav}} & \frac{p}{p_{cav}} < x_0 \\ (1 - \vartheta'_0 x_0) [(1 - m_\vartheta) \tilde{p}^2 (3 - 2\tilde{p}) + m_\vartheta \tilde{p}] + \vartheta'_0 x_0 & \text{for } x_0 \leq \frac{p}{p_{cav}} \leq 1 \\ 1 + \vartheta'_0 \left(\frac{p}{p_{cav}} - 1 \right) & \frac{p}{p_{cav}} > 1 \end{cases} \quad (4.32)$$

$$\frac{\partial \vartheta}{\partial p} = \begin{cases} \vartheta'_0 & \frac{p}{p_{\text{cav}}} < x_0 \\ \frac{\vartheta'_0}{m_\vartheta} [(1-m_\vartheta)6\tilde{p}(1-\tilde{p}) + m_\vartheta] & \text{for } x_0 \leq \frac{p}{p_{\text{cav}}} \leq 1 \\ \vartheta'_0 & \frac{p}{p_{\text{cav}}} > 1 \end{cases} \quad (4.33)$$

with the scaled pressure function \tilde{p} and the scaled slope m_ϑ

$$\tilde{p} = \frac{p/p_{\text{cav}} - x_0}{1 - x_0} \quad \text{and} \quad m_\vartheta = \vartheta'_0 \frac{1 - x_0}{1 - x_0 \vartheta'_0}. \quad (4.34)$$

The steepness is controlled with the parameter x_0 , which marks the onset of the slope, see figure 4.10. In the results shown in chapters 6 and 7 the parameter x_1 is used,

$$x_1 = \frac{x_0 + 1}{2}, \quad (4.35)$$

which is the location of the steepest gradient.

A polynomial of fifth degree does not yield an advantage to the polynomial of third degree. An additional parameter would be introduced, which offers only a slight margin between the extremal values, since overshoot has to be prevented.

Equation (4.32) has smooth derivatives at $p/p_{\text{cav}} = x_0$ and $p/p_{\text{cav}} = 1$. It has been found for the applications considered in this work that the influence is negligible for $\vartheta'_0 < 10^{-2}$ and that it would be sufficient

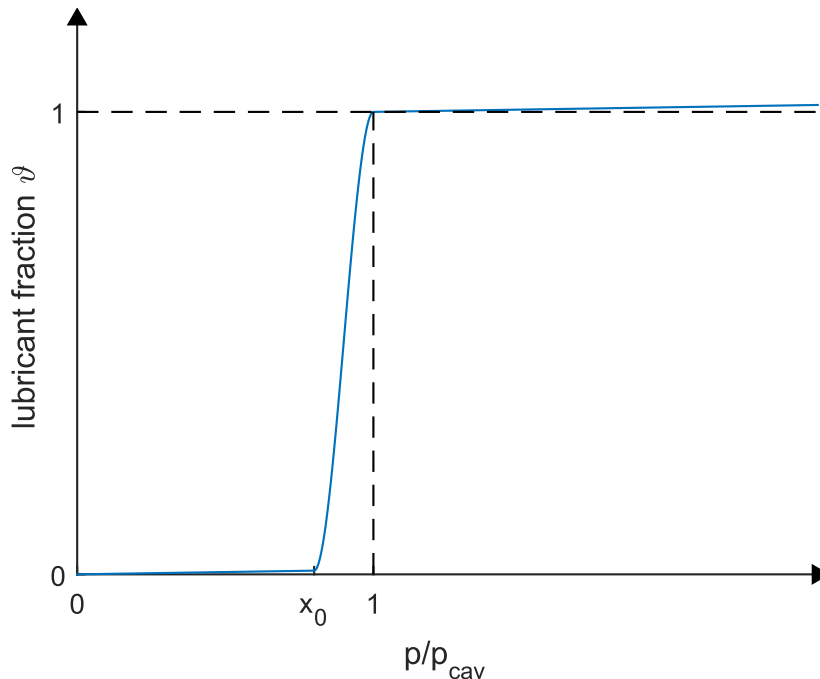


Figure 4.10.: Step-like ansatz function for the lubricant fraction ϑ as a function of the pressure p

to add ϑ'_0 only in the derivative $\partial\vartheta/\partial p$. Since the effort to implement equation (4.32) is small, it is used as shown.

The parameter x_0 influences the results of the model. The JFO boundary conditions are better reflected, the closer x_0 tends to 1. On the contrary, a steep gradient in $\vartheta(p)$ increases calculation times and leads to numerical instabilities. This is examined in chapter 6.

The ansatz function (4.32) is compared to the ELROD and the PEEKEN cavitation models in figure 4.11. Furthermore, also a detailed two-phase model from PRIEST introduced in [GPP06] is shown for a constant temperature, which is derived from the solubility of a refrigerant in synthetic oil. This mixture is used in cooling machines for the lubrication of the compressor and accurate material laws for the density and the solubility are available. The mass-fraction w_0 of gas at ambient condition is derived from the material laws given in [GPP06]. The bulk modulus β of the ELROD model is chosen small in order to illustrate the compressibility of the liquid lubricant for $p > p_{\text{cav}}$. The BUNSEN-coefficient α_B is an usual value for air in oil, see [PS61]. The steepness parameter x_0 is chosen relatively small to make the smoothed step visible. Furthermore, the gradient ϑ'_0 is exaggerated.

The models are similar, except the PEEKEN model. All models yield a zero lubricant fraction for $p=0$ and $\vartheta \approx 1$ for $p \geq p_{\text{cav}}$. The model used in this work qualitatively falls between the PRIEST and the ELROD model. The cavitation pressure p_{cav} from the PRIEST model depends on the temperature of the mixture, because it influences the solubility of the refrigerant in the liquid lubricant. Almost no difference between the ansatz function (4.32) and the ELROD model can be seen for usual values of β and x_0 . Furthermore, also the relation $\vartheta(p)$ from the PEEKEN model tends to the other models, if enough air is available, i.e. α_B is large.

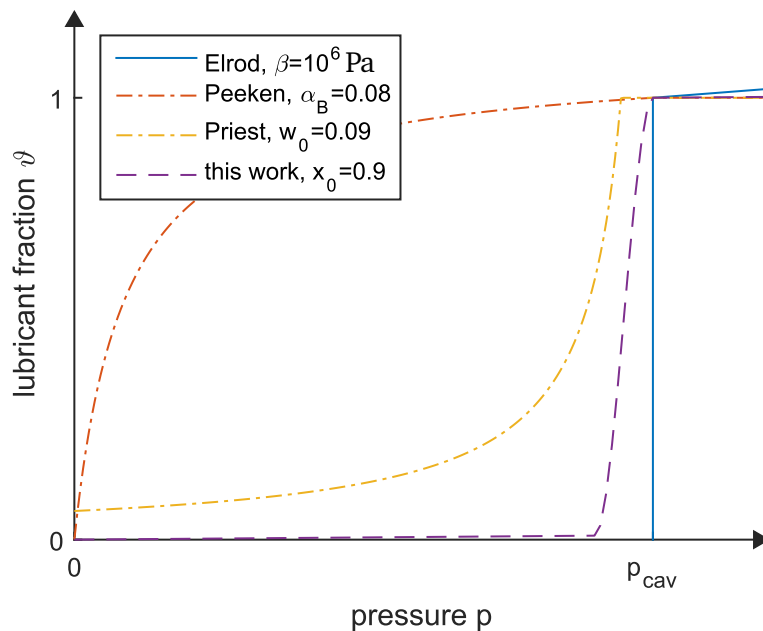


Figure 4.11.: Comparison of the ansatz function $\vartheta(p)$ with ELROD, PEEKEN and PRIEST cavitation models

4.2.1.2 Axial Boundary Conditions and Lubricant Supply

Usually, the pressure at the axial boundaries of the bearing is set to ambient pressure, see section 3.2.1. The pressure cannot drop below the ambient pressure p_0 in many cavitation models, e.g. half-SOMMERFELD or ELROD. Thus, the axial pressure gradient $\partial p/\partial \bar{z}$ always yields an outflow of the lubricant out of the bearing gap in the fully developed fluid film and zero axial flow in the cavitated region. With the use of a penalty approach (section 3.3.2), a two-phase model (section 3.3.3.2) or the cavitation model from this section, the pressure p drops below the ambient pressure p_0 in the cavitated region. If the pressure p is fixed to ambient pressure p_0 at the axial boundaries, lubricant flows from the surrounding atmosphere into the gap. This implicitly resembles a bearing submerged in a lubricant bath. Yet this is a rare case in practice. Most journal bearings are free to air at their axial boundaries, thus no lubricant can enter the bearing gap from the surrounding atmosphere.

In [NSS17], a NEUMANN boundary condition was introduced,

$$\left(\frac{R}{B}\right)^2 \frac{\psi^2}{6\eta} \left[H^3 \frac{\partial p}{\partial \bar{z}} \right]_{\phi, \bar{z}=0, t} = g(p), \quad \left(\frac{R}{B}\right)^2 \frac{\psi^2}{6\eta} \left[H^3 \frac{\partial p}{\partial \bar{z}} \right]_{\phi, \bar{z}=1, t} = -g(p), \quad (4.36)$$

with the pressure-dependent penalty function g

$$g = a e^{-b \frac{p-p_0}{p_0}}. \quad (4.37)$$

Axial flow from the surrounding into the cavitated region is prevented by $g \approx 0$ for $p \leq p_0$. A steeply increasing g for $p > p_0$ yields a strong outflow, which lowers the axial pressure to the ambient pressure p_0 . Thus, the boundary condition (4.36) acts similar to a DIRICHLET boundary condition for the fully developed fluid film. The parameters a and b have to be chosen analogous to the cavitation penalty approach in section 3.3.2. It has been found that $a=0.01$ and $b=100$ yield good results for all operating conditions.

The solution of the REYNOLDS equation (4.31) with only NEUMANN and periodic boundary conditions may yield problems, since the level of the pressure is not defined and all solutions with a constant offset also fulfill the boundary conditions. Thus, a lubricant inlet has to be defined, which is a DIRICHLET boundary condition with a constant feeding pressure p_{sup} . This is also plausible from a physical standpoint, since a journal bearing without lubricant supply would run dry.

4.2.1.3 Artificial Diffusion

The modified REYNOLDS equation (4.31) contains the convective term $-\omega H \partial \vartheta / \partial p \partial p / \partial \phi$, which is not present in the classical single-phase REYNOLDS equation (3.9). This term becomes very large compared to the diffusion terms for large rotation speeds ω and steep gradients $\partial \vartheta / \partial p$. This leads to numerical oscillations in p and ϑ , which distort the results, yield large calculation times and may prevent the solver to converge. Such oscillations usually occur in finite element problems, which are dominated by

convection, i.e. the ratio of velocity to viscosity is high, which yields steep gradients in the solution, see [Rod91]. The oscillations disappear with a finer mesh, i.e. the local element size has to be small enough to resolve the gradients of the solution. However, the required element size may be too small for practical calculations. Numerical stabilization techniques exist, which allow for a coarser mesh solution, while still suppressing numerical oscillations. In this work, an artificial diffusion approach is used, which is explained in this section.

As a simple example, a transport problem is considered, see [DR06],

$$\frac{\partial p}{\partial t} + \boldsymbol{\beta} \cdot \nabla p = \nabla \cdot (c \nabla p) + f, \quad (4.38)$$

with a source term f . Numerical oscillations occur, if the convection coefficient $\beta = \|\boldsymbol{\beta}\|$ is large compared to the diffusion coefficient c . This can also be expressed with the local PécLET number

$$Pe = \frac{h\beta}{2c} \quad (4.39)$$

with the local mesh element size h . No oscillations occur, if $Pe < 1$. This also illustrates that the solution can be stabilized by choosing a small enough element size h .

One approach to keep the PécLET number Pe below 1 is to add additional, so-called *Artificial Diffusion*

$$c_{\text{ad}} = \gamma h \beta, \quad (4.40)$$

to the diffusion coefficient c , see [Kuz10]. γ is a constant parameter. The resultant PécLET number with Artificial Diffusion is

$$Pe_{\text{ad}} = \frac{h\beta}{2c + 2\gamma h\beta} = \frac{1}{\frac{1}{Pe} + 2\gamma}. \quad (4.41)$$

It is evident that $Pe_{\text{ad}} < 1$ for $\gamma \geq 0.5$. The Artificial Diffusion term c_{ad} is added to both diffusion coefficients in equation (4.31), with $\beta = -\omega/2 H \partial\vartheta/\partial p$. This is so-called *Isotropic Artificial Diffusion*.

The addition of Artificial Diffusion suppresses numerical oscillations, yet the results are not exact, since the differential equation is altered. Assuming a constant element size h , the Artificial Diffusion term (4.40) is only large, where steep gradients $\partial\vartheta/\partial p$ occur. Yet it does not vanish, if the existing diffusion c is already large enough to yield $Pe < 1$.

RODDEMAN proposed an enhancement termed *Consistent Artificial Diffusion* in [Rod91], which makes the Artificial Diffusion term additionally dependent on the local PécLET number Pe :

$$c_{\text{ad,cons}} = \gamma h \beta f_{\text{cons}} \quad (4.42)$$

with the function

$$f_{\text{cons}} = \sqrt{\frac{Pe^2}{3^2 + Pe^2}}. \quad (4.43)$$

The resultant PécLET number with Consistent Artificial Diffusion is

$$Pe_{\text{ad,cons}} = \frac{h\beta}{2c + 2\gamma h\beta f_{\text{cons}}} = \frac{1}{\frac{1}{Pe} + 2\gamma f_{\text{cons}}}. \quad (4.44)$$

It follows that $Pe_{\text{ad,cons}} < 1$ for

$$\gamma f_{\text{cons}} \geq 0.5 \left(1 - \frac{1}{Pe}\right). \quad (4.45)$$

If $\gamma = 0.5$ is chosen as before, the condition simplifies to $f_{\text{cons}} \geq (1 - 1/Pe)$, which is visualized in figure 4.12. The function f_{cons} is already optimized to fulfill this condition. It is also visible that the Consistent Artificial Diffusion term (4.42) tends to 0, if the local PécLET number Pe is small enough. It has been found that the influence of consistent artificial diffusion on the results is small for the simulations performed in this work. Yet the additional effort to implement it is small and it has no significant impact on the calculation time, therefore it is used throughout this work.

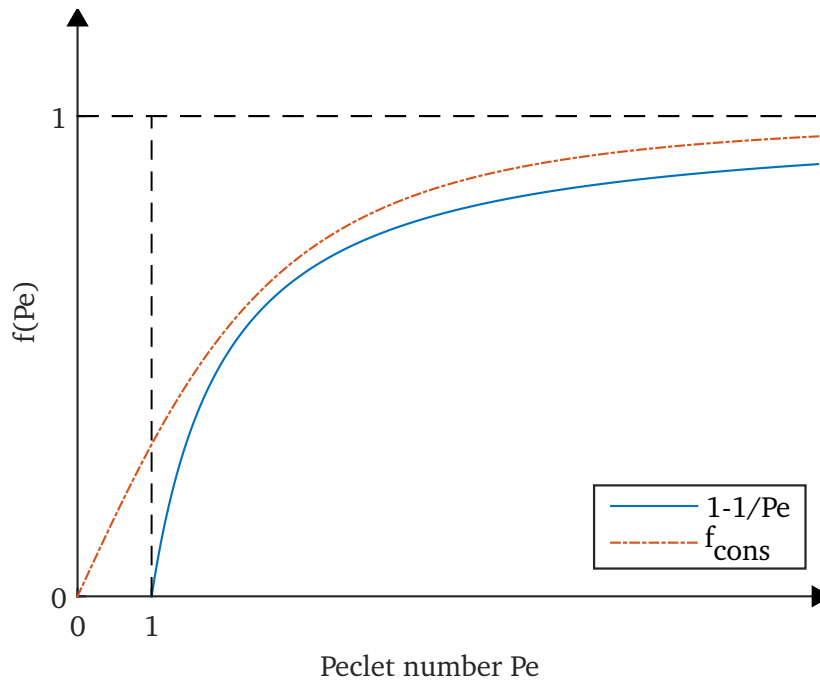


Figure 4.12.: Visualization of necessary condition for $Pe < 1$ with Consistent Artificial Diffusion

4.2.1.4 Influence on the Bearing Torque

During operation of a rotor-bearing system, the bearing gaps are partially filled with liquid lubricant and gas. Since the viscosity of gas is negligible compared to that of liquid lubricant, the shear stress τ_{xy} in the cavities is also negligible. However, the gas phase usually does not extend over the whole gap, see figure 3.4. The local amount of remaining liquid lubricant is described with the lubricant fraction ϑ . Thus, the factor

$$f_{M_R,\text{red}}(\vartheta) = \frac{1}{A} \iint_A \vartheta dA \quad (4.46)$$

is defined, which describes the global lubricant fraction in the bearing gap. The factor $f_{M_R,\text{red}}$ equals 1, if the gap is completely filled with lubricant and 0, if no lubricant is present. It is inserted in the integrals of the bearing torque (3.17) in order to account for the reduced shear stress τ_{xy} in the cavitated region. A similar approach has been used in [Nit17].

4.2.2 Comparison with Non Mass-Conserving Cavitation Approaches

In this section, the behavior of a journal bearing considering mass-conserving cavitation is compared to that of bearings with the non mass-conserving half-SOMMERFELD and penalty cavitation approaches. This lays the foundation to explain the influence on the rotordynamic stability, which is investigated in chapter 6 for rotors in single lubrication films and in chapter 7 for rotors in floating ring bearings. The journal is kinematically driven to investigate basic motions, namely pure rotation, radial squeeze and whirl. This enables a direct comparison of the resulting pressure profiles, which would be different in a dynamic simulation due to the different equilibrium positions.

The parameters of the considered bearing are given in table 4.1. The bearing is plain cylindrical with a free axial boundary, see equation (4.36). Lubricant is supplied to the bearing gap through a circumferential groove at one axial end of the bearing, i.e. $\bar{z}=1$, with $p_{\text{sup}} = p_{\text{cav}} = p_0$. The bearing dimensions comply with the inner fluid films of the rotors in floating ring bearings investigated in chapter 7. The oil viscosity corresponds to motor oil with a temperature of 100 °C. The deformation of shaft and housing described in section 4.1.5.4 is already accounted for in the *warm* gap size C . The steepness parameter x_1 of the mass-conserving cavitation model is 0.99.

Table 4.1.: Bearing parameters

Name	Symbol	Value	Unit
Bearing width	B	20	mm
Bearing diameter	D	25	mm
Nominal radial bearing gap (warm)	C	40	μm
Oil viscosity (warm)	η	10	mPas
Ambient pressure	p_0	1	bar
Supply pressure	p_{sup}	1	bar

4.2.2.1 Pure Rotation

Firstly, the pressure profiles resulting from pure rotation with a constant rotation speed of 20 Hz are compared. The equilibrium position of the mass-conserving two-phase model is calculated with a dynamic simulation using a rigid rotor (point mass) with mass ≈ 6 kg without unbalance. A stiff rotor with little unbalance exhibits a similar motion, as long as the rotation speed varies slowly and no sub- or super-synchronous oscillations are present. The resulting journal displacements are used as input values for the static calculations of the non mass-conserving models. Additionally, results using the ELROD and the PEEKEN model are shown, which also use the equilibrium position calculated with the two-phase model as input.

Figure 4.13 shows the cross-sections of the pressure profiles, the gap function H and the lubricant fraction ϑ in the centerline of the bearing, i.e. $\bar{z}=0.5$. The lubricant flows from left to right. In the converging part of the gap, the pressure rises and no gas is present, thus $\vartheta=1$. The highest pressure is reached in front of the smallest gap. At the location of the smallest gap the pressure collapses. As soon as the cavitation pressure $p_{\text{cav}}=p_0=1$ bar is reached, a cavity forms, which is seen in the declining lubricant fraction ϑ . Here, the bearing gap is partially filled with gas. At the location of the largest gap, the cavity ends and ϑ rises to 1.

The pressure profile calculated with the two-phase model is similar to that obtained with the penalty ap-

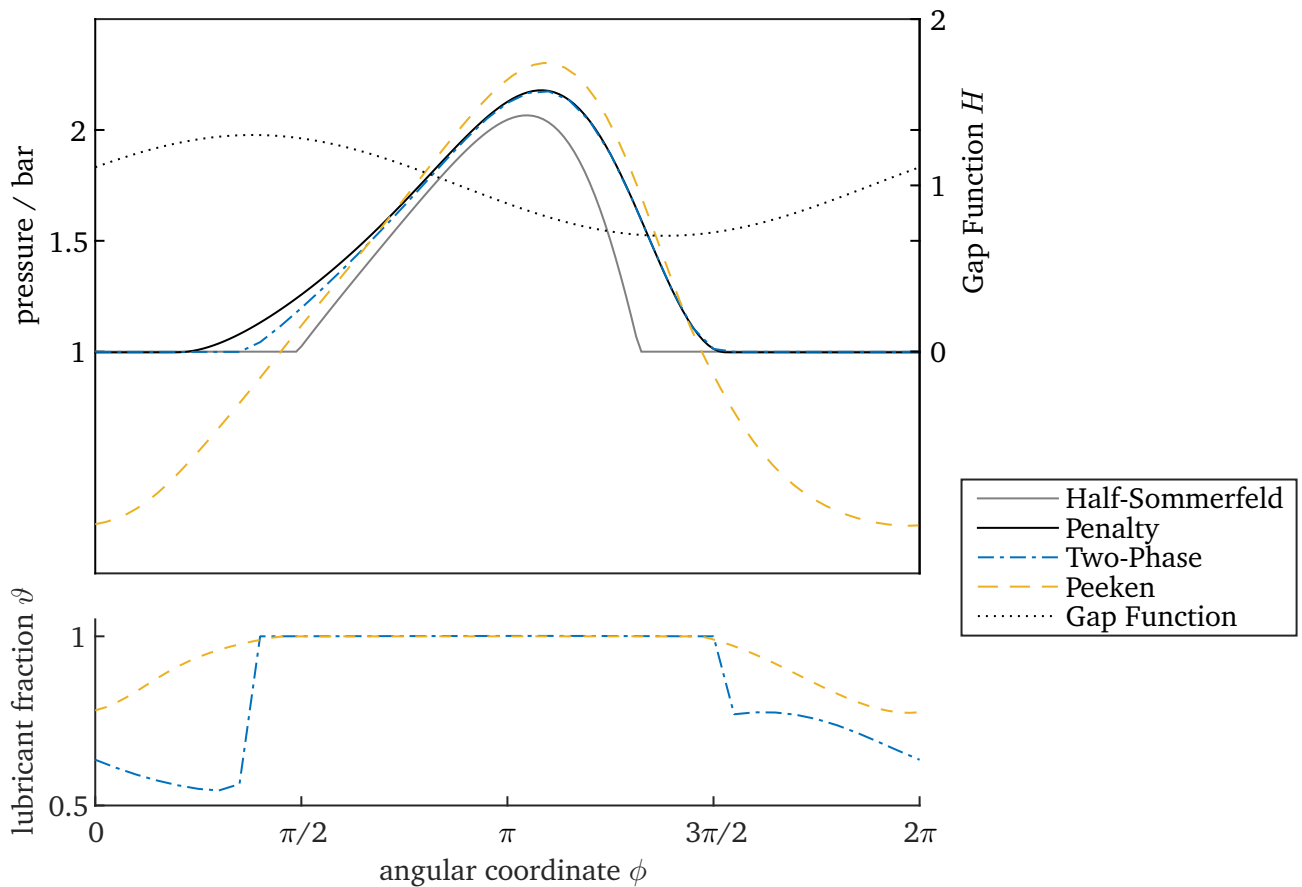


Figure 4.13.: Pressure profile p and lubricant fraction ϑ during pure rotation for different cavitation models, circumferential groove at $\bar{z}=1$

proach. No difference in the centerline pressure can be seen between free-to-air or oil-bath (not shown). Despite the different pressure profiles of the half-SOMMERFELD and the penalty cavitation approaches, they exhibit an almost identical stability behavior, see section 6.3. Yet the model with mass-conserving cavitation exhibits a reduced stability. Thus, no direct conclusions concerning the stability behavior can be drawn from the pressure profiles resulting from pure rotation.

The pressure calculated with the two-phase model drops only slightly below the cavitation pressure p_{cav} if the steepness parameter x_1 is close to 1. The pressure of the PEEKEN model drops far below p_{cav} , while the lubricant fraction is higher in the cavitated area.

Additionally, a bearing with one axial groove at the top of the bearing ($\phi=0=2\pi$) with the opening angle $\Theta_g=15^\circ$ is considered. Also the pressure calculated with the classical ELROD model is shown, see figure 4.14. The resulting pressures using different cavitation approaches are closer than for the bearing with a circumferential groove. The two-phase model is again close to the penalty approach. The maximum pressure of the ELROD and the PEEKEN model are close to the half-SOMMERFELD model, yet the beginning and end of the cavitated area are different. Again, the pressure of the PEEKEN model drops below p_{cav} , while the lubricant fraction in the cavitated area is higher than for the other models. The lubricant fraction is 1 at the location of the axial groove, thus the cavitated area is smaller compared to the bearing with a circumferential groove. The shape of the cavitated area is similar for the two-phase and the ELROD model, yet the reformation areas of the lubricant film at $\phi \approx \pi/2$ and $\phi \approx 2\pi$ are smaller

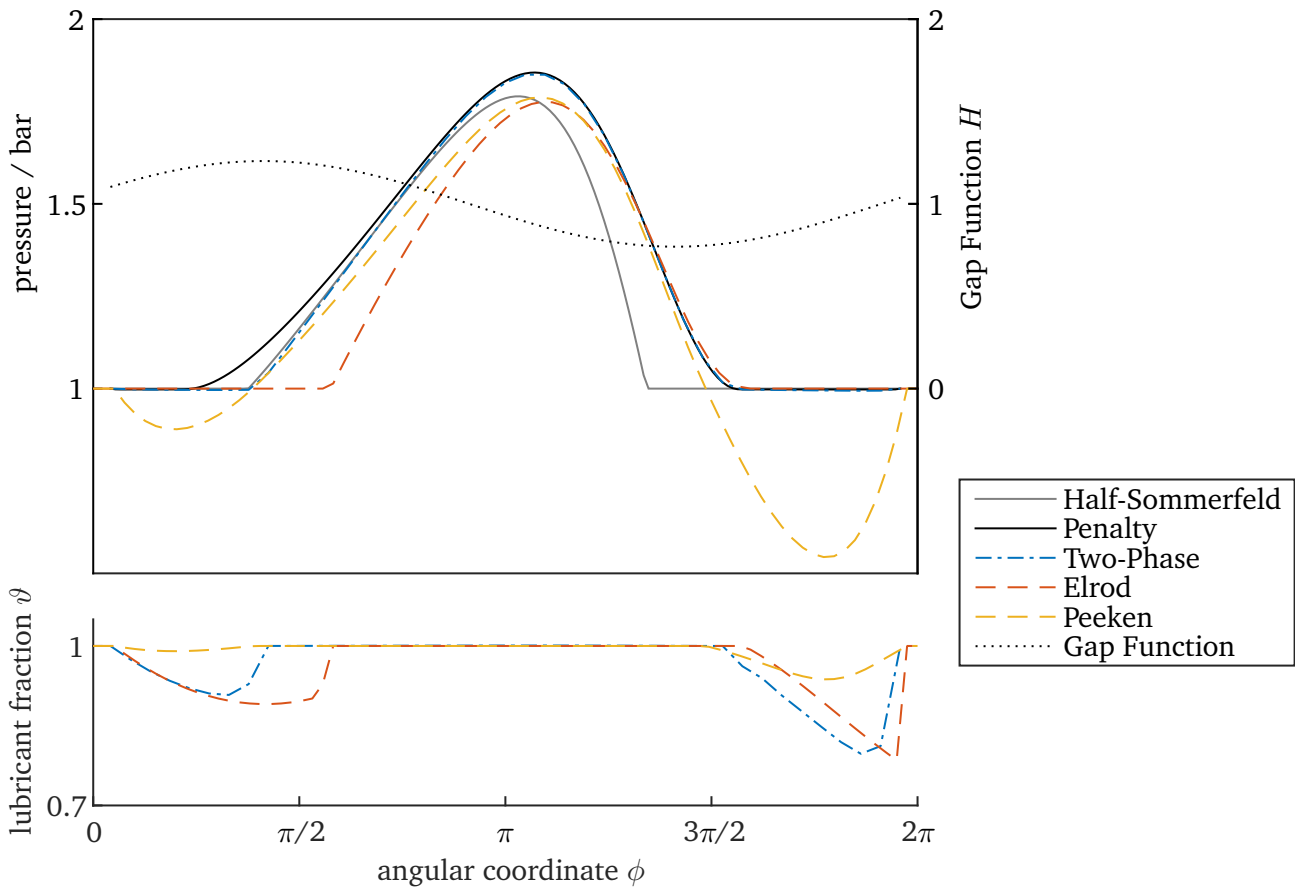


Figure 4.14.: Pressure profile p and lubricant fraction ϑ during pure rotation for different cavitation models, axial groove with opening angle $\Theta_g=15^\circ$ at $\phi=0=2\pi$

and the lubricant fraction rises later and more suddenly for the ELROD model. This is probably due to the infinitely high steepness of the density-pressure-relation $\rho(p)$ in the ELROD model, which is smooth in the two-phase model, see also figure 4.11.

4.2.2.2 Squeeze Motion

Now, a radial, sinusoidal squeeze motion of the journal is imposed by means of the vertical displacement $D_y(t)$,

$$D_y(t) = -C\varepsilon_{\max} \sin(2\pi ft) \quad (4.47)$$

with $\varepsilon_{\max} = 0.6$, $f = 10$ Hz. The journal does not rotate, i.e. $\omega_R = 0$. This investigation was performed experimentally in [Phe61] to research the influence of cavitation in squeeze film dampers. Related numerical studies have been conducted in [Boe10]. In this work, the resulting vertical bearing forces F_y are compared for different cavitation models and different axial boundary conditions. The use of an integrated result enables to compare the time history of the transient results. Three periods of the journal motion are shown in figure 4.15. Also the local gap size $H(\phi = \pi)$ at the bottom of the bearing is plotted. The journal firstly moves downward, which generates a positive vertical force F_y . As the journal reaches its lowest position $D_y = -C\varepsilon_{\max}$, its velocity and the vertical force become zero. The journal moves upwards and a negative vertical force is induced by the lubricant film.

The non mass-conserving half-SOMMERFELD and penalty approach yield an identical force in each period of the journal movement due to not being time-dependent. The change in direction of the journal yields a non smooth force graph for the half-SOMMERFELD approach, probably due to the non smooth pressure profile. The force calculated with the penalty approach is smooth and slightly larger.

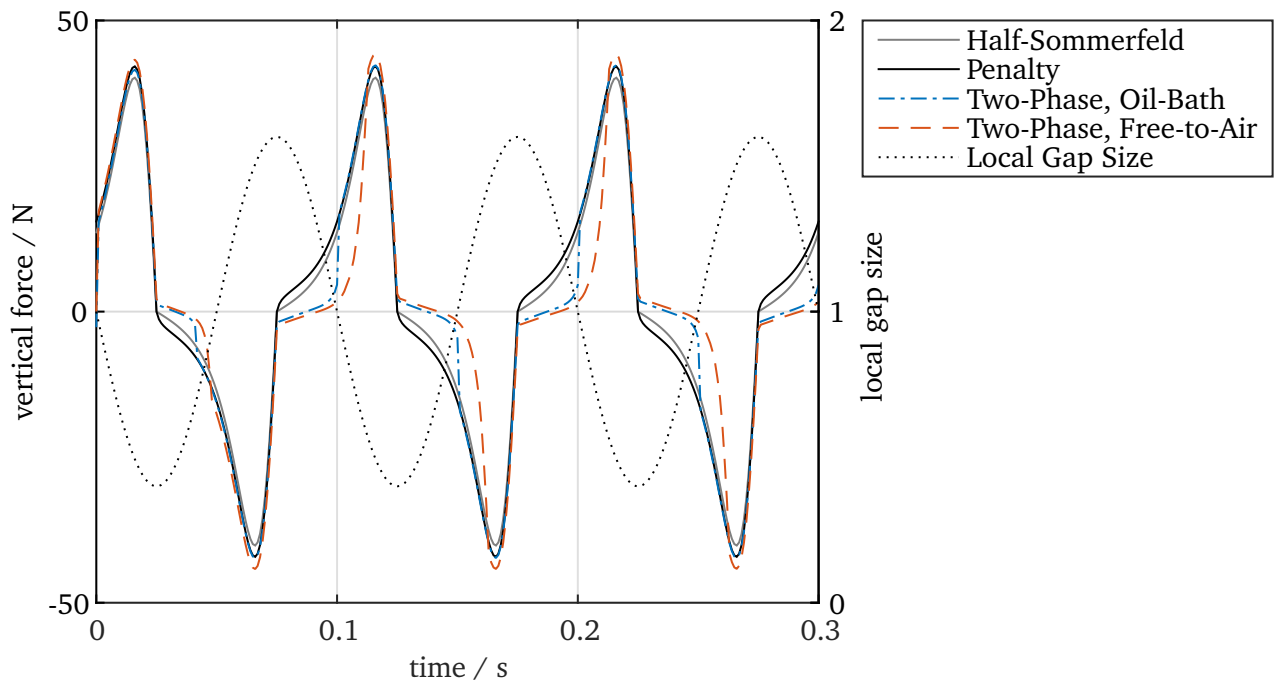


Figure 4.15.: Vertical bearing force during three periods of vertical, harmonic squeeze motion

A larger difference can be observed for the mass-conserving cavitation model. In the first half period of the journal motion, the force is close to the forces calculated with the non mass-conserving cavitation approaches. After the change of direction of the journal, the force stays small for some time and then suddenly rises. The delay in the build-up of the force becomes larger in the next oscillation of the journal and then reaches a steady state. This behavior can be explained by cavitation effects. The downward movement of the journal generates a cavitated area in the top of the bearing. When the journal moves back upwards, no hydrodynamic pressure can be generated until the gap on top of the bearing is again filled with lubricant, i.e. $\vartheta = 1$. The non mass-conserving cavitation approaches implicitly assume a fully developed lubricant film at all times, thus the force is generated immediately after the change of direction of the journal. This difference has also been pointed out in [Boe10].

When the oil bath axial boundary condition is used, the pressure can build up more quickly due to the additional lubricant supply through both axial boundaries. The bearing with the free-to-air boundary condition loses lubricant at one axial boundary. In both cases, lubricant is supplied through a circumferential groove at one axial boundary.

The difference between the non mass-conserving and the mass-conserving cavitation models becomes smaller, when the supply pressure p_{SUP} is increased. This is caused by the improved lubricant supply and thus a smaller cavitated area. This is further investigated in section 6.4.4.

A superimposed rotation $\omega_R = 2\pi f$ has little effect on the results (not shown). Then, the build-up of the bearing force is more gradual and the overshoot of the force with the free-to-air boundary condition is reduced.

In a dynamic simulation, the delayed pressure build-up yields larger eccentricities in oscillating journal motions when mass-conserving cavitation is considered. Radial motion components are present in sub-synchronous oscillations and in whirl motions due to unbalance. This behavior can explain the reduced stability threshold speed compared to rotors in bearings considering non mass-conserving cavitation, which is shown in chapters 6 and 7.

4.2.2.3 Whirl Motion

Lastly, a circular whirling motion of the journal center without rotation of the journal ($\omega_R = 0$) is considered according to

$$\begin{aligned} D_x(t) &= C\varepsilon \cos(\dot{\delta}t) \\ D_y(t) &= C\varepsilon \sin(\dot{\delta}t) \end{aligned} \tag{4.48}$$

with $\dot{\delta} = 2\pi 10$ rad/s. To start the calculation of the time-dependent mass-conserving cavitation model with an eccentric journal position, an accurate initial condition of the pressure profile p is required, whose calculation is costly. It is more efficient to quickly increase the eccentricity ε at the beginning of the simulation,

$$\varepsilon(t) = \varepsilon_{\text{max}} \left(1 - e^{-t/t_1} \right). \tag{4.49}$$

with $\varepsilon_{\max}=0.6$ and the time constant $t_1=10$ ms. The hydrodynamic pressure profile follows the movement of the journal and reaches a steady state in a rotating reference frame. The graph of the resulting bearing forces is thus mainly influenced by the whirl speed $\dot{\delta}$ and is sinusoidal when $\varepsilon(t)=\varepsilon_{\max}$. Thus, the pressure profile and the bearing forces are not well suited to compare the different cavitation approaches for this kind of motion.

Instead, the pressure at a fixed location at the bottom of the bearing is compared, i.e. $p(\phi=\pi, \bar{z}=0.25)$, see figure 4.1. This kind of investigation was also performed experimentally in [DSA98]. Figure 4.16 shows three periods of the whirl motion of the journal center. Again, the gap size $H(\phi=\pi)$ at the bottom of the bearing is plotted. It reaches a maximum, when $\dot{\delta}t=\pi/2$ and a minimum when $\dot{\delta}t=3/2\pi$. In the first rotation, the maximum is slightly smaller due to the time-dependent increase of ε . The pressure at the bottom of the bearing which is calculated with the non mass-conserving approaches increases immediately, when the local gap size starts to decrease. The pressure calculated with the penalty approach is again slightly larger than that using the half-SOMMERFELD condition. With the two-phase model, there is a delay in the pressure build-up, which is greater for the bearing with free-to-air boundary condition. It can be seen in a rotating reference frame that the pressure profile has a smaller circumferential extend for the two-phase model due to cavitation. The pressure suddenly vanishes for all models, when the local gap size starts to increase. Furthermore, the pressure drops below the cavitation pressure $p_{\text{cav}}=p_0=1$ bar when the mass-conserving model is used.

A superimposed rotation $\omega_R=2\pi f$ reduces the maximum pressure and makes the increase of the pressure more gradual for the two-phase model, yet has again no qualitative effect on the results (not shown).

The results are in good agreement to those obtained experimentally in [DSA98]. The results obtained with non mass-conserving cavitation models correspond to experimental results where no cavitation has been observed, while the results calculated with the two-phase model are similar to experimental results with gaseous cavitation. In [DSA98], the pressure occasionally drops far below p_{cav} during

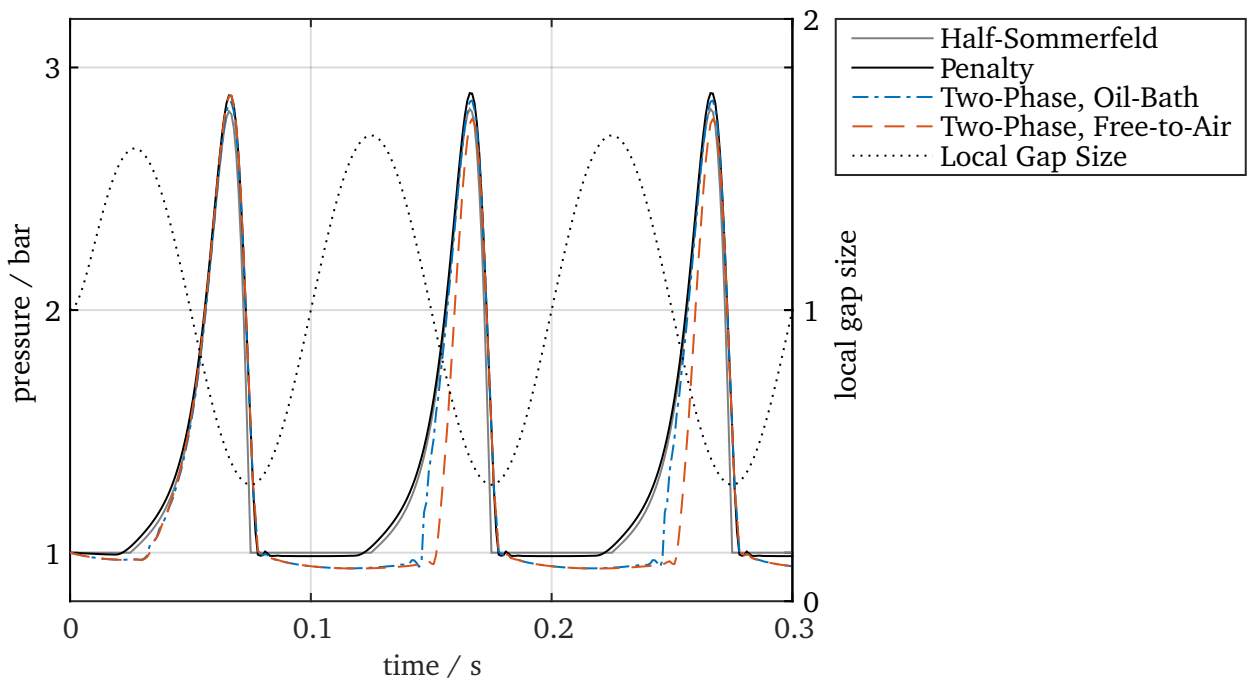


Figure 4.16.: Hydrodynamic pressure at the bottom of the bearing during three periods of circular whirl motion

an increasing local gap size due to vaporous cavitation, which is not modeled in the mass-conserving cavitation approach used in this work.

5 Solver Coupling

In this work, the rotor-bearing system is decomposed into subsystems, which exchange coupling variables through a coupling interface. The subsystems of rotor and bearings are modeled in separate software tools – namely multibody dynamics and FEM – which use different integration methods, different solvers and have different time-step sizes (i.e. *multi method*, *multi solver*, *multi scale*). Compared to a single monolithic model, the decomposition into subsystems allows easier upgrade, reuse and exchange of models, e.g. different rotors or different bearing geometries. Components of a complex system can be modeled by specialized engineers. Furthermore, the efficiency of the subsystem solvers can be increased, since they can be optimized for the individual equations.

An additional numerical error is introduced through the coupling procedure. Thus, a coupled system of physically and numerically stable subsystems can become unstable. In some cases, the decoupling can increase the overall efficiency of the method, since the subsystems have lesser degrees of freedom and can be calculated in parallel. The exchange of coupling variables requires an additional effort, which is small for the models considered in this work, since the number of coupling variables is small. An example for systems with many coupling variables is a bearing with a deformable shell, a so-called elasto-hydrodynamic bearing (EHD).

Two different coupling methods are applied in this work:

- *Dynamic-static solver-coupling* is used, if only one subsystem is explicitly time-dependent and the others are stationary. The stationary subsystems can be seen as complex sub-functions of the time-dependent system. The static subsystems do not have to be computed in every NEWTON iteration step of the time-dependent system, which greatly reduces the computational effort. The procedure is explained in the next section.
- *Co-simulation* methods are used to couple several time-dependent subsystems. The method used in this work is explained in section 5.2.

A detailed description can be found in [Sch15]. Different choices of coupling variables are possible for mechanical systems, see e.g. [SL14]. In this work, a force/displacement coupling approach is used, i.e. the forces and torques from the bearings and the displacements and velocities of the rotor and the floating rings are exchanged.

5.1 Dynamic-Static Solver-Coupling

The bearing subsystems are not time-dependent, if non mass-conserving half-SOMMERFELD or penalty cavitation approaches are used, see section 3.3.2. Discretizing the REYNOLDS equation yields a set of algebraic equations. The rotor subsystem is integrated using an implicit BDF method, which performs one predictor-step and multiple corrector-steps per time-step, see section 2.2.2.

In the simplest case, the hydrodynamic forces are calculated in every predictor- and corrector-step. This is the so-called *full-implicit* method. Additionally, the BDF-method requires the JACOBIAN for the corrector-steps, which are calculated using NEWTON'S method. The partial derivatives of the forces with respect to the coupling variables are calculated with difference quotients using perturbed coupling variables. If the partial derivatives are not specified, the multibody software *MSC Adams* calculates the perturbed forces with respect to every coupling variable sequentially, which is very time-consuming. Thus, the perturbed forces are calculated in parallel processes. At least 4 processes are required for each lubricant film, since the minimal number of input variables is 3, see section 3.2.5. The JACOBIAN does not have to be calculated in every corrector-step, since the partial derivatives usually change slowly. The amount of calculations of the JACOBIAN can be controlled with the *pattern*-option of the solver in *MSC Adams*.

In order to reduce the numerical effort, BUSCH proposed a *semi-implicit* method, which reduces the number of calculations of the bearing model, see [Bus12; BS12]. The forces and the perturbed forces are only calculated once per time-step. During the corrector-steps, the forces are extrapolated linearly using the partial derivatives with respect to the coupling variables, which are already needed for the JACOBIAN. BUSCH used the last (converged) corrector-step as the operating point of the linearization. SCHMOLL found that using the predictor-step as the operating point reduces the numerical error, see [Sch15], which is also applied in this work. During the predictor-step, the states are extrapolated. The JACOBIAN is calculated using the chain rule.

The *semi-implicit* method reduces the effort by a factor of 3-4, depending on the average number of corrector-steps. The results are congruent to those using the *full-implicit* method.

5.2 Dynamic Co-Simulation

A co-simulation scheme is used to couple several time-dependent subsystems. This is the case for a rotor-bearing with a mass-conserving cavitation model, which makes the REYNOLDS equation time-dependent, see section 4.2.1. The bearing subsystems also become time-dependent, if the equations of motion of the floating ring are included in the bearing model. This is necessary, if hydraulic coupling is considered, but also beneficial for non mass-conserving cavitation models. No partial derivatives with respect to the coupling variables are needed when using a co-simulation scheme, see [Sch15]. Thus, far less parallel processes are needed compared to the dynamic-static solver-coupling, which reduces the workload of the CPU and the number of licenses. The evaluation of one time-step takes longer due to the greater amounts of degrees of freedom, yet more parallel simulations (e.g. parameter studies) can be performed on a single PC, which increases the overall efficiency.

Since commercial software tools usually do not give the possibility to save the current solver state of the system and to repeat a time-step, an explicit co-simulation scheme has to be used, see e.g. [Bus12; Sch15; SS11; Sch+13; SLL15]. Currently, new standards such as the *Functional Mock-up Interface* are developed, see [Jun17], which will allow the use of more stable implicit co-simulation methods in the future, see e.g. [SL14; SLL15; Sch+15].

Both subsystems use their respective time-integration method. In this work, BDF-methods with variable step size and variable order of the extrapolation polynomials are used. Thus, the time-step sizes of the subsystems – the so-called *micro-step sizes* h – are different. Both subsystems require coupling variables from the other subsystem, e.g. the rotor subsystem needs the bearing forces and the bearing subsystems

need the kinematic quantities of the rotor. The coupling variables are only exchanged at so-called macro time points. Their time-difference is called *macro-step size* H . The macro-step size can be constant, fixed to the micro-step size of one subsystem or an automatic control can be implemented. The coupling variables are inter- or extrapolated during one macro-step using the previously computed values at the macro time points. This introduces an additional numerical error to the simulation. Two different schemes for approximating the coupling variables can be distinguished:

- In the JACOBI type, the coupling variables of both subsystems are extrapolated and the subsystems can calculate their micro-steps simultaneously. This is especially efficient, if the calculation times of the subsystems are in the same magnitude, since the calculation has to wait for the slowest subsystem before the next macro-step can be started.
- In the GAUSS-SEIDEL type, the coupling variables of one subsystem are interpolated, and extrapolated for every other subsystem. This improves the numerical stability, see [Sch15; Bus12], since interpolated coupling variables can not overshoot. However, the calculation of the subsystems has to be carried out sequentially.

The calculation time of the bearing subsystems dominates the calculation time of the coupled rotor-bearing systems investigated in this work. Thus, the parallel JACOBI type yields no advantage and the more stable GAUSS-SEIDEL type is used in this work, which is explained in the next section.

5.2.1 Sequential Gauß-Seidel Scheme

The GAUSS-SEIDEL scheme used in this work is implemented as a master-slave method, see [Sch15; Bus12]. The rotor subsystem is the master subsystem with micro-step size h_M , the bearings are slave subsystems with micro-step sizes $h_{S,i}$. The step sizes of the bearing subsystems are usually smaller than that of the rotor subsystem. The macro-step size H is set equal to the micro-step size of the master, i.e. $H = h_M$. A larger macro-step size H has no advantage for the rotor-bearing systems investigated in this work, since the calculation time of the subsystems is large compared to the overhead time of the coupling due to the large amount of degrees of freedom in the subsystems compared to the small number of coupling variables.

The procedure is schematically shown in figure 5.1. Two subsystems are considered with one output each, namely y_M and y_S . The filled circles represent values, which are calculated by the subsystem solvers. Firstly, the time-step from t_n to t_{n+1} of the master subsystem is calculated. Due to the use of implicit subsystem solvers, the integration requires the coupling variable of the slave subsystem at the time t_{n+1} , which is extrapolated using the function \tilde{y}_S defined by the known values of y_S at the macro time points t_{n-1} and t_n . Then, the slave subsystem is integrated. This requires coupling variables from the master subsystem, which are calculated using the interpolation \tilde{y}_M . The extra- and interpolated values are represented by blank circles. After the slave system has reached the next macro time-step t_{n+1} , the process is repeated. Ideally, the slave subsystem performs calculations at the macro time points. In commercial software tools, the micro-steps h_S are usually not directly controllable, thus the values at the macro-steps are interpolated. Linear functions \tilde{y}_S and \tilde{y}_M are shown in figure 5.1 for clarity. LAGRANGE-polynomials of order 2 are used in this work, which is a good compromise between stability and efficiency.

Due to the extrapolation, the coupling variables received by the master subsystem can overshoot, which might lead to a reduction of the micro-step size h_M and thus the macro-step size H . BUSCH proposed a continuous approximation technique in [Bus16], which yields more smooth coupling variables. However, a sharp decline of the macro-step size H has not been observed for the investigated systems. It has been found that for these problems, an equal maximum allowed solver step-sizes h_{\max} in the rotor and the bearing subsystems yields the fastest co-simulation.

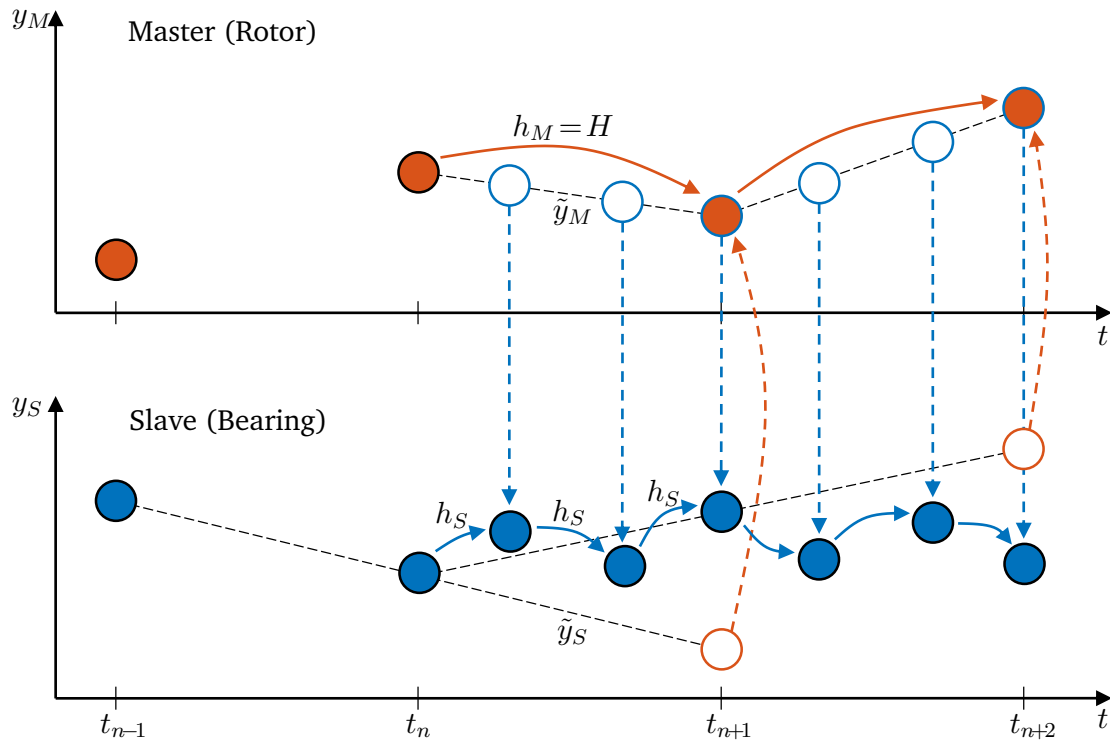


Figure 5.1.: Explicit co-simulation approach: sequential GAUSS-SEIDEL Master-Slave scheme

6 Jeffcott Rotor in Single Film Bearings

In this chapter, the behavior of a symmetric JEFFCOTT rotor in single film bearings is investigated using transient run-up simulations. Rotors in floating ring bearings are investigated in chapter 7. In order to understand the influence of different bearing designs and cavitation effects, a simple rotor is considered. A symmetric rigid rotor is the simplest rotor model. However, due to the lack of a linear system natural frequency, no oil whip occurs. The JEFFCOTT rotor on the other hand takes the flexibility of the rotor into account and can be used to study many effects of realistic rotors in journal bearings. In this work, the JEFFCOTT rotor is modeled in the commercial multibody software *MSC Adams*. This is because the ordinary differential equations of more complex rotor systems – such as turbochargers – are costly to obtain due to their many degrees of freedom and thus are usually modeled using commercial software. After the system parameters are given in the next section, two non mass-conserving cavitation approaches are compared in section 6.3, namely the half-SOMMERFELD and a penalty approach. In section 6.4, results obtained with the mass-conserving cavitation model introduced in section 4.2 are discussed. For comparison, also results obtained with the penalty approach are shown.

6.1 System Parameters

The reference parameters of the JEFFCOTT rotor are given in table 6.1. The rotor is prevented from tilting using a constraint. The total weight $m+m_J$ and the unbalance U of the rotor resemble a large engine turbocharger. The journal mass m_J – see figure 2.2 – must not be too small, otherwise the micro step size of the bearing model is greatly reduced. The shaft stiffness c is chosen rather low to reduce the natural frequency of the system. The stiffness of the journal bearings changes with the rotor-speed ω_R and is high compared to the stiffness of the shaft. If the bearings are assumed infinitely stiff, the natural frequency of the rotor is 145 Hz. The first natural frequency of the linearized rotor-bearing system is slightly lower due to the added flexibility of the bearings. Small external damping d_o and shaft damping d_i are added, which act on the disk as well as between the disk and the journals, respectively. The rotor-speed is linearly increased from 0 to $f_{\max} = 300$ Hz in $T_{\text{sim}} = 10$ s.

Table 6.1.: Reference parameters of the JEFFCOTT rotor

Name	Symbol	Value	Unit
Rotor mass	m	6	kg
Journal mass	m_J	100	g
Shaft stiffness	c	5000	N/mm
Unbalance	U	3	gmm
External damping	d_o	1	Ns/m
Shaft damping	d_i	0.1	Ns/m

The bearing dimensions are given in table 4.1 on page 60. The supply pressure p_{sup} in the groove equals the ambient pressure p_0 . Due to the axial symmetry of the system, only one bearing has to be calculated and the forces and the torque are doubled. Furthermore, the resulting pressure profile is axially symmetric, since misalignment is not considered. Thus, only one axial half of the developed bearing gap geometry has to be discretized.

6.2 Solver Parameters

Table 6.2 lists the solver parameters of the rotor, modeled in *MSC Adams*, and the bearings, modeled in *Comsol Multiphysics*. The output step size $\Delta T_{\text{out,A}}$ of the rotor model fulfills the NYQUIST–SHANNON sampling theorem up to frequencies of 10 kHz. The output step size $\Delta T_{\text{out,C}}$ of the bearing model is chosen larger due to difficulties of *Comsol Multiphysics* to handle large amounts of output data. However, all system variables which require a high time resolution can be extracted from the rotor model.

For non mass-conserving cavitation models, the REYNOLDS equation (3.9) is not time-dependent and only the relative error tolerance $\epsilon_{\text{rel,C}}$ is required in *Comsol Multiphysics*. The rotor and the bearing model are coupled with the dynamic-static solver coupling approach described in section 5.1. In order to reduce the effort of calculating partial derivatives of the bearing forces with respect to the coupling variables, the dimensionless REYNOLDS equation (3.19) is used in this case. Thus, the pressure p in the penalty approach (3.31) is replaced with the dimensionless pressure Π .

For simulations using the two-phase model, the master/slave co-simulation method of the GAUSS-SEIDEL type described in section 5.2.1 is applied with *MSC Adams* as master. Thus, the macro step size H of the co-simulation equals the variable step size of the implicit BDF method in *MSC Adams* and is limited by the maximum solver step size $h_{\text{max,A}}$. Second degree polynomials are used for the inter- and extrapolation

Table 6.2.: Time-dependent solver parameters

Name	Symbol	Value
Rotor model (<i>MSC Adams</i>)		
Maximum solver step size	$h_{\text{max,A}}$	10^{-3} ms
Initial solver step size	$h_{\text{init,A}}$	10^{-5} ms
Output step size	$\Delta T_{\text{out,A}}$	$5 \cdot 10^{-2}$ ms
Relative error tolerance	$\epsilon_{\text{rel,A}}$	10^{-6}
Bearing model (<i>Comsol Multiphysics</i>)		
Maximum solver step size	$h_{\text{max,C}}$	10^{-3} ms
Initial solver step size	$h_{\text{init,C}}$	10^{-5} ms
Output step size	$\Delta T_{\text{out,C}}$	1 ms
Relative error tolerance	$\epsilon_{\text{rel,C}}$	10^{-5}
Absolute error tolerance (scaled)	$\epsilon_{\text{abs,C}}$	10^{-6}
Absolute error tolerance coupling (scaled)	$\epsilon_{\text{abs,coupling,C}}$	10^{20}
Maximum BDF order	$p_{\text{max,C}}$	5
Minimum BDF order	$p_{\text{min,C}}$	1

of the coupling variables. The relative error tolerance $\epsilon_{\text{rel},C}$ of *Comsol Multiphysics* greatly influences the number of micro steps and thus the overall simulation time. The absolute tolerance regarding the coupling variables $\epsilon_{\text{abs,coupling},C}$ is chosen very large in order to make the time-dependent solver of *Comsol Multiphysics* insensitive to sudden changes of the coupling variables. However, the coupling variables given to the slave subsystem are quite smooth due to the interpolation of the states of the master subsystem, see section 5.2.1.

The solution of the nonlinear equation system using NEWTON's method also has a large influence on the calculation time, especially for the bearing model. *Comsol Multiphysics* gives several settings, which were optimized for the systems investigated in this work. They are given in table 6.3. The time-consuming calculation of the JACOBIAN is minimized, since it does not change significantly during the corrector-steps. A small number of iterations is sufficient, since the time-step size is small and thus the initial condition for NEWTON's method is already close to the solution.

Table 6.3.: Settings for NEWTON's method in *Comsol Multiphysics*

Name	Selection
Nonlinear method	Constant
Damping factor	1
JACOBIAN update	Minimal
Termination technique	Iterations or tolerance
Number of iterations	3
Relative error tolerance	10^{-5}

6.3 Comparison of Half-SOMMERFELD and Penalty Cavitation Approaches

Firstly, run-up simulations using two non mass-conserving cavitation approaches explained in section 3.3.2 are compared, namely the often used half-SOMMERFELD (GÜMBEL) approach and a penalty formulation. The bearings feature a central circumferential groove, see section 4.1.2. The axial width B of the bearings equals the sum of the widths b of the two subdomains, $B=2b$, see also figure 4.1.

Figure 6.1 a) shows the resulting eccentricities ϵ of the journals, which are equal in both bearings due to symmetry. At the beginning of the simulation, the rotor journal is located in the middle of the bearing shell, $\epsilon=0$ and $\omega_R=0$. Due to gravity, the rotor journal drops inside the oil film and the eccentricity ϵ increases. The drop is damped through the squeezing of the oil film. With increasing rotor-speed ω_R , the load carrying capacity of the oil film increases, i.e. the rotor weight can be supported at a lower journal eccentricity ϵ , thus the eccentricity decreases. Now, an equilibrium position for the journal exists, which moves on an approximate semicircle (the so-called GÜMBEL curve) towards the center of the bearing shell with increasing rotor-speed, see also the journal center orbit in figure 6.1 b). In typical turbocharger applications, the rotor-speed changes more rapidly and the journal orbit is more complex. The journal performs small oscillations around the equilibrium due to unbalance with increasing amplitudes for increasing rotor-speed ω_R . The amplitude of this *synchronous* oscillation is largest at the simulation time ≈ 4.8 s due to the critical speed of the shaft, which is strongly damped and thus barely visible. At a certain

rotor speed, another frequency component emerges, which is approximately half of the rotor-speed and is called an *oil whirl*. This rotor-speed corresponds to the stability threshold of the linearized system. The journal center performs a circular whirl motion with increasing radius. When the center of the journal is close to the center of the bearing shell, the bearing loses its load carrying capacity. At ≈ 6.5 s, The eccentricity ε increases rapidly until it reaches a high value. This behavior usually prevents the operation of the rotor system for higher rotation speeds. In this work, this point is referred to as stability threshold or instability for short.

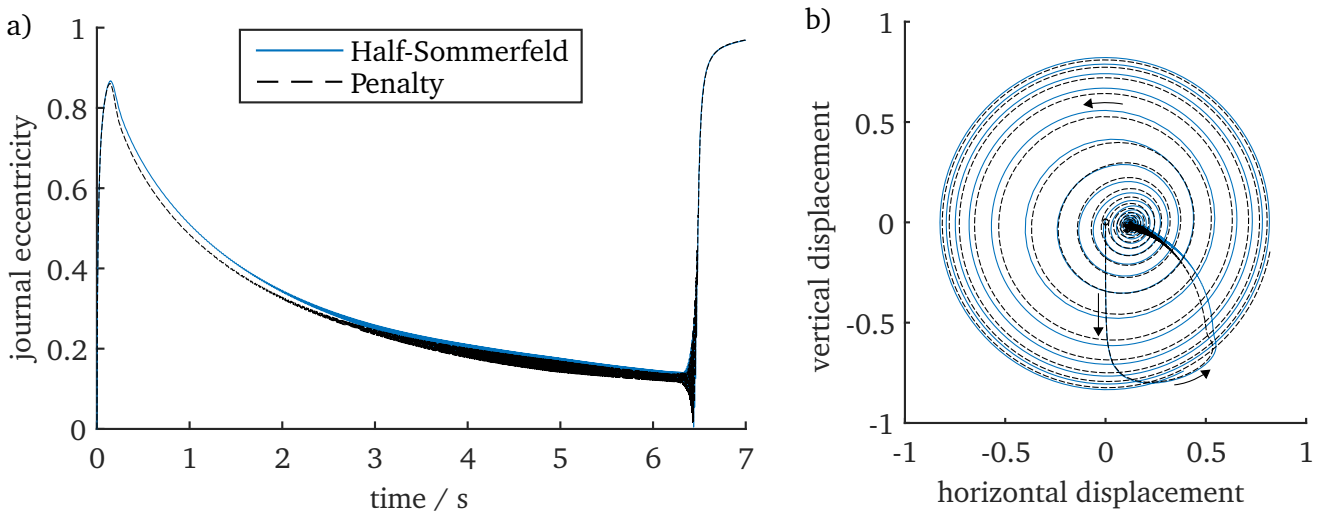


Figure 6.1.: Comparison of Half-SOMMERFELD and penalty cavitation approach; a) journal eccentricity ε ; b) dimensionless journal center orbit

The results obtained with the two different non mass-conserving cavitation approaches are very similar, especially the stability threshold is identical. The journal eccentricity of the system with the half-SOMMERFELD cavitation approach is slightly greater before the oil whirl. This is due to the smaller calculated pressure for identical input values, see also figure 4.13. In order to carry the same weight, a model which generates smaller pressure for the same input variables adjusts to a larger eccentricity in a dynamic simulation. However, even with large differences in the forces for constant input variables, the differences in the dynamic simulation stay moderate. This is due to the progressive stiffness of journal bearings in radial direction, i.e. a slightly higher eccentricity generates a much larger bearing force.

6.4 Mass-Conserving Cavitation

In the remainder of this chapter, the influence of the mass-conserving cavitation approach introduced in section 4.2 on the stability of the JEFFCOTT rotor in journal bearings is investigated. The *free-to-air* axial boundary condition (4.36) is used, which is more common in practice than an oil bath. With this boundary condition, a lubricant supply is necessary when mass-conserving cavitation models are used, otherwise the lubricant film runs dry. A cylindrical bearing with a central circumferential groove, which is described in section 4.1.2, yields a lubricant supply over the whole circumference of the bearing and is thus often used in practice. Furthermore, the lubricant film has a simple rectangular geometry (see figure 4.1), which enables easy generation and scaling of the numerical mesh for convergence studies.

For comparison, also lubricant supply through an axial groove at the top of the bearing is considered in section 6.4.4.1. A more complicated lubricant supply geometry, namely bore holes, is used in chapter 7.

6.4.1 Mesh Resolution and Steepness of the Ansatz Function

Firstly, the convergence of the time-dependent REYNOLDS equation (4.31) is verified using run-up simulations with increasing resolution of the numerical mesh. The tests are performed for different values of the steepness parameter $x_1 = (x_0 + 1)/2$ of the ansatz function (4.32). For comparison, also simulations using the penalty approach are performed, which are converged for the mesh resolution 10×20 (axial \times circumferential), see figure 6.2.

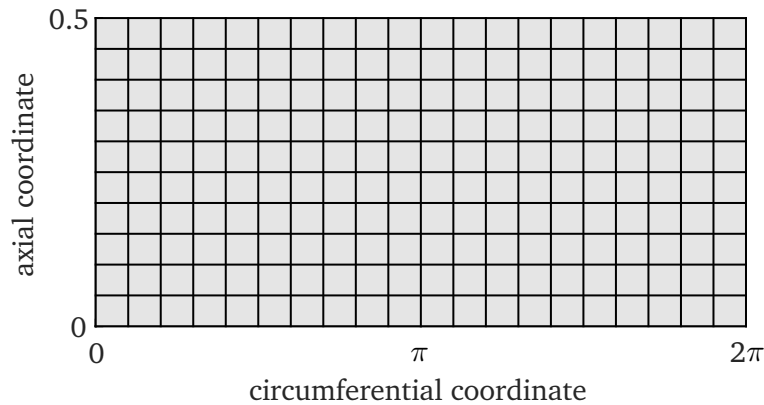


Figure 6.2.: Rectangular mesh of one axial half of the bearing with 10×20 elements

In figure 6.3, the resulting eccentricities of a JEFFCOTT rotor in bearings with a central circumferential groove are shown. The stability thresholds of the systems with mass-conserving cavitation are slightly different for each x_1 and are always at a lower rotor-speed than for the penalty approach. The threshold converges with finer mesh resolution to a higher rotor-speed for all x_1 except $x_1 = 0.99$, where it converges to a lower speed. The eccentricity before the stability threshold with mass-conserving cavitation converges to that with penalty approach for $x_1 \geq 0.999$. For $x_1 \leq 0.99$, the eccentricity is larger than for the penalty approach. Furthermore, for a constant mesh resolution, the results obtained with the mass-conserving cavitation model approach the result obtained with the penalty model for increasing x_1 . The threshold speeds for $x_1 = 0.9995$ are slightly lower.

The eccentricities with $x_1 = 0.9$ differ largely from the results with higher x_1 . The eccentricities before the stability threshold are larger and additionally, the transition into the oil whirl is more gradual. This qualitative difference can be explained through investigation of the pressure profile p and the lubricant fraction ϑ during simulation, which are shown for two different values of the steepness parameter x_1 in figure 6.4. Due to symmetry, only one subdomain of the bearing with circumferential groove is shown. The results are taken from the simulations shown in figure 6.3 using 20×40 mesh elements at the simulation time 4 s.

At this time, the rotor performs only small oscillations around the equilibrium position due to unbalance. Thus, the resulting pressure profile results almost entirely from the static weight of the rotor and is located at the bottom of the bearing ($\phi = \pi$). At the circumferential lubricant feeding groove ($\bar{z} = 0.5$), the pressure equals the supply pressure $p_{\text{sup}} = p_0 = 1$ bar and the lubricant fraction ϑ equals 1. At the

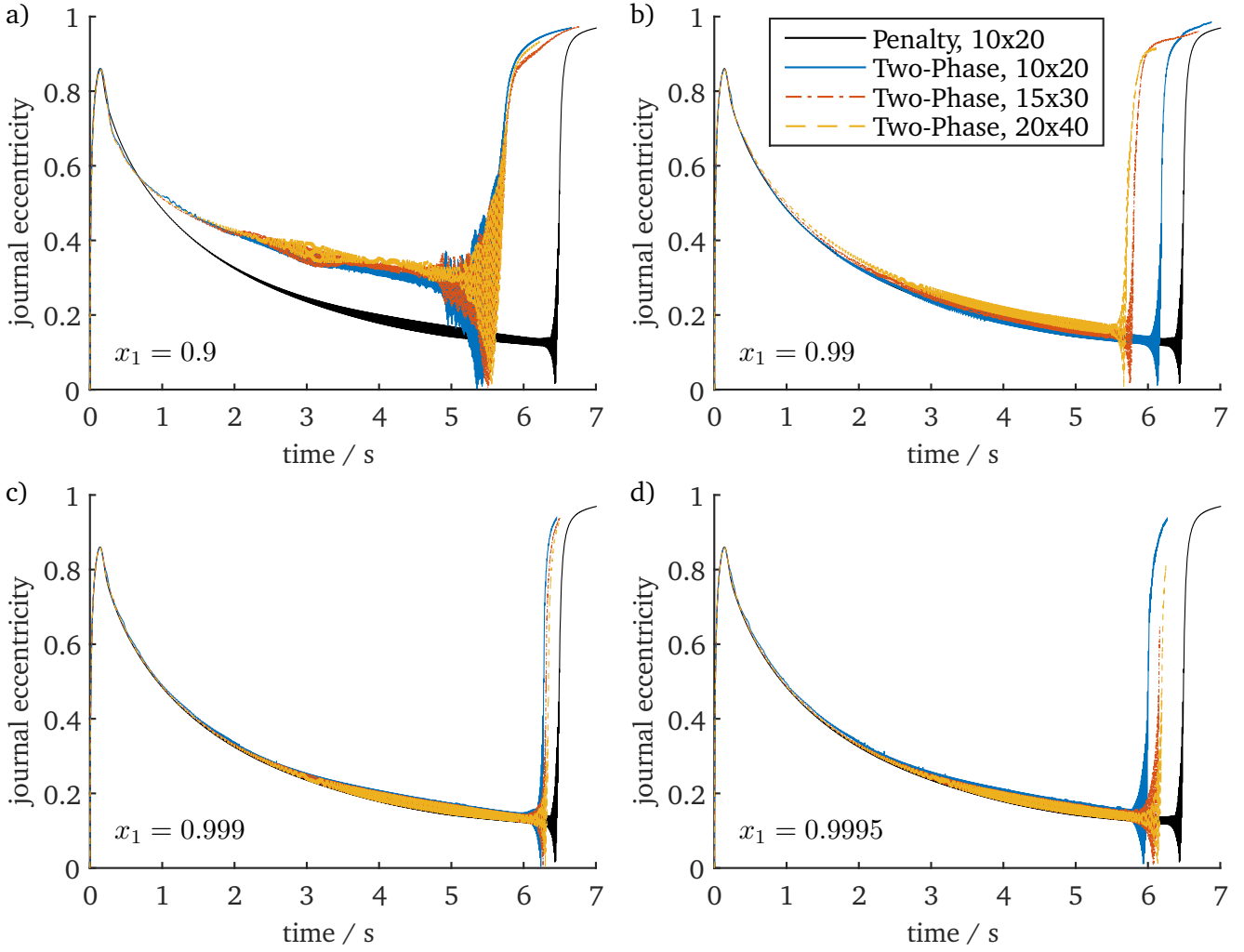


Figure 6.3.: Convergence study for the mass-conserving cavitation model with different steepness parameters x_1 using a cylindrical bearing with a central circumferential feeding groove

axial boundaries of the bearing ($\bar{z}=0$), the pressure in the fully developed lubricant film is approximately equal to the ambient pressure p_0 . The lubricant fraction ϑ is below 1, i.e. the cavitated area is open to the surrounding.

The area of hydrodynamic pressure, i.e. $p > p_0$, corresponds with the area where the bearing gap is completely filled with liquid lubricant, i.e. $\vartheta = 1$. For $x_1 = 0.9$, this area is substantially smaller than for $x_1 = 0.99$. As a consequence, the pressure profile with $x_1 = 0.9$ has to be steeper in order to yield the same load carrying capacity, which results in a higher eccentricity ε in figure 6.3 a). The area of the fully developed fluid film, i.e. $\vartheta = 1$, does not change significantly for $x_1 > 0.99$, yielding similar results in the run-up simulations. The pressure profile varies for $x_1 \leq 0.99$ and is insensitive to the mesh resolution for $x_1 \geq 0.999$. On the other hand, the lubricant fraction ϑ in the cavitated area is insensitive to the mesh resolution for $x_1 \leq 0.99$ and varies more strongly for $x_1 \geq 0.999$.

Another difference can be seen in the pressure in the cavitated area, which is visibly below p_0 for $x_1 = 0.9$, see figure 6.4 a). The minimal pressure is directly related to the steepness parameter x_1 , which is evident from the shape of the ansatz function $\vartheta(p)$, see figure 4.10. The lubricant fraction ϑ can strongly vary for $p < p_{cav} = p_0$, while the pressure can only drop to $\approx x_0 p_{cav}$ as long as $\vartheta > 0$. In all simulations performed in this work, ϑ stayed well above 0.

It has been observed that for large x_1 (e.g. $x_1 \geq 0.999$), numerical oscillations may occur in the result

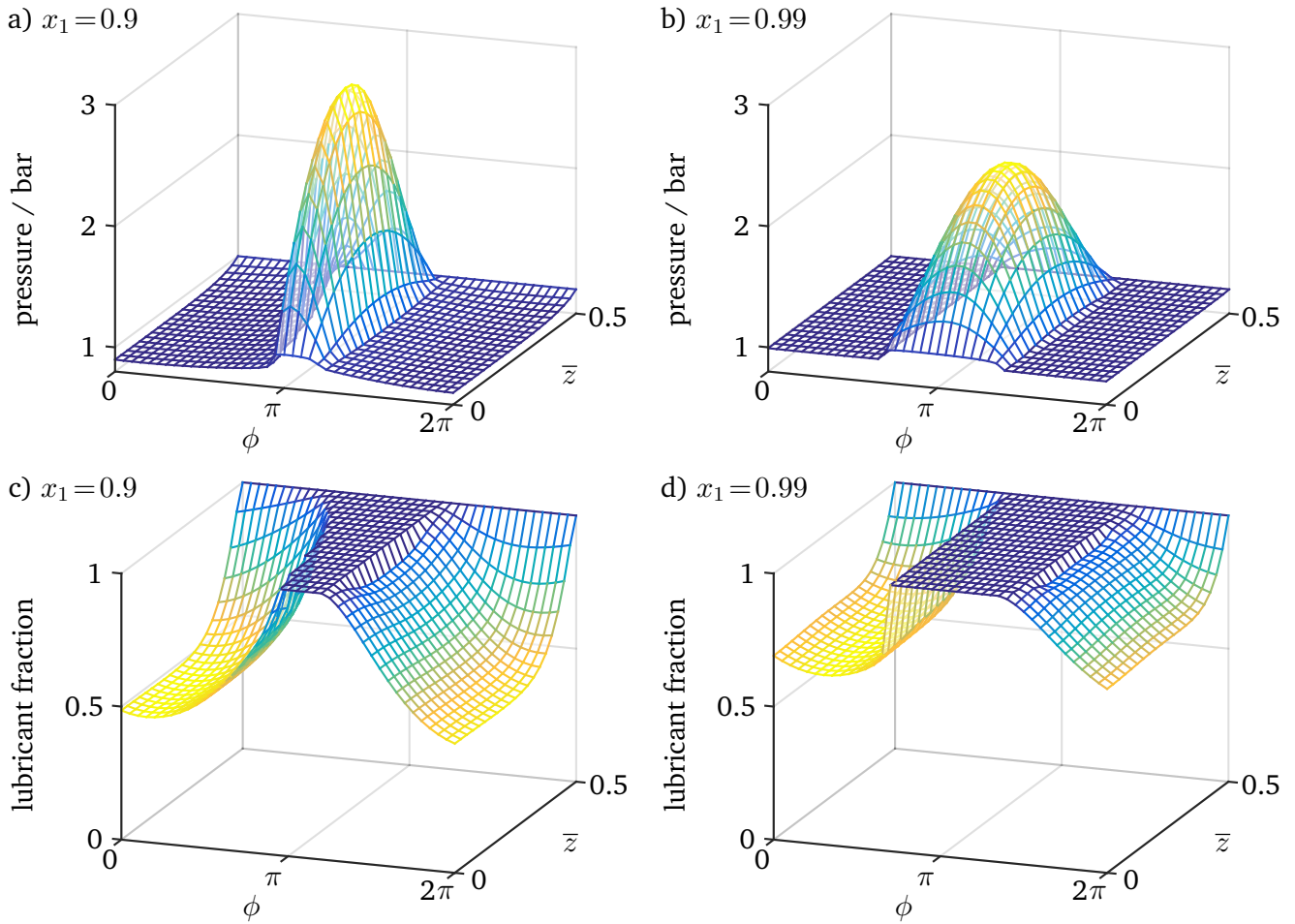


Figure 6.4.: Pressure profile p and lubricant fraction ϑ for different steepness parameters x_1 in one sub-domain of a cylindrical bearing with a circumferential feeding groove

despite artificial diffusion, which are especially visible in $\vartheta(\phi, \bar{z})$ and during whirling motion of the rotor, i.e. above the stability threshold rotor speed. This leads to large calculation times and sometimes failure of the simulation. These oscillations disappear with increasing mesh resolution, yet this may be too costly in simulation time. Simulations with low x_1 , e.g. $x_1=0.9$, are fast and do not experience these numerical oscillations, yet it is shown in figure 6.3 that their results can differ strongly from the results obtained with non mass-conserving cavitation approaches. In order to determine a value of x_1 , which yields the most physically accurate results, extensive comparisons with experimental data are needed, which are not within the scope of this work. Instead, the penalty approach is used as a qualitative reference. It yields smooth pressure profiles and experiences the same stability behavior than the widely used half-SOMMERFELD cavitation approach. For rotors in single film bearings using the mass-conserving cavitation model, a mesh resolution of 10×20 elements and the steepness parameter $x_1=0.99$ is a good compromise between accuracy and calculation time and is used in the remainder of this chapter, if not stated otherwise.

6.4.2 Rotordynamic Stability

In this section, the influence of the cavitation approach on the rotordynamic stability is investigated in more detail. In order to focus on the destabilizing effect of the journal bearings, a rigid rotor without unbalance ($U=0$) and without external damping ($d_o=0$) is considered. The other parameters remain unchanged, the total mass is $m+m_J$. The bearings are cylindrical with a central circumferential feeding groove. Figure 6.5 compares the stability obtained with the penalty approach and the mass-conserving cavitation model.

Figure 6.5 a) shows the journal eccentricity. It is qualitatively similar to the results obtained with the JEFFCOTT rotor. However, no synchronous response and no critical speed are present due to the lack of unbalance. The sudden increase of the eccentricity occurs at a lower rotor-speed when using the two-phase model, also small oscillations occur at ≈ 3 s.

The orbits of the journal center are very similar to those shown in figure 6.1 b). The orbit calculated with the two-phase model is less smooth during the transient motion towards the equilibrium position at the beginning of the simulation. The journal center moves slowly towards the bearing center for both models. When mass-conserving cavitation is considered, the journal center starts to spiral out at a

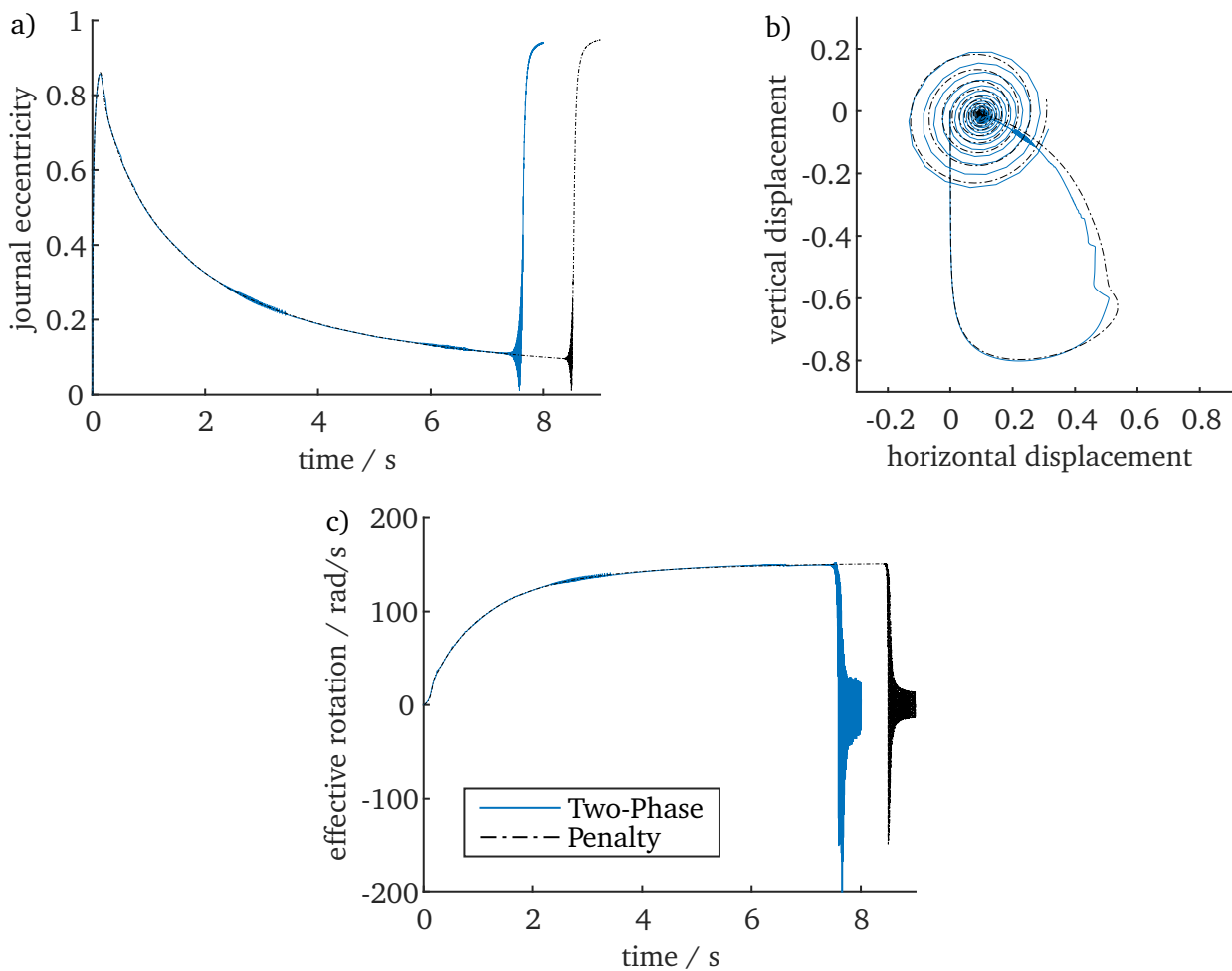


Figure 6.5.: Stability analysis of a rigid rotor without unbalance

position further away from the bearing center than for the penalty approach. The small oscillations at ≈ 3 s are visible in the orbit as well, but they vanish before the system becomes unstable.

A reliable criterion for the sudden increase of the journal eccentricity ε can be obtained through the right-hand side of the REYNOLDS equation (3.9). Considering that the bearings are cylindrical, i.e. $H = 1 + \varepsilon \sin(\phi - \delta)$, the right-hand side is evaluated in cylindrical ε - δ -coordinates, which yields

$$\frac{\omega}{2} \frac{\partial H}{\partial \phi} + \frac{\partial H}{\partial t} = \frac{\varepsilon}{2} (\omega - 2\dot{\delta}) \cos(\phi - \delta) + \dot{\varepsilon} \sin(\phi - \delta). \quad (6.1)$$

This expression is multiplied by ϑ in the mass-conserving cavitation model, see equation (4.31). The squeeze velocity $\dot{\varepsilon}$ and the journal whirl speed $\dot{\delta}$ are given in equations (3.22). From this formulation it is evident that the pressure is generated by two terms. The first term on the right-hand side induces the *physical wedge* and provides the load carrying capacity in hydrodynamic journal bearings. The term $\omega_{\text{eff}} = \omega - 2\dot{\delta}$ is called the *effective angular velocity* of the journal, see e.g. [LS78]. The second term generates pressure due to the *squeeze film damper* effect. The effective angular velocity ω_{eff} is a measure for the hydrodynamic load carrying capacity of the bearing. It has high peaks due to the singularity in $\dot{\delta}$ for $\varepsilon = 0$, which vanish when multiplying it with ε . The term $\varepsilon \omega_{\text{eff}}$ is plotted in figure 6.5 c) for the two different cavitation models.

Due to the slow increase of the rotor-speed and $U = 0$, the position of the journal center coincides with its equilibrium position on the GÜMBEL-curve for rotation speeds below the stability threshold and thus $\dot{\delta} \approx 0$. The effective angular velocity ω_{eff} increases due to the linear increase of ω . When the stability threshold speed is reached, small oscillations occur and the whirl speed $\dot{\delta}$ increases, thus ω_{eff} decreases. As soon as $\omega_{\text{eff}} = 0$, the first term in equation (6.1) vanishes. The bearing loses its load carrying capacity due to the physical wedge. The squeeze term is not able to carry the rotor weight alone and the eccentricity ε increases rapidly, until a new equilibrium is found, namely a stable limit cycle. The results are qualitatively similar for both cavitation approaches and the time where $\omega_{\text{eff}} = 0$ corresponds well with the sudden increase in ε , also for rotors with small unbalance (not shown). However, the whirling motion of the journal begins earlier, namely at the stability threshold of the linearized system. The small oscillations at ≈ 3 s do not significantly influence the effective angular velocity ω_{eff} .

6.4.3 Ambient Boundary Conditions

As can be seen in figure 6.4 a), the pressure can drop below the ambient pressure p_0 when using the mass-conserving cavitation model. The often used DIRICHLET boundary condition (3.11) – namely enforcing ambient pressure p_0 at the axial boundaries of the bearing gap – can then be interpreted as a bearing submerged in an oil bath, since the lubricant fraction ϑ equals 1 at the axial boundaries and the resulting axial pressure gradient entails lubricant flow from the surrounding into the gap. The *free-to-air* NEUMANN boundary condition introduced in section 4.2.1.2 yields an almost zero axial gradient of the pressure and $\vartheta < 1$ at the axial boundary of the cavitated area. This is the more common case in practice and thus this boundary condition is used in this work.

In this section, the influence of the free-to-air boundary condition on the run-up behavior is discussed by comparing the result to one obtained with the oil bath boundary condition. Since an lubricant supply is needed for free-to-air bearings, both simulations are performed with a circumferential feeding

groove. The bearings are discretized with 10×20 elements in one subdomain. For comparison, also a result obtained with the penalty cavitation approach is shown, which also uses the free-to-air boundary condition. However, it has been found that the influence of the axial boundary condition is negligible for the penalty approach. The journal eccentricities of run-up simulations with two different steepness parameters x_1 are shown in figure 6.6. The results with the free-to-air boundary condition are the same as in figure 6.3 a) and b).

The rotor in an oil bath has a higher stability threshold speed than the rotor with bearings which are free-to-air for both steepness parameters x_1 . For $x_1 = 0.99$, the result of the rotor in an oil bath obtained with the mass-conserving cavitation model is almost identical to the result obtained with the penalty approach. Using the oil bath condition, also the gradual transition into the oil whirl with $x_1 = 0.9$ vanishes and the result is closer to the penalty approach. This is likely due to the improved lubricant supply compared to the free-to-air bearing, since lubricant can flow into the bearing gap from both sides. The axial boundary condition has a significant influence on the stability and the qualitative behavior and thus the use of the classical DIRICHLET axial boundary condition is not sufficient for a mass-conserving cavitation model where $p < p_0$ can occur. Large differences in the resulting fluid film forces depending on the axial boundary condition were also observed in experiments conducted on squeeze film dampers in [DSA01b].

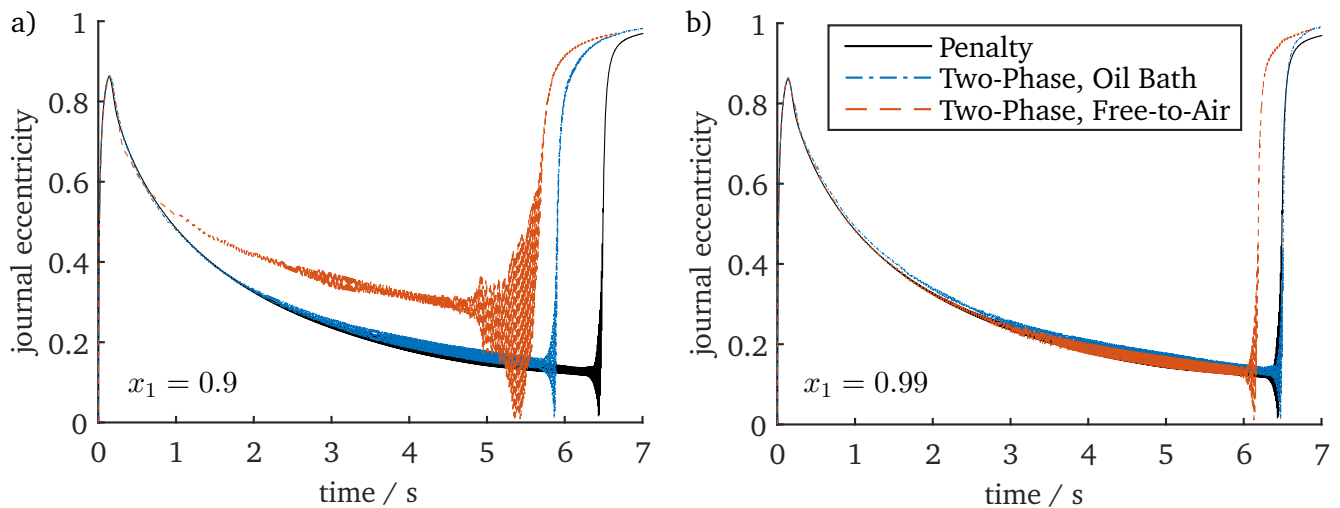


Figure 6.6.: Comparison of axial boundary conditions

The influence of the axial boundary condition on the pressure profile p and the lubricant fraction ϑ is investigated in figure 6.7. The results are taken from the simulations in figure 6.6 b) at the simulation time 4 s. The resolution of the mesh is 10×20 elements, the steepness parameter is $x_1 = 0.99$.

The resulting pressure profiles are similar, which is evident from the well matching eccentricities up to the threshold of instability. The maximum pressure for the free-to-air boundary condition is 2.13 bar and for the oil bath condition 2.17 bar. Differences are visible at the ambient boundary $\bar{z} = 0$. For the free-to-air boundary condition, the pressure at the axial boundary of the fully developed fluid film is above the ambient pressure p_0 . This is due to the fact that $p(\bar{z} = 0) \stackrel{!}{=} p_0$ is enforced using the penalty approach (4.36). A better approximation of the ambient pressure p_0 at the axial boundary could be enforced by choosing a higher exponent factor b in the penalty function $g(p)$. However, this impairs the condition of the numerical model and it has been found that a small offset in the axial pressure does not significantly influence the results of run-up simulations. For the oil bath, the axial pressure equals p_0 due

to the DIRICHLET boundary condition.

On the other hand, the lubricant fraction ϑ largely differs for the two axial boundary conditions. While pure lubricant ($\vartheta = 1$) is present at the circumferential feeding groove ($\bar{z} = 0.5$) in both cases, it is visible that the cavitated area is only open to the surrounding for the free-to-air boundary condition. When a DIRICHLET boundary condition is used at the ambient boundary ($\bar{z} = 0$), the lubricant fraction ϑ is 1 due to the shape of the ansatz function $\vartheta(p)$, see also figure 4.10. Thus, liquid lubricant is present over the whole circumference of the bearing, which can be interpreted as an oil bath.

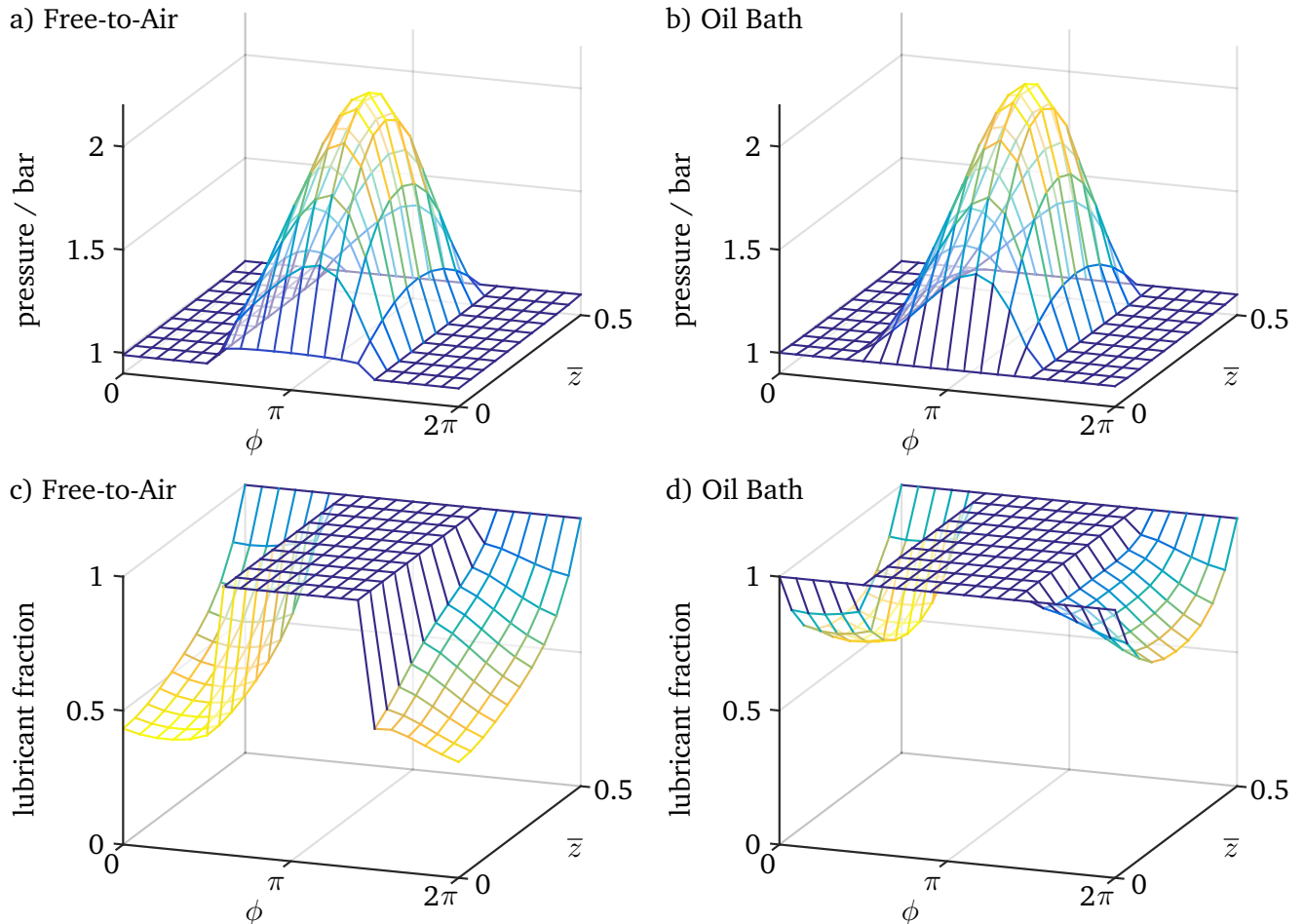


Figure 6.7.: Pressure profile p and lubricant fraction ϑ for oil bath and free-to-air axial boundary conditions in one subdomain of a cylindrical bearing with a circumferential feeding groove

6.4.4 Lubricant Supply

In this section, the influences of the lubricant supply geometry and the supply pressure p_{sup} on the rotordynamic behavior are investigated. Two different geometries are considered, namely a bearing with central circumferential feeding groove and a bearing with one axial feeding groove at the top of the bearing, which both entail a very simple rectangular developed gap geometry. The latter yields a behavior, which is very similar to a plain cylindrical bearing for $p_{\text{sup}} = p_0$. This is due to the fact that the groove is opposite of the pressure profile when the bearing mainly supports the weight of the rotor. On the other hand, the load carrying capacity of the bearing with a circumferential groove is reduced compared to a plain cylindrical bearing, since the pressure profile is split into two narrower subdomains,

see also [Now+15b]. The pressure profile has to become steeper in order to support the rotor weight, which results in a larger journal eccentricity ε .

6.4.4.1 Axial Feeding Groove

The developed bearing geometry with a single axial feeding groove is shown in figure 6.8. Due to symmetry, only one axial half of the bearing is discretized, using 10×20 mesh elements (axial \times circumferential). The symmetry is enforced by setting the axial pressure gradient to zero at $\bar{z}=0.5$. The groove is located at $\phi=0$, its opening angle Θ_{ag} is 15° . The lubricant can be supplied to the groove e.g. through a bore hole inside the groove. Thus, the pressure p_{ag} in the axial groove depends on the supply pressure p_{sup} . However, a constant groove pressure $p_{ag} = p_{sup}$ cannot be used in combination with a constant ambient pressure p_0 at the axial boundaries, as this leads to an inconsistency at the corners of the developed fluid film area. Instead, the relation

$$p_{ag} = p_0 + (p_{sup} - p_0) \left(1 - e^{-\bar{z}/\bar{z}_1}\right) \left(1 - e^{-t/t_1}\right) \quad (6.2)$$

is used. The groove pressure p_{ag} equals the ambient pressure p_0 for $\bar{z}=0$ and increases to p_{sup} for increasing \bar{z} . The parameter \bar{z}_1 is set to 0.1. Furthermore, the time-dependent term prevents inconsistent initial conditions, see also section 4.1.4.

The area of the groove is omitted in the calculation of the hydrodynamic forces due to its large gap size. Yet the hydrostatic force, which exists for $p_{sup} > p_0$, cannot be neglected. It is calculated by assuming the pressure distribution (6.2) over the whole circumference of the groove and integrating it over the surface of the groove.

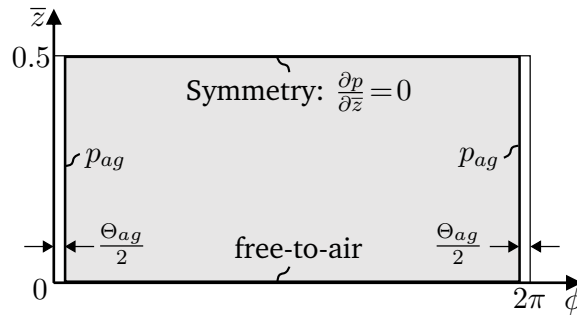


Figure 6.8.: Developed gap geometry and boundary conditions of the cylindrical bearing with one axial lubricant feeding groove

Figure 6.9 compares the journal eccentricities obtained with the penalty and the mass-conserving cavitation approach for increasing supply pressures p_{sup} . The journal eccentricity ε before the stability threshold increases with increasing supply pressure p_{sup} , which has also been reported in [Hor06]. Furthermore, the stability threshold also increases with the supply pressure for both the two-phase model and the penalty approach. This is due to a higher static load acting on the journal shaft, which has a similar effect than an increased rotor weight. Bearings with a feeding pocket or bore at the top of the bearing show an analogous behavior (not shown).

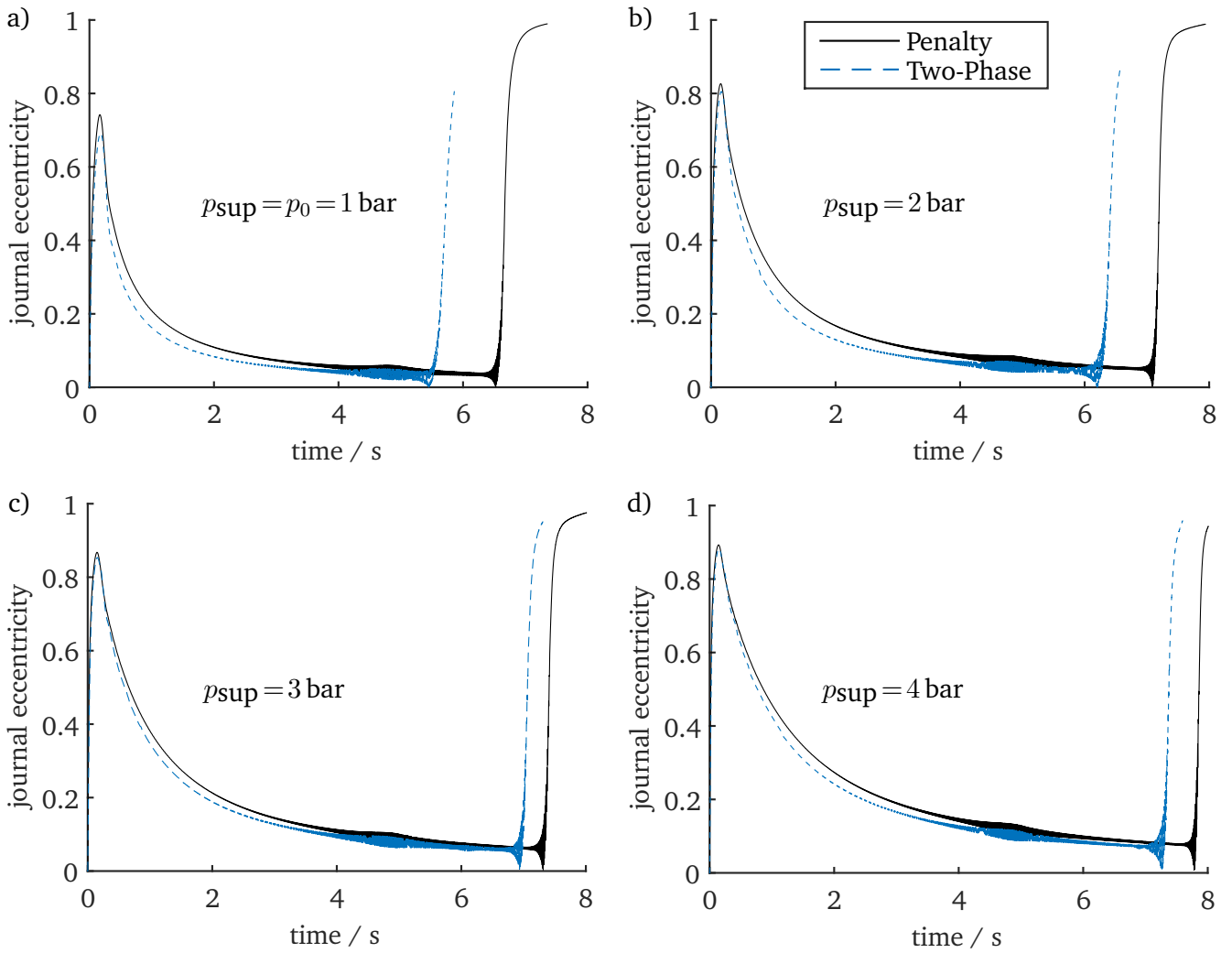


Figure 6.9.: Comparison of penalty approach and two-phase cavitation model for different groove pressures p_{sup} in cylindrical bearings with one axial feeding groove at the top

The influence of the supply pressure p_{sup} is also investigated by comparing the pressure profiles for two supply pressures in figure 6.10. The pressure profiles are calculated using the penalty approach assuming pure rotation ($\dot{\epsilon} = \dot{\delta} = 0$). The input variables are taken from figure 6.9 at the simulation time 1 s, i.e. $\omega_R = 30$ Hz and $\epsilon = 0.227$ for $p_{\text{sup}} = p_0$, $\epsilon = 0.311$ for $p_{\text{sup}} = 2$ bar.

The hydrodynamic pressure is higher for the higher supply pressure, which is due to the larger journal eccentricity. Even though the overall pressure is higher for $p_{\text{sup}} = 2$ bar, both pressure profiles provide the same load carrying capacity, since the pressure partially cancels out in the integration of the bearing forces (3.13). Furthermore, cavitation is only present in the part $\phi > \pi$, and the cavitated area becomes smaller for increasing supply pressure p_{sup} due to the inflowing lubricant. Contrary to the a bearing with periodic boundary conditions in circumferential direction, the end of the cavitated area does not depend on the gap function H , but is predetermined by the location of the axial feeding groove.

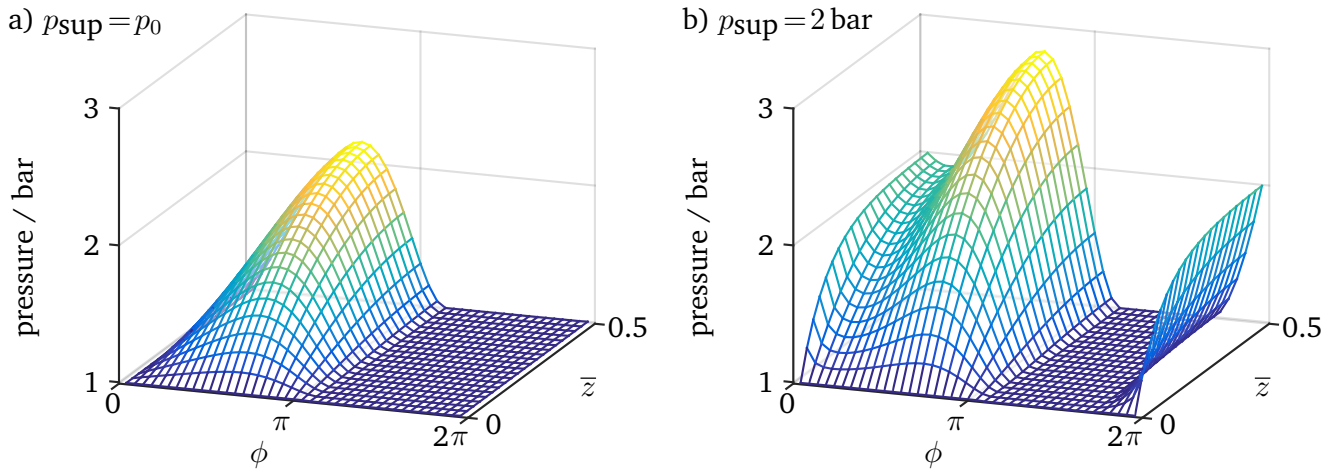


Figure 6.10.: Half pressure profiles p for different groove pressures p_{sup} of a cylindrical bearing with one axial feeding groove at the top of the bearing

6.4.4.2 Circumferential Feeding Groove

Now, the influence of the lubricant supply pressure p_{sup} is investigated for the cylindrical bearing with one central circumferential feeding groove. The groove pressure is set constant and equals the supply pressure p_{sup} . As before, the hydrodynamic pressure generated by the groove is neglected due to its large gap size. The hydrostatic pressure acting on the journal cancels out due to symmetry. The mesh resolution is 10×20 elements and the steepness parameter x_1 is 0.99.

The results obtained with the penalty and the mass-conserving cavitation approach for increasing supply pressure p_{sup} are shown in figure 6.11. The results with $p_{\text{sup}} = p_0 = 1$ bar are shown in figure 6.6 b). The amplitude at the critical speed at ≈ 4.8 s is less pronounced, i.e. the damping is higher, despite a larger eccentricity. Compared to the bearing with one axial feeding groove at the top of the bearing (see figure 6.9), the difference between the penalty approach and the mass-conserving cavitation model is smaller. The stability threshold speed is decreased with increasing supply pressure p_{sup} , which has also been observed in [Cho+11; Now+15b]. The system becomes immediately unstable for $p_{\text{sup}} = 4$ bar. The strong oscillations in the eccentricity at the beginning of the simulation in figure 6.11 d) are caused by a circular whirl motion of the journal, whose center does not coincide with the bearing center. The eccentricity sharply declines when the journal center closely passes the center of the bearing shell. With increasing rotor-speed, the radius of the whirling motion increases and its center moves towards the bearing center, thus the oscillations in the eccentricity vanish.

The reduction of the stability threshold speed due to increased supply pressure p_{sup} can be explained by comparison of the pressure profiles, see figure 6.12. The pressure profiles are calculated using the penalty approach, assuming pure rotation ($\dot{\varepsilon} = \dot{\delta} = 0$). The input variables are taken from figures 6.6 b) and 6.11 b) at the simulation time 1 s, i.e. $\omega_R = 30$ Hz and $\varepsilon = 0.485$ for $p_{\text{sup}} = p_0$, $\varepsilon = 0.393$ for $p_{\text{sup}} = 2$ bar.

If the supply pressure p_{sup} is larger than the ambient pressure p_0 , the resulting pressure profile is a superposition of the hydrodynamic pressure and a linear hydrostatic pressure distribution over the whole circumference of the bearing due to the boundary conditions. This can be shown using the short bearing approximation, see appendix B. The hydrostatic pressure does not contribute to the load carrying capac-

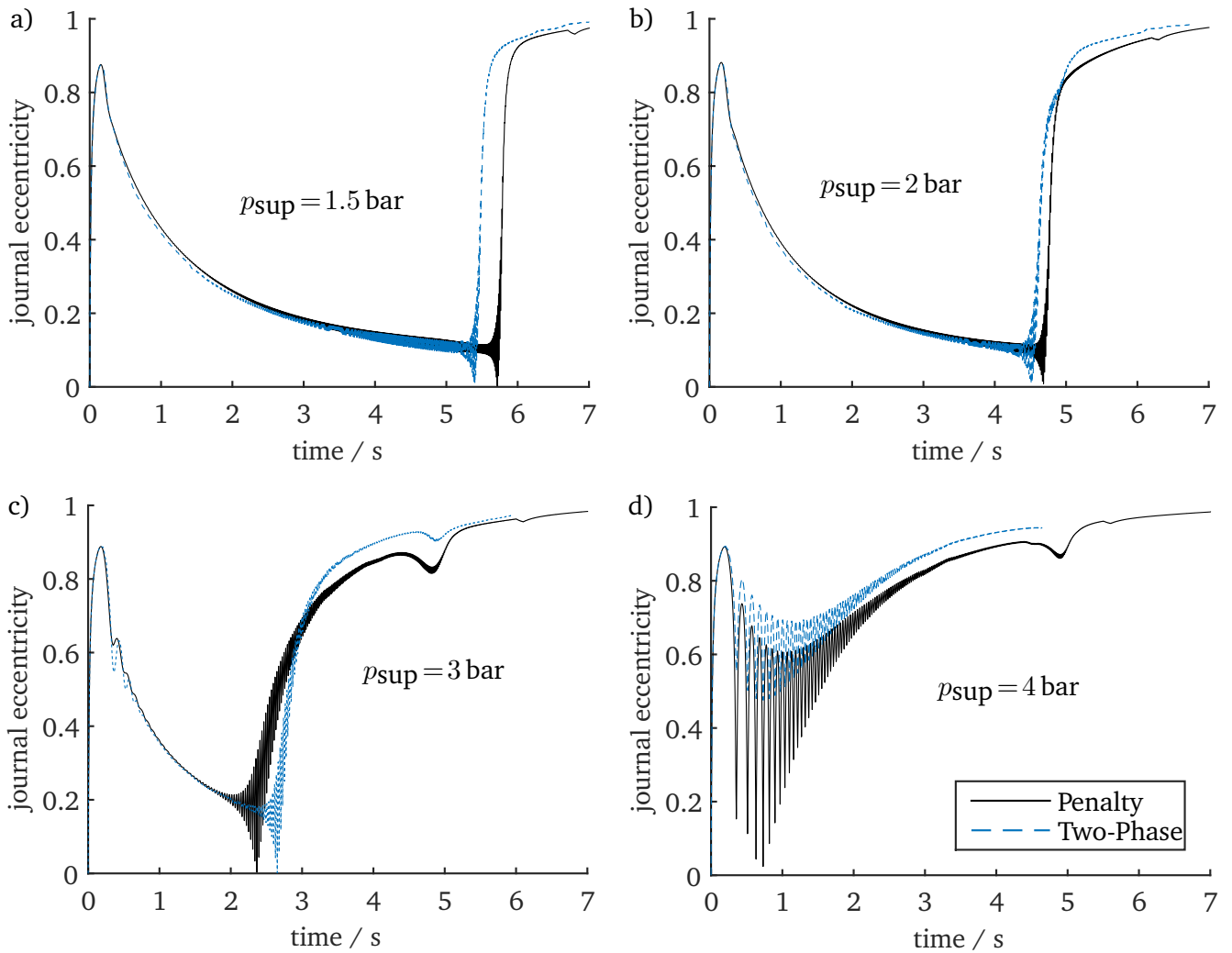


Figure 6.11.: Comparison of penalty approach and two-phase cavitation model for different groove pressures p_{sup} in cylindrical bearings with a circumferential feeding groove

ity, since the integrals in the calculation of the bearing forces (3.13) are zero if the pressure does not change in ϕ -direction. The maximum pressure is almost equal for both groove pressures (2.42 bar for $p_{\text{sup}} = p_0$, 2.44 bar for $p_{\text{sup}} = 2$ bar). Thus, the hydrodynamic pressure, which is the resulting pressure profile minus the hydrostatic pressure distribution, is smaller for the higher supply pressure p_{sup} . This entails a lower journal eccentricity ε for the same load carrying capacity. Similar to the bearing with an axial feeding groove, the size of the cavitated area decreases with increasing supply pressure p_{sup} due to the inflowing lubricant and can even vanish completely.

For high supply pressures p_{sup} and low journal eccentricities ε , the hydrostatic pressure can cover the hydrodynamic pressure completely. This reduces the load carrying capacity to zero, thus no equilibrium position exists with a low eccentricity. The system is almost immediately destabilized at a low rotation speed, which can be seen in figure 6.11 d).

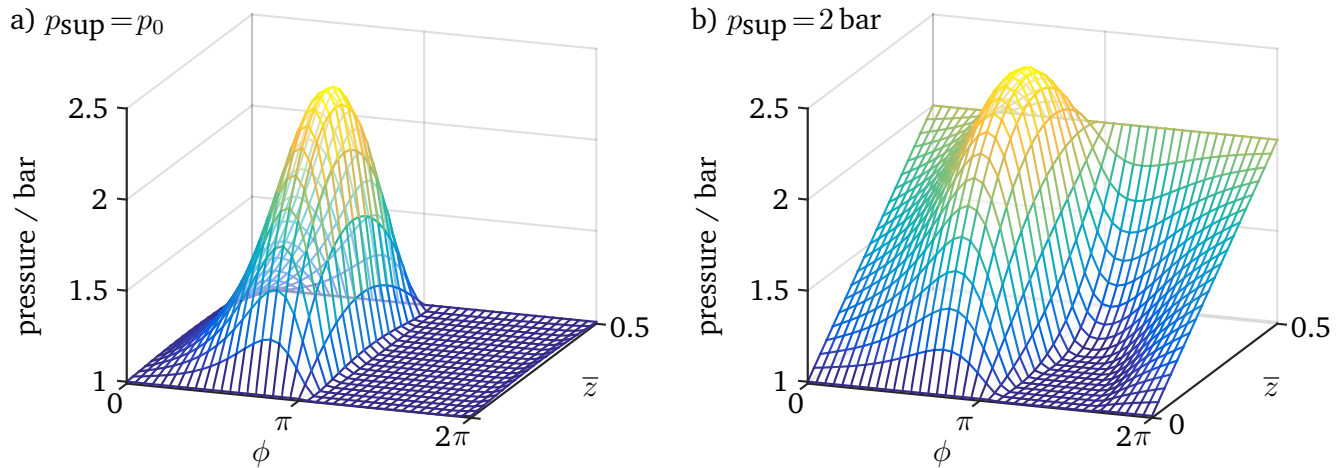


Figure 6.12.: Pressure profiles p for different groove pressures p_{sup} in one subdomain of a cylindrical bearing with a circumferential feeding groove

6.4.5 Rotor Shaft Stiffness

Now, the influence of the shaft stiffness c of the JEFFCOTT rotor on the stability of the system is investigated. The behavior with the mass-conserving cavitation model is compared to that obtained with the penalty approach. The bearings are free-to-air and the lubricant is supplied through an axial feeding groove at the top of the bearing. Due to symmetry, only one axial half of the bearing gap is discretized with 10×20 mesh elements. Figure 6.13 shows the results with the low stiffness 1000 N/mm and those obtained with a rigid rotor. The behavior using the default value $c = 5000 \text{ N/mm}$ falls in between the two cases shown in figure 6.13 and is shown in figure 6.9 a).

The less stiff rotors exhibit a lower stability threshold speed. This is expected, since there is a connection between the critical speed of the shaft and the whirl entry frequency, see [Hor06]. Furthermore, the critical speed is reduced for $c = 1000 \text{ N/mm}$ to $\approx 66 \text{ Hz}$ at $\approx 2.2 \text{ s}$. The critical speed of the rigid rotor is infinitely high, thus no resonance can be seen. The difference between the results with penalty approach

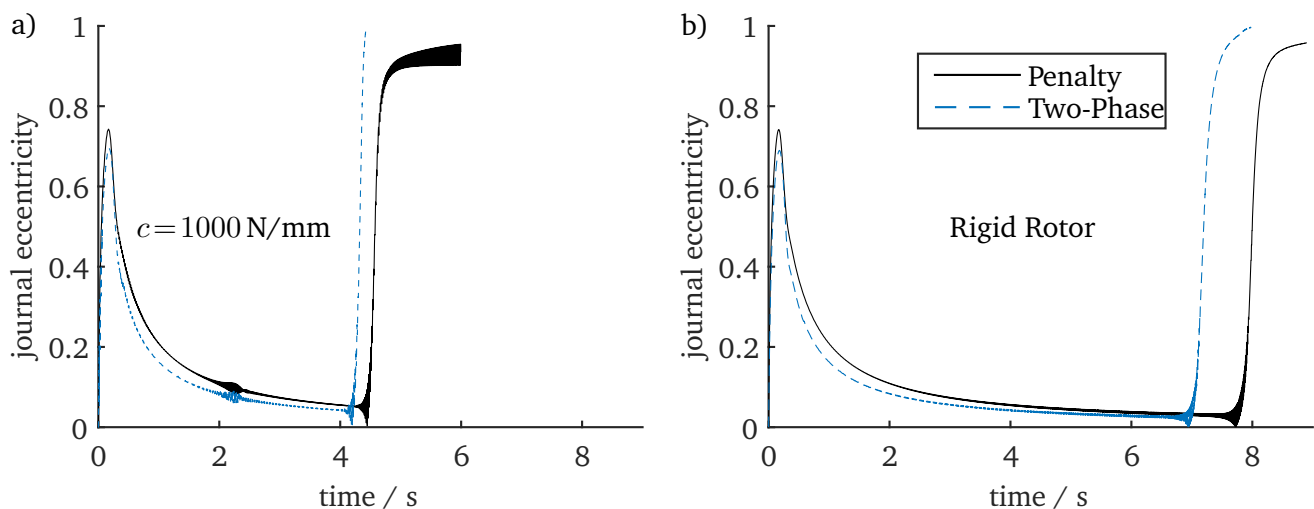


Figure 6.13.: Comparison of penalty approach and two-phase cavitation model for different shaft stiffnesses c of the JEFFCOTT rotor in cylindrical bearings with one axial feeding groove at the top

and the mass-conserving cavitation model is smaller for $c = 1000 \text{ N/mm}$. In this case, the bearings are rather stiff compared to the rotor shaft and might have a lower influence on the overall system behavior.

6.4.6 Rotor Unbalance

The influence of the rotor unbalance U is investigated using the same bearing geometry as in the previous section, namely one axial feeding groove at the top of the bearing. Figure 6.14 shows the results with two different large unbalances. The result with the reference unbalance $U = 3 \text{ gmm}$ can be seen in figure 6.9 a).

The stability threshold speed increases with increasing unbalance except for the penalty approach with $U = 50 \text{ gmm}$, where the threshold speed is slightly lower than for $U = 3 \text{ gmm}$. The critical speed of the system is clearly visible for higher unbalances. The synchronous oscillation amplitudes increase with the unbalance and are higher when the mass-conserving cavitation model is used. This is because the movement of the journal has a higher whirl component for larger unbalances, which entails a reduced radial force and thus higher eccentricities for the two-phase model, see section 4.2.2.3. A smaller minimal gap size considering mass-conserving cavitation was also observed in [NWD17]. The difference in the stability threshold speed between the penalty approach and the mass-conserving cavitation model is smaller for high unbalances than for $U = 3 \text{ gmm}$.

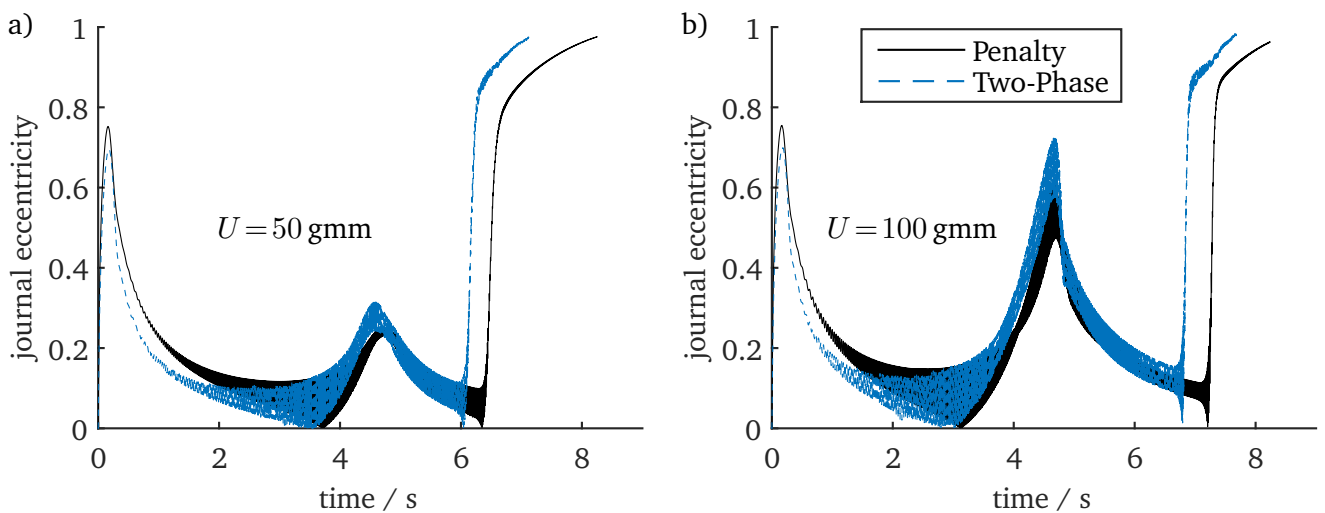


Figure 6.14.: Comparison of penalty approach and two-phase cavitation model for different unbalances U of the JEFFCOTT rotor in cylindrical bearings with one axial feeding groove at the top

7 Rotors in Floating Ring Bearings

In this chapter, rotors in floating ring bearings are investigated. The mutual damping of the inner and outer lubricant film of floating ring bearings enables operation speeds above the linear stability threshold of a rotor in single oil films. On the contrary, additional sub-synchronous oscillations can occur, which are induced by the interaction of the lubricant films with the natural modes of the rotor system.

The geometry of the floating rings is explained in the next section. Then, firstly a symmetric JEFFCOTT rotor is considered in section 7.2, with which various influences – such as cavitation modeling approach, supply pressure and bearing torque – are investigated. Finally, exhaust turbochargers are studied in section 7.3.

The solver parameters of the rotor and the bearing subsystems are the same as for single film bearings and are given in section 6.2.

7.1 Floating Ring Geometry

The floating rings used in this chapter correspond to those of the turbocharger investigated in section 7.3 and are schematically shown in figure 7.1. The dimensions are given in table 7.1. The inner and outer bearing gap are connected by 6 evenly spaced, circular bore holes with diameter D_{cc} . The geometry of the inner bearing gap is plain cylindrical besides the bore holes. The outer bearing gap is cylindrical and features a central circumferential groove, which divides the outer bearing gap into two sections. The bore holes are contained within the groove. For simplicity, it is assumed that also the lubricant supply from the bearing housing is contained within the groove. Thus, the pressure inside the circumferential groove

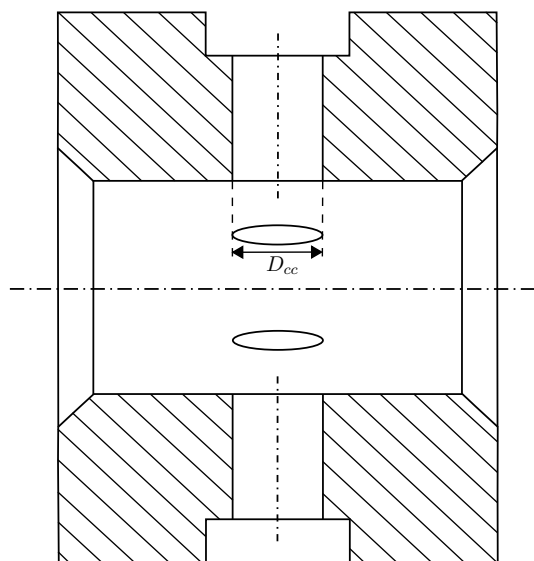


Figure 7.1.: Schematic cross-section of a floating ring with circumferential groove and connecting channels shown in figure 4.4

and the bore holes equals the supply pressure p_{sup} due to the much smaller height of the gaps. The supply pressure p_{sup} is thus imposed as a DIRICHLET boundary condition at the circumferential groove in the outer bearing gap and at the bore holes in the inner bearing gap. The axial boundary condition is free-to-air.

Due to symmetry, only one half of the bearing gaps needs to be discretized. The mesh used for the outer lubricant films is shown in figure 6.2. The mesh used for the inner lubricant films is shown in figure 7.2. The bore holes appear elliptic due to the dimensionless geometry.

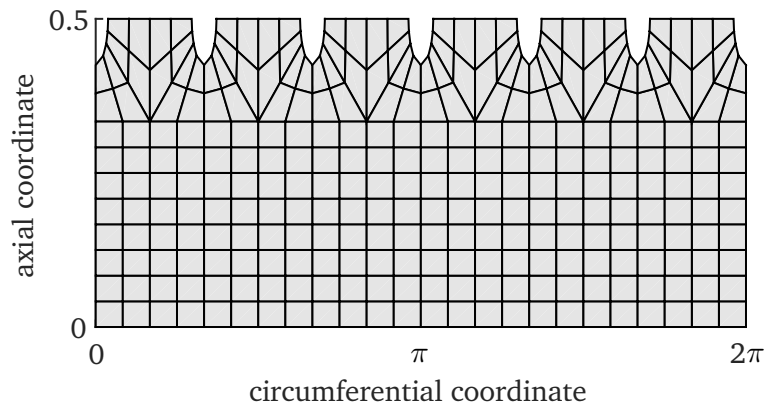


Figure 7.2.: Rectangular mesh of one axial half of the bearing with bores, discretized with 10×24 elements

7.2 Jeffcott Rotor

Firstly, a symmetric JEFFCOTT rotor which is described in section 2.1.2 is considered. The parameters of the rotor and the bearings are given in table 7.1. The parameters are similar to those used in chapter 6. A relatively high journal mass m_J improves the numerical stability behavior of the model. This is also a more accurate representation of a real rotor, where the mass is spread rather than lumped. The shaft stiffness c is increased to better reflect actual turbochargers, which are rather stiff. The rotor-speed is increased linearly from 0 to $f_{\text{max}} = 900$ Hz in $T_{\text{sim}} = 3$ s.

The two floating rings are identical. The mass is small and could be neglected, since it does not influence the results. The moment of inertia around the axis of rotation is small and only slightly influences the ring speed ω_F during transient operation.

The geometry of the inner lubricant film corresponds to the values given in table 4.1. The gap sizes change during operation due to warming. The lubricant supply temperature T_{sup} of the investigated turbocharger is 70°C . The lubricant temperatures T_o and T_i of the outer and inner film are assumed to be 80°C and 100°C , respectively. The inner temperature is higher due to the warm shaft and the higher friction losses. The temperature T_R of the rotor shaft equals T_i , while the temperature T_F of the floating rings is assumed to be $(T_i + T_o)/2$. The temperature of the housing equals the lubricant supply temperature, i.e. $T_H = T_{\text{sup}}$. The gap sizes given in table 7.1 are the *warm* gap sizes, which are rounded values based on calculated values using equation (4.24). The oil viscosities are rounded values based on equation (3.12).

Table 7.1.: Reference parameters of the JEFFCOTT rotor in floating ring bearings

Name	Symbol	Value	Unit
Rotor mass	m	5	kg
Journal mass	m_J	1	kg
Shaft stiffness	c	20000	N/mm
Unbalance	U	3	gmm
External damping	d_o	1	Ns/m
Shaft damping	d_i	0.1	Ns/m
Floating ring mass	m_F	75	g
Moment of inertia	θ_F	20	kgmm ²
Diameter of connecting channels	D_{cc}	2.5	mm
Inner bearing width	B_i	20	mm
Inner bearing diameter	D_i	25	mm
Inner nominal radial bearing gap (warm)	C_i	40	μm
Inner oil viscosity (warm)	η_i	10	mPas
Outer bearing width	B_o	2.8	mm
Outer bearing diameter	D_o	40	mm
Outer nominal radial bearing gap (warm)	C_o	50	μm
Outer oil viscosity (warm)	η_o	20	mPas
Ambient pressure	p_0	1	bar
Supply pressure	p_{sup}	2	bar
Oil density	ρ_l	830	kg/m ³

7.2.1 Cavitation Approach

Firstly, the influence of the cavitation model on the stability behavior is investigated by comparing run-up simulations calculated using the half-SOMMERFELD condition and the penalty approach explained in section 3.3.2 with results obtained with the two-phase model introduced in section 4.2. For the latter, two different values for the steepness parameter x_1 are used.

The outer and inner film eccentricities ε_o and ε_i , see equation (4.14), are shown in figures 7.3 a) and b), respectively. At the beginning of the simulation, the rotor journal and the floating ring are located in the center of the bearing and drop due to gravity. Thus, both eccentricities rise analogous to the results with single lubricant film bearings shown in chapter 6. The rotor-speed ω_R increases and also the rotation speed of the floating ring ω_F due to the friction torque in the inner lubricant film, which can be seen in the ratio ω_F/ω_R in figure 7.3 c). Thus, the load carrying capacities of the inner and the outer lubricant film increase and the eccentricities decrease. Both the floating ring and the rotor journal move towards a central position in their respective lubricant films.

The inner eccentricity ε_i increases suddenly (at ≈ 0.5 s for the system with half-SOMMERFELD condition). This is the instability (bifurcation) caused by the inner lubricant film, which is called *inner sub-synchronous oil whirl/whip* here or Sub_i for short. The rotation speed of the inner lubricant film is $\omega = \omega_R + \omega_F \approx 1.2 \omega_R$, thus the stability threshold is reached at a lower rotor-speed ω_R than for single

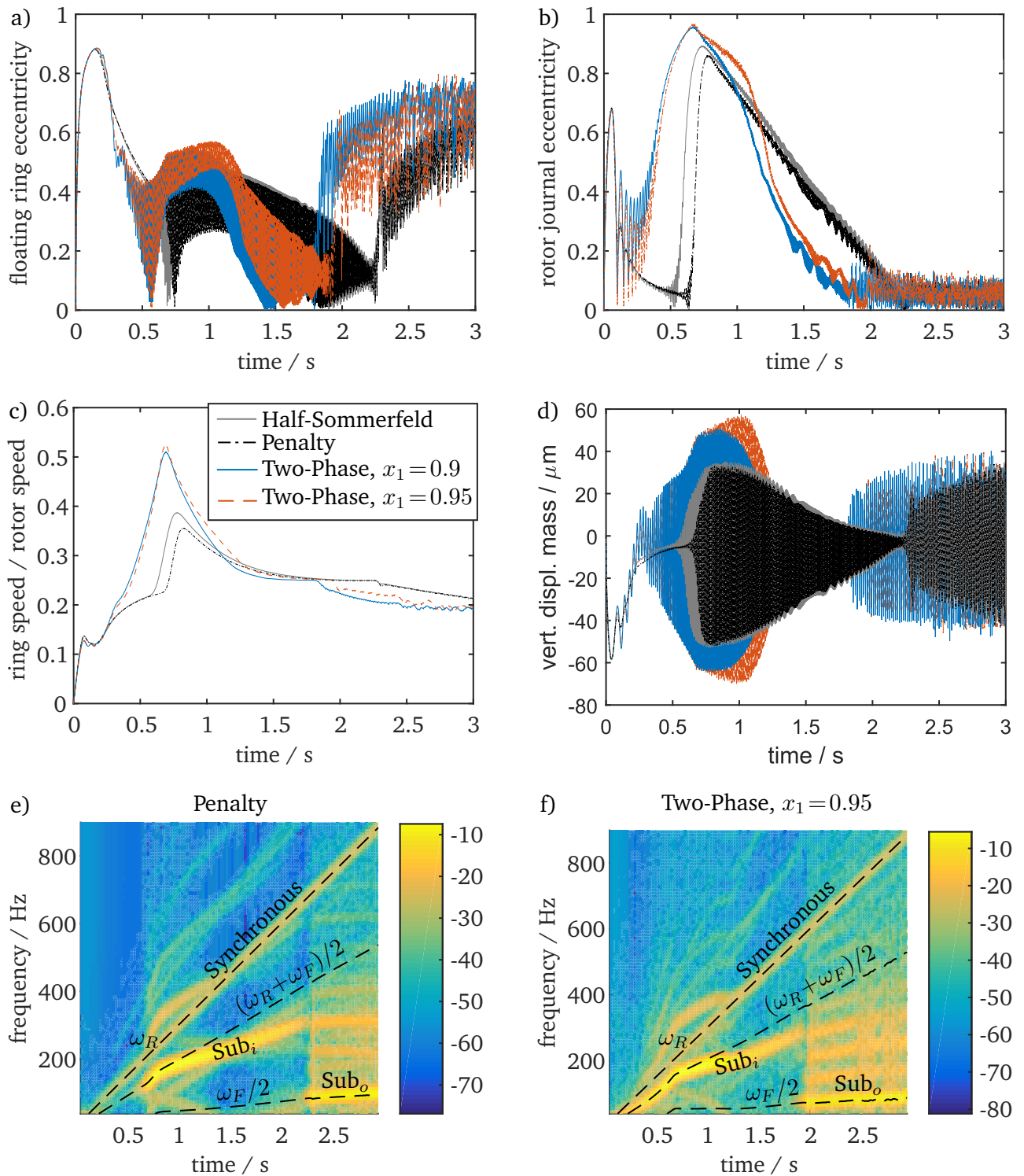


Figure 7.3.: Comparison of half-SOMMERFELD, penalty and mass-conserving cavitation models

lubricant films. The rotor journal moves on an approximately circular whirl motion. This motion is damped by the outer lubricant film, which is visible in strong oscillations in the outer eccentricity ε_o . Furthermore, the rotation speed ω_F of the floating ring increases sharply at the beginning of Sub_i due to the increase of ε_i , which increases the friction torque in the inner lubricant film. The ratio ω_F/ω_R decreases with increasing rotor-speed ω_R , yet the absolute speed ω_F still increases. The inner eccentricity ε_i decreases until the whirl motion vanishes.

After Sub_i , the system can return to pure synchronous oscillations due to unbalance. For this parameter set, the system directly enters the instability produced by the outer lubricant film, which is called *outer sub-synchronous oil whirl/whip* or Sub_o and can be identified in the sudden increase of the outer eccentricity ε_o at ≈ 2.25 s for the system with half-SOMMERFELD condition. The rotation speed of the outer lubricant film is $\omega = \omega_F \approx 0.25 \omega_R$, thus this instability occurs at a high rotor-speed ω_R . The oscillations are damped by the inner fluid film, yet the inner eccentricity ε_i stays small. The friction torque in the outer fluid film increases with the outer eccentricity ε_o , thus the ratio ω_F/ω_R decreases.

The absolute vertical displacements y_D of the rotor disk are shown in figure 7.3 d). The motion of the rotor disk is very similar to that of the journals, since the rotor is rather stiff. The displacement of the disk equilibrium position relative to the center of the bearing is caused by the weight of the rotor and is the sum of the journal displacement in the bearings and the bending of the rotor shaft.

The frequency content is investigated using a short FOURIER transform of the vertical displacement y_D of the rotor disk. For the penalty approach, it is shown in figure 7.3 e). The amplitude is given in dB, with the sum of the nominal bearing gap sizes $C_i + C_o$ as reference value. The synchronous oscillation with the frequency ω_R is rather small due to low unbalance. The two sub-synchronous oil whirls/whips are clearly visible. Additional multiple frequency components, also super-synchronous, have much smaller amplitudes. Sub_i starts with an oil whirl with the frequency $(\omega_R + \omega_F)/2$, which locks into the natural mode of the rotor at ≈ 0.8 s and becomes an oil whip. The frequency of the oil whip changes due to the nonlinear stiffness of the bearings. Sub_i bifurcates into Sub_o at ≈ 2.25 s, which is an oil whirl with the frequency $\omega_F/2$. Sub_i and Sub_o can also occur simultaneously for different parameters.

The two non mass-conserving cavitation models experience an almost identical behavior. The inner whirl occurs at a slightly lower rotation speed when using the half-SOMMERFELD condition.

The results obtained with the two-phase model are qualitative similar, yet the stability thresholds and amplitudes differ significantly. The influence of a small steepness parameter $x_1 = 0.9$ is smaller than for rotors in single lubricant films, see figure 6.3 on page 76. The stability threshold for $x_1 = 0.9$ is again lower than for higher x_1 .

The onset rotor-speeds of Sub_i and Sub_o are lower for the two-phase model, analogous to rotors in single lubricant films. The amplitudes of the whirl/whip motions are larger. The larger inner eccentricity ε_i yields a stronger increase of the floating ring speed ω_F , see figure 7.3 c). Also the outer eccentricity ε_o is larger during Sub_i . This is due to the delayed pressure build-up during whirl motion, which entails a larger eccentricity, see section 4.2.2.2. The inner whirl ends at a lower rotor-speed due to the more quickly decreasing ratio ω_F/ω_R , which is caused by the larger outer eccentricity ε_o . Again, the system directly enters Sub_o .

The vertical displacements y_D of the rotor disk shown in figure 7.3 d) show that the absolute oscillations of the rotor are much larger for the two-phase model during Sub_i and only slightly larger during Sub_o . This may be explained with the different lubricant supply geometries in the inner and outer bearing gaps. The circumferential groove in the outer gap provides a better lubricant supply than the bore holes used in the inner bearing gap. Thus, the lubricant film is less cavitated in the outer bearing gap, especially with higher supply pressure p_{sup} . This condition is closer to non mass-conserving cavitation models, which implicitly assume a fully developed lubricant film.

Figure 7.3 f) shows the short FOURIER transform for the two-phase model with $x_1 = 0.95$, which is very similar to the result with $x_1 = 0.9$ (not shown). The frequencies of Sub_i and Sub_o are very similar to those

of the result using the penalty approach. However, Sub_i starts almost at the beginning of the simulation. Sub_i bifurcates into Sub_o at a lower rotor speed at ≈ 1.9 s.

Lastly, the calculation times of the run-ups using different cavitation models and calculated with different simulation methods are compared. The simulations were performed on a desktop PC with *Intel i7-3770* CPU and 20 GB RAM. To make the results more general, not the passed time (i.e. *Wall-Clock-Time*) is compared, which is 5–9 days for the shown results. Instead, the following values are used, which give more insight into the differences:

- *Time/Reynolds* is the average calculation time of one micro-step, i.e. one converged solution of the REYNOLDS equation including all iterations of NEWTON'S method. Usually, the number of iterations does not change strongly during a simulation, since the time-steps are small and thus a good initial condition for NEWTON'S method exists. Thus, the calculation time of one micro-step depends mostly on the mesh resolution and the hardware, including the workload of the CPU.
- The ratio of the number of micro- and macro-steps is called *Multi Scale Factor*. Because the GAUSS-SEIDEL master-slave co-simulation scheme is used, the step size h_A of the rotor system equals the macro step size H , see section 5.2.1. The average step-size of the rotor is always close beneath the maximum allowed step size $h_{\max,A}$. The bearing system takes smaller steps h_C , especially during sub-synchronous whirl motions. A high Multi Scale Factor thus indicates many calculations of the bearing model, which almost completely determines the overall calculation time.
- The *Simulation Speed* is the ratio of simulated time T_{sim} and the Wall-Clock-Time. This value enables direct comparison of different models also for different T_{sim} , if the results are qualitatively similar.

Run-up simulations can also be performed with a monolithic *Comsol* model, which includes all 4 lubricant films and the ordinary differential equations of the JEFFCOTT rotor and the floating rings. Usually, this enables the use of the greater maximum allowed step size $h_{\max} = 1$ ms, since no error is made due to the coupling. A co-simulation enables the consideration of more complex rotors and is the standard method used in this work.

The REYNOLDS equation for non mass-conserving cavitation models is not time-dependent, thus the implicit dynamic-static solver-coupling is normally used, see section 5.1. Asymmetrical rotor systems with floating ring bearings require at least 16 parallel processes, which requires CPUs with many cores or parallel calculation on different PCs. Furthermore, the large number of required licenses also reduces the profitability of this method.

Including the differential equations of the floating ring into the bearing model enables co-simulation of systems with non mass-conserving cavitation models, which reduces the number of processes to 1 per bearing. However, this requires the simultaneous calculation of the inner and outer lubricant film in one bearing model, which increases the calculation time of one micro-step.

The efficiency of different cavitation models and simulation methods is compared in table 7.2. The Multi Scale Factor is only valid for co-simulations, since a monolithic model and the dynamic-static solver-coupling have only one time-dependent solver.

For the non mass-conserving half-SOMMERFELD and penalty approaches, the calculation time of one micro-step is much larger when using co-simulation or a monolithic model than for the dynamic-static solver-

coupling. This is due to the greater amount of degrees of freedom in the bearing model, which incorporates the inner and the outer lubricant film and the equations of motion of the floating ring. However, the use of co-simulation is nevertheless favorable compared to dynamic-static solver coupling, since many more parallel calculations can be performed on a single PC.

The calculation time of one micro-step is greater for the penalty approach than the half-SOMMERFELD model due to the introduced nonlinearity, which yields a reduced calculation speed for the solver-coupling. However, calculations with the penalty approach require less micro-steps, which leads to an overall increase of the calculation speed when using co-simulation or a monolithic model.

Table 7.2.: Efficiency of different cavitation models and simulation methods

Simulation Method	Cavitation Model	Time/Micro-step / ms	Micro-steps / Macro-steps	Speed / ms/h
Solver-Coupling	Half-SOMMERFELD	39	-	93
Solver-Coupling	Penalty	42	-	66
Co-Simulation	Half-SOMMERFELD	73	2.1	23
Co-Simulation	Penalty	124	1.0	28
Co-Simulation	Two-Phase, $x_1 = 0.9$	47	4.4	18
Co-Simulation	Two-Phase, $x_1 = 0.95$	48	5.3	14
Monolithic Model	Half-SOMMERFELD	74	-	55
Monolithic Model	Penalty	111	-	74
Monolithic Model	Two-Phase, $x_1 = 0.9$	90	-	7.8
Monolithic Model	Two-Phase, $x_1 = 0.95$	91	-	5.7

The calculation time of one micro-step of the two-phase model using co-simulation is higher than for the half-SOMMERFELD and penalty models using dynamic-static solver-coupling. In both methods, only one lubricant film is computed in the bearing model. There is no need to include both lubricant films and the equations of motion of the floating ring into the bearing model for the two-phase model, since the REYNOLDS equation is already time-dependent. The amount of micro-steps is much larger for the two-phase model compared to the co-simulation of the non mass-conserving models. The number of macro-steps taken by the rotor model is only slightly increased (not shown). The smaller micro-step size strongly affects the simulation speed, which is much lower for the two-phase model. A greater steepness parameter x_1 strongly increases the number of micro-steps and thus decreases the simulation speed.

The calculation of a monolithic model is faster than co-simulation for the half-SOMMERFELD and penalty models, which is expected due to the higher maximum allowed solver step-size $h_{\max} = 1$ ms. Interestingly, a monolithic model performs far worse than co-simulation when using the two-phase model. This is mainly due to a strongly increased calculation time of one micro-step, which is caused by an increased number of NEWTON iterations. The average micro-step size is slightly reduced compared to the co-simulation, which worsens the performance of the monolithic model. Due to the small micro-step sizes taken by the solver, a greater allowed maximum step-size h_{\max} yields no advantage over the co-simulation.

It has been observed that the step-size taken by *Comsol* strongly varies. A large step-size yields a poor starting condition for the NEWTON procedure in the next time-step, which increases the amount of it-

erations. A lower allowed maximum step-size h_{\max} yields more evenly step-sizes, which reduces the number of NEWTON iterations. A trade-off has to be found between a large number of micro-steps with few NEWTON iterations or a small number of micro-steps with many NEWTON iterations.

Additionally, an option is available in *Comsol*, which reduces the number of recalculations of the JACOBIAN, which greatly reduces the calculation time of the micro-steps. Yet with this option enabled, the time-dependent solver performs more micro-steps and the overall calculation time is similar. The option is used for the half-SOMMERFELD and the two-phase model. However, the penalty model does not converge with this option enabled.

7.2.2 Run-down

In this section, the results of a consecutive run-up and run-down using the penalty cavitation approach are shown. The rotor-speed is increased linearly from 0 to 700 Hz in 10 s, then kept constant for 0.5 s and after that linearly decreased to 0 in 10 s. The acceleration and deceleration are chosen low in order to reduce transient effects. The outer bearing gap size is increased to $C_o = 90 \mu\text{m}$ to yield smaller eccentricities.

The inner and outer eccentricities are plotted versus the rotor-speed in figure 7.4, which allows a direct comparison of the sub-synchronous whir/whips during run-up and run-down. The on- and offset rotor-speeds of the sub-synchronous whir/whips are very different for the run-down, whereas the amplitudes are almost equal. This is amplified with increasing acceleration and deceleration of the rotor-speed. This illustrates that several stable limit cycle solutions can be present at the same rotor-speed. When the rotor-speed is increased, the whirl motion starts, when the synchronous motion becomes unstable. During run-down, the system remains in the whirl/whip motion until it becomes unstable. However, it is possible for the system to jump to the other solution earlier due to external excitation, see [Hor06].

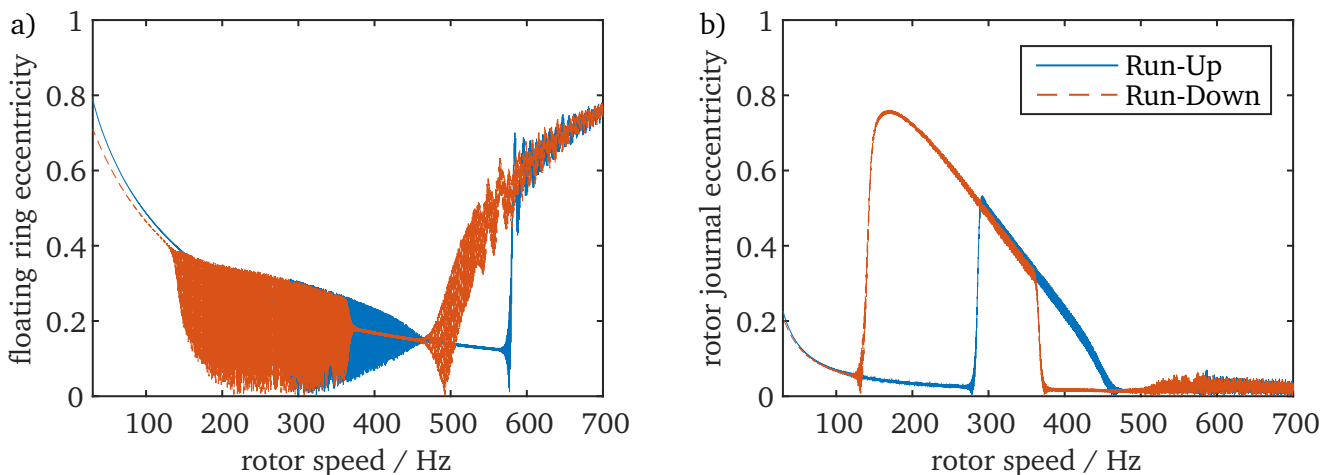


Figure 7.4.: Hysteresis effect of run-up and run-down simulation

7.2.3 Outer Bearing Gap Size

The bearing gap sizes have a large influence on the behavior of rotors in journal bearings. They determine the stiffnesses and damping capabilities of the individual lubricant films and the overall bearing. Thus, they influence the appearance and severity of sub-synchronous oscillations. The ratio ψ_i/ψ_a with $\psi_i + \psi_a = \text{const.}$ is commonly used to tune the sub-synchronous oscillations of turbochargers, see [Die15].

The bearing has the highest linearized stiffness and damping, if both the inner and the outer fluid film provide equal stiffness and damping due to the series connection. The inner film of the considered floating ring bearing is relatively stiff due to the small nominal gap size, thus the influence of a lower outer gap size C_o is investigated. Figure 7.5 shows the results of run-up simulations performed with three different outer gap sizes C_o , using the penalty approach on the left and the two-phase cavitation model on the right. The results with $C_o = 50 \mu\text{m}$ are the same as in figure 7.3. Figures 7.5 a) and b) show the the outer eccentricities ε_o , figures 7.5 c) and d) the inner eccentricities ε_i . The onset of the inner sub-synchronous is not influenced by C_o , yet the eccentricities are larger and it extends over a larger rotor speed range with smaller C_o , which is undesirable. The onset of the outer sub-synchronous is shifted to a higher rotor speed with smaller C_o .

The influences are much greater for the two-phase model, yet qualitatively similar, except for $C_o = 40 \mu\text{m}$. For $C_o = 50 \mu\text{m}$, the amplitude of Sub_i gradually decreases until it vanishes, which is also the case when using the penalty approach. For $C_o = 45 \mu\text{m}$, the amplitude decreases slowly and Sub_i suddenly bifurcates at $\approx 1.6 \text{ s}$. Sub_i does not end in the investigated rotor speed range for $C_o = 40 \mu\text{m}$ and has high eccentricities. This behavior is undesirable, since it leads to loud noise and damages in the bearing. Furthermore, this simulation took the longest calculation time due to a high amount of micro-steps in the bearing model.

The ratios of floating ring speed ω_F to rotor speed ω_R are shown in figures 7.5 e) and f). The floating ring speed increases more strongly during Sub_i for smaller C_o . This is counter intuitive, since a smaller C_o should lead to an increase of the outer, decelerating bearing torque. However, this effect is overlaid by the higher inner eccentricities. The increase of the floating ring speed is higher for two-phase model, due the slightly higher eccentricities compared to the penalty approach, which progressively increase the inner, accelerating bearing torque.

7.2.4 Supply pressure

The inclusion of a mass-conserving cavitation model allows a more accurate investigation of the lubricant supply pressure p_{sup} . Figure 7.6 shows results with three different supply pressures for the penalty approach on the left and the mass-conserving two-phase model on the right. For both cavitation models, the onset rotor-speed of the sub-synchronous oil whirls is reduced with increasing supply pressure. For the outer whirl this is due to the circumferential groove, which destabilizes the system with higher supply pressure, see section 6.4.4.2. If all bore holes have the same supply pressure, they have a similar effect, yet to a lesser extent. This explains the lower onset rotor-speed of the inner whirl. Furthermore, also the eccentricities during the inner whirl increase.

For the two-phase model, these effects are more pronounced. For $p_{\text{sup}} = p_0 = 1 \text{ bar}$, no inner whirl is present. The oscillations at $\approx 1 \text{ s}$ are due to the natural mode of the system. For higher supply pressures,

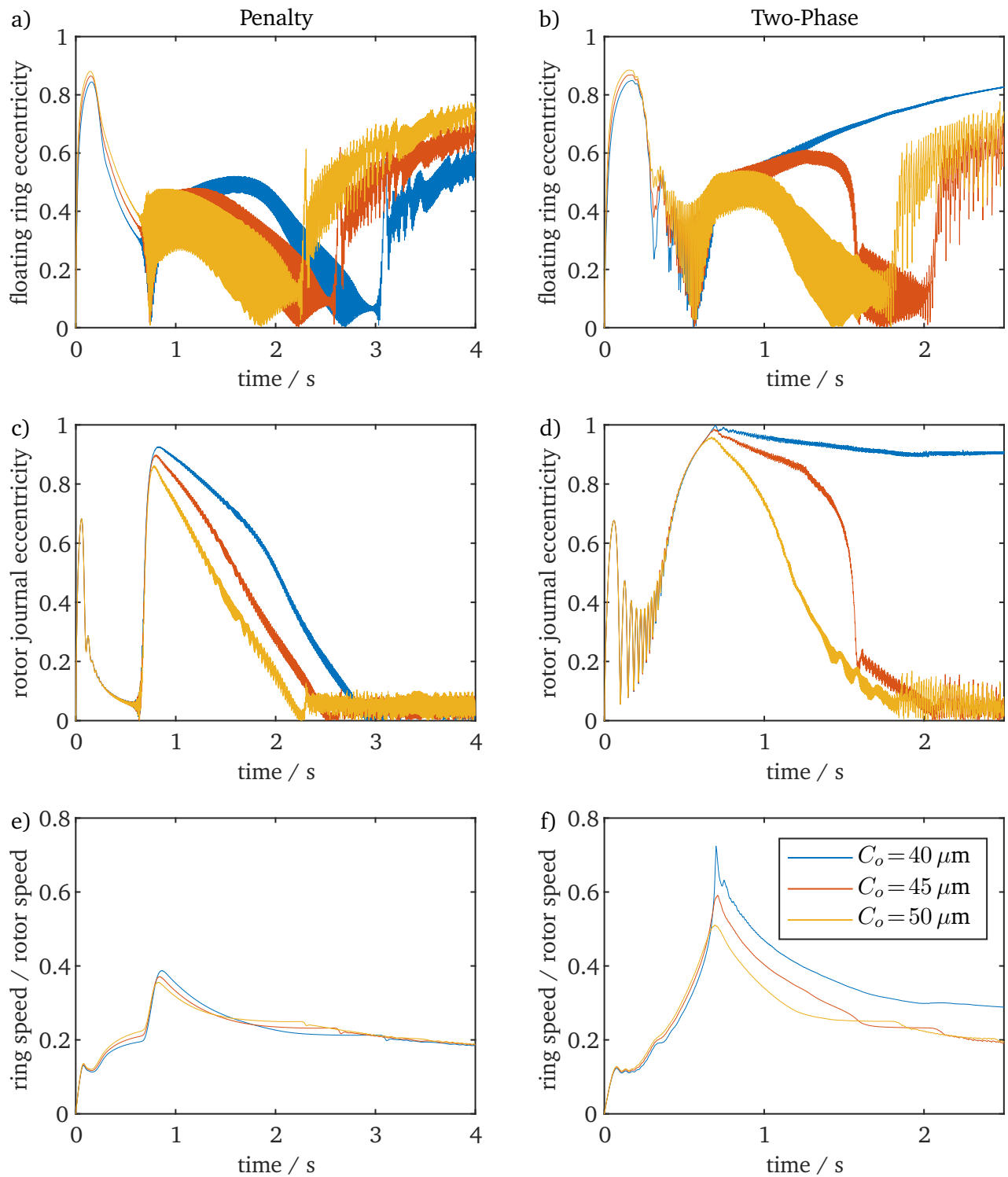


Figure 7.5.: Influence of outer gap size C_o for penalty and two-phase cavitation models

the inner eccentricity during the inner whirl is severely increased. This leads to a rapid increase of the floating ring speeds, see figure 7.6 f). Furthermore, a higher supply pressure leads to less cavitation in the bearings, while a too low supply pressure can drastically reduce the load carrying capacity, a so-called starved condition.

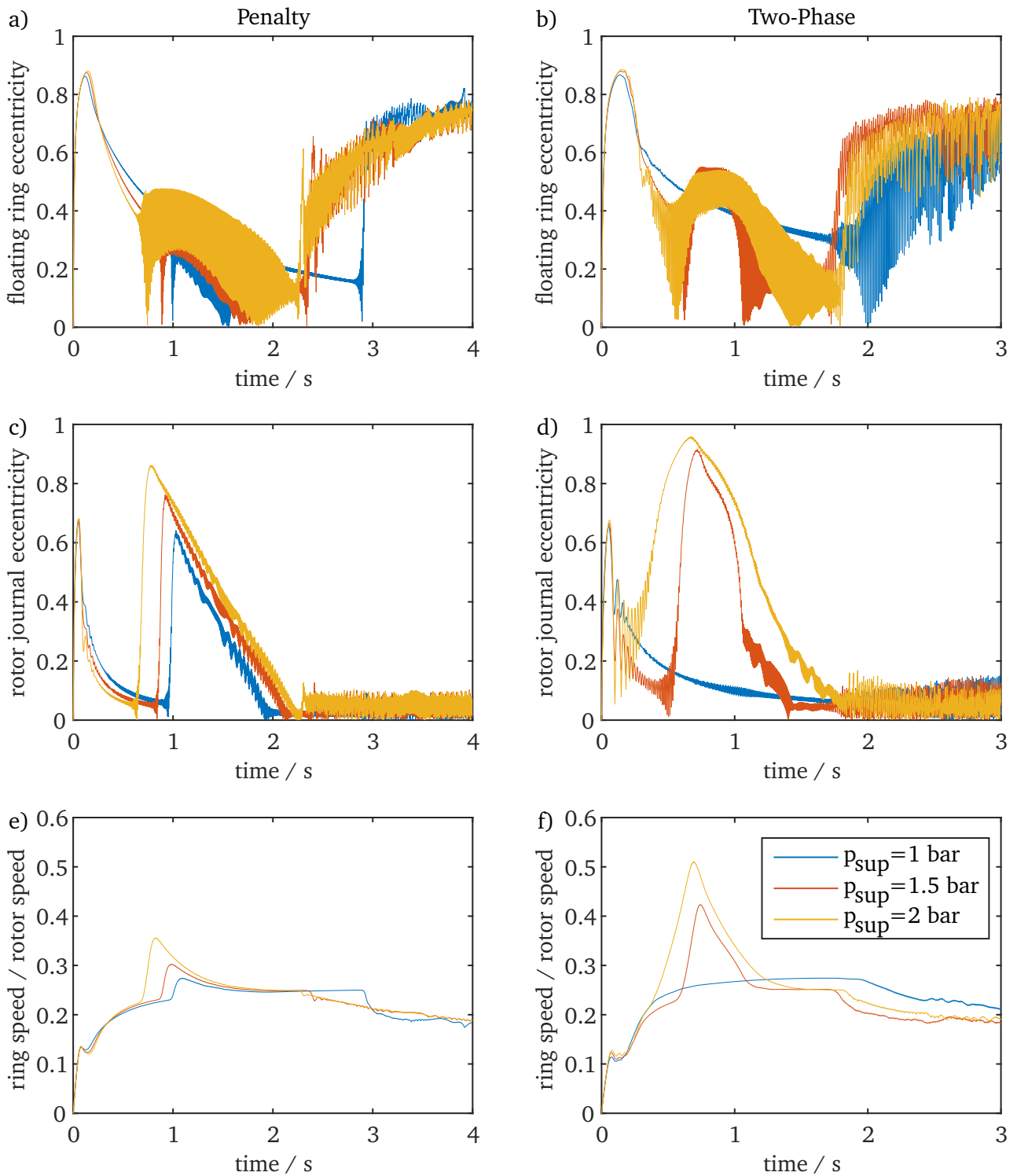


Figure 7.6.: Influence of lubricant supply pressure p_{sup} for penalty and two-phase cavitation models

7.2.5 Bearing Torque

The bearing torque given in equation (3.17) consists of two terms, which result from the shear-driven TAYLOR-COUPETTE flow and the pressure-driven HAGEN-POISEUILLE flow. The latter term is often neglected, since the shear flow dominates at high rotation speeds. Furthermore, its calculation is elaborate in approximate solutions such as short bearing or look-up tables, since the pressure profile is not explicitly calculated. In these cases, the simple formula (4.6) is often used. In a coupled simulation, where the REYNOLDS equation is solved in every time-step, the pressure-driven term can be easily calculated. Additionally, the bearing torque is reduced due to cavitation, since the lubricant film is not completely filled with liquid and gases have almost no resistance to shear stress, see section 4.2.1.4.

Both influences are investigated in figure 7.7. The mass-conserving two-phase model is used. The supply pressure is reduced to $p_{\text{SUP}} = 1.5$ bar, to increase the influence of cavitation. Three results are compared:

- *All Terms* considers TAYLOR-COUPETTE flow and HAGEN-POISEUILLE flow and the reduction due to cavitation
- *Only Couette* considers only the shear-driven TAYLOR-COUPETTE flow with reduction due to cavitation
- *One-Phase* considers both terms without reduction due to cavitation.

The outer eccentricity shown in figure 7.7 a) is very similar for all cases, only the offset rotor-speed of the inner sub-synchronous whirl is different. The influence on the inner eccentricity is analogous, with almost unchanged amplitudes and is therefore not shown here. The ratio ω_F/ω_R given in figure 7.7 b) shows almost no influence of the pressure-driven HAGEN-POISEUILLE flow on the ring speed. The floating ring speed differs only slightly when no reduction due to cavitation is considered, probably because the effects of the inner and outer films partially cancel out. When the supply pressure p_{SUP} is increased, this difference becomes even smaller, since less cavitation is present.

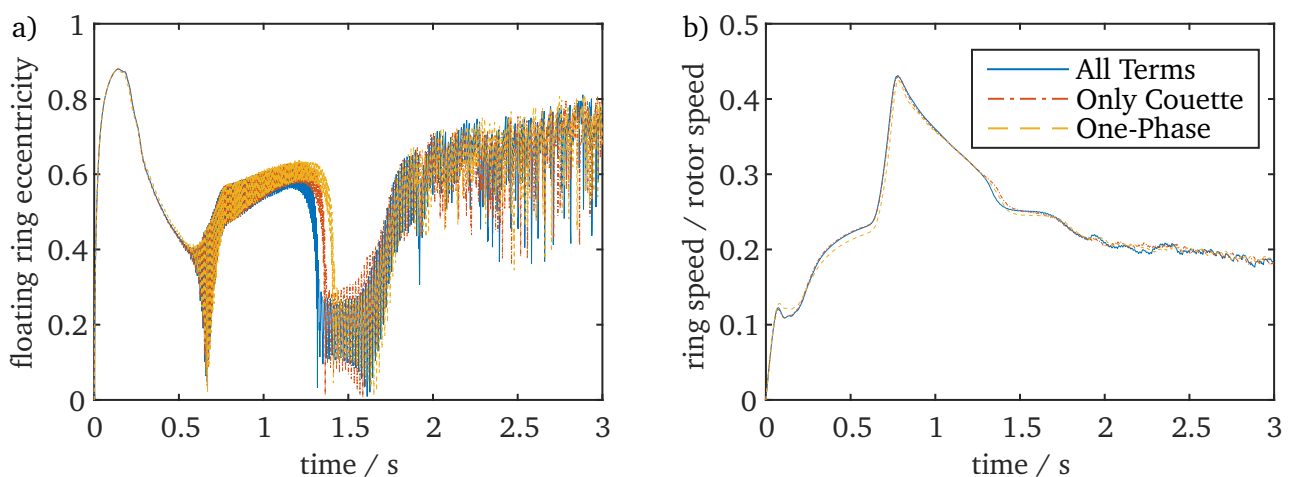


Figure 7.7.: Influence of contributing terms in the friction torque on the oscillation behavior

7.2.6 Connecting Channels

The hydraulic coupling between the outer and the inner fluid film is neglected due to the circumferential groove in the outer bearing gap, which determines the pressure in the connecting channels. However, their geometry is modeled and it is shown in section 7.2.4 that the supply pressure in the inner bearing gap has a significant influence on the rotordynamic behavior. A result with bore hole geometry according to figure 7.2 in the inner bearing gap is compared to a result obtained with plain inner surfaces of the floating ring in figure 7.8. The floating rings have a circumferential groove in their outer surface. The penalty approach is used for both simulations, since a free-to-air bearing with two-phase model and without lubricant supply geometry runs dry. The supply pressure is chosen as $p_{\text{sup}} = p_0 = 1$ bar, since no lubricant supply is present in the inner film when the inner surface of the floating ring is plain.

The outer eccentricity shown in figure 7.8 a) is very similar for both inner ring geometries, since the geometry in the outer bearing gap is not changed. One can see that the onset rotor-speed of the outer sub-synchronous whirl is slightly lower for the floating ring with plain inner surface. The inner eccentricity shown in figure 7.8 b) is larger with bore hole geometry, especially in the inner sub-synchronous whirl, whose onset rotor-speed is decreased. When a bore hole passes the hydrodynamic pressure profile, the resulting force is reduced due to the low predefined pressure. However, the effect on the hydrodynamic pressure profile is only local. The diffusion is proportional to the third power of the gap size C , see equation (3.6). Usually the gap size C is smaller for the inner bearing gap. This yields a high pressure gradient at the bores.

When the supply pressure p_{sup} is increased, the rotor-bearing system is destabilized. The hydrodynamic carrying force is diminished by the hydrostatic pressure of the bores, which generates no resulting force due to symmetry. This is analogous to bearings with circumferential grooves, see section 6.4.4.2.

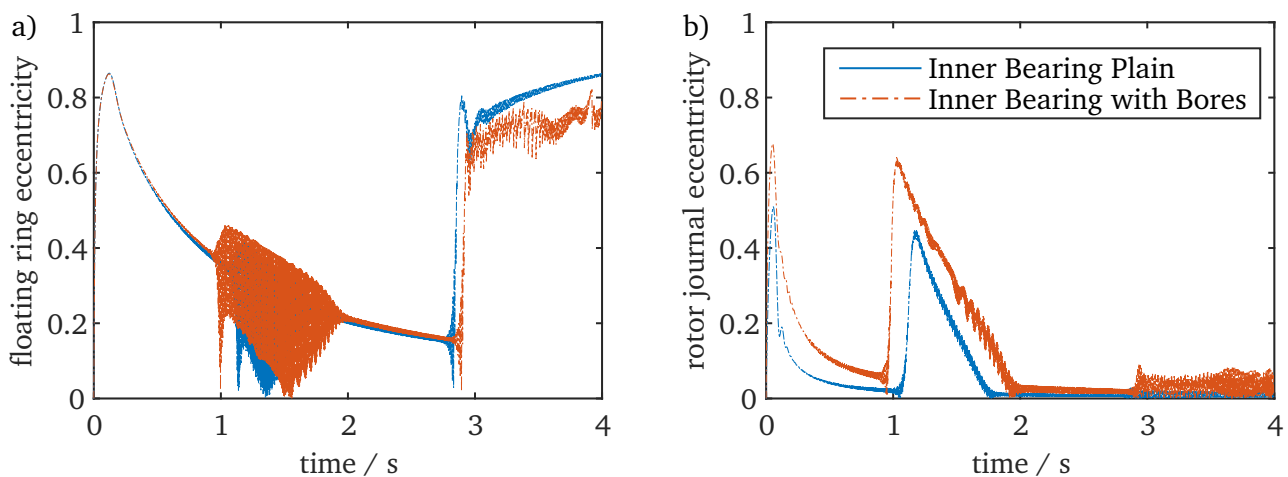


Figure 7.8.: Influence of the geometry of the inner lubricant film using the penalty approach

Furthermore, the pressure difference Δp in the connecting channels between the inner and outer fluid film due to the centrifugal acceleration of lubricant is considered, see section 4.1.5.5. The influence of Δp is investigated in figure 7.9 by comparing the result to one obtained with neglected pressure difference. The two-phase model is used for both simulations. The influence is small, since the centrifugal acceleration is small due to small radii and rotation speed of the floating rings. Only at high rotor-speeds the pressure difference Δp becomes significantly large and slightly influences the oscillations of the outer

whirl.

This test was conducted with parameters of the heavy turbocharger given in table 7.1. When a light turbocharger according to table A.1 is considered, the resulting floating ring speed is higher, yet the radii are smaller, yielding a comparable pressure difference Δp . Furthermore, bubbles start to appear in the lubricant films during sub-synchronous oscillations at high rotor-speeds, see [Köh15]. This reduces the density of the lubricant in the channels and thus Δp .

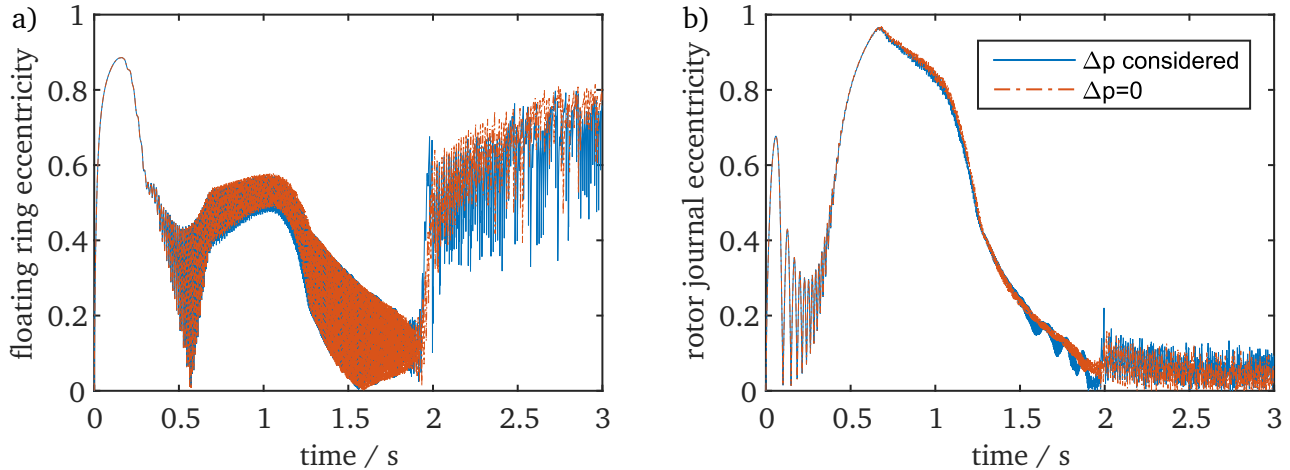


Figure 7.9.: Influence of the pressure difference Δp due to centrifugal acceleration using the penalty approach

7.3 Exhaust Turbocharger

In this section, run-up simulations of a heavy turbocharger used in large engines are performed using the penalty cavitation approach and the two-phase model. The total mass of the rotor is ≈ 6 kg. The turbine wheel weights ≈ 4 kg, the compressor wheel ≈ 1 kg. The unbalances are set to 2 gmm at the turbine wheel and 1 gmm at the compressor wheel. No external damping is applied to the rotor. The rotor speed is increased linearly from 0 to 1200 Hz in 4 s.

The floating ring bearing geometry is schematically shown in figure 7.1. The mass and the geometry parameters of the floating rings are given in table 7.1. During operation, the gap sizes change due to thermal deformation of the shaft, the floating rings and the housing. The temperatures of the solids are determined by the oil temperatures, see section 4.1.5.4. The oil supply temperature is 70°C . The oil temperatures in the outer films are assumed 75°C on the compressor and 80°C on the turbine side. The oil temperatures in the inner films are assumed 95°C on the compressor and 105°C on the turbine side. The temperatures on the turbine side are higher due to the hot exhaust gas. The *warm* gap sizes are calculated with equation (4.24). The oil viscosity also depends on the temperature and is calculated with equation (3.12). The *warm* gap sizes and *warm* oil viscosities are similar to those used for the JEFFCOTT rotor (table 7.1), yet different for the two bearings due to different temperatures.

The ambient pressure p_0 is 1 bar. The steepness parameter of the two-phase model is chosen as $x_1 = 0.9$. The lubricant supply and the boundary conditions for the lubricant films are the same as in section 7.1. Two different supply pressures p_{sup} are considered.

Three distinct sub-synchronous oscillations can occur in turbochargers supported in floating ring bearings, which are usually termed with Sub 1 to Sub 3, see [Sch10]. For a rotor with low load, the frequency of the whirl is approximately half of the effective fluid viscosity in the bearing gap, which is ω_F in the outer gap and $\omega_F + \omega_R \approx 1.3\omega_R$ in the inner gap. The whirl changes into a whip at the intersections of these frequencies with the forward modes of the rotor-bearing system. Furthermore, a jump can occur from one sub-synchronous oscillation into another or several sub-synchronous can be present at the same time. Usually, two natural modes exist in the rotor-speed range of the system, namely a conical and a cylindrical mode, see also section 2.1.3. The three sub-synchronous oscillations are characterized as follows:

- The first sub-synchronous (Sub 1) is generated by the oil whirl/whip of the inner oil film. The rotor oscillates in the conical mode. This oscillation is of little interest due to its small amplitudes and occurrence at low rotor-speeds.
- The second sub-synchronous (Sub 2) also results from the inner oil film, yet the rotor oscillates in the cylindrical mode. The frequency is high and does change slowly with increasing rotor speed, resulting in unwanted acoustics. Sub 2 is characterized by high eccentricities in the inner lubricant films.
- The third sub-synchronous (Sub 3) is generated by the oil whirl/whip of the outer oil film. The rotor again oscillates in the conical mode. The amplitude of the rotor oscillation is usually very high, yet the frequencies are low. Sub 3 is characterized by high eccentricities in the outer lubricant films and does not vanish for increasing rotor-speed.

7.3.1 Supply pressure 2 bar

Firstly, the oil supply pressure p_{sup} is set to 2 bar. Figures 7.10 a) – d) show the outer and inner eccentricities. All three sub-synchronous oscillations are present in both results. Sub 1 begins at ≈ 0.2 s (i.e. 60 Hz rotor speed) and is only little affected by the cavitation model. Sub 1 ends at ≈ 1.1 s (i.e. 330 Hz) for the penalty approach and at ≈ 0.9 s (i.e. 270 Hz) for the two-phase model. The onset of Sub 2 directly follows the end of Sub 1. Sub 2 begins at a lower rotor speed and has higher amplitudes for the two-phase model. This behavior corresponds to that of the inner sub-synchronous of the symmetric JEFFCOTT rotor in floating ring bearings. Due to the higher weight of the turbine wheel compared to the compressor wheel, the eccentricities at the onset of Sub 2 change less suddenly on the turbine side. The amplitudes of Sub 2 rise with increasing rotor speed. For the two-phase model, unstable motions appear at ≈ 1.5 s (i.e. 450 Hz). Sub 2 suddenly ends at ≈ 1.9 s (i.e. 570 Hz) for the two-phase model. This bifurcation is not present in the result obtained with the penalty approach. The amplitudes of Sub 3 are almost equal for both cavitation approaches, yet its onset is at a lower rotor speed when the two-phase model is considered (≈ 3.3 s with penalty approach and ≈ 2.5 s for the two-phase model, i.e. 990 Hz and 750 Hz, respectively). This behavior corresponds to that of the outer sub-synchronous of the JEFFCOTT rotor in floating ring bearings. The run-up using the two-phase model is only performed up to 3 s (i.e. 900 Hz rotor speed) due to the reduced onset speed of Sub 3.

The ratios between the floating ring speed and the rotor speed are shown in figures 7.10 e) and f). For both cavitation approaches, the floating ring speed on the compressor side is higher due to the higher

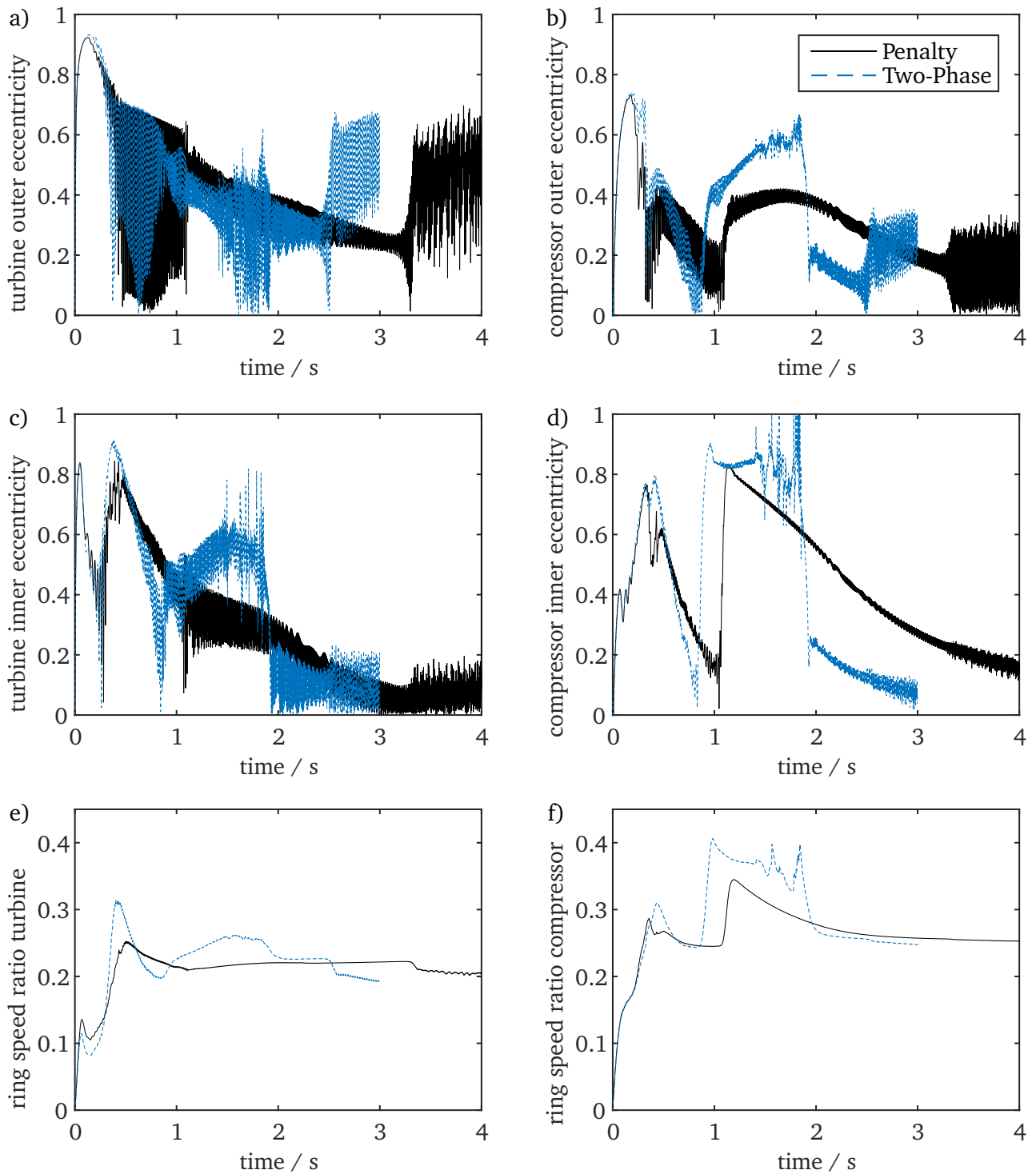


Figure 7.10.: Comparison of penalty and mass-conserving cavitation model for an exhaust turbocharger with $p_{sup} = 2$ bar

inner eccentricity on this side, which increases the accelerating torque of the inner lubricant film, and the lower outer eccentricity on this side, which decreases the decelerating torque of the outer lubricant film. Differences in the floating ring speeds for the two cavitation models directly correlate with differences in the eccentricities. The lower torque of the two-phase model due to a partially filled lubricant film seems to have little effect on the ring speed.

The frequency contents of the results are investigated in figures 7.11 g) and h) using a short time FOURIER

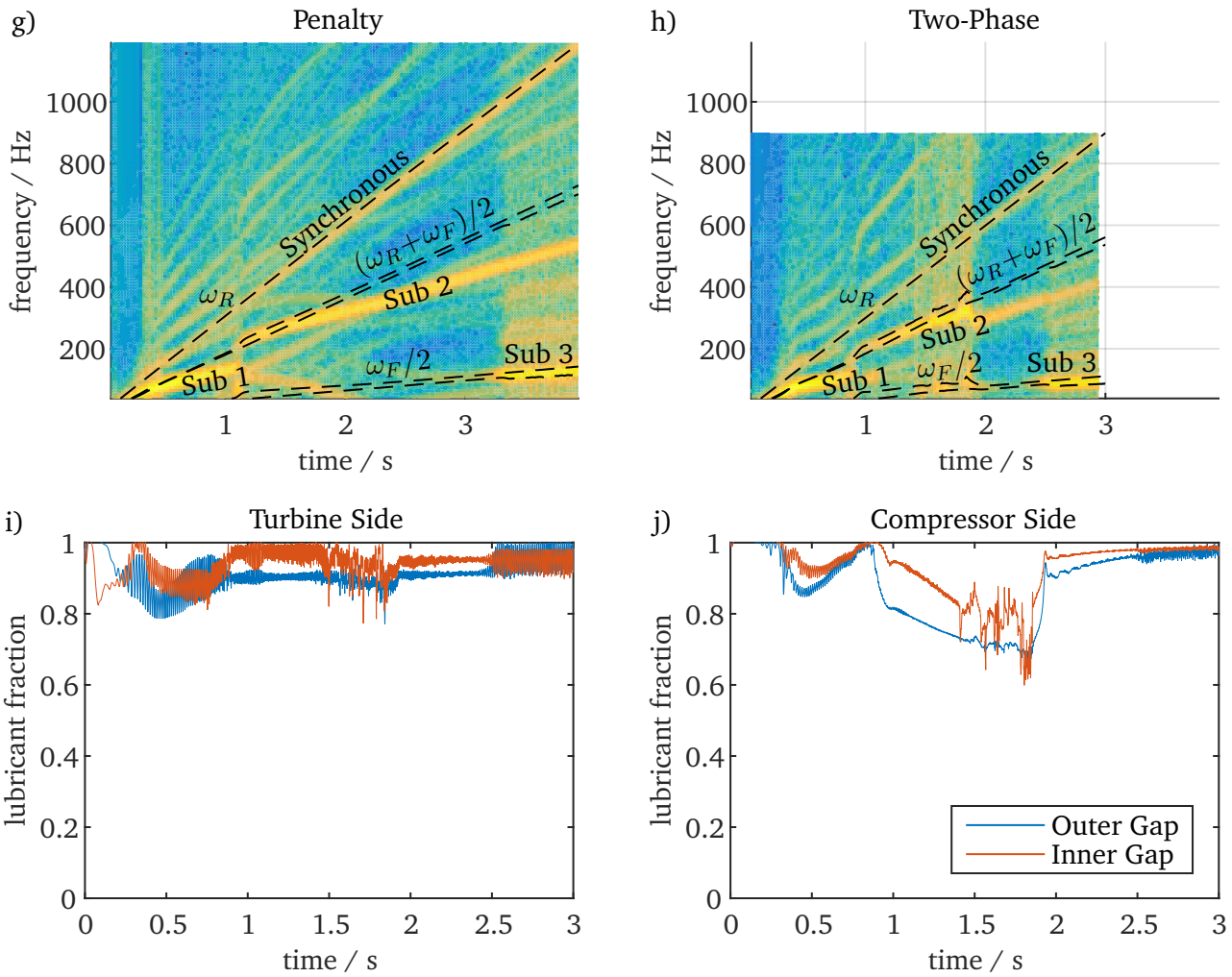


Figure 7.11.: Comparison of penalty and mass-conserving cavitation model for an exhaust turbocharger with $p_{\text{sup}} = 2$ bar (continued)

transform. The synchronous oscillations due to unbalance can be seen over the whole rotor speed range. Sub 1 – Sub 3 are clearly visible, furthermore many combination frequencies with low amplitudes can be seen. Sub 1 starts with an oil whirl, whose frequency correlates with $(\omega_R + \omega_F)/2$. At ≈ 0.5 s (i.e. 150 Hz rotor speed), this frequency locks into the conical mode of the rotor and becomes an oil whip. Sub 2 also starts with an oil whirl, which becomes an oil whip as soon as $(\omega_R + \omega_F)/2$ locks into the cylindrical mode of the rotor. The frequency of the mode changes over time due to the nonlinearity of the bearings, which entails a rotor-speed-dependent stiffness. Sub 2 is present up to the maximum rotor speed. Sub 3 is a whirl in the investigated rotor speed range, whose frequency correlates with $\omega_F/2$. The onset rotor speeds of Sub 2 and especially Sub 3 are lower for the two-phase model, yet the frequencies are similar due to the similar floating ring speeds. A different behavior of Sub 2 at ≈ 1.9 s (i.e. 570 Hz) for the two-phase model is probably due to a synchronization effect.

Figures 7.11 i) and j) show the lubricant fraction in the whole bearing gap over time, i.e. $\int_A \vartheta(t) dA$, which is only available in the mass-conserving two-phase model. Cavitation is present in both lubricant films over the whole rotor speed range. The relative lubricant fraction is lower in the outer gaps. However, the volume of the outer gap is ≈ 1.5 times larger and thus the absolute amount of oil is higher. The lubricant fraction decreases during Sub 1 and Sub 2. Since the lubricant fraction is 1 at the lubricant supply per definition ($p_{\text{sup}} > p_0$), the only possible source of air has to be sucking-in from the surroundings.

The pressure difference Δp due to centrifugal forces stays well below $p_{\text{sup}} - p_0 = 1$ bar during the whole rotor speed range, thus sufficient lubricant supply is also present at the oil bores in the inner film. The lower lubricant fraction on the compressor side is caused by the higher eccentricities due to the lower static load.

7.3.2 Supply pressure 1.2 bar

Now, a low oil supply pressure of $p_{\text{sup}} = 1.2$ bar is considered. Low supply pressure can yield insufficient lubricant supply, also called starvation. This is especially critical in the inner bearing gaps due to lubricant supply through small communication bore holes. The outer bearing gap is usually supplied through a large pocket which extends over a large portion of the bearing. Furthermore, often circumferential grooves in the floating ring are used to further distribute the lubricant, which is also the case for the investigated turbocharger. If not enough lubricant is present to support the rotor, the solid surfaces are not completely separated by lubricant and mixed friction occurs. This is not considered in the present lubrication model and large eccentricities lead to numerical difficulties. Thus, only the influence of smaller, but still sufficient lubricant supply is investigated.

Again, run-up simulations with the penalty approach and the mass-conserving two-phase model are performed. Figures 7.12 a)–d) show the outer and inner eccentricities. The influence of the supply pressure is small for the penalty approach. Only the onset of Sub 3 occurs at a significantly higher rotor speed of 1110 Hz at ≈ 3.7 s. The result obtained with the two-phase approach on the other hand is heavily affected by the lower supply pressure. The inner eccentricities differ from those of the penalty approach also at low rotor speeds. Large oscillations are present, which vanish suddenly at ≈ 1.3 s (i.e. 390 Hz rotor speed). The turbocharger performs small oscillations up to the onset rotor speed of Sub 3, which is not significantly influenced by the supply pressure.

The ratios between the floating ring speed and the rotor speed are shown in figures 7.12 e) and f). The differences between the two cavitation models again correlate with the different eccentricities. The floating ring speed ratio of the two-phase model changes less over the rotor speed range than for the higher supply pressure. Again, the influence of the eccentricities is dominant over the reduced friction torques due to smaller lubricant fractions.

The short time FOURIER transforms are shown in figures 7.13 g) and h). The result obtained with the penalty approach is only slightly influenced by the supply pressure, except the earlier onset rotor speed of Sub 3. For the two-phase model, the bifurcation behavior is different. Sub 1 extends up to ≈ 1.3 s (i.e. 390 Hz rotor speed). The amplitudes of Sub 2 are low, thus the oscillations are almost purely synchronous between ≈ 1.3 s and ≈ 2.5 s (i.e. 390 Hz and 750 Hz). Sub 2 vanishes completely with the onset of Sub 3 for the two-phase model.

The lubricant fractions of the two-phase model over time are shown in figures 7.13 i) and j). The different behaviors on the turbine and compressor side are due to the different loads on the bearings caused by the asymmetry of the turbocharger. Less oil is present in the inner and the outer film on the heavily loaded turbine side compared to $p_{\text{sup}} = 2$ bar over the whole rotor speed range. This is due the high oscillations of Sub 1. The amount of air does only slightly increase during the synchronous motion starting at ≈ 1.3 s. The motions of the journal and the floating ring have a larger radial squeeze component, which leads to sucking-in of air and prevents the reformation of the lubricant film. On the lightly loaded compressor side, the lubricant fraction is only reduced during sub-synchronous oscillations of Sub 1 and Sub 3. The lubricant fraction suddenly decreases with sub-synchronous oscillations and quickly returns to 1 as soon

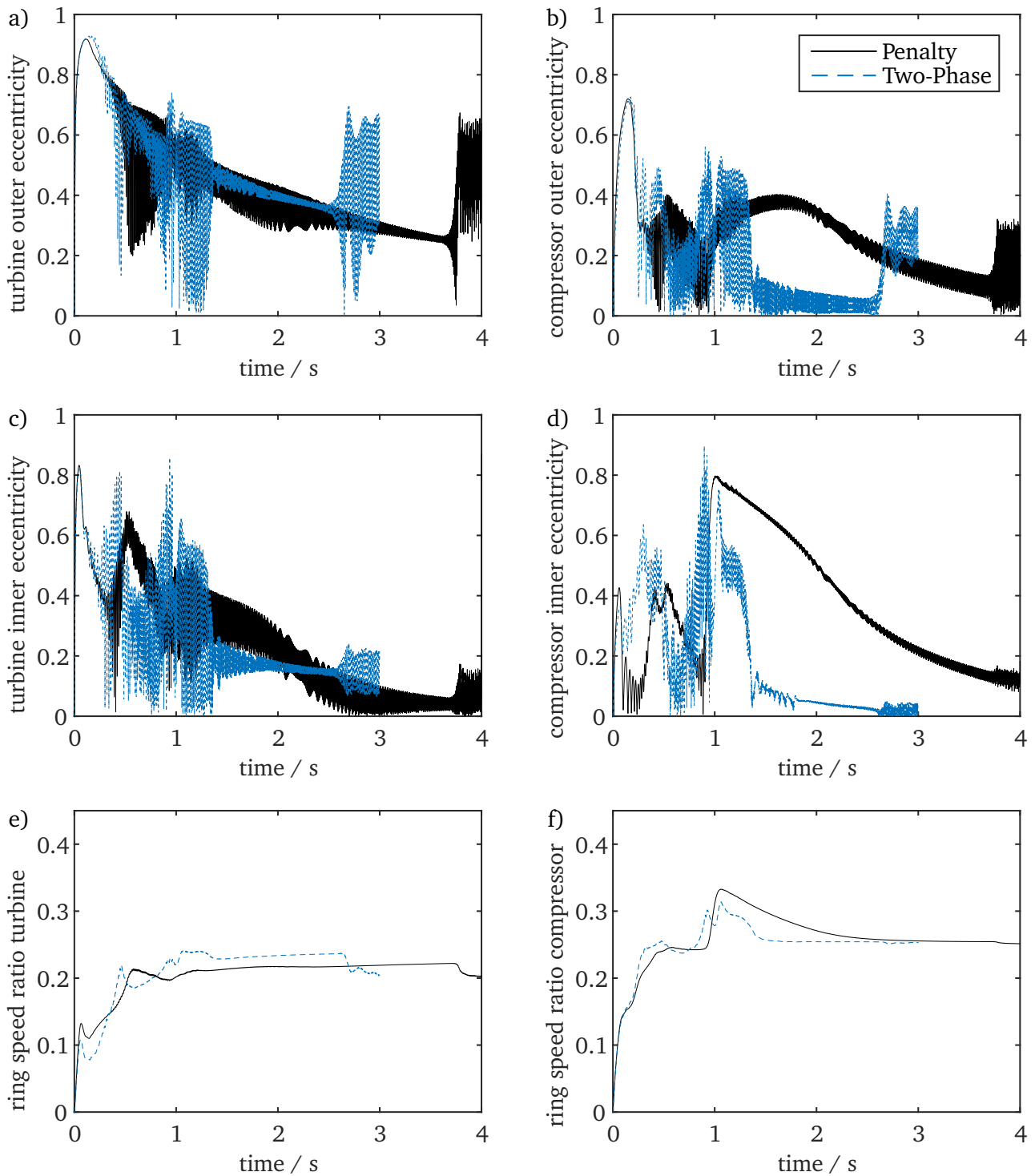


Figure 7.12.: Comparison of penalty and mass-conserving cavitation model for an exhaust turbocharger with $p_{sup} = 1.2$ bar

as mostly synchronous oscillations are present, similar to the result with higher supply pressure. The journal and the floating ring perform mostly circular motions with little squeeze in radial direction.

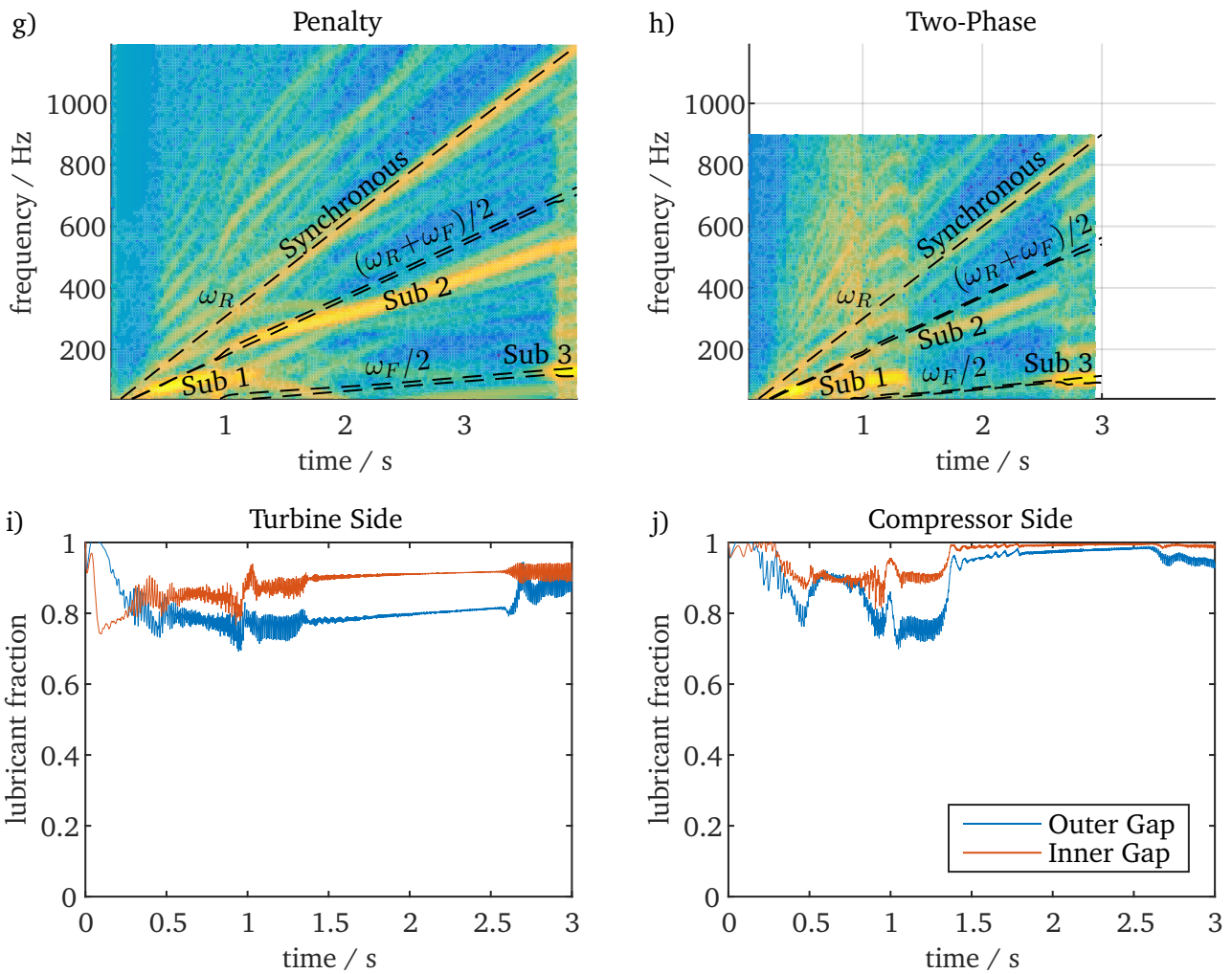


Figure 7.13.: Comparison of penalty and mass-conserving cavitation model for an exhaust turbocharger with $p_{sup} = 1.2$ bar (continued)

8 Conclusion

In this work, the influences of lubricant supply geometry and a mass-conserving cavitation model on the nonlinear oscillation behavior of rotors in single lubricant film journal bearings and in floating ring bearings have been investigated numerically by means of transient run-up simulations. The time-dependent rotor and bearing models have been implemented in commercial software tools with implicit solvers, which have been coupled using an explicit co-simulation approach. This procedure facilitates the development of detailed, easily interchangeable and updateable subsystems by specialized engineers with specialized software tools.

8.1 Summary

A literature review given in section 1.1 showed that cavitation effects in journal bearings have been mostly investigated under steady-state operating conditions, i.e. constant or slowly changing rotor speeds with none or little synchronous oscillations due to unbalance around an equilibrium position. In this case, complimentary cavitation algorithms – which divide the fluid film into a fully developed and a cavitated area – are sufficient. Lightweight rotors such as turbochargers exhibit a highly transient behavior and sub-synchronous whirl motions are present during a large part of the operating range. Many works have investigated cavitation effects in squeeze film dampers, where a large reduction of the damping capability has been observed. In these cases, usually a two-phase cavitation approach is employed, which considers the physical process of bubble generation and is valid in the whole fluid film.

The physical properties of the rotor models investigated in this work have been explained in chapter 2. The rotor-bearing systems are externally excited by unbalance and self-excited through the nonlinear, anisotropic hydrodynamic bearing forces. A symmetric JEFFCOTT rotor is the simplest flexible rotor, which has been used to systematically investigate the influence of mass-conserving cavitation. The behavior of turbocharger rotors is dominated by rigid body modes with slight bending. These modes in combination with the lubricant films are responsible for typically encountered sub-synchronous oscillations. An implicit BDF-method is used to solve the algebraic differential equation systems resulting from the multibody representation of the rotor systems.

The hydrodynamic lubrication theory has been revised in chapter 3. Only laminar flow is encountered in typical floating ring bearing geometries used in turbochargers. The compressible REYNOLDS equation is the basis for mass-conserving cavitation models. General formulas for the calculation of the bearing forces and the friction torque have been given. A dimensionless REYNOLDS equation with few input variables is beneficial for the dynamic-static solver coupling used for rotor-bearing models with non mass-conserving cavitation models. The number of input variables can be reduced through the introduction of a dimensionless time and further decreased for plain cylindrical bearings through a coordinate transformation.

Different types of cavitation and their physical processes have been described in section 3.3.1. Non

mass-conserving and mass-conserving cavitation models have been explained. The latter can be roughly divided into two categories. Complimentary models such as the famous ELROD algorithm divide the fluid film into two distinct areas, while two-phase models consider the whole fluid film. Usually, only the degassing of dissolved air is considered in the latter. The sucking-in of air from the surroundings may be dominant in open-ended bearings with transient journal motions.

Finally, the numerical solution of the REYNOLDS equation has been discussed. The Finite Element method has the highest flexibility concerning the geometry and is thus used in this work.

Bearing geometries commonly used in turbochargers have been described in section 4.1. Grooves and bore holes used for oil supply are not modeled as part of the hydrodynamic fluid film due to their larger gap size. The hydrostatic force generated by oil pressure in the omitted areas has to be considered separately. This has a significant influence, especially for light rotors.

Floating ring bearings form a series connection of an inner and an outer fluid film, which can be calculated individually with the general REYNOLDS equation. It is beneficial to use a coordinate system fixed to the floating ring for rotating geometries such as connecting channels or axial grooves. The thermal deformation of shaft, floating ring and housing increases the inner and reduces the outer bearing gap significantly. The influence of centrifugal acceleration on the deformation was found to be much smaller. Including the equations of motion of the floating rings into the bearing model enables co-simulation also for non mass-conserving cavitation models. This is less computationally expensive than the dynamic-static solver coupling usually employed, since no partial derivatives with respect to the coupling variables have to be computed.

In section 4.2, the mass-conserving two-phase model used in this work is explained. The mixture density and viscosity are assumed proportional to the lubricant fraction, since the density and viscosity of gas are negligible. This yields a single differential equation valid in the whole bearing gap, which is easy to implement into commercial software. An arbitrary relation between the pressure and the lubricant fraction can be used. In this work, it is tuned to reflect the ELROD algorithm using a smooth step function for better comparison with non mass-conserving cavitation models. Artificial Diffusion is necessary to achieve results without numerical oscillations for coarse discretization meshes used in run-up simulations, due to the steep gradient in the relation between pressure and the lubricant fraction.

The axial boundary conditions of the fluid film have to be changed when a two-phase model is used, since the assumption of a constant ambient pressure implies a bearing submerged in an oil bath, which is a rare case in practice. A special NEUMANN boundary condition based on a penalty approach acts as a DIRICHLET boundary condition for the fully developed fluid film and prevents inflow of liquid lubricant in the cavitated area, which better reflects an open-ended bearing. Furthermore, a reduction of the bearing torque in a cavitated lubricant film due to the negligible viscosity of gas is considered.

Comparison of the two-phase model with other cavitation approaches showed good qualitative agreement considering pure rotation. The present model yields a pressure profile similar to the ELROD model and the half-SOMMERFELD approach. For classical two-phase models based on bubble dynamics, the pressure drops far below the ambient pressure in the cavitated area, while the lubricant fraction stays high. This yields a completely different rotordynamic behavior.

Significant differences between non mass-conserving approaches and the two-phase model used in this work have been found for kinematic squeeze and whirling motions. During squeeze motion, the two-phase model shows a delayed pressure build-up when the bearing gap expands, which is stronger in open-ended bearings. Non mass-conserving cavitation models implicitly assume a completely filled bear-

ing gap at all times, which yields an instantaneous pressure build-up after load reversal. This may entail a reduced radial damping capability for the two-phase model. During whirl motion, the pressure profile has a smaller circumferential extend for the two-phase model, which may yield a lower load carrying capacity and thus higher eccentricities during sub-synchronous whirl motions.

The rotor and bearing subsystems use different solvers and have different time-step sizes. Coupling procedures are needed to inter- and extrapolate coupling variables, which are explained in chapter 5. Two different coupling methods are used in this work, namely dynamic-static solver coupling for rotor-bearing systems with non mass-conserving cavitation models, and co-simulation for systems with mass-conserving cavitation models or with floating ring bearings. The bearing subsystems dominate the calculation time of the overall systems due to the higher amount of degrees of freedom and smaller time-step sizes.

A reduction of costly calculations of the bearing subsystem for the dynamic-static solver coupling is achieved using the semi-implicit method developed by BUSCH, see[BS12]. However, many parallel evaluations of the bearing subsystems are required in order to compute the JACOBIAN for the rotor system. Co-simulation of the GAUSS-SEIDEL type computes the subsystems sequentially, yet a better stability is obtained compared to the parallel JACOBI type, due to the partially interpolation of coupling variables. The macro-step size is coupled to the rotor system (Master-Slave method).

In chapter 6, the influence of the mass-conserving cavitation model on the rotordynamic behavior has been evaluated using a JEFFCOTT rotor in single oil films. The parameters of the rotor and the bearings resemble a heavy turbocharger and its inner oil film.

Firstly, the penalty approach has been compared to the widely used half-SOMMERFELD condition. The results were very similar, especially the stability threshold is almost identical. Thus, the penalty approach has been used as a qualitative reference in this work, since the resulting pressure profiles are smooth and more similar to those obtained with the mass-conserving cavitation model.

Then, the convergence behavior of the mass-conserving cavitation model was investigated for different values of the steepness parameter x_1 . Good convergence to the ELROD model is achieved for high values of x_1 . However, the simulation time is increased considerably and the simulation may fail after the stability threshold has been reached. The results with $x_1=0.9$ differ notably from those using higher x_1 . The influence of the cavitation model on the rotordynamic stability has been investigated using a rigid rotor without unbalance. It could be seen that the sudden increase of the journal eccentricity coincides with the loss of load carrying capacity, which is caused by an increasing whirl speed $\dot{\delta}$ of the journal center.

Since the pressure can drop below the ambient pressure p_0 , flow of lubricant from the surrounding into the bearing gap has to be prevented numerically when an open-ended bearing is considered, which is the usual case in practice. It has been shown that this axial boundary condition has a significant influence on the rotordynamic behavior of the system and further reduces the stability threshold compared to a bearing in an oil bath.

The use of a mass-conserving cavitation model and the free-to-air boundary condition enables the detailed investigation of oil supply geometry and the supply pressure p_{sup} . It was found that for a bearing with lubricant supply at the top of the bearing, e.g. an axial feeding groove or a pocket, the eccentricity and the stability threshold speed increase with the supply pressure. This is due to an increased load on the journal, which is mainly induced by hydrostatic pressure. In contrast to that, the system in bearings with circumferential feeding grooves is destabilized with increasing supply pressure. In this case, the

hydrostatic pressure on the groove reduces the load carrying capacity of the bearing.

Finally, the influences of the shaft stiffness and rotor unbalance were examined. The stability threshold is decreased for a more flexible rotor and the difference between the penalty approach and the mass-conserving cavitation model is smaller. The synchronous oscillation amplitudes increase with the unbalance and are larger for the mass-conserving cavitation model.

With only one exception (figure 6.11 c)), the onset of instability is predicted at a lower rotation speed when mass-conserving cavitation is considered. The results resemble those using the penalty approach more with increasing x_1 . The differences are small during purely synchronous oscillations with small unbalance.

The influence of mass-conserving cavitation on rotors in floating ring bearings has been investigated in chapter 7. The inner and outer lubricant films are connected in a series connection, which allows rotor speeds above the linear stability threshold of a rotor in single film bearings with the same geometry due to mutual damping.

Firstly, a symmetric JEFFCOTT rotor was considered. Two sub-synchronous oscillations appear, which are caused by the inner and outer fluid films. The onset rotor speeds of the sub-synchronous oscillations are lower for the two-phase model than for non mass-conserving cavitation models. Additionally, the eccentricity during the inner sub-synchronous is larger. The outer film is less influenced by cavitation, probably due to better lubricant supply with a circumferential groove compared to bore holes in the inner film. The influence of the steepness parameter x_1 is smaller than for rotors in single film bearings. The efficiency of different cavitation models and simulation methods has been compared. Co-simulation with non mass-conserving cavitation models entails higher calculation times of one time-step of the bearing model compared to dynamic-static solver coupling, yet far more parallel computations are possible. The number of micro-steps has a large influence on the overall calculation time for co-simulation and monolithic models, especially for the two-phase model. A trade-off has to be found between the number of micro-steps and iterations of NEWTON's method, which is tuned through the maximum allowed solver step-size.

The influences of the outer gap size and the supply pressure have been examined for the penalty and the two-phase model. A lower outer gap size increases the stiffness of the considered floating ring bearings, which yields larger amplitudes and a larger speed range of the inner sub-synchronous. A higher supply pressure entails a lower onset rotor speed of both sub-synchronous oscillations, due to the destabilizing effect of circumferential grooves and bore holes. These effects are more severe for the two-phase model. Furthermore, different bifurcation scenarios can appear.

Two different effects on the bearing torque have been studied. It has been found that the pressure-driven HAGEN-POISEUILLE flow is negligible in the considered application. The influence of a reduced bearing torque due to cavitation is very small, since the effects on the inner and outer film partially cancel out. The floating ring speed is mostly determined by the inner and outer eccentricities.

The effect of the pressure difference in the connecting channels due to the centrifugal acceleration of the floating rings has only a small influence at high rotor speeds. Even if full hydraulic coupling of inner and outer oil film (no circumferential groove) is considered, the pressure profile is mainly influenced locally, see [Zei16; Nar17].

Finally, a turbocharger with two different supply pressures was considered, which experiences three sub-synchronous oscillations. The onset rotor speeds of Sub 2 and Sub 3 are lower with the two-phase model. A lower supply pressure has a small effect for the non mass-conserving penalty approach, yet the

result with the two-phase model is heavily affected. Unstable motions in the inner lubricant films appear and the bifurcation behavior is different. The lubricant fraction decreases during sub-synchronous oscillations, due to sucking-in of air from the surroundings. On the lighter loaded compressor side, more air is present due to the sudden increase of the eccentricities, yet the bearing gaps are refilled more quickly due to a weaker squeeze component of the eccentricities compared to the heavily loaded turbine side.

8.2 Outlook

The steepness parameter x_1 of the mass-conserving two-phase model was chosen close to 1 in order to reflect the often used ELROD cavitation model. It remains to be tested through experiments if this assumption is valid for lightweight rotors. Furthermore, most cavitation models available in literature and also the one used in this work assume instant degassing and reabsorption of gas. Persistent bubbly flow has been experimentally observed for high rotation speeds and during sub-synchronous whirl/whip motions, see [Köh15; ZV88]. It should be determined in future research, if the assumption that the gas is not reabsorbed in these operating conditions is a better reflection of the actual behavior. For this reason, different cavitation models could be appropriate during sub-synchronous whirl/whip motions than for purely synchronous motion. In the present model, this can be easily achieved through variation of the steepness parameter x_1 depending on the journal motion.

An important step to increase the physical accuracy of the present rotor-bearing model is the inclusion of an efficient temperature model, in order to automatically determine the transient temperature profiles in the lubricant films. This includes a (lumped) thermal model of the rotor, the housing and the floating rings as well as a thermal model of the lubricant films.

In this work, the hydraulic coupling of the inner and outer fluid film was implemented for a bearing with a circumferential groove in the outer fluid film, which is not part of the hydrodynamic fluid film. Full hydraulic coupling for plain surfaces with boreholes is easily implemented and should be investigated in detail.

A detailed investigation of starvation effects in the fluid films is only possible considering mass-conserving cavitation. However, mixed friction can occur, which is not covered in the present model.

Finally, the calculation time of the present cavitation model could be further reduced using more sophisticated stabilization approaches.

A Tables

Table A.1.: Reynolds number Re for critical turbocharger parameters, calculated with (3.3)

Application	Passenger Car Turbocharger	Large Engine Turbocharger
Rotor Weight	100 g	6 kg
max. Rotor-Speed	5000 Hz	1500 Hz
Inner Oil Film:		
Angular Velocity ω	1.3·5000 Hz	1.3·1500 Hz
Bearing Diameter D	7 mm	25 mm
Nominal Bearing Gap C	15 μm	35 μm
Oil Viscosity η	12 mPas	12 mPas
Oil Density ρ	0.9 g/cm ³	0.9 g/cm ³
Reynolds Number Re	193	482
Outer Oil Film:		
Angular Velocity ω	0.3·5000 Hz	0.3·1500 Hz
Bearing Diameter D	11 mm	40 mm
Nominal Bearing Gap C	35 μm	50 μm
Oil Viscosity η	12 mPas	12 mPas
Oil Density ρ	0.9 g/cm ³	0.9 g/cm ³
Reynolds Number Re	136	212

Table A.2.: Deformations of rotor shaft, floating ring and housing assuming a two-dimensional stress state

Application	Passenger Car Turbocharger	Large Engine Turbocharger
Rotor weight	100 g	6 kg
max. Rotor-Speed	5000 Hz	1500 Hz
Rotor Shaft (Steel):		
YOUNG's modulus E	210 GPa	210 GPa
POISSON's ratio ν	0.27	0.27
Density ρ	7870 kg/m ³	7870 kg/m ³
Thermal expansion coefficient α_T	$1.18 \cdot 10^{-5} \text{ K}^{-1}$	$1.18 \cdot 10^{-5} \text{ K}^{-1}$
Angular Velocity ω	5000 Hz	1500 Hz
Diameter D	7 mm	25 mm
Temperature $T_R = T_i$	100 °C	100 °C
Rotation Strain $\epsilon_{r,rot}$	$0.083 \cdot 10^{-3}$	$0.095 \cdot 10^{-3}$
const. Temperature Strain $\epsilon_{r,Tconst.}$	$0.944 \cdot 10^{-3}$	$0.944 \cdot 10^{-3}$
Floating Ring (Brass):		
YOUNG's modulus E	78 GPa	78 GPa
POISSON's ratio ν	0.37	0.37
Density ρ	8860 kg/m ³	8860 kg/m ³
Thermal expansion coefficient α_T	$1.85 \cdot 10^{-5} \text{ K}^{-1}$	$1.85 \cdot 10^{-5} \text{ K}^{-1}$
Angular Velocity ω	0.4 · 5000 Hz	0.4 · 1500 Hz
Inner Diameter D_i	7 mm	25 mm
Outer Diameter D_o	11 mm	40 mm
Inner Oil Temperature T_i	100 °C	100 °C
Outer Oil Temperature T_o	80 °C	80 °C
Inner Surface:		
Rotation Strain $\epsilon_{r,rot}$	$0.492 \cdot 10^{-3}$	$0.584 \cdot 10^{-3}$
Temperature Field Strain $\epsilon_{r,T}$	$1.450 \cdot 10^{-3}$	$1.450 \cdot 10^{-3}$
const. Temperature Strain $\epsilon_{r,Tconst.}$	$1.295 \cdot 10^{-3}$	$1.295 \cdot 10^{-3}$
Outer Surface:		
Rotation Strain $\epsilon_{r,rot}$	$0.271 \cdot 10^{-3}$	$0.314 \cdot 10^{-3}$
Temperature Field Strain $\epsilon_{r,T}$	$1.281 \cdot 10^{-3}$	$1.281 \cdot 10^{-3}$
const. Temperature Strain $\epsilon_{r,Tconst.}$	$1.295 \cdot 10^{-3}$	$1.295 \cdot 10^{-3}$
Housing (Cast Iron):		
POISSON's ratio ν	0.28	0.28
Thermal expansion coefficient α_T	$1.17 \cdot 10^{-5} \text{ K}^{-1}$	$1.17 \cdot 10^{-5} \text{ K}^{-1}$
Diameter D	11 mm	40 mm
Temperature $T_H = T_{sup}$	60 °C	60 °C
const. Temperature Strain $\epsilon_{r,Tconst.}$	$0.468 \cdot 10^{-3}$	$0.468 \cdot 10^{-3}$

B Extended Short Bearing Theory

The numerical calculation of the REYNOLDS equation in every time-step of a run-up simulation yields accurate results and can easily incorporate complex bearing geometries and additional effects such as mass-conserving cavitation, yet it requires a high computational effort. Analytical approximations such as the infinitely long or short bearing are very fast, yet are usually only valid for plain cylindrical bearings without additional effects and only yield good results under certain requirements.

If the diameter-to-width ratio D/B of a bearing is large, the diffusion in circumferential direction is negligible compared to the diffusion in axial direction. A rule of thumb is $D/B \geq 4$, see [Sze11]. This yields the so-called *short bearing theory* (see e.g. [Vra01; Boy11; Sze11; LS78]), which is often used in rotordynamic studies. Its application also yields acceptable results for turbochargers with smaller ratio D/B .

A very suitable application is a bearing with a circumferential groove (see section 4.1.2), since each individual hydrodynamic bearing section with width $b = B/2$ has a high ratio D/b . However, the groove pressure p_{sup} is usually higher than the ambient pressure p_0 and the classical short bearing theory is only given in literature for equal axial boundary conditions. For this reason, an extended short bearing theory with arbitrary axial boundary conditions was introduced in [Now+15b] and is given in this appendix. It was applied to a turbocharger in floating rings with circumferential grooves and the results were compared to a calculation with finite-length journal bearings using dynamic-static solver-coupling explained in section 5.1. It was shown that the extended short bearing theory yields good results for bearings with a circumferential groove while greatly reducing the calculation time.

As for the short bearing theory, a plain cylindrical bearing (gap function $H = 1 + \varepsilon \cos \Theta$, see e.g. [LS78]) without tilting is assumed. If the diffusion in circumferential direction is neglected, the dimensionless REYNOLDS equation (3.19) for one bearing section simplifies to an ordinary differential equation,

$$\left(\frac{R}{B}\right)^2 \frac{\partial}{\partial \bar{z}} \left(H^3 \frac{\partial \Pi}{\partial \bar{z}} \right) = \varepsilon(2\delta' - \Omega_0) \sin(\Theta) + 2\varepsilon' \cos(\Theta) = f_{\text{rhs}}(\Theta). \quad (\text{B.1})$$

Note that the relative angular coordinate Θ starting at the widest gap is used, see figure 3.2. Equation (B.1) is integrated twice with respect to \bar{z} . The axial boundary conditions are

$$\Pi(\Theta, \bar{z}=0) = \Pi_0 \quad \text{and} \quad \Pi(\Theta, \bar{z}=0.5) = \Pi_{\text{sup}}, \quad (\text{B.2})$$

see figure 4.1. The periodic boundary condition (3.10) is already satisfied due to the periodicity of the gap function H . This yields an analytical expression for the pressure profile $\Pi(\Theta, \bar{z})$ with the SOMMERFELD cavitation condition:

$$\Pi(\Theta, \bar{z}) = \frac{1}{2} \left(\frac{B}{R}\right)^2 \frac{f_{\text{rhs}}(\Theta)}{H(\Theta)^3} \bar{z} \left(\bar{z} - \frac{1}{2} \right) + \Pi_0 (1 - 2\bar{z}) + \Pi_{\text{sup}} 2\bar{z}. \quad (\text{B.3})$$

The dimensionless hydrodynamic bearing forces generated by one bearing section are calculated using (3.27), in which the upper integration boundary of \bar{z} is replaced by 0.5.

In the classical short bearing theory, the non mass-conserving half-SOMMERFELD (GÜMBEL) cavitation approach is applied by only integrating over regions where $p \geq p_0$. Since $\Pi_0 = \Pi_{\text{sup}} = 0$ is assumed, the boundaries of the cavitated area are straight lines in axial direction and their positions in Θ -direction can be calculated as a function of ε , ε' and δ' . Closed-form solutions of the appearing integrals are given in literature, see e.g. [LS78].

The cavitation boundaries are complex for the asymmetric boundary conditions (B.2), see e.g. figure 6.12 b). In this case, an analytical integration of (B.3) is rather sophisticated and thus a numerical integration was used in [Now+15b]. The resulting calculation time is slightly larger than for the analytical short bearing solution, yet far lower than the calculation time of the discretized REYNOLDS equation for finite bearings.

Bibliography

- [AF81] P.E. Allaire and R.D. Flack. “Design of journal bearings for rotating machinery”. In: *10th Turbomachinery Symposium, College Station, TX, December*. 1981, pp. 1–3.
- [AME80] M. Akkok and C.M. McC. Ettles. “The effect of grooving and bore shape on the stability of journal bearings”. In: *ASLE Transactions* 23.4 (1980), pp. 431–441.
- [ANG77] P.E. Allaire, J.C. Nicholas, and E.J. Gunter. “Systems of finite elements for finite bearings”. In: *ASME Journal of Lubrication Technology* 99.2 (1977), pp. 187–194.
- [AOE15] S. Alakhramsing, R. van Ostayen, and R. Eling. “Thermo-Hydrodynamic Analysis of a Plain Journal Bearing on the Basis of a New Mass Conserving Cavitation Algorithm”. In: *Lubricants* 3.2 (2015), pp. 256–280.
- [BAG77] L.E. Barrett, P.E. Allaire, and E.J. Gunter. “Stability and dynamic response of pressurized journal bearings with nuclear water pump applications”. In: *Annals of Nuclear Energy* 4.2-3 (1977), pp. 115–126.
- [Bar10] D. Bartel. *Simulation von Tribosystemen: Grundlagen und Anwendungen*. In German. Vieweg+Teubner research. Vieweg Verlag, Friedrich & Sohn Verlagsgesellschaft mbH, 2010.
- [Bau11] K. Baumann. “Dynamische Eigenschaften von Gleitlagern in instationären An- und Auslaufvorgängen”. In German. PhD thesis. Technische Universität Darmstadt, 2011.
- [BBK89] D.E. Brewster, J.H. Ball, and M.M. Khonsari. “Current research in cavitating fluid films”. In: *STLE Special Publication* 28 (1989).
- [Ber+17] L. Bernhauser et al. “The Effect of Non-Circular Bearing Shapes in Hydrodynamic Journal Bearings on the Vibration Behavior of Turbocharger Structures”. In: *Lubricants* 5.1 (2017), p. 6.
- [BH10] M.J. Braun and W.M. Hannon. “Cavitation formation and modelling for fluid film bearings: a review”. In: *IMEchE Journal of Engineering Tribology* 224.9 (2010), pp. 839–863.
- [BH84] M.J. Braun and R.C. Hendricks. “An experimental investigation of the vaporous/gaseous cavity characteristics of an eccentric journal bearing”. In: *ASLE Transactions* 27.1 (1984), pp. 1–14.
- [Bob08] L. Bobach. “Simulation dynamisch belasteter Radialgleitlager unter Mischreibungsbedingungen”. In German. PhD thesis. Otto-von-Guericke-Universität Magdeburg, 2008.
- [Boe10] S. Boedo. “Mass conserving cavitation effects in squeeze-film journal bearings subjected to sinusoidal loads”. In: *Tribology Transactions* 54.1 (2010), pp. 21–35.
- [Boy11] A. Boyaci. “Zum Stabilitäts- und Bifurkationsverhalten hochtouriger Rotoren in Gleitlagern”. In German. PhD thesis. Karlsruher Institut für Technologie, 2011.
- [Bre86] D.E. Brewster. “Theoretical modeling of the vapor cavitation in dynamically loaded journal bearings”. In: *ASME Journal of Tribology* 108 (1986), pp. 628–638.

-
- [BS12] M. Busch and B. Schweizer. “Coupled simulation of multibody and finite element systems: an efficient and robust semi-implicit coupling approach”. In: *Archive of Applied Mechanics* 82.6 (2012), pp. 723–741.
- [BS15] A. Boyaci and B. Schweizer. “Nonlinear oscillations of high-speed rotor systems in semi-floating ring bearings”. In: *IFTToMM 9th International Conference on Rotordynamics, Milan, Italy*. Springer. 2015, pp. 845–854.
- [BS17] A. Boyaci and W. Seemann. “Vibro-acoustical behavior of a turbocharger housing excited by oil-film-induced rotor oscillations”. In: *SIRM 2017 – 12th International Conference on Vibrations in Rotating Machines, Graz, Austria, February 15th–17th*. 2017.
- [Bus12] M. Busch. “Zur effizienten Kopplung von Simulationsprogrammen”. In German. PhD thesis. Universität Kassel, 2012.
- [Bus16] M. Busch. “Continuous approximation techniques for co-simulation methods: Analysis of numerical stability and local error”. In: *ZAMM – Journal of Applied Mathematics and Mechanics* 96.9 (2016), pp. 1061–1081.
- [Car92] V.P. Carey. *Liquid-vapor phase-change phenomena*. Hemisphere, New York, NY (United States), 1992.
- [Cha+16] I. Chatzisavvas et al. “On the influence of thrust bearings on the nonlinear rotor vibrations of turbochargers”. In: *ASME Turbo Expo 2016, Seoul, South Korea, June 13th–17th*. 2016.
- [Cha+93] K. Chamniprasart et al. “Lubrication with binary mixtures: bubbly oil”. In: *ASME Journal of Tribology* 115.2 (1993), pp. 253–260.
- [Cho+11] M. Chouchane et al. “Stability analysis of hydrodynamic bearings with a central circumferential feeding groove”. In: *IFTToMM 13th World Congress, Guanajuato, Mexico, June 19th–25th*. 2011, pp. 19–25.
- [Cra90] S. Crandall. “From whirl to whip in rotordynamics”. In: *IFTToMM 3rd International Conference on Rotordynamics, Lyon, France*. 1990, pp. 19–26.
- [Dan+13] C. Daniel et al. “Identifikation des Einfluss konstruktiver Lagerparameter eines in Schwimmbuchsen gelagerten Rotorsystems”. In German. In: *SIRM 2013 – 10th International Conference on Vibrations in Rotating Machines, Berlin, Germany, February 25th–27th*. 2013.
- [Dia99] S. Diaz. “The effect of air entrapment on the performance of squeeze film dampers: experiments and analysis”. PhD thesis. Texas A&M University, College Station, TX, 1999.
- [Die15] J. Diebener. “Einfluss thermischer und mechanischer Effekte auf das Stabilitätsverhalten von ATL-Gleitlagerungen”. In German. PhD thesis. Technische Universität Clausthal, 2015.
- [Dow+85] D. Dowson et al. “An analysis of the circumferentially grooved journal bearing with consideration of lubricant film reformation”. In: *IMEchE Journal of Mechanical Engineering Science* 199.1 (1985), pp. 27–34.
- [DR06] W. Dahmen and A. Reusken. *Numerik für Ingenieure und Naturwissenschaftler*. In German. Springer-Verlag, 2006.
- [DSA01a] S. Diaz and L. San Andrés. “A model for squeeze film dampers operating with air entrapment and validation with experiments”. In: *ASME Journal of Tribology* 123.1 (2001), pp. 125–133.

-
- [DSA01b] S. Diaz and L. San Andrés. “Air entrainment versus lubricant vaporization in squeeze film dampers: an experimental assessment of their fundamental differences”. In: *ASME Journal of Engineering for Gas Turbines and Power* 123.4 (2001), pp. 871–877.
- [DSA98] S. Diaz and L. San Andrés. “Measurements of pressure in a squeeze film damper with an air/oil bubbly mixture”. In: *Tribology Transactions* 41.2 (1998), pp. 282–288.
- [DT79] D. Dowson and C.M. Taylor. “Cavitation in bearings”. In: *Annual Review of Fluid Mechanics* 11.1 (1979), pp. 35–65.
- [Ein05] A. Einstein. “Eine neue Bestimmung der Moleküldimensionen”. In German. PhD thesis. Universität Zürich, 1905.
- [Eli+16] R. Eling et al. “Towards Accurate Prediction of Unbalance Response, Oil Whirl and Oil Whip of Flexible Rotors Supported by Hydrodynamic Bearings”. In: *Lubricants* 4.3 (2016), p. 33.
- [Elr81] H.G. Elrod. “A cavitation algorithm”. In: *ASME Journal of Lubrication Technology* 103.3 (1981), pp. 350–354.
- [EOR15a] R. Eling, R. van Ostayen, and D. Rixen. “Multilobe Floating Ring Bearings for Automotive Turbochargers”. In: *IFTToMM 9th International Conference on Rotordynamics, Milan, Italy*. 2015, pp. 821–833.
- [EOR15b] R. Eling, R. van Ostayen, and D. Rixen. “Oil Flow in Connecting Channels of Floating Ring Bearings”. In: *SIRM 2015 – 11th International Conference on Vibrations in Rotating Machines, Magdeburg, Germany, February 23th–25th*. 2015.
- [ES10] L. Esmaili and B. Schweizer. “Fully Coupled Thermo-Hydrodynamic Simulation Model for Journal Bearings”. In: *Proceedings Applied Mathematics and Mechanics*. Vol. 10. 1. Wiley Online Library, 2010, pp. 365–366.
- [ES11] L. Esmaili and B. Schweizer. “Coupling of the Reynolds Fluid-Film Equation with the 2D Navier-Stokes Equations”. In: *Proceedings Applied Mathematics and Mechanics*. Vol. 11. 1. Wiley Online Library, 2011, pp. 567–568.
- [Fel16] P. Felscher. “Rückwirkung des Gleitlagermoments auf die Drehbewegung des Rotors”. In German. PhD thesis. Technische Universität Darmstadt, 2016.
- [FH86] N.S. Feng and E.J. Hahn. “Density and viscosity models for two-phase homogeneous hydrodynamic damper fluids”. In: *ASLE transactions* 29.3 (1986), pp. 361–369.
- [FKB02] R.D. Flack, G.J. Kostrzewsky, and L.E. Barrett. “Experimental and Predicted Rigid Rotor Stability Threshold of Axial Groove and Three-Lobe Bearings”. In: *International Journal of Rotating Machinery* 8.1 (2002), pp. 27–33.
- [FL82] R.D. Flack and R.F. Lanes. “Effects of three-lobe bearing geometries on rigid-rotor stability”. In: *ASLE Transactions* 25.2 (1982), pp. 221–228.
- [Fuc02] A. Fuchs. “Schnelllaufende Radialgleitlagerungen im instationären Betrieb”. In German. PhD thesis. Technische Universität Braunschweig, 2002.
- [GE01] M. Groper and I. Etsion. “The effect of shear flow and dissolved gas diffusion on the cavitation in a submerged journal bearing”. In: *ASME Journal of Tribology* 123.3 (2001), pp. 494–500.

-
- [GE02] M. Groper and I. Etsion. “Reverse flow as a possible mechanism for cavitation pressure build-up in a submerged journal bearing”. In: *ASME Journal of Tribology* 124.2 (2002), pp. 320–326.
- [GNP02] R. Gasch, R. Nordmann, and H. Pfützner. *Rotordynamik*. In German. Springer, 2002.
- [Goo+07] M.J. Goodwin et al. “Theoretical and experimental investigation of the effect of oil aeration on the load-carrying capacity of a hydrodynamic journal bearing”. In: *IMEchE Journal of Engineering Tribology* 221.7 (2007), pp. 779–786.
- [GPP06] F.P. Grando, M. Priest, and A.T. Prata. “A two-phase flow approach to cavitation modelling in journal bearings”. In: *Tribology Letters* 21.3 (2006), pp. 233–244.
- [Hag12] T. Hagemann. “Ölzuführungseinfluss bei schnell laufenden, hoch belasteten Radialgleitlagern unter Berücksichtigung des Lagerdeformationsverhaltens”. In German. PhD thesis. Technische Universität Clausthal, 2012.
- [Hor06] Y. Hori. *Hydrodynamic Lubrication*. Springer Science & Business Media, 2006.
- [JF57] B. Jakobsson and L. Floberg. “The finite journal bearing considering vaporization”. In: *Transactions of Chalmers University of Technology Gothenburg* 190 (1957).
- [Jun17] Andreas Junghanns. *Functional Mock-up Interface (FMI)*. Online; accessed 02-Dec-2017. 2017. URL: <http://fmi-standard.org/>.
- [KB08] M.M. Khonsari and E.R. Booser. *Applied Tribology: Bearing Design and Lubrication*. Tribology in Practice Series. Wiley, 2008.
- [KB91a] A. Kumar and J.F. Booker. “A finite element cavitation algorithm”. In: *ASME Journal of Tribology* 113.2-4 (1991), p. 276.
- [KB91b] A. Kumar and J.F. Booker. “A finite element cavitation algorithm: application/validation”. In: *ASME Journal of Tribology* 113.2-4 (1991), p. 255.
- [Kir14] R.G. Kirk. “Experimental evaluation of hydrodynamic bearings for a high speed turbocharger”. In: *ASME Journal of Engineering for Gas Turbines and Power* 136.7 (2014), p. 072501.
- [KKF14] W. Köhl, M. Kreschel, and D. Filsinger. “Experimental and numerical investigations on an automotive turbocharger with a transparent bearing section”. In: *IMEchE 11th International Conference on Turbochargers and Turbocharging, London, UK, May 13th–14th*. Vol. 1384. Elsevier. 2014, p. 349.
- [Kou+15] P. Koutsovasilis et al. “Quantification of sub-synchronous vibrations for turbocharger rotors with full-floating ring bearings.” In: *Archive of Applied Mechanics* 85.4 (2015).
- [KS17] J. Kraft and B. Schweizer. “Reduction of Computation Time by Parallelization Incorporating Co-Simulation Techniques”. In: *CIMNE 2017 – 7th International Conference on Computational Methods for Coupled Problems in Science and Engineering*. 2017, pp. 779–787.
- [KSR15] A. Krinner, T. Schindler, and D.J. Rixen. “Fluid-Struktur-Kopplung in elasto-hydrodynamischen Gleitlagern”. In German. In: *SIRM 2015 – 11th International Conference on Vibrations in Rotating Machines, Magdeburg, Germany, February 23th–25th*. 2015.
- [Kuz10] D. Kuzmin. *A guide to numerical methods for transport equations*. Lecture, Friedrich-Alexander-Universität Erlangen-Nürnberg. 2010.

- [Köh15] W. Köhl. “Stabilisierung von leichten Rotoren in Schwimmbuchsenlagern durch statisch unbestimmte Lagerung”. In German. PhD thesis. Technische Universität Darmstadt, 2015.
- [LCA80] D.F. Li, K.C. Choy, and P.E. Allaire. “Stability and Transient Characteristics of Four Multi-lobe Journal Bearing Configurations”. In: *ASME Journal of Lubrication Technology* 102.3 (1980), pp. 291–299.
- [LF82] R.F. Lanes and R.D. Flack. “Effects of three-lobe bearing geometries on flexible rotor stability”. In: *ASLE Transactions* 25.3 (1982), pp. 377–385.
- [LFL82] R.F. Lanes, R.D. Flack, and D.W. Lewis. “Experiments on the stability and response of a flexible rotor in three types of journal bearings”. In: *ASLE Transactions* 25.3 (1982), pp. 289–298.
- [Li+12] X. Li et al. “Cavitation mechanism of oil-film bearing and development of a new gaseous cavitation model based on air solubility”. In: *ASME Journal of Tribology* 134.3 (2012), p. 031701.
- [LS78] O.R. Lang and W. Steinhilper. *Gleitlager: Berechnung und Konstruktion von Gleitlagern mit konstanter und zeitlich veränderlicher Belastung*. In German. Springer, 1978.
- [Mar11] R. Markert. *Rotordynamik*. In German. Lecture notes, TU Darmstadt. 2011.
- [Mer08] Ü. Mermertas. “Nichtlinearer Einfluss von Radialgleitlagern auf die Dynamik schnelllaufender Rotoren”. In German. PhD thesis. Technische Universität Clausthal, 2008.
- [Mit90] N. Mittwollen. “Betriebsverhalten von Radialgleitlagern bei hohen Umfangsgeschwindigkeiten und hohen thermischen Belastungen: theoretische Untersuchungen”. In German. PhD thesis. Technische Universität Braunschweig, 1990.
- [Nar17] F. Narrog. “Entwicklung eines Lagermodells für Schwimmbuchsenlager unter Berücksichtigung von Kommunikationsbohrungen”. In German. Bachelor thesis. Technische Universität Darmstadt, 2017.
- [NCL10] S. Naïmi, M. Chouchane, and J. Ligier. “Steady state analysis of a hydrodynamic short bearing supplied with a circumferential groove”. In: *Comptes Rendus Mecanique* 338.6 (2010), pp. 338–349.
- [NFG17] B.R. Nichols, R.L. Fittro, and C. P. Goynes. “Subsynchronous Vibration Patterns Under Reduced Oil Supply Flow Rates”. In: *ASME Turbo Expo 2017, Charlotte, USA, June 26th–30th*. 2017.
- [Nik99] J.L. Nikolajsen. “Viscosity and Density Models for Aerated Oil in Fluid-Film Bearings”. In: *Tribology Transactions* 42.1 (1999), pp. 186–191.
- [Nit+11] S. Nitzschke et al. “Simulation von Schwimmbuchsenlagerungen in Abgasturboladern”. In German. In: *Journal of Mechanical Engineering of the National Technical University of Ukraine KPI, Kiew*. 2011.
- [Nit+13] S. Nitzschke et al. “Einfluss der masseerhaltenden Kavitation auf gleitgelagerte Rotoren unter instationärer Belastung”. In German. In: *SIRM 2013 – 10th International Conference on Vibrations in Rotating Machines, Berlin, Germany, February 25th–27th*. 2013.
- [Nit+16] S. Nitzschke et al. “Regularised cavitation algorithm for use in transient rotordynamic analysis”. In: *International Journal of Mechanical Sciences* 113 (2016), pp. 175–183.

- [Nit17] S. Nitzschke. “Instationäres Verhalten schwimmbuchsenlagerter Rotoren unter Berücksichtigung masseerhaltender Kavitation”. In German. PhD thesis. Otto-von-Guericke-Universität Magdeburg, 2017.
- [Now+15a] G. Nowald et al. “Influence of axial grooves in full-floating-ring bearings on the nonlinear oscillations of turbocharger rotors”. In: *SIRM 2015 – 11th International Conference on Vibrations in Rotating Machines, Magdeburg, Germany, February 23th–25th*. 2015.
- [Now+15b] G. Nowald et al. “Influence of Circumferential Grooves on the Non-Linear Oscillations of Turbocharger Rotors in Floating Ring Bearings”. In: *IFTToMM 14th World Congress, Taipei, Taiwan, October 25th–30th*. 2015.
- [Now10] G. Nowald. “Numerische Simulation von Hoch- und Ausläufen eines magnetgelagerten Rotors mit einem Versuchsgleitlager”. In German. Bachelor thesis. Technische Universität Darmstadt, 2010.
- [NS13] H. Nguyen-Schäfer. “Nonlinear Rotordynamic Computations of Automotive Turbochargers Using Rotating Floating Ring Bearings at High Rotor Speeds”. In: *SIRM 2013 – 10th International Conference on Vibrations in Rotating Machines, Berlin, Germany, February 25th–27th*. Vol. 10. 2013, pp. 25–27.
- [NS15] H. Nguyen-Schäfer. *Rotordynamics of automotive turbochargers*. Springer, 2015.
- [NSS16] G. Nowald, R. Schmoll, and B. Schweizer. “Influence of fluid film cavitation effects on the stability of rotors in journal bearings”. In: *VIRM 11 – Vibrations in Rotating Machinery, Manchester, United Kingdom, September 13th–15th*. 2016.
- [NSS17] G. Nowald, R. Schmoll, and B. Schweizer. “Transient Run-Up Simulations of Rotors in Journal Bearings Considering Mass-Conserving Cavitation Approaches”. In: *Technische Mechanik* 37.2–5 (2017), pp. 400–408.
- [NWD17] S. Nitzschke, E. Woschke, and C. Daniel. “Dynamisches Verhalten von EHD-Kontakten unter Nutzung eines regularisierten, masseerhaltenden Kavitationsalgorithmus”. In German. In: *SIRM 2017 – 12th International Conference on Vibrations in Rotating Machines, Graz, Austria, February 15th–17th*. 2017.
- [Ols65] K.O. Olsson. “Cavitation in dynamically loaded bearings”. In: *Transactions of Chalmers University of Technology Gothenburg* 308 (1965).
- [PB85] H. Peeken and J. Benner. “Beeinträchtigung des Druckaufbaus in Gleitlagern durch Schmierstoffverschäumung”. In German. In: *VDI-Berichte* 549 (1985), pp. 373–397.
- [Phe61] R. M. Phelan. “Non-Rotating Journal Bearings Under Sinusoidal Loads”. In: *ASME Lubrication Symposium, Miami, USA, May 8th–9th*. 1961, Paper No. 61–LubS–6.
- [Pin90] O. Pinkus. *Thermal aspects of fluid film tribology*. ASME, 1990.
- [Por+14] D. Porzig et al. “Thermal analysis of small high-speed floating-ring journal bearings”. In: *IMEchE 11th International Conference on Turbochargers and Turbocharging, London, UK, May 13th–14th*. Vol. 1384. Elsevier. 2014, p. 421.
- [PS61] O. Pinkus and B. Sternlicht. *Theory of hydrodynamic lubrication*. McGraw-Hill Book Company, Inc., 1961.
- [Raj+93] K.R. Rajagopal et al. “Lubrication with binary mixtures: bubbly oil”. In: *ASME Journal of Tribology* 115.2 (1993), pp. 253–260.

-
- [Rod91] D.G. Roddeman. “Some aspects of artificial diffusion in flow analysis”. In: *Heron: Computational Mechanics: Recent Developments in DIANA 36* (1991), pp. 65–71.
- [SA+10] L. San Andrés et al. “Turbocharger nonlinear response with engine-induced excitations: predictions and test data”. In: *ASME Journal of Engineering for Gas Turbines and Power* 132.3 (2010), p. 032502.
- [SA+12] L. San Andrés et al. “On the effect of thermal energy transport to the performance of (semi) floating ring bearing systems for automotive turbochargers”. In: *ASME Journal of Engineering for Gas Turbines and Power* 134.10 (2012), p. 102507.
- [SA10] L. San Andrés. *Modern Lubrication Theory*. Lecture, Texas A&M University. 2010. URL: <http://oaktrust.library.tamu.edu/handle/1969.1/93197>.
- [SAK04] L. San Andrés and J. Kerth. “Thermal effects on the performance of floating ring bearings for turbochargers”. In: *IMEchE Journal of Engineering Tribology* 218.5 (2004), pp. 437–450.
- [SAKH17] L. San Andrés, B. Koo, and M. Hemmi. “A Flow Starvation Model for Tilting Pad Journal Bearings and Evaluation of Frequency Response Functions: A Contribution Towards Understanding the Onset of Low Frequency Shaft Motions”. In: *ASME Turbo Expo 2017, Charlotte, USA, June 26th–30th*. 2017.
- [SAV10] L. San Andrés and A. Vistamehr. “Nonlinear rotordynamics of vehicle turbochargers: parameters affecting sub harmonic whirl frequencies and their jump”. In: *IFTToMM 8th International Conference on Rotordynamics, Seoul, South Korea*. 2010.
- [SB92] D.C. Sun and D.E. Brewe. “Two reference time scales for studying the dynamic cavitation of liquid films”. In: *ASME Journal of Tribology* 114.3 (1992), pp. 612–615.
- [Sch+13] R. Schmoll et al. “Solver coupling between multibody and electro-magnetic systems”. In: *ECCOMAS Conference on Multibody Dynamics, Zagreb, Croatia, July 1st–4th*. 2013.
- [Sch+15] B. Schweizer et al. “Stabilized implicit co-simulation methods: solver coupling based on constitutive laws”. In: *Archive of Applied Mechanics* 85.11 (2015), pp. 1559–1594.
- [Sch09a] B. Schweizer. “Numerical approach for solving Reynolds equation with JFO boundary conditions incorporating ALE techniques”. In: *ASME Journal of Tribology* 131.1 (2009), p. 011702.
- [Sch09b] B. Schweizer. “Total instability of turbocharger rotors – physical explanation of the dynamic failure of rotors with full-floating ring bearings”. In: *Journal of Sound and Vibration* 328.1 (2009), pp. 156–190.
- [Sch10] B. Schweizer. “Dynamics and stability of turbocharger rotors”. In: *Archive of Applied Mechanics* 80.9 (2010), pp. 1017–1043.
- [Sch15] R. Schmoll. “Co-Simulation und Solverkopplung: Analyse komplexer multiphysikalischer Systeme”. In German. PhD thesis. Universität Kassel, 2015.
- [Sch99] M. Schäfer. *Numerik im Maschinenbau*. In German. Springer-Verlag Berlin Heidelberg, 1999.
- [Sha13] A.A. Shabana. *Dynamics of multibody systems*. Cambridge university press, 2013.

-
- [SL14] B. Schweizer and D. Lu. “Semi-implicit co-simulation approach for solver coupling”. In: *Archive of Applied Mechanics* 84.12 (2014).
- [SLL15] B. Schweizer, P Li, and D. Lu. “Explicit and Implicit Cosimulation Methods: Stability and Convergence Analysis for Different Solver Coupling Approaches”. In: *Journal of Computational and Nonlinear Dynamics* 10.5 (2015), p. 051007.
- [SM09] S. Stupkiewicz and A. Marcinişzyn. “Elastohydrodynamic lubrication and finite configuration changes in reciprocating elastomeric seals”. In: *Tribology International* 42.5 (2009), pp. 615–627.
- [SP02] F. Shi and R. Paranjpe. “An implicit finite element cavitation algorithm”. In: *Computer Modeling in Engineering and Sciences* 3.4 (2002), pp. 507–516.
- [Spu13] J. Spurk. *Strömungslehre: Einführung in die Theorie der Strömungen*. In German. Springer-Verlag, 2013.
- [SS11] R. Schmoll and B. Schweizer. “Co-simulation of multibody and hydraulic systems: comparison of different coupling approaches”. In: *ECCOMAS Conference on Multibody Dynamics, Brussels, Belgium, July 4th–7th*. 2011.
- [Sze11] A.Z. Szeri. *Fluid Film Lubrication*. Cambridge University Press, 2011.
- [Tom+10] U. Tomm et al. “Rotor dynamic analysis of a passenger car turbocharger using run-up simulation and bifurcation theory”. In: *IMEchE 9th International Conference on Turbochargers and Turbocharging, London, UK, May 19th–20th*. 2010, pp. 19–20.
- [TWP11] L. Tian, W.J. Wang, and Z.J. Peng. “Dynamic behaviours of a full floating ring bearing supported turbocharger rotor with engine excitation”. In: *Journal of Sound and Vibration* 330.20 (2011), pp. 4851–4874.
- [VAS09] M. Valasek, M. Arnold, and W. Schiehlen. “Modeling, simulation and control of mechanical systems”. In: *Simulation Techniques for Applied Dynamics* 507 (2009), pp. 75–140.
- [VK89] D. Vijayaraghavan and T.G. Keith. “Development and Evaluation of a Cavitation Algorithm”. In: *Tribology Transactions* 32.2 (1989), pp. 225–233.
- [Vra01] B.L. van de Vrande. “Nonlinear dynamics of elementary rotor systems with compliant plain journal bearings”. PhD thesis. Technische Universiteit Eindhoven, 2001.
- [Wan+17] Z. Wang et al. “The dynamic characteristic analysis of elastic ring squeeze film damper by fluid-structure interaction approach”. In: *ASME Turbo Expo 2017, Charlotte, USA, June 26th–30th*. 2017.
- [Wos+11] E. Woschke et al. “Numerical run-up simulation of a turbocharger with full floating ring bearings”. In: *Vibration Problems ICOVP 2011: the 10th International Conference on Vibration Problems*. ICOVP 2011 Supplement. 2011, p. 334.
- [Wos+15] E. Woschke et al. “Influence of bearing geometry of automotive turbochargers on the nonlinear vibrations during run-up”. In: *IFTOMM 9th International Conference on Rotordynamics, Milan, Italy*. Springer. 2015, pp. 835–844.
- [WR17] Y. Wang and X. Ren. “Investigation of air-oil-thermal distribution in floating bush bearings”. In: *ASME Turbo Expo 2017, Charlotte, USA, June 26th–30th*. 2017.

-
- [Wu86] S.R. Wu. “A penalty formulation and numerical approximation of the Reynolds-Hertz problem of elastohydrodynamic lubrication”. In: *International Journal of Engineering Science* 24.6 (1986), pp. 1001–1013.
- [Zei16] M. Zeitler. “Untersuchung des Einflusses von Kommunikationsbohrungen auf das Verhalten von Rotoren in Schwimmbuchsenlagern”. In German. Master thesis. Technische Universität Darmstadt, 2016.
- [ZV88] F.Y. Zeidan and J.M. Vance. “Cavitation effects on the pressure distribution of a squeeze film damper bearing”. In: *NASA, Lewis Research Center, Rotordynamic Instability Problems in High-Performance Turbomachinery*. 1988, pp. 111–132.

Publications

G. Nowald, A. Boyaci, R. Schmoll, P. Koutsovasilis, N. Driot and B. Schweizer. “Influence of axial grooves in full-floating-ring bearings on the nonlinear oscillations of turbocharger rotors”. In: *SIRM 2015 – 11th International Conference on Vibrations in Rotating Machines*, Magdeburg, Germany, February 23th–25th (2015).

G. Nowald, A. Boyaci, R. Schmoll, P. Koutsovasilis and B. Schweizer. “Influence of Circumferential Grooves on the Non-Linear Oscillations of Turbocharger Rotors in Floating Ring Bearings”. In: *IFTOMM World Congress*, Taipeh, Taiwan, October 25th–30th (2015).

G. Nowald, R. Schmoll and B. Schweizer. “Influence of fluid film cavitation effects on the stability of rotors in journal bearings”. In: *VIRM 11 – Vibrations in Rotating Machinery*, Manchester, United Kingdom, September 13th–15th (2016).

I. Chatzisavvas, G. Nowald and B. Schweizer. “Experimental and Numerical Investigations of Turbocharger Rotors on Full-Floating Ring Bearings with Circumferential Oil-Groove”. In: *ASME Turbo Expo 2017: Turbomachinery Technical Conference and Exposition*, Charlotte, NC, USA, June 26th–30th (2017).

G. Nowald, R. Schmoll and B. Schweizer. “Transient Run-Up Simulations of Rotors in Journal Bearings Considering Mass-Conserving Cavitation Approaches”. In: *Technische Mechanik* 37.2–5, pp. 400–408 (2017).

Curriculum Vitae

Personal Information

Name: Gerrit Edgar Nowald
Date and place of birth: 18.03.1987 in Darmstadt

School Education

1993 – 1997 Grundschole Nieder-Ramstadt
1997 – 2006 Ludwig-Georg-Gymnasium, Darmstadt

University Education

10/2006 – 12/2012 Mechanical Engineering studies at Technische Universität Darmstadt
10/2009 – 02/2010 Bachelor-Thesis at the Institute for Structural Dynamics of Prof. R. Markert at Technische Universität Darmstadt
08/2010 – 01/2011 Study abroad at Technische Universiteit Eindhoven, the Netherlands
06/2012 – 12/2012 Master-Thesis at the Institute for Mechatronic Systems in Mechanical Engineering of Prof. S. Rinderknecht at Technische Universität Darmstadt

Work Experience

04/2009 – 06/2009 Internship at Volkswagen, Wolfsburg
09/2011 – 12/2011 Internship at Volkswagen, Wolfsburg
01/2013 – 12/2017 Research Assistant at the Institute of Applied Dynamics of Prof. B. Schweizer at Technische Universität Darmstadt
since 01/2018 Computation Engineer at Continental, Frankfurt am Main